Positron Emission Particle tracking of inclusions in cast liquid metals

By

David John Burnard

A thesis submitted to the College of Engineering
and Physical Sciences of
TheUniversity of Birmingham
For the degree of
Doctor of Philosophy

School of Metallurgy and Materials
College of Engineering and Physical Sciences
The University of Birmingham
Birmingham B15 2TT
United Kingdom
July 2014

ABSTRACT

Non metallic inclusions in cast components cause many problems, they reduce mechanical strength, create nucleation sites for fatigue cracks and metal processing problems, both when machining and rolling. It is thought that control of larger inclusions, which are typically the defects which cause such problems, can be achieved with a greater understanding of the movement of inclusion particles within the liquid metal.

Nuclear imaging techniques are routinely used in the medical field, and the Positron Emission Tomography (PET) technique is used in conjunction with a glucose based radioactive tracer to show metabolic activity in patients. This imaging technique can also be used with metals following a casting operation and can give some insight into the final location of suitably radioactively labelled particles.

A development based on the same technology used in PET can be used to track particles in opaque liquids or granular solids, this technique has been named Positron Emission Particle Tracking (PEPT). The PEPT process can be used to display the path taken by particles, allowing experiments investigating the dynamic movement of particles in a manner not possible by PET, due to the protracted timescales necessary to generate PET images.

Alumina and silica, two major forms of inclusions found in both steel and aluminium, can be used in conjunction with an indirect (water based) radioactive labelling technique. (This technique creates particles with far more radioactive ^{18}F, than it is possible to create by direct bombardment of the particles themselves). The use of artificially introduced radioactive particles labeled in this manner, allows the use of the PEPT technique through a reasonable thickness (100mm Al or 20mm steel) of molten metal. The particles are used as analogues of naturally occurring inclusions, allowing the study of inclusion transport, and its mechanisms.

A greater understanding of the PEPT process in dense materials, both its capabilities and its limitations has been achieved. PEPT is dependant upon the γ-ray attenuation placed between a tracer particle and the detectors of a positron camera.and a lower limit for the radioactivity requirement for the positron camera used, was determined.

This work builds upon the previous experience using PEPT in metal casting, the process itself was verified by recovering a particle from the location it had been tracked to during an experiment. An increase in the maximum temperature used with the process was also achieved. The work also studied the effectiveness of ceramic foam filters, showing the proportion of particles which passed through a number of ceramic foam filter with pore sizes ranging from 10 to 30ppi. The passage of inclusions through an open topped launder was also physically studied; A new geometry for a PEPT positron camera was developed specifically for this purpose. In addition to the physical experiments a computer model was written which gives some additional insight into the behaviour of these particles travelling through the launder. The model shows particles within the steady state flow of an industrial launder, into which a baffle was placed in the path of both the metal and the particles. The physical experiment described above matched the geometry of the simulation and direct comparisons between the two were drawn.

ACKNOWLEDGMENTS

I would like to thank Dr W.D.Griffths for his supervision and the opportunity to work towards this degree, Professor D.Parker for his assistance and the use of the facilities of the school of physics and Engineering and Physical Sciencies Research Council (EPSRC) for thier financial support.

I would like to thank Dr T.W. Leadbeater for the use of the mobile PEPT camera, and his time and effort making this work both in old and new configurations, Dr J. Gargiuli for his assistance making radioactive particles.

I thank my parents for their support, particularly during my illness.

I would like to thank Ms M.Higham for last minute proof reading.

I would like to thank Mr P. Cranmer for his advice, support and coffee during the course of my PhD.

Finally I would like to thank Mr A.Caden for his physical assistance with the experiments and his unique form of advice and encouragement.

Table of Contents

EXPERIMENTAL PROCEDURE

DISCUSSION

CONCLUSIONS

FURTHER WORK

APPENDICES

REFERENCES

List of Figures

Page

Page

List of Tables

Chapter 1
INTRODUCTION

1. Introduction

PET (Positron Emission Tomography) is a method using positron annihilation used to create images of processes in which a positron emitting tracer can be observed over an extended period of time. PET has been used for a considerable period of time in medical physics, where it is used to make scans of the human body, to show where a radioactive tracer accumulates, indicating the operation of various organs. In the medical world, a radioactive glucose substitute is used as a tracer, which concentrates in areas of high metabolic activity.

PEPT (Positron Emission particle Tracking) is a relatively new process, and uses components from PET machines to build a device called a positron camera. The positron camera does not generate images as PET scanners do but it can track a point source of radioactivity from a positron emitting radioactive tracer.

These two processes show promise in their industrial applications, e.g., washing machines, mills, fluidised beds and in preliminary studies of inclusions in liquid metals. Previous studies have shown that particles can be tracked in liquid metal, however the scale upon which the process has been demonstrated has been limited, as has the maximum temperature.

These two scenarios are a challenge for the PEPT process because elevated temperatures reduce the efficiency of the detectors, whilst the metal acts as an attenuating barrier to the gamma rays emitted as a result of positron-electron annihilations. This means these

processes can only work though a limited depth of liquid metal and the PEPT process has not yet been applied to studying inclusion removal techniques in situations representative of industrial conditions.

Inclusions in castings reduce quality, and are the source of many fatigue cracks. Al_2O_3 and SiO_2 inclusions larger than 60μm are a major cause of problems in shape casting of both aluminium and steel, DC casting of light alloys, and continuous casting of steel.

It was intended that by a combination of experiment and simulation that the advantages of the positron-emitting processes could be investigated and that some insights into inclusion transport could be obtained.

The objectives of this work were to increase the temperature at which the PEPT process could be used, and to perform inclusion removal experiments both with ceramic foam filters in shape castings and baffles in launders representing the DC casting process.

The fundamental work to increase the working temperature of the process, has been held back by the difficulties imposed by the susceptibility of the detectors, the high radioactivity levels required, and the physical restrictions caused by the high γ-ray attenuation of the metals of interest. Solving these problems will allow future investigations using metals commonly used such as aluminium and steel.

The work using ceramic filters will show if these devices effectively filter inclusions from metal. The restrictions to these experiments are primarily the particle sizes that can physically be radioactively labeled and physically handled. The radioactive particle sizes currently

available are equivalent to very large inclusions and their passage through filters to date has been observed by metallography, which has limitations regarding locating and quantifying these macro inclusions. The work using baffles in launders was aimed at advancing the use of the process to include hot, dense liquid materials. Previous work with liquid metals was carried out in shape castings or at low temperature. In order to increase the value of this work a simulation of the particles in the same launder system was developed and compared with the physical results.

Chapter 2
LITERATURE REVIEW

2.1 Positron Emission Tomography (PET)

2.1.1 The Positron Emission Tomography Process

2.1.1.1 Overview of the PET process

Positron Emission Tomography is the name given to a process which can be used to create images showing the location and concentration of positron emitting radioactive isotopes after projection onto an imaginary plane. The process starts with a radionuclide which emits positrons. Positon emission decay is referred to as β+ decay, in which atoms which have an excess proton for their mass achieve equilibrium within the nucleus by converting a proton into a neutron. A side effect of this conversion is that the nucleus needs to lose the charge of the proton, and to do this a positron is emitted. The positron is emitted from the nucleus with an inconsistent energy level within a spread of energies up to a maximum value. The equation for the conversion of a proton to a neutron, releasing a positron and a neutrino, is as follows;

$$ {}_{1}^{1}p^{+} \rightarrow {}_{0}^{1}n + {}_{1}^{0}\beta^{+} + \nu \qquad \text{Eq. 1.} $$

.

Particle	symbol
Proton	p^+
Neutron	N
Positron	β^+
Neutrino	N

Table 1. Sub atomic particles involved with positron annihilation (see Eq. 1).

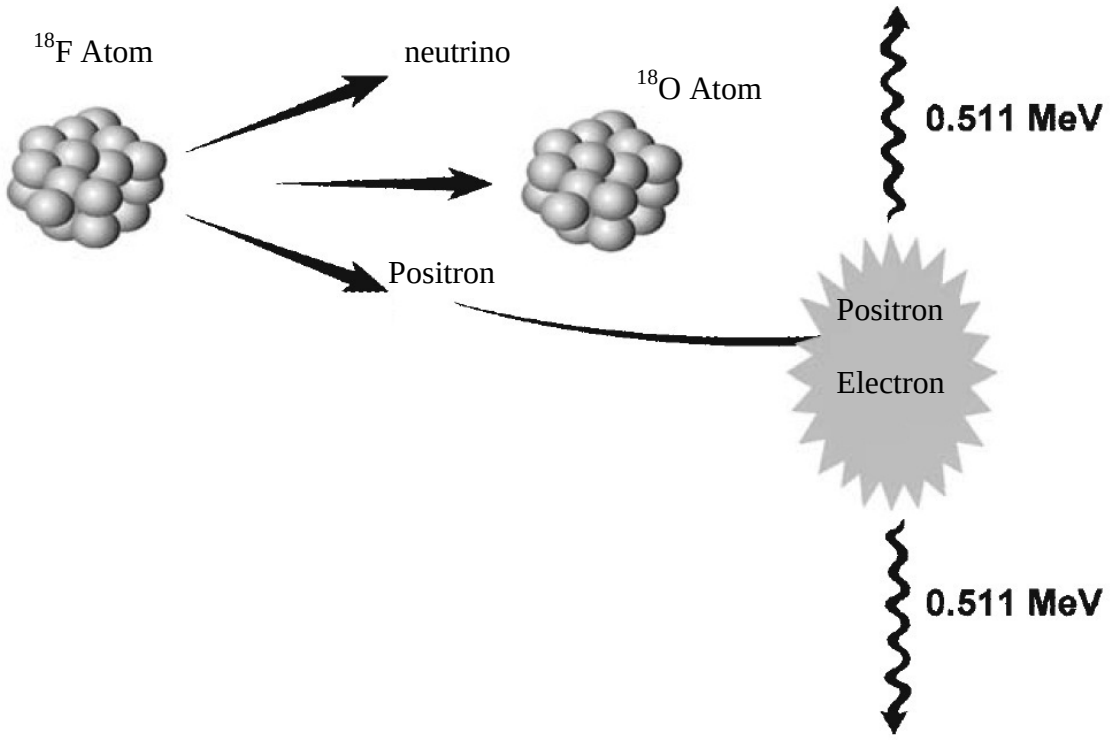

Figure 1 Beta + decay process by positron emission and annihilation [1]

After being ejected from the nucleus the positron is at a high energy but quickly loses momentum through interactions with other nuclei and electrons. These scattering events cause the positron to lose its energy in ionisation events with the surrounding matter, by inelastic scattering where it emits Bremsstrahlung radiation. Bremsstrahlung (braking) radiation is the energy given off when a charged particle changes direction, this typically results in X-rays being emmited as positrons decelerate within a material. The path a positron takes due to these ionisation events is very convoluted and therefore difficult to predict from the energy level it started with. The positron loses a large proportion of its kinetic energy within 0.5 picoseconds [2] and travels within the bulk of the material at thermal energies, the charge of the positron means it is repelled by any nucleus and it eventually annihilates with an electron, (see Fig 1). Each material has its own "positron lifetime", the average time

between the positrons emission and its annihilation, though for dense materials such as metals this is typically around 500 picoseconds, in which time the positron can move anything up to a millimetre.

The annihilation event creates two nearly back to back γ photons which travel through the material until they strike the detectors of the PET scanner, a neutrino is also emitted but this is inconsequential for PET. Due to the conservation of momentum the γ photons are not exactly back to back, the positron in the collision is travelling at thermal energies, but the electron has a considerable motion from its orbit around the nucleus, this provides a momentum which causes the γ-photons to deviate (by less than 0.5^{o}), from being truly back-to-back. The detectors of a PET scanner are commonly made of bismuth germinate oxide. They interact with the γ-photons and emit visible light photons as a consequence. The visible light photons are then recorded using photo detectors and coincidence matching electronics. If two light photons are detected nearly simultaneously they are said to be co-incidence matched, and are counted. The PET scanner collects the data in the form of a collection of coincident events from pairs of detectors. These points, once defined, are connected together to give a dataset consisting of many Lines of Response (LOR). The co-incidence matching in early PET scanners was of the order of several nanoseconds and was sufficient to accept or reject a line of response from the detected γ-rays. Newer PET scanners have better temporal resolution and can isolate the source of the detected γ-rays to a section of a Line of Response based on the timing difference of the two received photons and the calculated "time of flight".

From this dataset an image can be reconstructed, the most common reconstruction method being the filtered backprojection algorithm. This is a discrete implemention, equivalent to

Fourier analysis for continuous sampling. In this technique, the data is converted from its polar co-ordinate form as collected, to a 2D Cartesian grid which then has a Fast Fourier Transform applied to it to extract the image data.

Iterative reconstruction methods have been developed to allow for detector geometries other than the conventional complete continuous rings, used in the majority of scanners. To directly manipulate 3D datasets extensive processing is required, which is computationally and financially expensive [3].

There are several sources of error in PET, due to the positron annihilation occurring up to a millimetre from the positron emission event and the reliance upon photons from an annihilation event arriving at the detectors within a small time window, without suffering any deflection to their original path after being emitted from the positron annihilation event. Photons which travel through the material without deflection are known as "true events", see Fig 2.

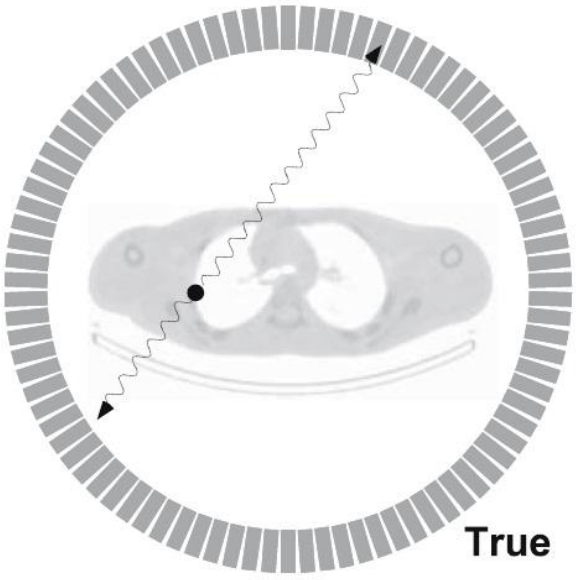

Figure 2 A true coincidence event in Positron Emission Tomography [3]

In practice annihilation γ-photons can be scattered by a process called Compton scattering. This process transfers energy from the photon to an electron which is ejected from its parent atom (these γ-photons are referred to as scatter, see Fig 3). The deflection in the path of the photon is proportional to the energy transferred to the electron which caused the scattering event. The deflected γ-rays arrive at the PET detectors and give a Line of Response, which is out of position, adding an error into the data which is later used to create a PET image. These scattered events are recorded because of the inability of the detectors to discriminate between the energy level of the γ-rays. γ rays scattered by ionization events, which are the majority of scattering events, reduce the energy of the photon and these scattered events could be removed from the collected data if the energy discrimination of the detectors was higher.

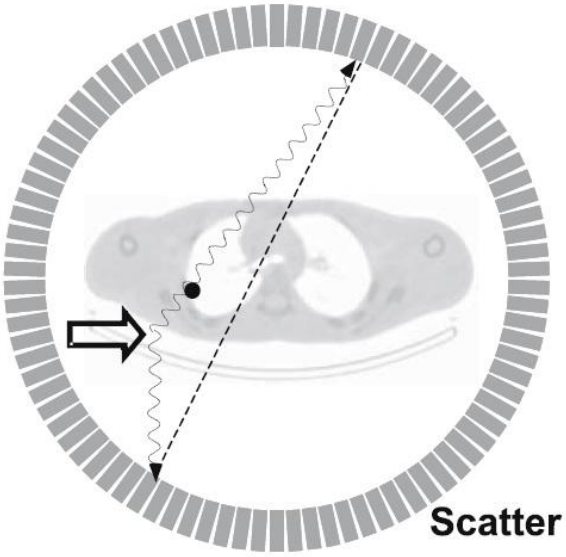

Figure 3. A scattered coincidence event in Positron Emission Tomography [3]

Another error source in PET is when two or more γ rays from a different origin strike the detectors simultaneously, A mismatch of the detected end points gives a Line Of Response (LOR) which is not related to the true position of the tracer, but is an artefact of the process, and are referred to as random events, see Fig 4.

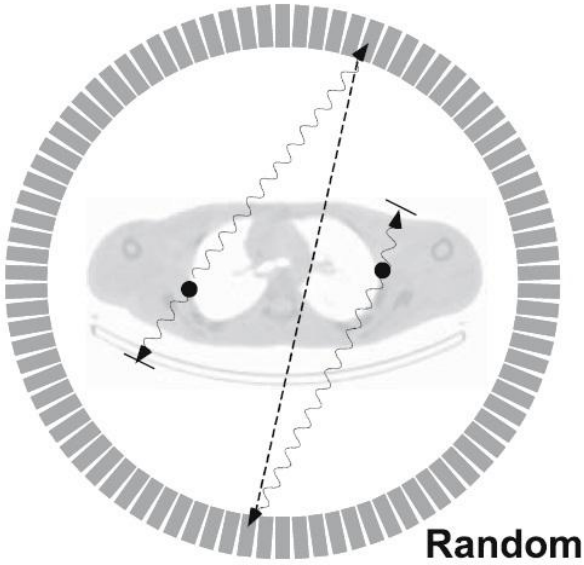

Figure 4. A random coincidence event in Positron Emission Tomography [3]

It is also possible for γ rays to simultaneously strike the detectors in such a manner that it is not possible to assign a line of response due to an obvious confusion as to which detector strikes are from the same source (these are known as multiple events, see Fig 5)

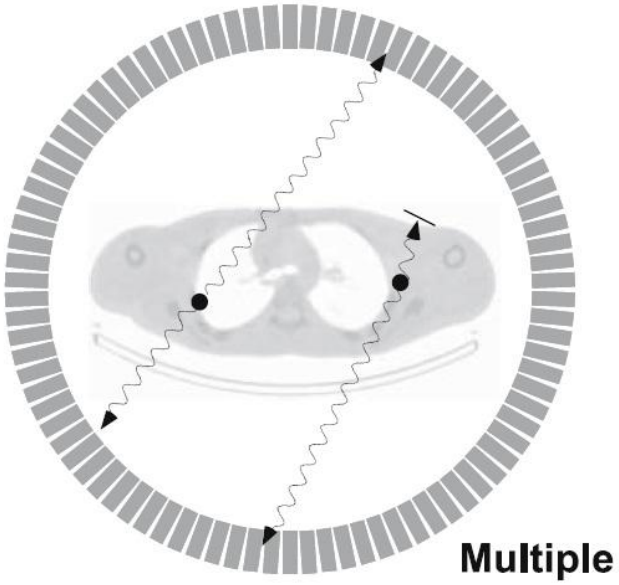

Figure 5 Multiple simultaneous coincidence events in PET [3]

2.2 Positron Emission Particle Tracking (PEPT)

There is a problem with studying opaque materials, in that only the surface can be observed, in order to observe the action of particles within these materials another technique is required, PEPT is one such technique.

The equipment used for Positron Emission Particle tracking (PEPT) is derived from the components of Positron Emission Tomography machines, routinely used in medical imaging scanners. The device used for PEPT to track particles is normally called a positron camera.

2.2.1 The Positron Emission Particle Tracking Process

2.2.1.1 Overview of the PEPT process

In PEPT a radioactive tracer is used to label a particle, enabling it to be tracked as it moves within an opaque material, whether this is a granular material or a fluid. The process relies upon the same phenomena as PET in that when a positron from the tracer and an electron collide they annihilate and emit a pair of γ-rays which are almost co-linear. The radioactive isotope used to label the tracer must therefore decay by β+ decay, (also known as positron emission). A large number of isotopes could therefore be used for this tracking process, however for safety and storage reasons, those with a reasonably short half life (from 20 minutes to 2 hours) are favoured.

As in PET, a positron is emitted by a radioactive isotope but in PEPT this isotope is attached to a particle, called a tracer, the emitted positron travels within the bulk of the material until it encounters an electron, creating γ-ray pairs.

The γ-rays produced are derived from the energy of the positron and electron involved in the collision. The positron is emitted at high velocity from the nucleus (for F^{18} it can have an energy up to 633 keV) [3] but almost all of the energy above the rest mass of the positron is absorbed within 0.5ps by coulomb interactions [2]. By the time the positron and electron collide they each have the same energy of 511keV and the γ-rays produced are also 511 keV each. (and in addition a neutrino is emitted [3]). Each pair of γ-rays is emitted at a random angle and the distance the positron can travel before annihilation means the γ-rays are all emitted within 1mm of the isotope attached to the tracer.

The γ-rays travel through the material and eventually strike the detectors of the positron camera, which converts them into light, which is subsequently detected by photo multiplier tubes, in the same manner as PET, to create a Line of Response.

By detecting a large number of LOR events and knowing that the particle lies close to the intersection of all of them it is possible to determine the location of the radioactive tracer. Any line defined by a LOR lies within 1mm of the tracer, and the tracer is a finite size typically 600μm to 3mm, The intersection of the lines of response is therefore defined as a volume which is within 1 to 2 mm of the tracer centre. If the sample size of LOR events is increased, the centre of the particle can statistically be located with increasing accuracy (See Fig 6).

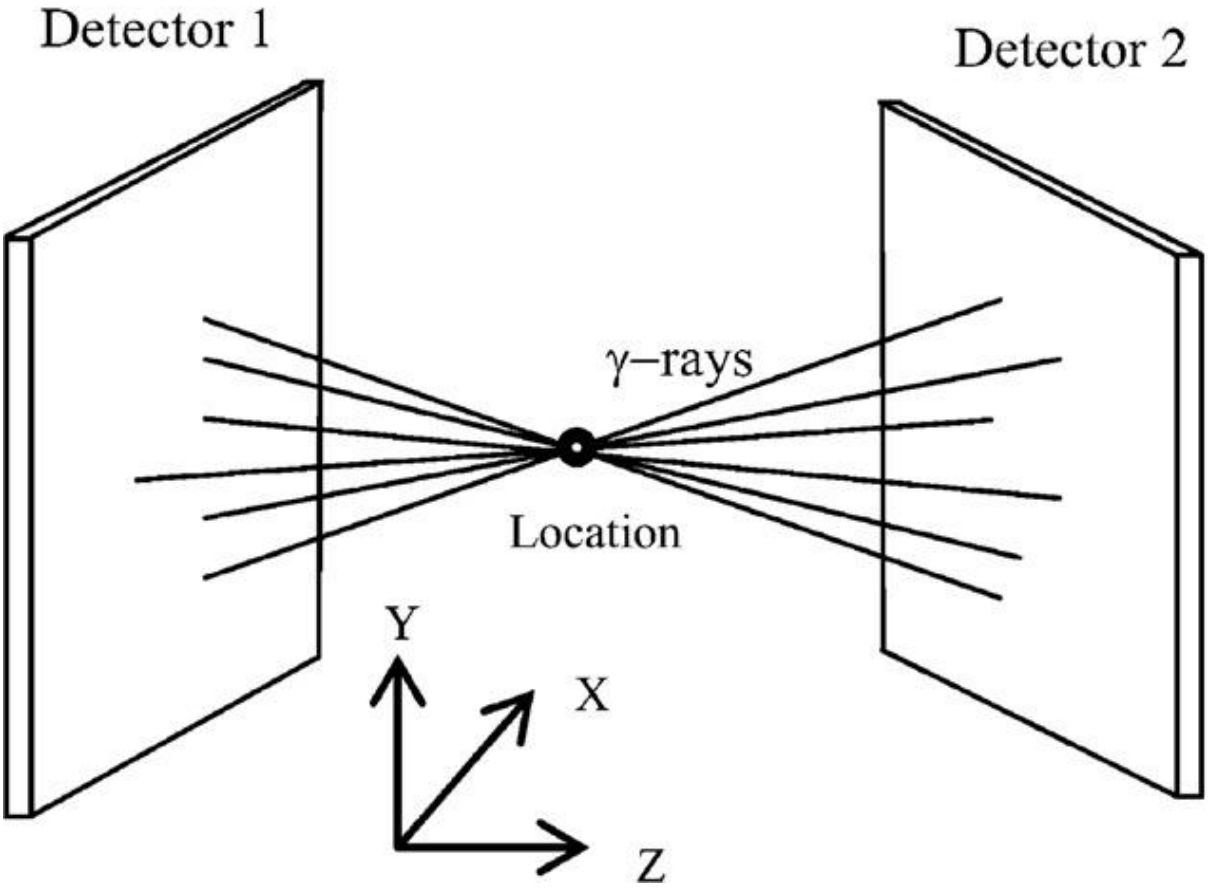

Figure 6 Particle location at the intersection of many Lines Of Response [4,5]

The PEPT process has several sources of error, as in PET. Compton scattering causes a deflection in the path of one or both of the γ-rays causing a misalignment of the detected end points and the originating source position. It is also possible that γ-rays from simultaneous annihilation events (within the temporal detection limits of the detection electronics), which happen from separate positron electron interactions arrive at the detector faces at the same time, but represent the ends of different lines of response, resulting in a false LOR event which does not pass close to the particle.

The multiple events problem experienced in PET when γ-rays originate from separate locations is not an issue when tracking a single particle, as the tracking algorithm discards the

worst correlated LORs automatically, but is possible when tracking multiple particles. They will fall close to another particle and reduce the accuracy of the data (to date the process has been used to track a maximum of three particles), as these events could get mistaken for real LOR from other particles.

2.2.1.2 The PEPT Algorithm

In order to reduce the inaccuracies of the process the LOR data collected is processed to find the best fit of the particle location. This uses an algorithm to determine the location of the particle based upon minimising the sum of the perpendicular distances from the LOR's to determine a three dimensional point approximating the centre of the particle. Once an initial point has been determined the algorithm works out the mean deviation from the calculated point

This is achieved by splitting the data into sets of sequential response lines, each set being a fixed size (provided as a parameter) and working out the position of the minimum sum of perpendicular distances from all lines to give the approximate position of the particle. The sum of distances from a point is given by;

$$D_s(x,y,z) = \sum_s \delta_i(x,y,z) \qquad \text{Eq. 2.}$$

[4]

Where

$\delta_i(x,y,z)$ = distance of the *i*th LOR from the point (x,y,z) which gives the sum of perpendicular distances from any point x,y,z,

The minimum sum of perpendicular distances from LOR's is given when the differential of the sum of distances from any point (x, y, z) (see Eq. 2) with respect to x,y and z are all equal to 0, and gives an approximation of the particle location.

$$\frac{\partial D_s(x,y,z)}{\partial x} = 0$$

$$\frac{\partial D_s(x,y,z)}{\partial y} = 0$$

$$\frac{\partial D_s(x,y,z)}{\partial z} = 0$$

Eq. 3. [4]

Having found this initial approximation of the particle location the algorithm rejects any LOR for which the perpendicular distance is greater than a coefficient *k,* multiplied by the mean deviation from this point, where the coefficient is given as a parameter. The remaining LORs are then used to repeat the process. With each iteration the approximation to the location of the particle centre will improve as the mean deviation decreases. The iterative loop continues until only a fixed percentage, again given as a parameter, of the original LORs remain. At this point the location is given, along with a margin of deviation for the particle.

The mean deviation of the perpendicular distances from the LORs to the approximation of the particle centre $d_s(x_0,y_0,z_0)$ is given by;

$$d_s(x_0, y_0, z_0) = \frac{D_s(x_0, y_0, z_0)}{N(S)}$$

Eq. 4.

Where N(S) is the number of events in the set S of sequential LORs.

Any LORs which are further from a set point than a fraction of $d_s(x_0,y_0,z_0)$ are rejected. The fractional term k is given as a parameter, therefore if $\delta_i(x,y,z) > kd_s(x_0,y_0,z_0)$ the particle position is rejected and the remaining LORs are re-evaluated to give a new point of minimum sum of distances and a new (smaller) mean deviation.

$$d_s(x_1, y_1, z_1) \qquad \text{Eq. 5.}$$

When the number of remaining LORs drops below the fixed percentage (expressed as a fraction of the original LORs) the subset of LORs remaining represents the final subset S_F. The number of LORs in this final subset is represented by the term N_F. The final minimum perpendicular distance point $d_s(x_F,y_F,z_F)$ is the most accurate approximation of the position of the particle. Each of the locations in the final dataset are timestamped, and the average time of the LORs from this dataset is assigned to the approximation of the position of the particle.

This is given by;

$$t = \frac{1}{N_F} \sum_{S_F} t_i \qquad \text{Eq. 6.}$$

Where

N_F which is the same as $N(S_F)$

t = averaged time

t_i = time of individual LOR from S_F

The next set of fixed size data starts at the LOR immediately following the last LOR in the final subset S_F, defined for the previous particle location, despite the fact that many of the

LORs in the new set may have previously been discarded in the previous iterations used to calculate the previous particle location, as the retained LORs may not have been evenly distributed in time throughout the original selected set.

Using this algorithm the optimum value for the retained fraction *f* should lie between 0.20 and 0.33 and the optimum value for the rejection coefficient *k* is between 1 and 1.5 [4].

A modified version of this algorithm is used to track up to three particles. For this purpose the particles need to have different radioactivity levels. The first particle is located using the standard algorithm, the LOR's of the second and third particles being rejected along with the random and scattered LOR's. The higher activity level of the first particle gives more LORs at its location and this particle is therefore located preferentially. The LOR's used to construct the trajectory of the first particle are then removed from the dataset. The process is repeated to recover the trajectory of the second particle and again the LOR's used in its trajectory construction are removed from the dataset. The algorithm is used one last time to recover the trajectory of the final particle. [6].

2.2.1.3 Construction of the modular positron camera

The first modular camera at Birmingham University was built using parts from an ECAT931 PET Scanner [5]. A second modular camera was built from parts from an ECAT951 scanner, the detectors of this second camera blocks of Bismuth Germanate ($Bi_4Ge_30_{12}$ or BGO) scintillator 50 x 60 mm^2 , 30mm thick and each of these is subdivided into an 8 x 8 crystal cell array. Each of the blocks has four photomultiplier tubes arranged so that light detected can be "assigned to an individual crystal element" [5]

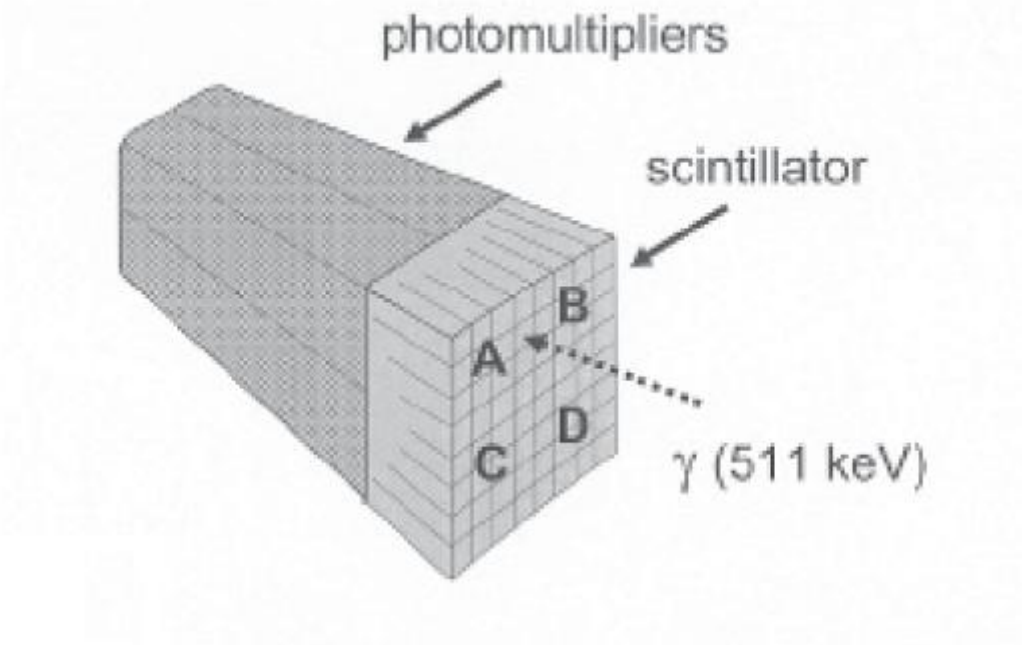

Figure 7. BGO Detector block used for PET [7]

Each block of scintillator is subdivided into 8x8 small elements within the main block by cutting it into squares using cuts to differing depths. Following a scintillation event, when a γ-ray strikes the detector, light is created and shared between the four photomultiplier tubes bonded to the scintillator as determined by the cuts in the scintillator block. This causes a pattern with 64 distinct detection locations to be generated out of the four photomultipliers (this pattern will not line up on an exact 8x8 grid due to differing gains in the phototubes, but these signals can still be separated out to indicate where 511 keV photons strike the scintillator).

These blocks have been mounted into cases 360mm x 95mm x 460mm each holding four detectors. The detectors are mounted at spacings of 88mm between face centres, with the four blocks centred within the case end face.

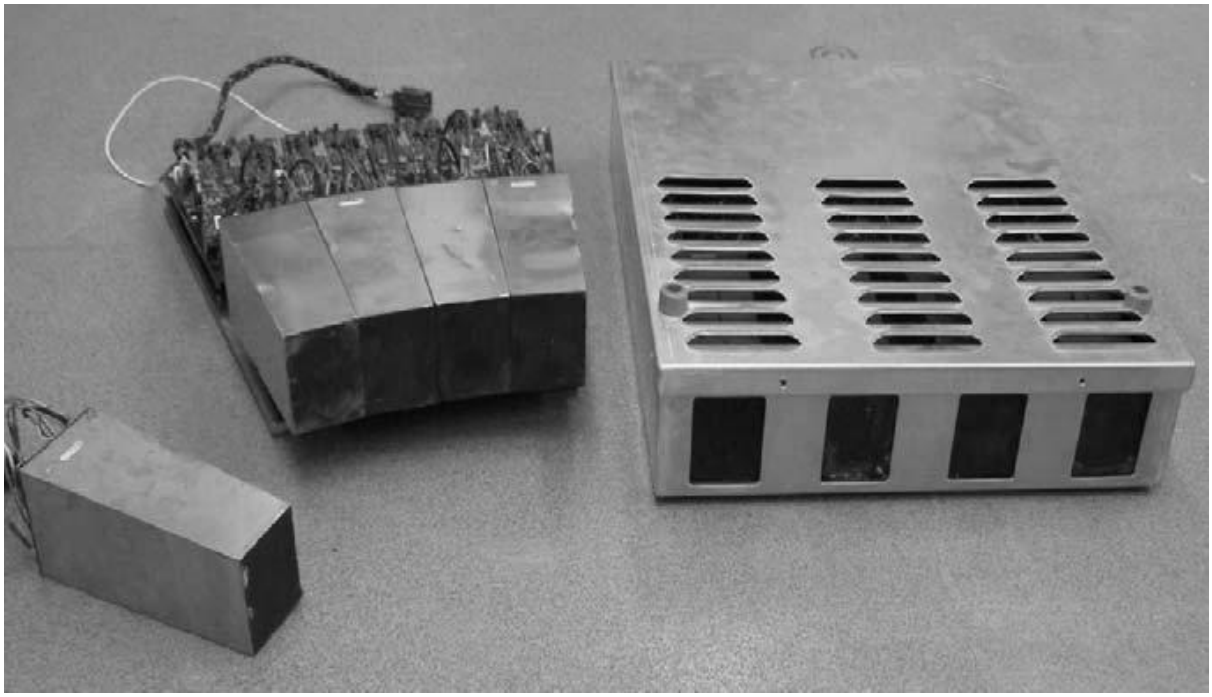

Figure 8. Left to right: BGO Detector block, detector bucket, Encased module. [5]

The detector blocks, as they were originally positioned in the PET scanner, are arranged into groups of four, termed a bucket. For use as a modular PEPT camera the detector blocks no longer need to be immediately adjacent to each other, as required for PET. As for tracking particles, gaps between the individual blocks within a module make the viewable space between opposing banks of detectors have areas of reduced sensitivity. The reduction in sensitivity is a consequence of a reduction in the number of available acceptance angles of γ-rays originating from the tracer. As such, generating an image from the data collected is very difficult, but for the purpose of tracking a particle the effect is merely to create blind spots in the positron camera when a particle is particularly weakly radioactive. If the particle is sufficiently active, tracking continues unhindered.

2.2.1.4 Previous uses of PEPT

Hawkesworth et al. had a positron camera developed by the Rutherford Appleton laboratory in 1986 [8] and Parker continued work with PEPT studying industrial process applications and published an algorithm for PEPT in 1993 [8,9], since which time the process has been used for many purposes. Broadbent[10] and Jones [11] studied mills, Stewart [13] studied bladed mixers and Laurent [12] studied a ploughshare mixer, Yang [14] studied particles in rotating drums, and conclusions were drawn by trajectory analysis and, in later experiments by comparisons to DEM models, the results of which studies were said by Jayasundara to be "reasonably good". Jayasundara [15] went on to study IsaMills^{TM} (large scale grinding machines) comparing his results (for the first time using PEPT) to a CFD-DEM model, claiming that PEPT had validated his model. Stein [16] studied gas fluidised beds making determinations about various viscous effects. Cole studied foam liquid networks using PEPT, initially with 2.5mm glass tracers, which were also visually tracked to verify the process, which was achieved with an accuracy of ±2.7mm [17]. Later she tracked much smaller particles, down to 50µm (using indirect labeling with 2.3µCi ^{68}Ga particles), where there determined tracks were to an accuracy of ±2.6mm [18]. MacNamara has used PEPT to study the action of textiles within washing machines where a 'dead' zone in the centre of the washing machine drum was observed [19]. Beshay and Griffiths have performed investigatory experiments using PEPT with low melting point alloys and aluminium, which involved a series of experiments in shape casting [20, 21].

2.2.2 Radioactive Tracers for Positron Emission Particle Tracking

2.2.2.1 Tracer requirements and types

The tracers used in PEPT at Birmingham University are ^{66}Ga,^{18}F, ^{22}Na,^{61}Cu and ^{64}Cu [4,22]. ^{18}F is the most commonly used as it has several advantages. It does not create any γ-rays other than 511 keV annihilation photons (97% of decay is by β+ positron emission and 3% by electron capture). It has a half-life of 109.7 minutes, which with the activity levels currently achievable with a 200 to 600μm particle allows the positron camera to track the particle in many materials for a reasonable period of time (2 to 4 hours) [22].

In order to produce ^{18}F in the Birmingham cyclotron ^{16}O is transmuted by bombardment with a 33 MeV ^{3}He beam. This results in the reactions ^{16}O(^{3}He,p) ^{18}F and ^{16}O(^{3}He,n)^{18}Ne→^{18}F [23] where the half life of ^{18}Ne is 1.672 ± 0.008 sec [24] (Hence the Neon is not observed outside of the cyclotron where it is created). There are two forms of radioactive activation but the same nuclear reactions are used in both.

2.2.2.2 Tracer production by direct activation

Direct activation of particles is performed by transmuting a suitable element within a tracer particle by placing it directly in the path of the cyclotron beam. To form ^{18}F the target particle must contain oxygen and must not create any dangerous isotopes during the process. Silica and alumina (which are of interest as analogues for inclusions in metals) may both be used.

The particles are placed on an Al target in a blind hole and covered with aluminium foil. The back of the target is cooled by water. The target is then bombarded by the 33 MeV ^{3}He beam and some of the oxygen in the oxides which make up the particles transmutes to ^{18}F [22].

Elements present in the particle other than oxygen also get transmuted, but for many substances of interest these additional isotopes created have very short half lives, (see table 2).

Isotope	Half Life
^{10}C	19.3s
^{12}N	11ms
^{24}Si	1.16s
^{29}P	4.1s
^{26}Al	6.4s

Table 2. Half lives of short lived isotopes typically created by direct activation

The particles are left for 20 minutes to allow these short lived isotopes to decay, before use of the particle and after this period in excess of 90% of the activity originates from the ^{18}F alone. The penetration of the layer containing the ^{18}F is around 0.3mm and the activity is actually part of the material and thus not able to detach or leech into a fluid, should the particle be tracked in such an environment [22].

2.2.2.3 Tracer production by Ion exchange/surface adsorption

Water is distilled and deionised, with an electrical conductivity of 18.2MΩ, it is then placed inside a target made from silver or titanium and bombarded by the 33 MeV ^{3}He beam of the cyclotron for 30 min at a current of 10μA. When the specific radioactivity is measured (20 min after production again to allow the short lived isotopes to decay) it has an activity of 15-18 mCi/ml and the ^{18}F produced is in an ionic state in an aqueous suspension and can therefore be adsorbed onto solid materials by ion exchange or surface adsorption, by placing the particles in the water whilst it is evaporated. The ^{18}F is left behind, now attached to the surface of the particle [22].

2.3 Computer Simulation of particles in a fluid flow

There are several computer models that can be applied to resolve the location and distribution of particles within a fluid and three main types can be considered; microscopic, macroscopic and stochastic models. All three types of model are discussed here to determine which is most applicable to modeling particles studied by PEPT, traditionally macroscopic models have been used to study agglomeration processes however inclusions in liquid metals are typically quite dispersed and PEPT can only track a maximum of three particles at a time so potentially modeling individual particles is more representative of the experimental process being used. Stochastic models are also considered and can be useful in other areas of this field of study.

2.3.1 Types of computer simulations

2.3.1.1 Microscopic Models

A computer model of particles in a fluid can be constructed in a manner such that a set of the forces acting upon the particle can be represented and hence it is possible to predict its path within the fluid and whether or not it adheres to other objects or rebounds off them following a collision.[25]. This type of model when applied to inclusions needs to model the external forces (gravity) , the interaction of the particle with the fluid flow and the interaction of the particle with other particles and the walls of the containing vessel [26].

2.3.1.2 Macroscopic Models

It is also possible to build a model based upon mass conservation and rate laws. Such a model then yields the macroscopic distribution of particles without considering the individual forces

that underlie the movement of each particle. [25]. Macroscopic models, when applied to inclusion models, usually model the inclusion particles themselves in terms of a population balance; the transfer function, a function describing how a process affects the particles and the population balance needs to be validated by some method. This can be achieved by recording empirical data for known sets of conditions and fitting this data to a function curve. This method was used by Warke et al (see fig. 9) [27] to consider the hydrogen and inclusion removal from an aluminium melt using a rotary degasser.

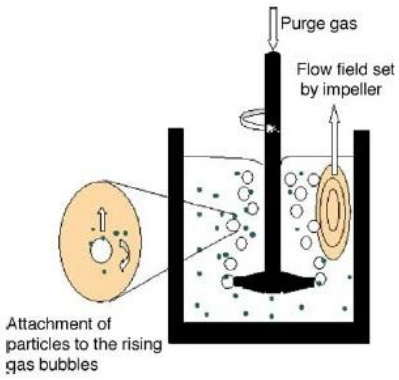

Hydrogen content (C) is given by:

$$C = \left(\frac{K_1 C^{eq}}{K_1 + K_2}\right) - \left(\frac{K_1 C^{eq} - (K_1 + K_2)C_o}{K_1 + K_2} \times \exp\left(\frac{-(K_1 + K_2)}{V_{Al}} \times t\right)\right)$$

The solution to the particles population balance equation gives the change in the particle size distribution density with time and allows tracking the removal of particles from the melt.

$$\frac{\partial n_v(v,t)}{\partial t} = \frac{\partial}{\partial v}[I_v(v,t)n_v(v,t)] + \int_0^{v/2} W_v(v-\tilde{v},\tilde{v})n_v(v-\tilde{v},t)n_v(\tilde{v},t)\mathrm{d}\tilde{v} - n_v(v,t)\int_0^{\infty} W_v(v,\tilde{v})n_v(\tilde{v},t)\mathrm{d}\tilde{v} + S_v[n_v(v,t),v,t]$$

Figure 9. Warkes Schematic representation of the rotary degassing process and his derived equations for hydrogen content and particle size distribution density [27]

Mirgaux et al. extended this method to include the bubbles [28] by modelling the bubbles as large particles.

Most agglomeration models are of the macroscopic type and thus make use of assumptions and averaging effects in order to derive a figure for the number or volume of inclusions removed.

The most significant variable for agglomeration is the collision rate, which along with a collision efficiency term, defined as the ratio of particles which agglomerate following a collision, will determine how many particles agglomerate over a specific time period. This work is typically presented as the formula for a collision rate for a population consisting of two sets of particles, which differ either in size and/or density from each other. From this. other formulas for more complex situations, such as when the larger particles created by this agglomeration mechanism themselves agglomerate, must be derived.

Initial consideration of collision rates for agglomeration processes were limited to laminar flows, where particles were randomly distributed in a fluid, following the (laminar) fluid streamlines until they collided, due to differing accelerations for different sizes and densities of particles, (see Fig 10). Smouluchowski, in Abrahamson [29], reported the formula for this condition:

$$Z_{12} = \frac{4}{3} N_1 N_2 d_{12}^3 G \qquad \text{Eq. 7.}$$

Where

Z_{12} = number of collisions per unit time between particles type 1 and 2
N_1 = number density of type 1 particles
N_2 = number density of type 2 particles
d_{12} = sum of particle radii
G = velocity gradient perpendicular to particle travel direction
(Assuming for laminar flow fields that particle's follow the fluid streamlines and that the velocity gradient is perpendicular to the fluid flow)

Camp and Stein modified this formula by replacing G with a mean velocity gradient in a turbulent fluid ($\bar{G}$) [29,31].

$\bar{G}$ was taken to be a relationship between the dissipated energy per unit mass of the fluid (ϵ) and the kinematic viscosity (ν):

$$\bar{G} = \left(\frac{\epsilon}{\nu}\right)^{1/2}$$

Eq. 8.

Giving

$$Z_{12} = \frac{4}{3} N_1 N_2 d_{12}^3 \left(\frac{\epsilon}{\nu}\right)^{1/2}$$

Eq. 9.

Later Saffman and Turner whilst studying water droplets [30] further refined this, with an equation which had a constant which was 3% smaller to give:

$$Z_{12} = \left(\frac{8\pi}{15}\right)^{1/2} N_1 N_2 d_{12}^3 \left(\frac{\epsilon}{\nu}\right)^{1/2}$$

Eq. 10.

Saffman and Turner also showed that this method of calculating collision rates also had serious constraints upon particle size. The size of eddy currents from any turbulence must be large compared to the size of the particles as the formula relies upon the particles experiencing the eddy currents as local laminar flow. The sum of the particle radii (d_{12}) must be small relative to the turbulent eddies in the fluid and the particles must completely follow the fluid flow.

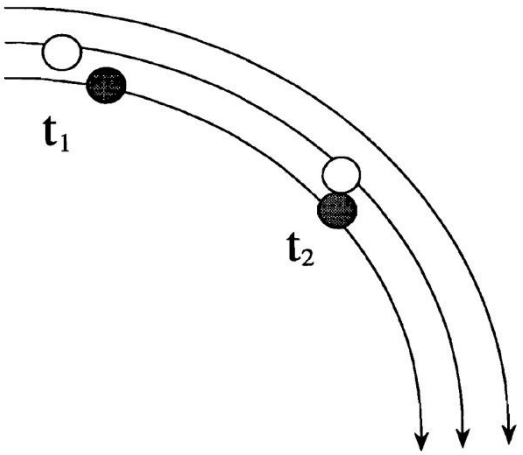

Figure 10. Shear model for collisions (as used by Saffman and Turner) [32]

Saffman and Turner modified their model first to account for the inertia of larger particles allowing them to cross streamlines within a turbulent eddy [32] (see Fig 11) and later to also include fluid acceleraration and gravity as well as the shear gradient[29], to give;

$$Z_{12} = (8\pi)^{1/2} d_{12}^3 N_1 N_2 \left[\left(1 - \frac{\rho_p}{\rho_f}\right)^2 (\tau_1 - \tau_2)^2 \left(\overline{a^2} + g^2\right) + \frac{d_{12}}{9}\frac{\epsilon}{v} \right]^{1/2} \quad \text{Eq. 11.}$$

Where

$\overline{a^2} = 1.3\ (\epsilon^3/v)^{1/2}$

Which Abrahamson reports was taken from Batchelor [33].

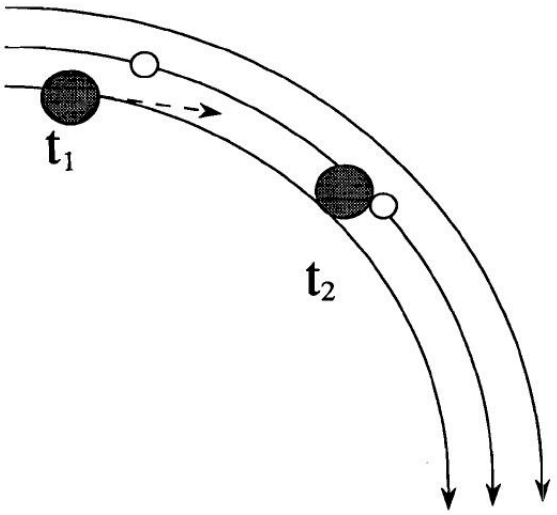

Figure 11. Larger particles do not follow the fluid stream lines exactly, this can be a cause of additional collisions [32]

Whilst this equation took these additional factors into account, it did so, as explained by Abrahamson, by using a constant term in the calculation for describing the random velocity of the particle and the equation also relied upon the colliding particles moving within the same velocity field within the fluid immediately before any collision.

The previous models all assumed that to some degree the particles in the fluid were carried by the same local laminar flow (possibly within an eddy) before they collided.

However, when particles are large compared with the scale of the turbulent eddies this is not the case, particles also have momentum and when they pass from one eddy to another they do not follow the flow of the new eddy immediately, (see Fig 12).

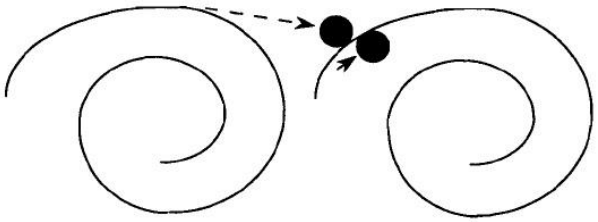

Figure 12.A Large particle colliding with another in a separate eddy [32].

.

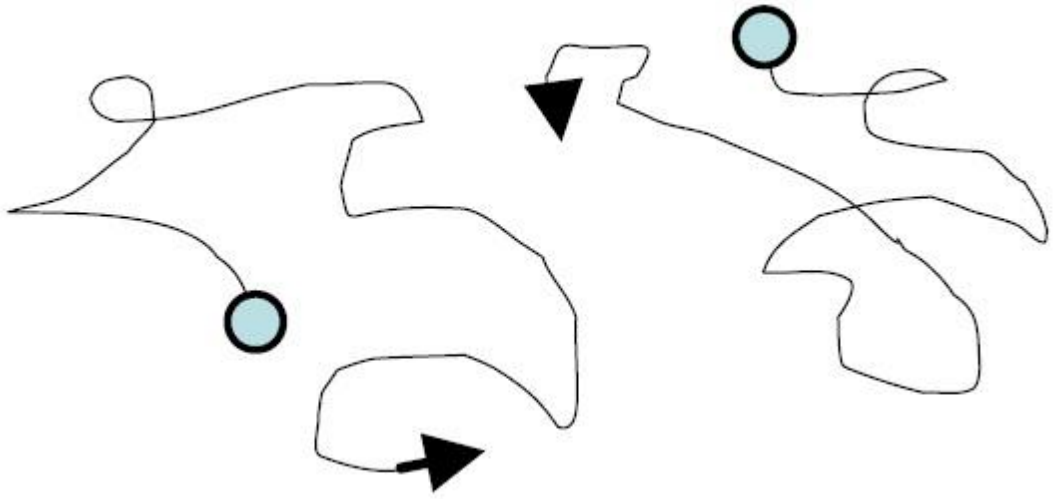

Figure 13 Accelerative model for collisions (as used by Abrahamson) [28].

Abrahamson developed a model for high turbulence environments where the inertia for a particle causes it to have a poor response to changes in the fluid velocity (see Figs 12 and 13). When particles come into close proximity to each other in such a situation, the particle velocities, relative to each other, tend not to reduce as they approach each other, as is the case for small particles where the same flow entrains both of them. Under the conditions described, the large particles will travel though the fluid being "pulled" by drag forces in a manner which superficially looks chaotic (see Fig 13). It was concluded that this approach becomes applicable, with particles > 10μm in a gas, and > 100 μm in water, Abrahamson studied water droplets in air, the threshold for liquid metals was therefore not stated, but

would be expected to be greater than 100 μm as the flow would have more inertia (at the same velocity) than water due to its greater density.

.

Essentially the Saffman Turner solution works for colliding particles that move within the smallest eddies, (where the Kolmogorov length microscale applies, the scale at which turbulent energy is dissipated in a fluid, and the flow is thus viscous), which implies the particles must be very small. Abrahamson's solution applies to particles having large inertia relative to the flow they reside in.

Kruis and Kasters derived an equation which was valid for all turbulence regimes and accounted for both shear and accelerative modes of fluid flow and particle interaction.

$$Z_{12}^{k} = N_1 N_2 \sqrt{\frac{8\pi}{3}}\, d_{12}^2 \sqrt{\overline{w_{accel}^2} + \overline{w_{shear}^2}}$$

Eq. 12.

Where

$\overline{w_{accel}^2}$ = the mean squared relative velocities of the particles (accelerative mechanism)
$\overline{w_{shear}^2}$ = the mean squared relative velocities of the particles (shear mechanism)

Where w_{accel}^2 and w_{shear}^2 are defined on page 208 [32]

Based on the equations presented in this section, models use particle populations to arrive at a number of collisions and hence the possible number of agglomeration events. From the number of agglomeration events, a coefficient can be used, based upon the collision efficiency (the rate at which particles coalesce following a collision) to arrive at a model, for average particle agglomeration sizes.

2.3.1.3 Stochastic Models

A stochastic model uses a probabilistic approach [25], such as Monte Carlo modeling. This method is not widely used for inclusions in a metallic fluid flow, but it has, however, been used to model colloidal systems [34]. This method can be used when complete knowledge of the system being modeled is not known [34]. Monte Carlo modeling uses random numbers (or pseudo random numbers) to create distributions of data points which are then used to approximate (through averaging) a value for a function. The function itself need not be known, but a test which can be applied to each data point must be available. Using this method, phenomena which can be difficult to quantify can be modeled. An example of this would be the calculation of π, the ratio of the area of a square and its inscribed circle is known to be $\pi/4$, given a square of side X mm centred such that the co-ordinates range from –X/2 to X/2. In both x and y axes, a co-ordinate within the square can be generated using a random number generator. The random number generator must create a number between –X/2 and X/2 for both the x and y position of the co-ordinate. If the co-ordinate lies inside the inscribed circle then its count is added to the number of points of the inscribed circle, all points are added to the count of points inside the square. A test for if a point lies inside the inscribed circle would be if the x,y hypotenuse, defined by the x,y coordinates from the origin, was less than the side of the square, denoted by X. The length of the hypotenuse can be determined by taking the square root of x^2 squared plus y^2. After generating a large number of random co-ordinates and testing if they lie inside the inscribed circle, the ratio of the points inside the inscribed circle and the square, multiplied by 4 should give the value of π [35]. BASIC code for this example is given in appendix A

(This modeling technique was used to determine the sensitivity maps for the viewable volume of a positron camera in this work).

2.3.2 Computational Fluid Dynamics (CFD)

2.3.2.1 Conventional CFD

Since the work presented in this thesis will concentrate upon the tracking of radioactive particles which will be primarily released individually it makes intuitive sense to create a computer model to simulate the path taken by individual particles. There are a number of computer packages to model fluid flow but the options for also modeling particles is limited. A solution in which a standard fluid flow modeling package was used in conjunction with bespoke code to model the particles was adopted. This bespoke code accounted for the forces exerted by the fluid on a particle and was therefore classed as a microscopic model.

The first step to create this model was to use a computational fluid dynamics package to simulate the fluid flow. Computational Fluid Dynamics (CFD) model fluids as a continuum, requiring solutions of partial differential equations. The Navier-Stokes and other equations, which cannot be solved analytically, are broken down into approximations which can be solved over discrete timesteps. In this way the fluid flow can be calculated for discrete locations and time intervals. The accuracy of the final result will depend upon the step size of both the locations, (i.e., the element or cell size), and the time.

CFD can be used to model both laminar flow and turbulent flows by finite difference, finite volume or finite element methods. Two phase flows can be modeled, as can compressible or inviscid flows [36].

The algorithms used are normally iterative with a preset convergence criteria and it is important that the model does not exit its iterative loop until the desired level of accuracy

from the simulation has been achieved, this means that the selection of the convergence criteria and its value are very important to the outcome of the simulation [36].

Initially the general transport equation

$$\frac{\partial(\rho\phi)}{\partial t} + div(\rho\vec{u}\phi) = div(\Gamma grad\phi) + S \qquad \text{Eq. 13.}$$

Where

Φ is the variable of interest
S is a source term for the partial differential equation
Γ is the diffusivity in m^2s^{-1}
ρ is the density in kg m^{-3}

which was derived by Spalding et al. in the 1960s [37] and which was used in the formulation of an iterative solution for several partial differential equations necessary to solve for fluid flows [37,38].

The next step taken was to model for turbulence using the *k-ε* model, which was developed by Spalding and Launder in 1972 [38,39], since which time numerous variations of this model have been devised by various researchers. These allowed solutions for additional complications such as low Reynolds number flows and for boundary walls. Patankar and Spalding then went on to develop an algorithm for solving pressure linked equations [37,38]. As a consequence of these works there are now many software packages for solving for fluid flow [38]. Most CFD work is now performed using software packages, which usually consist of a pre-processor, a solver and a post processor.

The pre-processor is used to set up the simulation i.e., a mesh is created which defines the boundaries of the model. Then the boundary conditions and the initial state of the fluid and any external forces are configured. The solver is then run to process the data from the pre-

processor, to arrive at the results for the fluid flow. The post processor is used to generate graphs and diagrams from the data produced, either as colour coded slices, contour plots or vector plots and the variable to be displayed can normally be selected by the user [40].

2.3.2.2 Smoothed Particle Hydrodynamics (SPH)

Smoothed particle hydrodynamics is a technique used as an alternative to traditional CFD in order to achieve solutions to fluid flow problems. In SPH the fluid is modeled as a set of particles which have many elements and this has some advantages and some disadvantages. It models interfaces between fluids easily, and also the movement of sections of the simulation well, for instance when a solid is moving (not just the overall mass of the fluid). Fragmentation and breakup of solids modeled as tightly bound particles, is handled naturally and the resolution can be adjusted both temporally and spatially. It has a relatively low computational overhead. Smoothed particle hydrodynamics is subject to errors due to its inherent interpolation and these errors are hard to quantify due to the disordering of the particles, in addition it does not handle shocks with small perturbations well as they can be indistinguishable from the noise between particles [41].

2.3.3 Discrete Element Modelling

This type of model has been used for granular solids and fluidised beds [42], where there are a large numbers of particles in close proximity within the volume being modeled.

2.3.3.1 Brief Description of DEM

DEM is the term used for a system which models many particles and their interaction with each other and a liquid or gas. There are two types of DEM model, namely hard sphere and soft sphere. In a hard sphere simulation the particles are modeled as completely rigid spheres

which process each collision as instantaneous events which are handled in the order in which they occur. Soft sphere models by comparison are more complex and they use a time step to move the simulation forward, allowing an overlap of particles when they collide. The overlap is accounted for in the simulation by calculating the contact forces created by deforming the particles by the amount of the overlap. As these are reaction forces they change the path of the particles involved. The contact model used to calculate the forces can be as sophisticated as necessary. A soft sphere approach saves processing time but cannot account for simultaneous collisions The first soft sphere model was presented by Cundall and Strack in 1979 using a spring dashpot model, since then many contact models have been used by various researchers and were reviewed by Shäfer et al [43]. Newer schemes were put forward by Walton and Braun, [44] which used two different spring constants, one in the normal direction and the other in the tangential direction.

Langston et al. used an equation of exponential form to model the forces [45] and Thornton introduced peeling, microslip and sliding conditions to his model [46,47]. The DEM technique can be used along with CFD to present a complete model of particles moving in a liquid or gas. [42].

It was argued by Hirt [48] that in a particle-fluid model, volume exclusion and momentum exchange are the two predominant effects of particles immersed in a fluid. Of the two effects he argued that momentum exchange between the particles and the fluid was the most important. In systems with small volume fractions of particles, (as is the case with respect to inclusions in metals), there will only be a small effect from the volume exclusion. However, if there is a large density difference between the particles and the fluid medium then a small volume of particles may represent a large percentage of the momentum in the system.

Hirt gave the example of water droplets (particle) in air (fluid), stating that at a liquid fraction of 1 x 10^{-4} , 10% of the momentum in the system would be accounted for by the water. The implication of this was that two-way coupling, where the particle effects on the fluid are taken into account, was needed in a system with large density differences between phases , but only one-way coupling is needed, where the effect of density differences was negligible. One way coupling may be used in a system where the density of the fluid and the particle is of the same magnitude as each other and the volume fraction of the particles to the fluid is small.

2.3.4 Contact Theory Models

2.3.4.1 Hertz Model

Hertz investigated the contact between elastic bodies, assuming two bodies where the strains are small, and the area of contact is much smaller than the radius of the body. He took the surfaces involved to be continuous and frictionless [49]. Under these conditions the derived equations for the contact area between two spheres are:

$$a_0^3 = \frac{3}{4}\pi(k_1 + k_2)\frac{R_1 R_2}{R_1 + R_2}P_0$$

Eq. 14. [49]

where

a_0 = Contact radius
R_1=Radius of sphere 1
R_2=Radius of sphere 2
P_0=Load pressing spheres together
k_1=Elastic constant of particle 1
k_2=Elastic constant of particle 2

$$k_1 = \frac{1-v_1^2}{\pi E_1} \quad \text{and} \quad k_2 = \frac{1-v_2^2}{\pi E_2}$$

Eq.15. [49]

Where

v=Poission's ratio
E=Youngs modulus

δ, the overlap of the two spheres, was shown to be given by :

$$\delta^3 = \frac{9}{16}\pi^2 (k_1 + k_2)^2 \frac{R_1 + R_2}{R_1 R_2} P_0^2.$$

Eq. 16. [49]

Hertz verified his results experimentally using an optical microscope, by studying the changes to Newtons optical interference fringes, in the gap between two lenses in contact.

2.3.4.2 Bradley Model

The Bradley model was put forward in 1932 to describe the adhesive force between a rigid sphere and a rigid plane [50**];**

$$F_A = 4\pi\gamma R$$

Eq. 17. [51]

Where

F_A = Force of Adhesion
R = Radius of sphere
γ = Surface energy

For rigid spheres of radii R_1 and R_2, the adhesion force, P_A, between them given by the Bradley theory, is:

$$P_A = 2\pi\Delta\gamma R$$

Eq. 18. [52]

where

$\Delta\gamma = \gamma_1 + \gamma_2 - \gamma_{12}$ is the work of adhesion
γ_1 and γ_2 are the surface energies of materials of spheres 1 and 2
γ_{12}, is the interfacial energy.
$R = R_1R_2 / R_1 + R_2$

This equation applies only when the contact radius is zero, as the particles are assumed to be rigid spheres , whereas in reality the spheres do deform when placed in contact due to their elasticity. However, so long as they are sufficiently rigid, Bradley theory is valid but it does not take elastic deformation into account.[50,51,52].

2.3.4.3 The Johnson Kendal Roberts (JKR) Model

In 1971 Johnson et al. put forward a theory that described the adhesive effect of surface forces between elastic surfaces under load [49]. They noted that under light loading conditions the Surface's forces make a significant contribution to the contact equilibrium.

Hertz theory was found to match well with reality in experiments involving high loads, but was found lacking as the loads were reduced. In 1968, Roberts used smooth rubber spheres to show that under low loads the contact area between the spheres was greater than predicted by Hertz. This was also observed by Kendal in 1969, using glass spheres. Both observed that the contact area tended to a finite value as the load was reduced, which was attributed to adhesion which was most evident on clean, dry surfaces. This suggested that adhesion forces were of little significance under high loading but under low loads their effect was noticeable. In previous work in 1958, Johnson had calculated the stress distribution at the contact patch and this indicated that the stresses were tensile at the edge of the contact patch and compressive at its centre. Based upon these observations an approximate theory was put forward which neglected the tensile forces at the edge of the contact area, and a more rigorous theory was put forward which did not.

In both cases the contact radius of two spheres in contact under a load was related to the elastic displacement δ (see Fig 14), but in the approximate theory, compressive loading was assumed across the contact area, as used by Hertz.

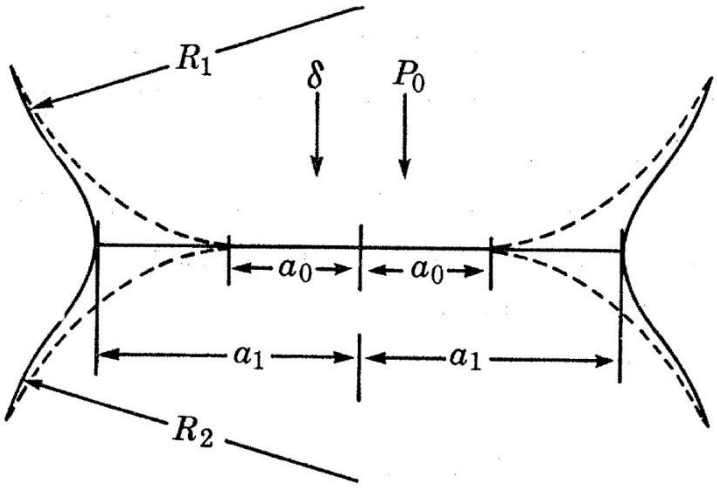

Figure 14. Contact between two convex bodies as defined by JKR theory [49]

Where

R_1 = Radius of 1st sphere
R_2 = Radius of 2nd sphere
P_0 = Normal load
δ = elastic displacement
a_0 = contact radius without adhesion
a_1 = contact radius with adhesion

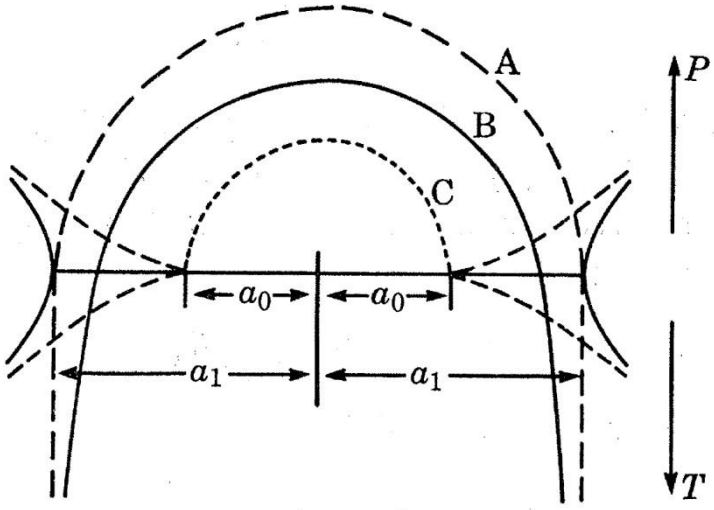

Figure 15. Stress distribution curves for the JKR model. [49]

Where

P = Compressive stress
T= Tensile stress
a_0 = contact radius without adhesion
a_1 = contact radius with adhesion

Both an approximate and a rigorous theory was put forward by Johnson et al. The approximate JKR theory gives an approximation of a_1 using the compressive stress distribution, Fig 15 (curve A). The full JKR theory gave a value for a_1 using the compressive and tensile stress distribution, Fig 15 (curve B). Hertz defined equations which gave a contact radius a_0 assuming a compressive stress distribution, shown as Fig 15 (curve C).

In the approximate JKR theory, surface attraction was explained in terms of surface energy, where surface energy is lost to create an elastic displacement, and the displacement reaches equilibrium at a radius a. For two spheres in contact but with no load applied the loss in surface energy U_s is given by:

$$U_s = -\pi a^2 \gamma \qquad \text{Eq. 19.}$$

Where

U_s = Loss in surface energy
γ = Energy per unit contact area. (from the two surfaces)

The energy loss U_s creates a balancing force F_s which is given by:

$$F_s = \frac{-dU_s}{dx} \qquad \text{Eq. 20.}$$

F_s causes a movement of x of the spheres, the equivalent of the displacement δ in Hertz theory, but it cannot be worked out exactly as the surface forces alter the stress distribution across the contact area. If the change in the stress distribution is neglected the theory can only approximate the movement caused to the particles, given by:

$$x \approx \frac{a^2(R_1 + R_2)}{R_1 R_2}$$

Eq. 21.

and an approximation to the force from the surface energy, which is given by:

$$F_s \approx \frac{\pi\, R_1 R_2 \gamma}{(R_1 + R_2)}$$

Eq. 22.

This force acts in addition to the normal force P_0 between the spheres and its effect on the contact area becomes more pronounced when P_0 is close in value to F_s from Eq. 20 and Eq. 22. It can be seen that the loss of surface energy varies with respect to a^2, the square of the contact radius from Eq. 19.

The load P_0 has a large effect upon the contact area when it is close in value to F_s such that:

$$P_0 \approx \frac{\pi\, R_1 R_2 \gamma}{(R_1 + R_2)}$$

Eq. 23. [49]

From the formulas presented, a contact force can be derived and its effects upon the spheres in contact calculated. The exact analysis is too long to be shown here. It takes into account the fact that the stresses across the contact, between the particles, are tensile at the edge, but compressive at the centre.

In 1985 Johnson published a book [48] on the subject of contact mechanics, based on this theory, with a description of sliding and rolling forces allowing the JKR-theory to be applied to planes, rolls and spheres. [49, 51].

2.3.4.4 Derjaguin Miller Toporov *(DMT) Model*

In 1975 Derjaguin et al. put forward another theory. They claimed their work also took into account the molecular attraction of the area of non-contact adhesion surrounding the contact patch. The two theories differed regarding the magnitude of the pull-off force, the force necessary to separate two particles, following a collision. DMT theory claimed $F_c = -4\gamma\pi R$ whereas JKR theory defined this as $F_c = -3\gamma\pi R$. The work of Derjaguin et al. centred around an energy balance to determine the forces acting. They concluded that electric attraction forces contributed more than the molecular sticking force during particle separation, the justification being a measurement of charge density when tearing off particles [50]. This measurement was achieved by detaching polyvinyl chloride particles from the sides of a steel tube, by firing a bullet of known mass and speed at its base. The particles released then had their charge measured by a charge spectrometer, developed by Derjaguin et al. [53]. They also noted that the region of non-contact attractive forces deceased as the spheres deformed and the contact patch flattened, and described the additional adhesive forces as an addition to the molecular forces presented by Hertz. At the point of particle separation they asserted that there was no deformation of the spheres, which have a point contact and that the pull-off force was entirely due to attractive forces.

2.3.4.5 Modified JKR model

In 1976 Tabor realised that the JKR-theory and the DMT theory are both special cases of a general problem [51]. He concluded that Bradley-theory applies for absolutely rigid spheres, DMT-theory applies to small rigid spheres, and JKR-theory to large elastic spheres. He stated "The difference between all these cases, is very minor and the JKR-theory describes adhesion relatively well, even in the scope of DMT theory" [51].

In 1991 Thornton and Yin derived the tangential and normal forces for collisions between particles at varying oblique angles. They combined this with JKR-theory to give a modified version, which also takes account the ability of particles to both peel apart and slide past each other as surface energy and contact loading thresholds are passed [46]. Thornton argued that contacts occur in stages; initial contact followed by peeling, where the surfaces in contact decrease in size with negligible relative movement, then microslip, (where the particles partially slip due to contact forces holding them together), followed by sliding, where the particles slip past each other. This combined the work of Savkoor and Briggs [54] to account for the peeling part of a particle contact, along with Mindlin's microslip equations [55], immediately before the particles pass into a fully slipping mode, which was proposed by Thornton [26]. Thornton derived the thresholds for the transitions between contact states and the work was presented in a comprehensive and complete form by Guo in his literature survey for his thesis "A coupled DEM/CFD analysis of die filling process" of 2010 [26].

2.3.4.6 Muller, Yushchenko and Derjaguin (MYD) model

There was a difference as to the contact radii and separation forces for the JKR and DMT theories. Tabor performed an analysis of the two existing theories, and this later led Muller et al. to develop the Muller, Yushchenko and Derjaguin (MYD) model which described the adhesion force using a Lennard–Jones potential, (a simple model that approximates the interaction between a pair of neutral atoms or molecules). Analysis by Muller indicated that there was a flaw in the DMT model. The attraction force is given as $2\pi R\Delta\gamma$ at the initial contact, decreasing to $\pi R\Delta\gamma$ as the contact progressed, returning to $2\pi R\Delta\gamma$ or more at separation. In Mullers analysis the pull-off force could decrease to $1.5\pi R\Delta\gamma$, similar to that in the case of the JKR-theory, indicating that the DMT model was incorrect [56]. The MYD model showed that as the particles were about to separate and the contact area was zero, the

pull-off force of the JKR and DMT models represented the extremes of a dimensionless parameter now known as the Tabor number,μ [57,52];

$$\mu = \left(\frac{R\Delta\gamma^2}{E^{*2}\varepsilon^3}\right)^{1/3} \quad \text{Eq. 24.}$$

where

R = Radius of sphere
E^* = Combined Elastic Modulus
Δ γ= work of adhesion
ε = intermolecular spacing

and

$$E^* = \left(\frac{1-\nu_1^2}{E_1} + \frac{1-\nu_2^2}{E_2}\right)^{-1} \quad \text{Eq. 25.}$$

Where

E = Elastic modulus
v = Poisson's ratio

By using the Dugdale square well potential (a more sophisticated model of the interaction between a pair of neutral atoms than the Lennard-Jones potential), the Maugis–Dugdale (MD) model was presented in 1992. It was found that the MD model was the general case, describing the contact for which both the JKR and DMT models were special cases. This model added another parameter Λ (a dimensionless parameter derived from the equations for surface shape and surface adhesive interaction) which is described as a transition parameter,. For values of n (n being one of the terms of the transition parameter, the shape parameter,

where n = 1 for a cone, n = 2 for a sphere, and n→∞for a flat punch) greater than 0, this parameter starts at 0 and extends to infinity and a transition from DMT-theory to JKR-theory can be seen when Λ is plotted against the pull off force for differing values of n [57] (see Fig 16).

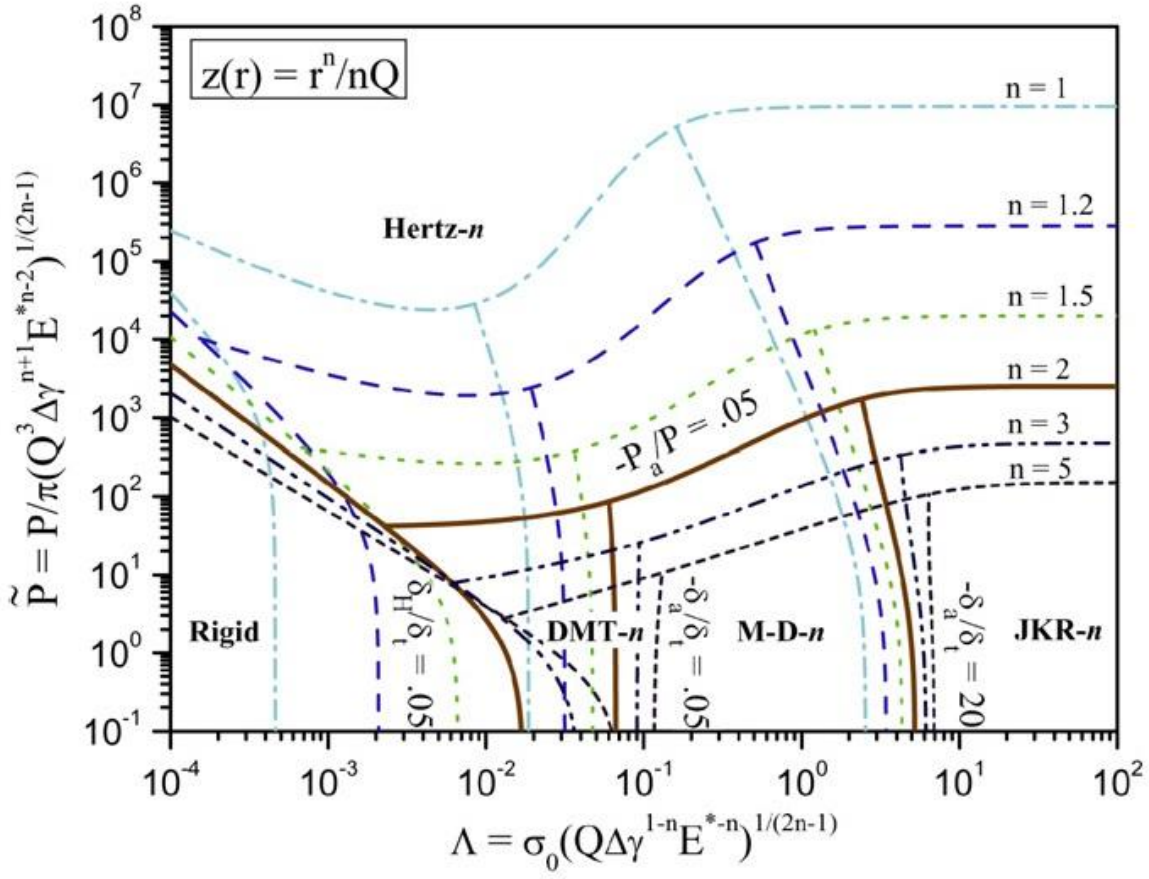

~
P = Pull off force
Λ= Transition parameter

Figure 16. Relationship between the transition parameter Λ and the pull-off force [57].

Consequently there are now a range of theories of varying complexity, each with their own strengths and weaknesses and for a simulation to be implemented one must be chosen (see Table 3).

Theory	Properties
Hertz	**Simple, but limited to no elastic deformation, pull- off force does not take adhesion into account**
Bradley	**Valid for absolutely rigid spheres, adhesion introduced.**
JKR	**Elastic deformation taken into account, suitable for large elastic spheres**
Modified JKR (Thornton)	**Adds peeling,and slipping of particles to JKR-Theory, tangential forces from tractions included**
DMT	**Alternative to JKR-theory, suitable for small hard spheres.**
MYD	**Covers all cases of hardness and elasticity, but complex**
MD	**Improvement on MYD-theory by using more sophisticated model of molecular bonds, must be solved numerically.**

Table 3. Comparison of Contact mechanics theories.

It was decided that the JKR theory with Thorntons modifications would be used in this work, as it takes into effect many stages of a collision and a comprehensive step by step description was available.

2.4 Inclusions In Aluminium

Aluminium typically contains a large number of inclusions The volume fraction of inclusions in a melt ranges from 0.1% down to 0.1 parts per million by volume [58] these are in part due to its high reactivity and the difficulty of refining a melt and the subsequent problems cleaning the metal and preventing inclusion entrainment and the creation of new inclusions. Aluminium oxidizes easily and the amount of oxidation increases with the length of time the aluminium is held at a high temperature [59]. Inclusions are also introduced as part of the production process, and also when it is alloyed and when it is remelted and handled. Table 4 shows typical inclusion sizes and types.

Inclusion Material	Size µm	Source
Al_2O_3	0.2-30	Oxide film and particles (interaction with oxygen).
MgO, $MgAl_2O_4$	10-5000	Magnesium oxides from alloying with magnesium.
SiO_2		from refractory material.
NaCl, KCl	0.1-5	from fluxing treatments.
Al_4C_3,SiC	0.5-25	from carbon anodes and cathodes used in the original production of the aluminium.
TiB_2	30	Intentionally added as a grain refiner.
AlN	10-50	Degassing with nitrogen.
AlB_2	0.1-3	Intentionally added to improve conductivity.

Table 4 Typical types and sizes of inclusions in aluminium alloys [60,58]

2.4.1 Types of Inclusions In Aluminium

2.4.1.1 Non-metallic inclusions in aluminium alloys

Aluminium forms amorphous alumina (Al_2O_3) upon its surface almost instantaneously upon the surface being exposed to air. Underneath this amorphous alumina layer crystalline alumina forms, at temperatures of around 750^{o}C. This will initially form a γ-phase monolayer

film, before thickening, creating more γ-phase alumina, for up to 24 hours, this time can be reduced significantly (by up to 10 hours) if the melt surface is skimmed [61].

Aluminium when alloyed with magnesium (1% -5%) forms an amorphous alumina layer at the surface of the metal, but this undergoes a reduction reaction with the magnesium to form magnesium oxide and aluminium. In regions where local magnesium depletion occurs, spinel $MgAl_2O_3$ crystals form, which can be caused by skimming the surface of the melt. The oxidation of magnesium occurs in preference to aluminium and the rate decreases until the the magnesium is consumed and conditions are suitable for converting magnesia to spinel. Following this transformation further oxidation can then occur by the creation of α-phase alumina. The oxidation of magnesium containing alloys is faster than that of pure aluminium (~ 5 hours) [61]. The density of spinel and other oxide inclusions can be similar to, or greater than that of the molten aluminium. This means that these inclusions may not always float out as dross, however many entrainment inclusions will contain air pockets making them buoyant. Inclusions folded into the melt in this manner have an oxide film on both sides of a gas bubble and are referred to as bifilm inclusions [60]. The surface oxide layer protects the rest of the melt from further oxidation, but when the surface is disturbed, freshly exposed melt surface, creates more fresh oxide, which can subsequently be entrained by further events which disrupt the surface of the melt.

Campbell suggested that 80% of inclusions in castings are formed by bifilm bubble entrainment processes and that the bubbles leave oxide trails as they move throughout the melt [58]. The oxide layer once formed cannot be reabsorbed into the melt so as bubbles move within the melt the gas moves but the layers themselves remain as a film trailing from the bubble which formed them [58]. Bubbles can also close up as their constituent gases are

consumed, first by thickening of the oxide layer and then by creating a nitride layer, once the oxygen content of the bubble drops below 5%. (shown by Raiszadeh and Griffiths [62]).

In addition to the bifilm oxide inclusions, some non-metallic inclusions are intentionally added as grain refiners, the most popular being $TiB_{2,}$ which is intended to be widely dispersed throughout the melt as sub 5µm particles. These are intended to act as nucleation sites for crystal formation during solidification. TiB_2 is added in the form of a master alloy containing 3-10 wt% Ti and 0-3 wt% B (excess Ti forms Titanium aluminides which also act as grain refiners [63]) , added in a rod form to holding furnaces, or as a rod and continuously fed into the melt in transfer launders [64]. Grain refiners increase the number of nucleation sites and this results in smaller, more equiaxed grains. The smaller grain size results in greater yield strength and ductility. Sometimes the grain refiner agglomerates to form a larger particle. TiB_2 agglomerates are particularly hard and can score the rolls and cause significant damage to foil stock during rolling processes. The TiB_2 agglomerates cause the strip to break and tear, due to the difference in hardness and ductility, around the TiB_2 agglomerations which causes large stresses to develop and leads to a pin hole followed by a tear [65].

2.4.1.2 Exogenous inclusions in aluminium alloys

Inclusions can persist from the original refining process. Such as residual carbon, which can form Al_2OC, Al_4O_4C and Al_4C_3, this having been transferred into the melt from the carbon electrodes used for electrolysis during the primary extraction of the aluminium [66]. Refractory materials from the vessels, furnace linings, launders and crucibles used to hold the molten metal can break off and create inclusions, of up to several millimeters size. These inclusions come from the refractory materials and are typically SiO_2 or alumina.

2.4.2 Effects upon material properties.

Inclusions in aluminum alloys reduce their ductility and tensile strength [67]. For most castings which have small, well bonded inclusions such as borides and carbides, they do not present a problem and their grain refinement effect may actually improve mechanical properties. Inclusions which do not bond with the metal matrix such as oxide films, nitrides and sulphides can initiate cracks [58]. The relationship between metal ductility and the percentage of inclusions is logarithmic, as shown by Liu for a an Al-Si-Mg (T6 tempered) , where he derived the relationship, percentage elongation=9.5/2.98 log area percentage inclusions/oxide (see Fig 17).

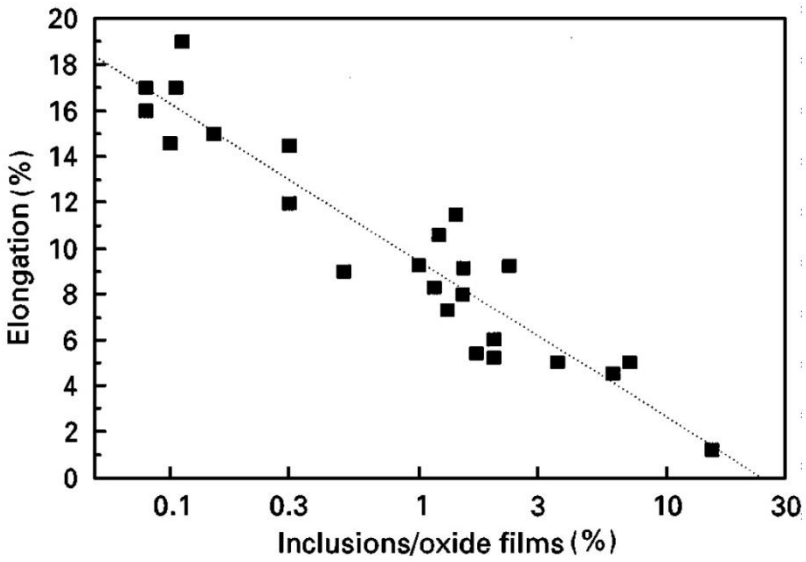

Figure 17. Elongation to percentage inclusions relationship as found by Liu [68].

Fractography showed this relationship was due to cracks nucleating at the interface of the inclusion and the metal matrix when they are not well atomically bonded [68].

Fatigue resistance in aluminium alloys is determined mainly by several types of inclusions and pores. Fatigue occurs when, under cyclic loads cracks develop and grow within a material. Eventually these cracks can lead to a catastrophic failure and how long this takes is dependant upon the magnitude of the cyclic load and the flaws in the material.

The fatigue strength will depend upon the dendritic arm spacing (DAS), the shape and the size of grains, the microstructural characteristics of the phases, (and for silicon containing alloys the size of the eutectic silicon particles [69]). Also the amount, size and shape of both porosity and inclusions [70]. The flaws allow cracks to start and propagate. In aluminium alloys, the initial phases of the fatigue crack formation typically begin from oxides, pores and other 2nd phase particles. Cast parts can display a wide variation in their fatigue life, (a variation of a factor of ten is not unusual), dependant upon the size and type of the inclusions and pores present. The size of an inclusion in large part determines the time taken to incubate a crack under fatigue inducing conditions; larger inclusions decrease the number of cycles necessary for a crack to form. Dependent upon the fatigue resistance required in a part it may be essential to ensure that no inclusions above a critical size exist [71]. Wang et al [69] performed experiments using Sr modified A356-T6 alloy, in which their specimens were tested at stress amplitudes of up to 100 MPa, at 55 Hz and a stress ratio (The ratio of minimum to maximum stress in fatigue testing) of 0.1. The tested samples contained porosity, oxide films and slip bands and it was possible to make a linear fit for each of the crack initiators using a two-parameter Weibull distribution, with the relationship between secondary dendrite arm spacing being displayed (Fig 19). They determined that the critical pore size of around 25 μm was agreement with Couper et al [72]. Wang et al. found that samples containing oxide films up to 50μm were similar to samples free of oxide film. They concluded that the critical oxide film size was therefore slightly larger than the critical pore

size, for the same loading conditions. For a given dendrite arm spacing they found a relationship in the number of cycles to failure of their test bars (see Fig 18).

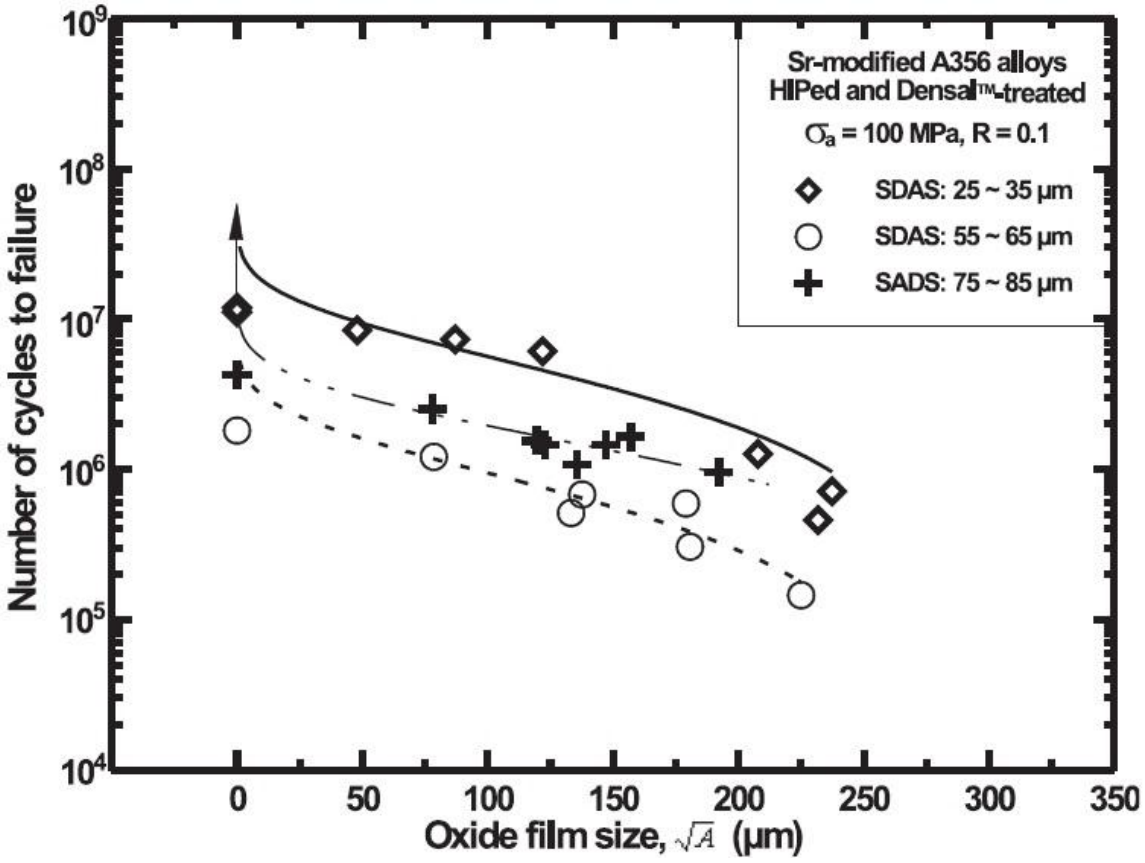

Figure 18. Effect of oxide film size on fatigue failure [69]

Seniw reported that fatigue strength was not only dependent upon the size of a defect but also upon its location within a casting. Inclusions and pores near the free surface being significantly more detrimental to the fatigue resistance of the material. He illustrated this for fatigue failure due to porosity, Fig 19, where pores close to the surface (< 0.25mm) of the sample cause an early fatigue failure (<50000 cycles). He noted that when testing pores in the body of the sample that smaller inclusions near the surface would become the site of crack initiation and treated pores and inclusions in a similar manner with respect to fatigue.

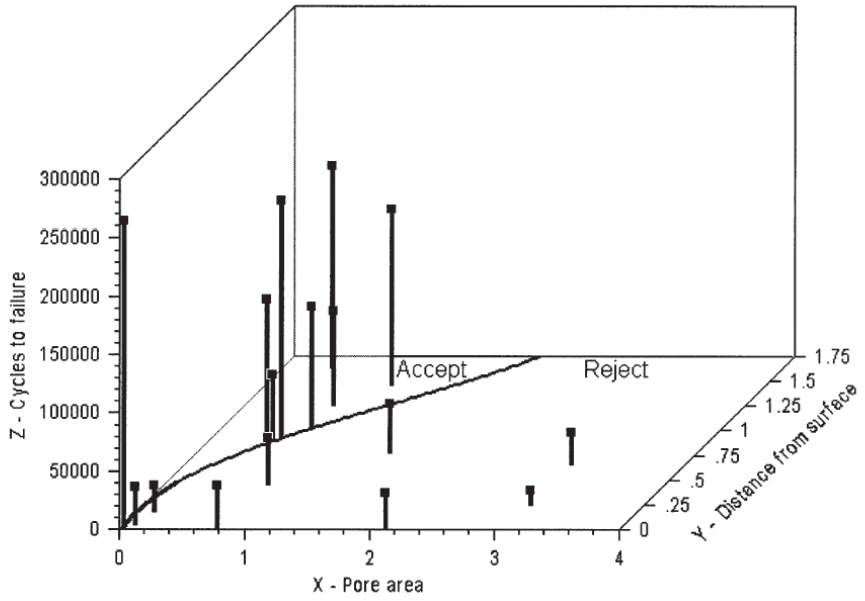

Figure 19. Cycles to failure versus pore area (mm^2) versus distance from free surface (mm) [69].

2.4.3 Inclusion Control in aluminum alloys.

2.4.3.1 Agglomeration

Agglomeration is due to particles adhering when they come into contact with each other. In metallic melts this will normally be seen as particles coalescing to form larger particles. This process and its causes are quite complex and this complexity is increased in turbulent systems. The mechanisms by which agglomeration occur are thought to be, by (i)-Brownian motion, (ii)-velocity gradients, (iii)-turbulence and (iv)-gravity or electromagnetic forces.

Brownian motion causes small macroscopic particles to collide (and possibly agglomerate, dependent upon mass, velocity and surface energies) by the thermal energy within the melt causing the particles to have chaotic motion. Velocity gradients such as those caused by a boundary layer can cause particles to collide as a particle subject to the flow in one part of the gradient will travel faster than a particle in another part of the flow. If the particle radii still

overlap within the flow stream lines they will not be able to pass each other and will thus collide. Turbulence within a flowing melt causes a particle motion for small particles similar to Brownian motion causing particle collisions. In systems with particles of differing sizes and densities, the forces acting upon the individual particles within the same flow field differ and the particles' motion therefore also differs, leading to particle collisions [73,74]. For agglomeration to occur the particles have to be in contact for long enough for a bond between them to form, whether this be by van der Waals forces, caused by their mutual surface energy, or another mechanism. Agglomeration does not directly remove inclusions but amplifies the effect of other inclusion removal processes. For a turbulent melt Frisvold used a relationship between the dissipation of the turbulence and the time constant for agglomeration. He calculated this to be 3.8 minutes in an aluminium melt with a dissipation rate of 1 m^3/s^2, with an inclusion concentration of 10ppm. He concluded agglomeration was independent of particle size and was the only efficient mechanism for removing small inclusions. He noted that the stirring must not be too vigorous as it would then break the agglomerates formed and that the time the particles must be resident in the turbulence must be longer than the time constant to form agglomerates [74]. Electromagnetic separation of inclusions relies upon a differential Lorentz force, this force is created by inducing a magnetic field in the melt, which causes a pressure gradient in the conducting metal, but not in the non-conducting inclusions, which consequently experience a force acting upon them. In theory inclusions may be driven in any direction by a magnetic field.

Alumina inclusions are only weakly wetted by liquid aluminium (with a wetting angle of ~90^o) and the sticking force and attachment bond, as determined by Cournil [75], is strong. Cournil modeled 3-10µm alumina particles using hydrophobic silica particles in a water–ethanol solution, he stated that this was to be used as a model for alumina particles in steel.

The wetting properties of the two systems are similar but the silica-water system could be visually observed and high temperatures, a major barrier to experiments, were not required. The optical properties of the aggregates formed were explained by gas pockets on the surface of the particles, binding the particles together. He argued the bond formed by the merging of bubbles of previously separate particles, (see Fig 20), may provide the force which holds alumina particles together in the form of aggregates in molten steel, that persist despite the highly turbulent environment in which they exist. There is nothing to suggest that this work is not also valid for aluminium, though the effect of the oxide layer may potentially interfere with the surface bubble dynamics and the high temparatures in both molten aluminium and steel may cause the gases in the bubbles to be consumed by reaction with the metal, (as investigated by Raiszadeh and Griffiths [62] and El-Sayed et al. [76])

.

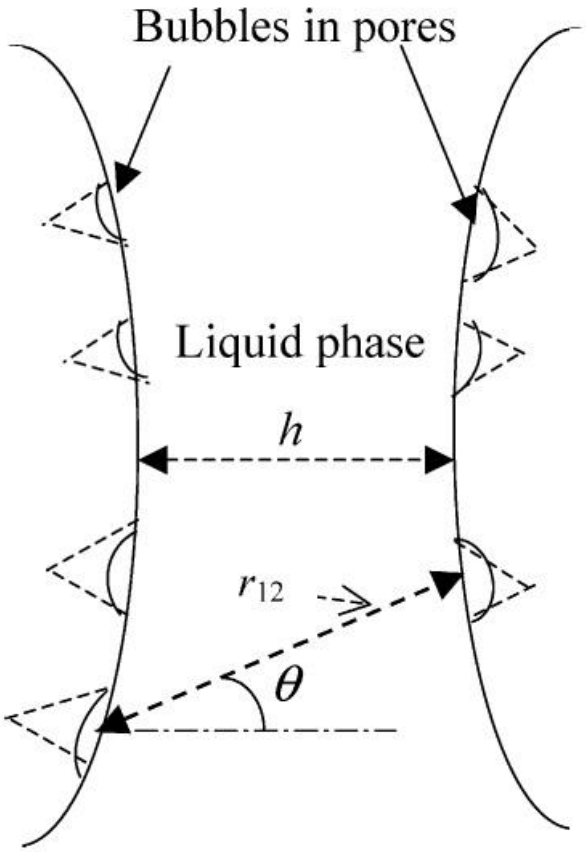

Figure 20 Bubbles in pores in two particles in close proximity [75]

2.4.3.2 Floatation and settling

The floatation process usually involves injecting an inert gas (N,Ar) through a rotary impeller, which is normally performed whilst the aluminium is in the furnace, but may also be performed in the crucible before the metal is poured. The rotary action causes a great deal of turbulence which assists in the agglomeration of inclusion particles.

The floatation process works by inclusion particles attaching themselves to the surface tension of a gas bubble; this has the opportunity to occur when the bubble and the particle collide. These collisions can occur where the metal is in turbulent or laminar flow, although the probability of a collision is higher in turbulent flow. Particles do not always attach to a bubble following a collision. In a water based experiment, in which a 4 mm bubble was maintained at the end of a capillary, with water flowing past it (Re_b 200-1400), it was observed that 100µm copolyamide particles can strike the upper surface of a bubble and slide along the surface of it. The particles may detach at the equator if they only slide for a short time. After a longer sliding time they reached the equator and did not detach. The sliding time may be related to the velocity of the particle along the bubble surface, but this was not stated by Mirgaux [28], who performed the experiment. Particles which did not detatch continued sliding to a position on the bubble to form a ring of particles. The location of the ring of particles was interpreted as being a position where a minimum force is exerted upon the particle, as it is the zone where the boundary layer separates from the bubble causing a ring of minimum stress (see Fig 21) [28] .

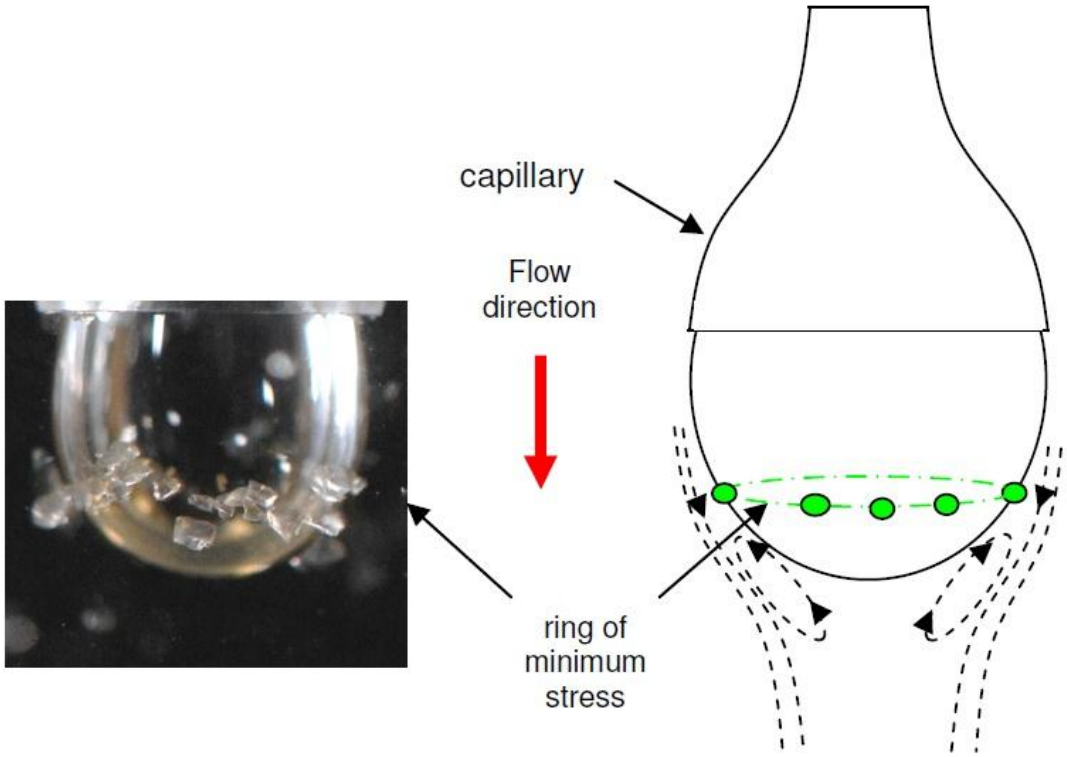

Figure 21 Copolyamide bubbles forming as a ring in a water based experiment [28]

Models for floatation mechanisms typically use a population balance, as detailed by Ramkrishna [77], and utilized by Mirgaux, who tried to arrive at a inclusion removal rate based upon a collision rate. The collision rate can be based upon a purely deterministic movement of the particles and the bubble, which gives a reasonably realistic particle removal rate for particles > 40µm. For particles smaller than 40µm a model more normally used for agglomeration, which included a random element to the movement of the particles created a better match to experimental results. The random element of the particle movement is said to model the turbulence better, which has a greater effect upon smaller particles. A compromise model combining random movements of the particles and a deterministic bubble sweeping them from the metal has been proposed [28].

Inclusion removal by floatation is in competition with removal by settling (particles sinking under the influence of gravity to the bottom of the melt). Course inclusions settle out faster than finer ones. In experiments using a 155mm diameter Alpur^{TM} rotor (see Fig. 22), bubbling argon and chlorine into a melt held at 1000K. Mirgaux found that most inclusions > 75µm had settled out after 600 seconds. The percentage of the inclusions removed by settling as out of the total inclusions removed is shown in Fig 23. It was found by varying the rotor speed and the gas flow rate, that a low gas flow rate with a strong agitation was more effective than a larger gas flow rate with weak agitation [28].

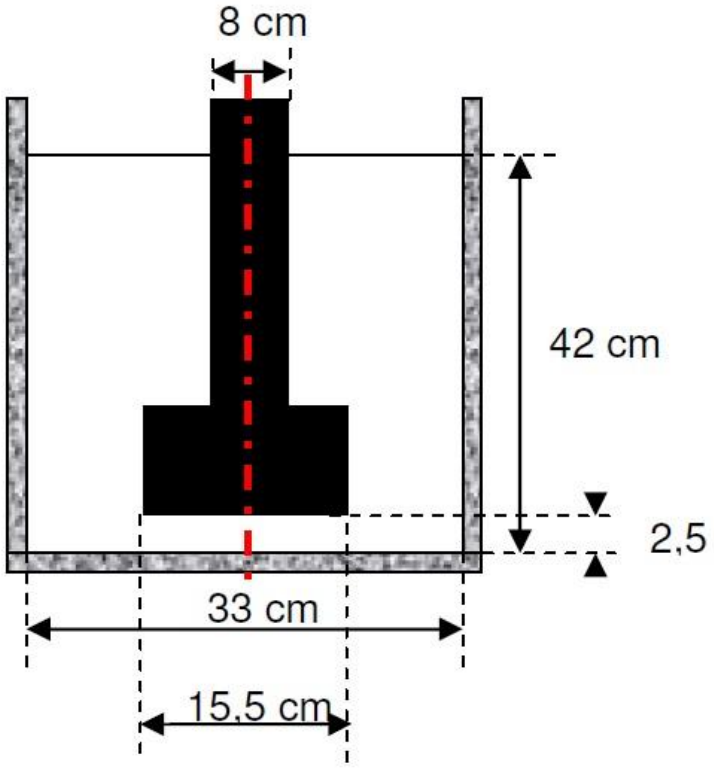

Figure 22. Mirgauxs' apparatus for bubbling gas in molten aluminium

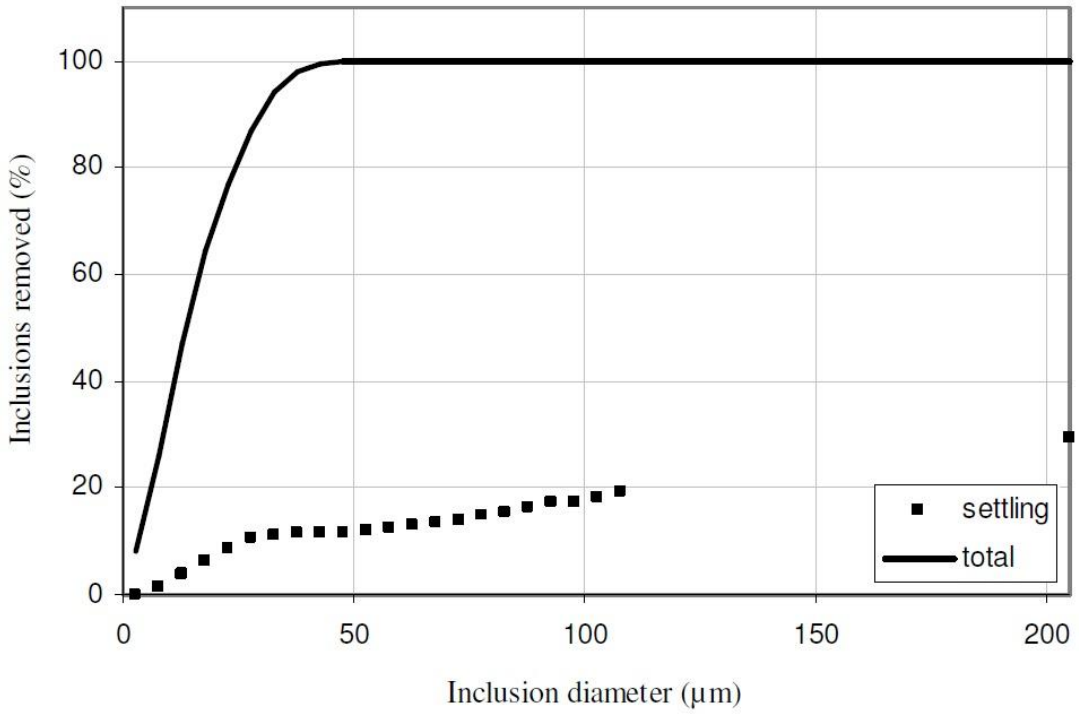

Figure 23. Inclusions removed by settling after 600 seconds of gas bubbling

2.4.3.3 Filtration

There are two main types of ceramic block filters, cellular filters and ceramic foam filters. Cellular filters have long straight parallel holes whilst ceramic foam filters are made from polyurethane foams coated with a ceramic slurry. They are then fired to sinter the ceramic and burn out the polymer[58]. Leaving an open porous structure consisting of interconnecting struts, with pore sizes in the range of 0.6 – 3.0mm (20-55 pores per inch). They have a large surface area and are said to be capable of operating in a deep bed filtration mode (depth mode), in which inclusions smaller than the pore size become entrapped in the filter due to the torturous path taken by the metal through the filter. In doing so inclusions come into contact with the filter struts and adhere to them [78,73]. The maximum metalostatic height when using filters is limited to around 1m as the filter must offer a sufficiently low resistance to the metal flow and the pores cannot practically be made any smaller [60].

Ceramic foam filters also reduce turbulence in the melt and partially prevent the passage of entrained air (see Fig 24).

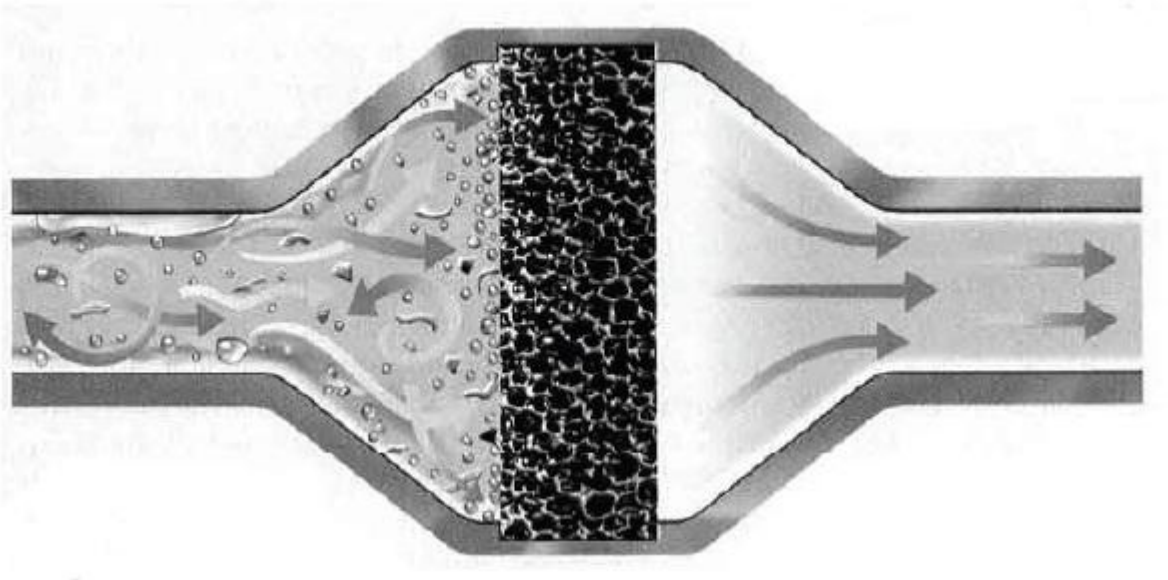

Figure 24 Effect of a filter on inclusions, air and the metal flow [79].

There are three main mechanisms proposed for filtration (see Fig 25), the sieve mode, cake mode and depth mode. In sieve mode filtration particles are trapped in the mesh or pores of the filter if they are too large to pass through the filter pores. In cake mode filtration large particles collect at the entrance of the filter and effectively reduce the mesh or pore size in order to remove smaller particles from the melt. This is associated with an increase in the pressure drop across the filter as the outer layer builds up. It is also associated with an increase in metallostatic head and is not used for aluminium. Depth mode filtration relies on a torturous path through the filter, causing particles to collide with and adhere to the walls or struts of the filter.

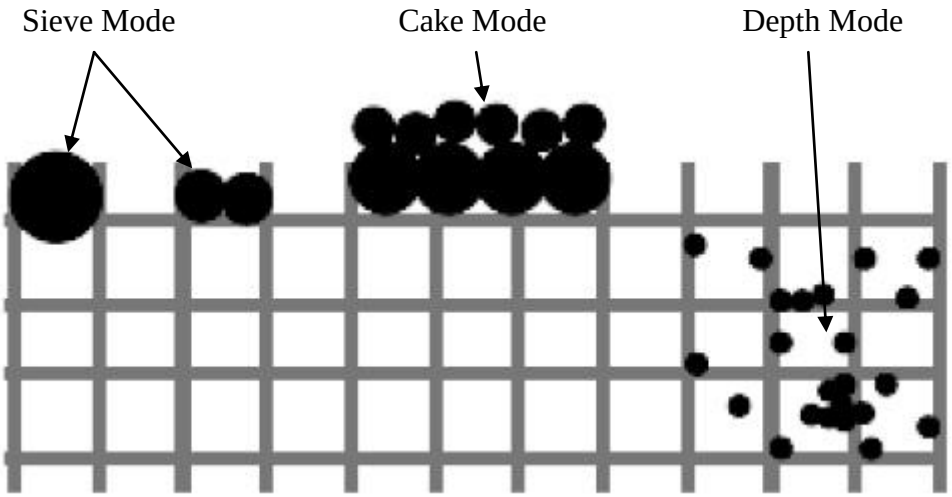

Figure 25 Filtration Mechanisms [80].

It is possible to filter molten aluminium using packed beds of alumina, silicon carbide or other ceramics, using a filter box containing unbonded balls, tabs or grains, with a size normally ranging from 0.7 to 2.5mm. This is so that the liquid metal passes through it, being filtered as it does so [60]. These packed beds have mainly been replaced by ceramic foam filters, but it was reported by Boa'de that by using ceramic particles coated with enamel (borophosphate enamel intended to improve wettablility) in a packed bed in conjunction with a ceramic foam filter, elongation of a test sample was increased by over 17% whilst the UTS was unchanged, (compared to unfiltered metal) [81].

Ni et al. claimed that all inclusions greater than 10 μm can be removed from the melt by ceramic filters, and they also claimed that inclusions between 1μm and 10μm cannot be eliminated by sole use of such a filter. 50% of these smaller inclusions being removed along with 95% of inclusions greater than 10μm [67]. Ni performed experiments using A356 alloy and a ceramic foam filter coated with a flux. The flux used was called JDN-I and this was melted and held at 700^{o}C for 10 minutes, and then a common 10ppi ceramic foam filter

(preheated to 300^{o}C), was dipped into the molten flux. The filter was then taken out and allowed to air dry for 10 minutes. The resulting filter was referred to as a composite filter. With the additional wetting of inclusions provided by the flux it was claimed that 6µm Al_2O_3 inclusions, deliberately introduced at a concentration of 1.72%, were removed, (at least the inclusions could not be found by metallography). In comparison, unfiltered alloy had many inclusions which had agglomerated to form clusters, many over 20µm in size. When filtered without flux inclusions averaging 10 µm were found. It was found that micro sized inclusions had clustered upon the filter filaments with the filter which had been immersed in flux and several possible methods for the capture of these inclusions were discussed by Ni, including sedimentation, cake mode filtration and inclusions being trapped by the flux layer [67].

Work by Reilly et al. was performed to simulate and track the motion of entrained double oxide films, in this work entrainment events were created within a simulated mould geometry in which the fluid surface folded and met. The simulation (see Fig.26) suggested that the role of a filter reducing turbulence in a mould has a direct effect upon the number of oxide inclusions created, which may be as important as its role of actually filtering inclusions from the melt, experiments supported this theory to a limited degree [82].

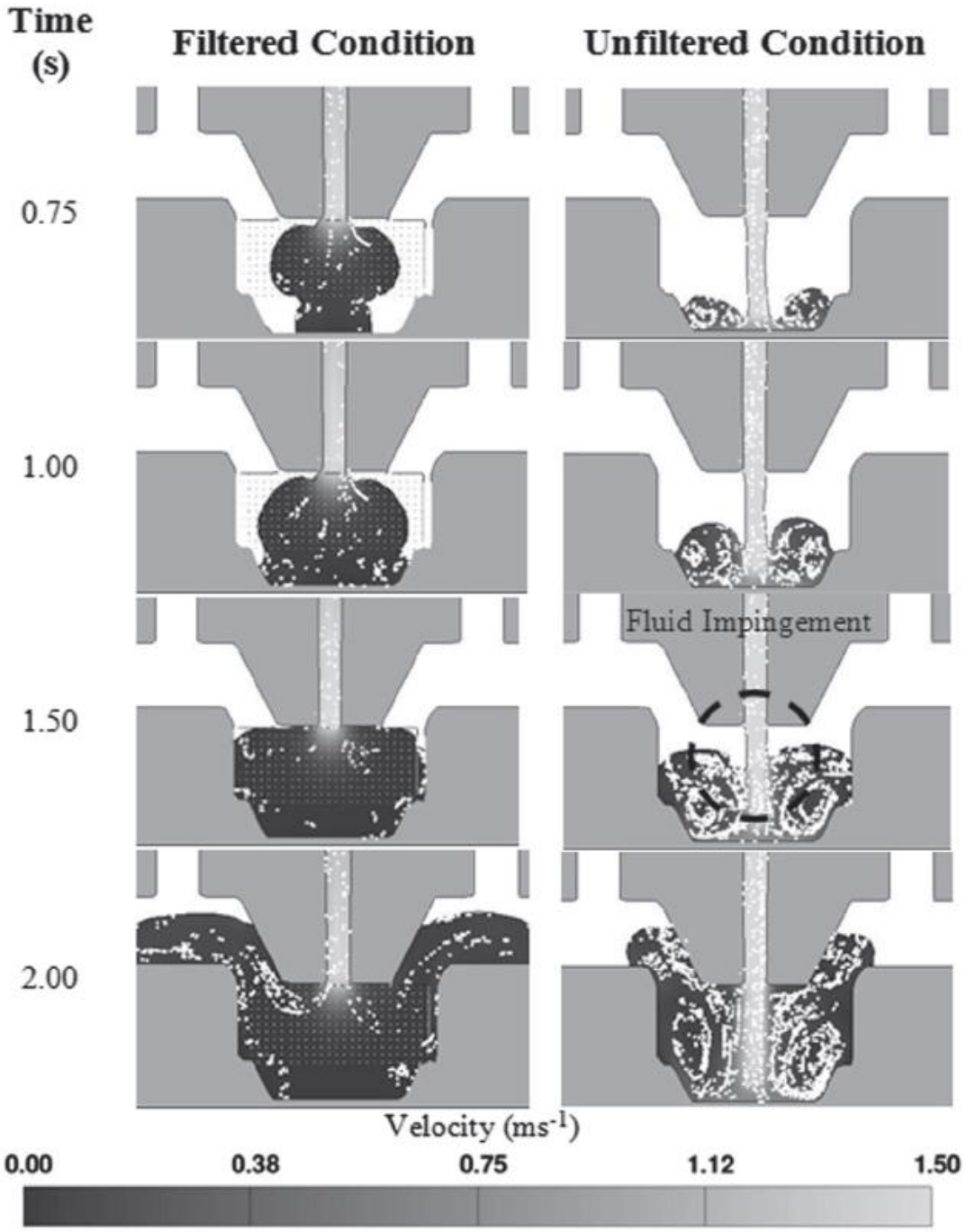

Figure 26. Simulated effect of a filter upon the creation of oxide films, where the flow with a filter (left) is less turbulent and leads to the formation of fewer oxide bifilms than without a filter (right) [82]

2.4.3.4 Fluxing

The purpose of a flux treatment is to reduce melt oxidation, accelerate inclusion removal and allow the recycling of aluminium metal from dross.

Most salt (cover) fluxes are based on a combination of NaCl and KCl salts in a 50:50 ratio by mass. In this form they have a eutectic temperature of around 660^{o}C. Cover fluxes based on MgCl-KCl melts at 424 ^{o}C and $MgCl_2$-KCl at 485 ^{o}C [83] form a liquid cover on the melt in aluminium to prevent oxidation. [84].

Rabbling fluxes work by increasing the wettability of the oxide inclusions and normally contain fluorides such as Na_3AlF_6, CaF_2 or Na_2SiF_6 to help accelerate this process [84]. Inclusions in molten aluminium have a higher surface tension than the surface tension of inclusions in the flux as the wettability of the inclusions is increased in the flux. This causes the inclusions to tend to transfer from the metal into the molten flux, which then helps lift them out as it rises to form dross.

2.4.4 Melt Conditioning

Melt conditioning by advanced shear technology is a new process, which uses a twin screw mechanism to shear the liquid metal, before being poured into a mould. The shearing action produces considerable bulk turbulence and it is claimed this causes the metal to form a uniform temperature and chemical composition. The oxide particles are said to become completely wetted and evenly dispersed, and are reduced to a small size (50-60 μm), with little variation [85].

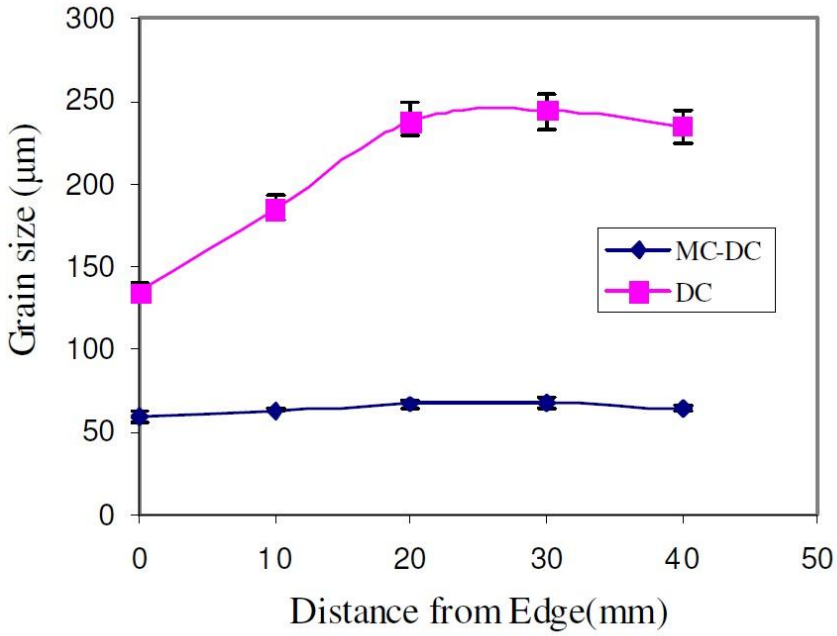

Figure 27. Grain size distribution for Direct Chill (DC) cast and Melt Conditioned Direct Chill cast metal in the same experiment [85]

The melt conditioning machine also fragments and evenly distributes the oxides throughout the melt (see Fig. 27) and this it is said improves nucleation, and in conjunction with the uniform temperature during freezing, leads to effective nucleation. It has been seen to produce castings without the normal dendritic structures and large inclusions, giving instead a fine equiaxed structure throughout [85]. A newer apparatus for melt shearing was announced, which uses a high speed rotor inside a stator in order to make the process easier to use, (possibly at an industrial scale) [86].

2.5 Inclusions In Steel

Non metallic inclusions in steel are described as being indigenous or exogenous dependent upon their source; indigenous inclusions are formed primarily by deoxidation of the steel or by precipitation during cooling and solidification [87]. Exogenous inclusions are formed by chemical and mechanical interaction of the liquid steel and its environment.

2.5.1 Types of Inclusions In Steel

2.5.1.1 Indigenous inclusions in Steel

Indigenous inclusions occur as a result of the reactions taking place in the molten or solidifying steel [88], and are caused by deoxidation of the steel forming primarily, alumina (Al_2O_3), in low carbon Al-killed steel (LCKA), and silica (SiO2) in Si-killed steel. In both cases these products are formed by the reaction between dissolved oxygen (from the production of the steel in a blast furnace or from the charge used in an electric arc furnace) [89], and the added deoxidant. Alumina inclusions in a high oxygen environment take a dendritic form, (see Fig 28), or otherwise appear as a cluster of aggregates (Fig 29), or coral-like structures formed by Ostwald ripening of dendritic inclusions, or as spheres of complex oxides from liquid slag entrainment, Fig 30 [90].

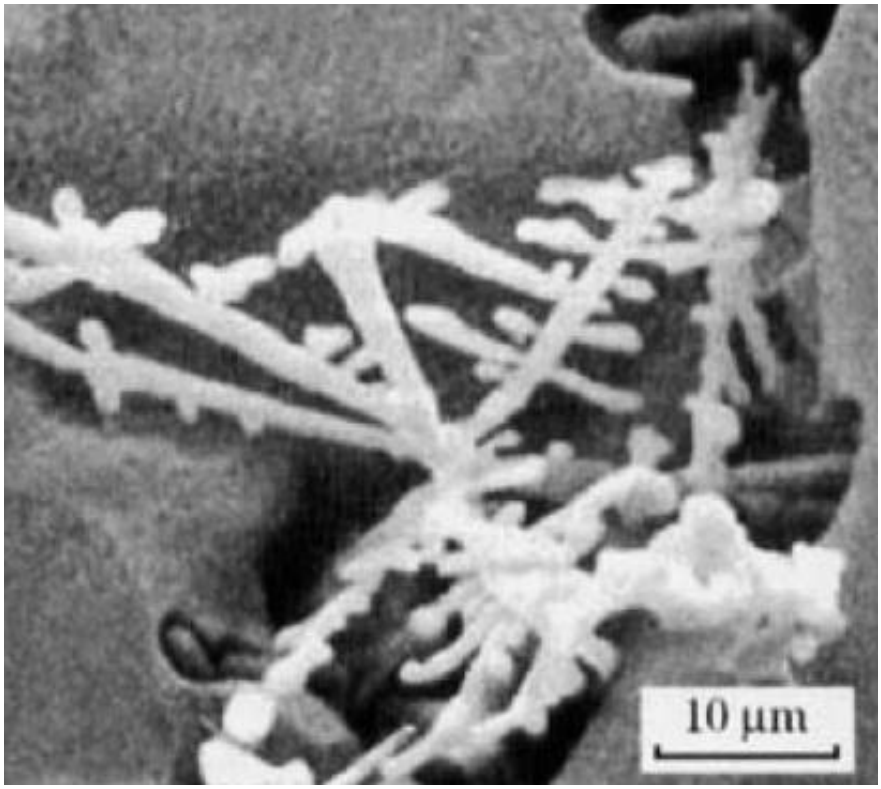

Figure 28. Dendritic alumina [91].

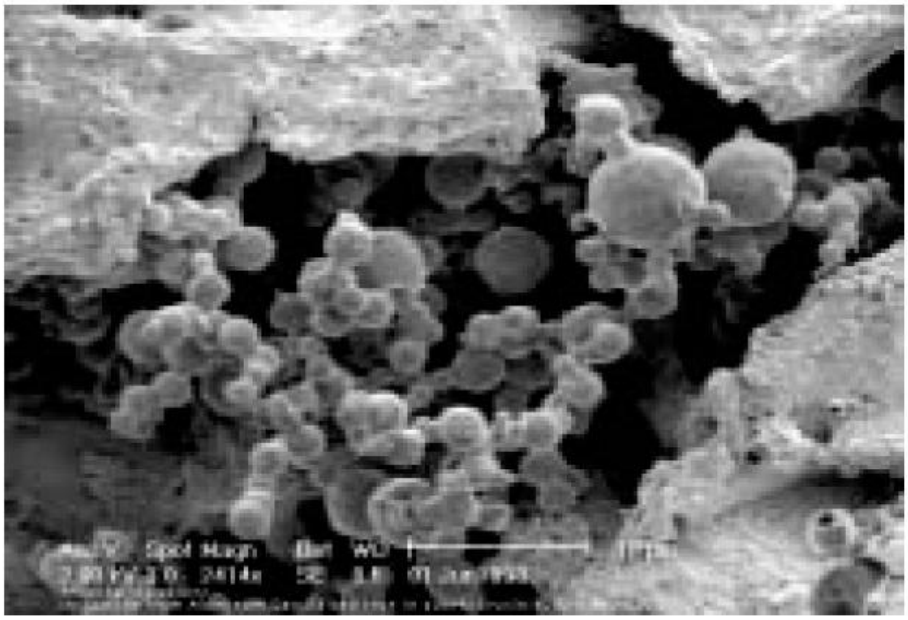

Figure 29.Alumina cluster inclusion formed during deoxidation or reoxidation [91]

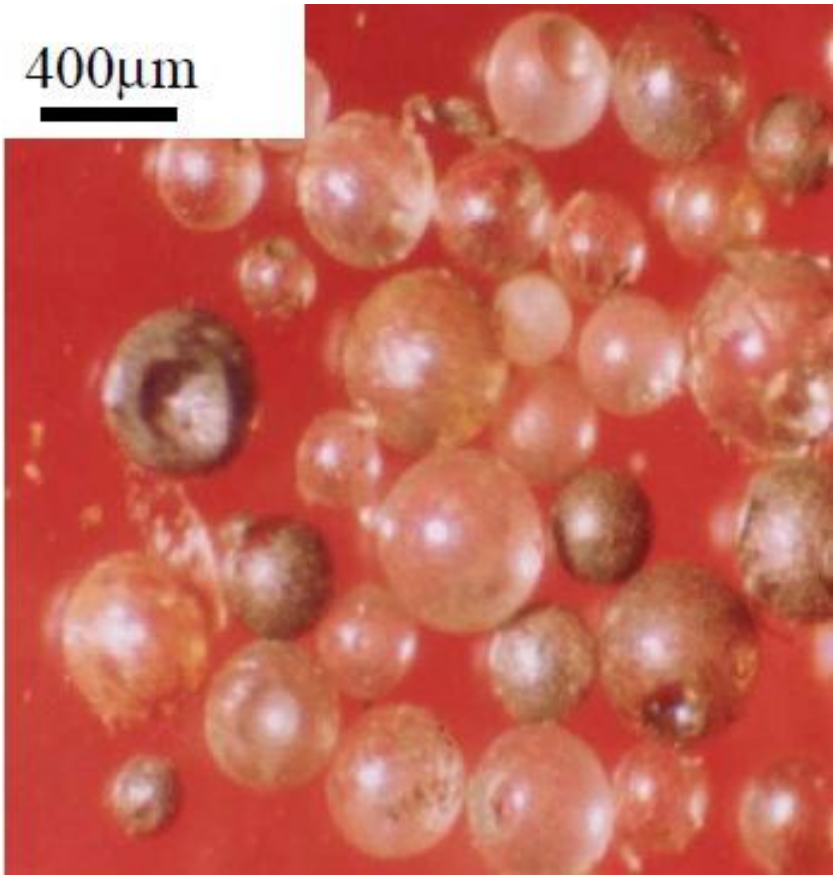

Figure 30. Inclusions from slag [92]

Silica inclusions are generally spherical as they are in a liquid or glassy state in molten steel and can form into clusters [87] and easily float out [93]. Other inclusions can also be formed, such as spinel and other compounds of alloying elements . Table 5 shows inclusions found on submerged entry nozzles during argon purging, indicative of some of these other compounds [87].

Inclusions	Comments
Al_20_3	Always found during casting Al-killed steels, can be caused by inclusion agglomeration, reaction between the steel and the nozzle or air aspiration through the nozzle
$FeO\text{-}Al_20_3$	The formation of hercynite is normally due to reoxidation of the clag after it is removed from the caster. The solidified iron oxidizes and reacts with alumina. This phase is not stable in Al-killed steels, unless in very oxidizing transitory conditions.
$MgO\text{-}Al_2O_3$ (Spinel)	Due to magnesium was injected into liquid steel.
TiN	A precipitation product during casting, especially for Ti-treated stainless steel.
$CaO\text{-}TiO_2$	Found during calcium treatment for Ti-treated stainless steel.
$CaO\text{-}Al_2O_3$ (solid or semi solid)	Found during calcium treatment if insufficient calcium is added or there is reoxidation.
$CaO\text{-}Al_20_3\text{-}CaS$ (Solid)	Typical buildup in high sulfur Al-killed steels where CaS precipitates from the liquid calcium aluminate.
$CaO\text{-}Al_20_3\text{-}MgO.\ Al_20_3$ (Solid)	Typical buildup in calcium treated steels when soluble magnesium levels in the steel are too high.

Table 5. Solid materials found in clogged submerged entry nozzles [87].

2.5.1.2 Exogenous inclusions in Steel

The physical interaction between the melt which creates exogenous inclusions mainly consists of reoxidation, slag entrainment and erosion of furnace lining refractory material. Slag and reoxidation inclusions can also react with the refractory lining to dislodge additional material into the melt. Exogenous inclusions are generally large compared to indigenous inclusions [88], due to the manner in which they are formed they can be >50 μm [87]. As exogenous inclusions move through the melt, due to their large size, they can trap deoxidation inclusions (mainly Al_2O_3) on their surface [92]. Exogenous inclusions tend to have an irregular shape and consist of multiphase material; they tend to be less prevalent than the smaller deoxidation inclusions and due to their density relative to the steel can float out. However, as they are caused by accidental dislodgement and entrapment in the steel during teeming they are randomly distributed and under certain circumstances do not have sufficient time to float out and become trapped in the casting [87]. Kiessling showed that the majority of exogenous inclusions in low carbon steel are due to re oxidation (83%) with the remainder made up of mould erosion (14%), slag entrainment (2%), refractories (1%) and deoxidation products (1%) [88].

Large reoxidation inclusions, newly formed inclusions created after the deoxidation operation, are formed when steel in the tundish mixes with air at its top surface at the start of pouring. Turbulence from the pour creates weak oxide films which then become entrained in the metal. Air can also infiltrate the melt at joints between the ladle and the tundish, and between the tundish and the mould. When this occurs the deoxygenating elements are typically Al, Ca and Si, and these oxidise to form non-metallic inclusions (up to several millimetre [94]). Reoxidation inclusions are usually an order of magnitude larger than those formed by deoxidation (around 5μm [87]). An estimated 83% of the macro-inclusions in

carbon and low-alloy steel castings are reoxidation inclusions, which in these steels are partially liquid in the molten metal, (see Fig 31), as opposed to the solid reoxidation inclusions in high alloy steels [94].

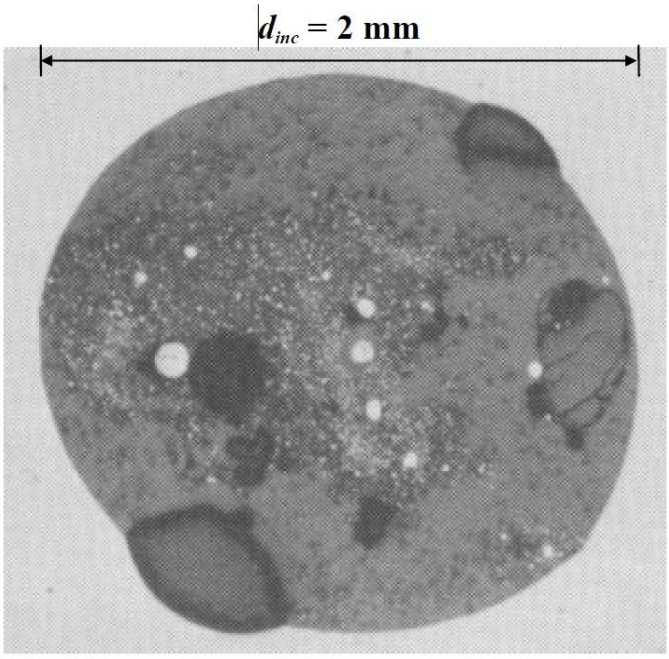

Figure 31. Typical reoxidation inclusion in carbon and low alloy steel [94]

To prevent this form of reoxidation the melt contact with the air must be controlled, which can be achieved by an inert cover gas and by purging Ar gas into the tundish before pouring or onto the tundish surface during pouring. Additional reoxidation occurs from SiO_2 , FeO or MnO in the slag being reduced by the remaining aluminium in the melt to form alumina, which leads to large alumina rich inclusions of inconsistent composition. The reaction can erode the refractory lining which can break and release inclusions from the refractory lining into the melt. It is therefore important to control the level of oxides in the slag.

Slag can be entrained into the steel in any operation where surface turbulence occurs. Inclusions entrained from the slag are typically 10-300µm and contain a significant amount of CaO and MgO so they are liquid and spherical within the molten steel and result in beads within the solid steel [91].

2.5.2 Effects of inclusions in steel upon material properties.

Steel is affected in a detrimental manner by large inclusions, large alumina and other oxide inclusions which are a major cause of fatigue. They also impair the strength and ductility of the steel and can have an adverse effect upon its corrosion resistance.

2.5.2.1 Effect upon Mechanical properties.

In high strength steels, oxide inclusions can cause ductile fractures, in lower strength steels it is sulphide inclusions which cause the majority of ductile fracture failures [95]. Refractory and slag entrainment inclusions also cause problems for machining processes (causing chatter, pits and gouges) [87]. It is therefore important that the larger inclusions are removed prior to casting. Smaller inclusions, <10 µm, [96], while not responsible for ductile fracture initiation, do contribute to the propagation of such cracks and both size and spacing are relevant and need to be controlled [96].

Ductile fracture in steel starts at a nucleation site, a hard particle, pearlite nodule, carbide or a large inclusion. Inclusions are harder than the matrix of the steel at room temperature and when steel is deformed a stress/strain concentration occurs at the inclusion, due to the applied force. The inclusion creates a void either by fracturing itself or by breaking away from the matrix to form a void. The void forms a crack as further force is applied, other cracks occur

around other inclusions at the same time and as the crack grows these smaller cracks join up and cause the steel to fail prematurely [96].

2.5.2.2 Effect upon fatigue resistance

The critical inclusion size for steel below which they do not initiate cracks for bearing steel is about 10 µm (just below the surface), due to the stress distribution, rising to 30 µm, 100 µm or more below [97,95]. Oxide inclusions raise the stress where they meet the metal matrix as they are hard and brittle. Manganese sulphide inclusions deform more easily and are thus less damaging. Silicates behave somewhere between oxides and sulphides, but slag or refractory inclusions are large and have irregular shape and increase stresses. Large inclusions concentrate tensile stresses under cyclic loads and are more likely to nucleate fatigue cracks and smaller inclusions help the crack to grow [95]. Beretta et al reported that for carbon steel (S45C Japanese Industrial standard) fatigue strength was dependent upon the size of an inclusion and not upon its chemical composition, claiming the composition of the inclusion merely affected its size [98].

2.5.2.3 Effect upon Corrosion resistance

Steel always contains some sulphur impurities which are insoluble in steel and form Iron Sulphide (FeS) inclusions. These FeS inclusions are good electrical conductors and create a electrical cells with the steel, causing it to corrode. It also causes brittleness at red heat temperatures, termed red shortness, and the steel has a tendency to crack under hot working (hot tearing). The addition of manganese in a ratio exceeding 4:1 relative to the sulphur content of the steel, converts the sulphides to manganese sulphide MnS [99], which is a poor conductor and does not set up corrosion cells. It also cures the hot and red shortness problems

[100] as the Iron sulphides it replaces lie in the grain boundaries and melt below the temperature of the molten steel causing the metal to become brittle, whereas the MnS has a melting point above that of the metal [101].

Ray found that for an EN1 steel in a chloride solution corrosion resistance also appears to be related to cyclic loading [99]. The loading applied was between 177-309 MPa on a 7.5mm test bar. A band of ferrite existed around any inclusions and this band will corrode regardless of any externally applied load. When a cyclic load was applied all inclusions tended to dissolve and the corroded area extended into the metal matrix where there was manganese and sulphur. Inclusion shape did not seem to affect the pattern of corrosion, however the cyclic load did encourage pitting which then led to cracking. [102]

2.5.3 Inclusion Control in Steel.

It is possible to measure the dissolved oxygen in steel, using total oxygen sampling techniques or an inert gas fusion method (as employed by Leco^{TM} TC600 [103] and ONH836 [104] analysers). This allows the total oxygen content to be estimated which can be used as an indicator of metal cleanliness as oxides are perceived to be the most damaging form of inclusion and many foundries control the oxygen level as their criteria for clean steel [105].

Aluminium is routinely added to steel to "kill" the steel (prevent CO-formation). It acts as a reducing agent and removes oxygen from the rest of the steel melt. The effect of this addition of aluminium is to form 3-10 μm alumina inclusions, and these can form into clusters 50-300 μm in size. It is claimed that the size and strength of these clusters can be attributed to surface gas bridges, as described by Cournil and in section 2.4.2.1 [75]. His work does not appear to have accounted for the effect of temperature upon the gases inside the bubbles attached to the

inclusions. This is however an example of how agglomeration can work against a casting process as these large cluster inclusions can cause significant reduction in strength and fatigue life if they do not float out to the top slag or onto the refectory lining. It was stated by Holappa in 1995 that previously (<1%) silicon or (<0.5%) manganese additions were used to kill the steel resulting in oxygen concentrations of 50-100 ppm, but with (0.02 – 0.03%) Al killed steel, concentrations as low as 5 ppm can be achieved [106].

In continuous casting of steel it is normal to bubble argon gas through the submerged entry nozzle to remove inclusions. Using a submerged nozzle helps to prevent clogging by solid inclusions [107,98]. A collection of solid inclusions can occur on any surface aided by surface tension effects, including that of the argon bubble and they tend to collect inclusions and lift them from the melt. This can however be a problem if the bubbles themselves get trapped in the cast billet. It has been reported that 93% of bubbles in continuously cast steel slab are argon bubbles from this process, with the remaining 7% being nitrogen and hydrogen [87].

It was noted by Braun that floatation rate of alumina could be increased by stirring mechanisms within the melt; the increased agglomeration rates create larger alumina particles which float out at a higher rate, in accordance with Stokes Law. Inert gas bubbling, induction stirring and mechanical stirring with an alumina paddle can all cause this agglomeration effect [108].

Sulphide and oxide inclusions can also be controlled by adding calcium to the melt; this is achieved by adding calcium using a power injection technique [109]. The calcium addition

forms calcium silicate which in low sulphide steels (<0.005%) is not deformable, but with higher sulphide content (>0.03%) is usually found bound to manganese sulphide and the combined sulphides are more deformable than iron sulphide, but less than pure manganese sulphide [106]. The Al_2O_3 inclusions combine with the calcium to form calcium aluminate inclusions. When the CaO content passes a threshold of 35% these inclusions become liquid at 1600^{o}C. The inclusions become liquid and take on a globular form and reduce the nozzle blocking problems caused by alumina inclusions during argon gas purging. These two inclusion forms often combine to form oxysulphides and the size of these inclusions is typically around 5µm. Following calcium additions and gas purging the steel must be prevented from coming into contact with the air as much as possible, as this causes reoxidation. A synthetic slag layer can be used for this purpose [106].

Exogenous inclusions originate from a variety of sources and so have differing characteristics when it comes to detecting them. Techniques which can be used include Ultrasonic scanning, optical microscopy, Sulphur Print, Slime extraction (Electrolysis), X-ray measurement of the composition of the slag, and observing the refractories to look for erosion and/or damage [105]. No single method can guarantee a casting is free from large inclusions but a combination can give an increased confidence level [105].

Steel can be filtered to remove inclusions, and three types of filters are used; foam filters, extruded cellular ceramic filters and pressed filter cores. The ceramic foam filters have an efficiency of less than 75% for non-metallic inclusions in ferrous metals for inclusions ranging from 1µm to 100µ, and are subjected to temperatures between 1400^{o}C and 1650 ^{o}C for up to 30 seconds for each ton of steel cast [110]. Janiszewski et al. theoretically and practically showed that multi-hole ceramic filters could also remove liquid calcium aluminate

inclusions, as well as solid inclusions [111], The filters reduce turbulence in the melt and therefore also reduce the risk of re oxidation [110].

2.6 Literature Review Summary

Both aluminium and steel suffer from the effects of inclusions, which degrade the performance of these materials in service. In order to better control undesirable inclusions a better understanding of their motion within liquid metal is required. The processes of PET and PEPT, carefully applied so as to circumvent the limitations of the processes in dense materials, should be able give a greater insight into the movement of solid particles within a melt. This data can then be used to validate computer simulations of the same particles, providing the basis for new development techniques.

Chapter 3
EXPERIMENTAL PROCEDURE

3.1 Tracer Labelling

Particles used for tracking experiments were γ alumina or glass spheres, these were used having a diameter of 600μm or 200μm. In all the experiments presented here the particles were made into radioactive tracers by the ion exchange process. The process gives activity levels of up to 2mCi with a 600μm γ alumina particle and 300μCi with a 200μm γ alumina particle. Activity levels for glass particles were considerably lower at 120μCi and 50μCi respectively. Ionic bonding of the ^{18}F ions to the surface of the γ alumina particles was assumed, It was also thought that this would be more efficient than the ionic bonding to glass particles, γ phase alumina being known for its ability to form ionic bonds with fluorine ions, as the intended use of the particles used, is to remove fluorides from drinking water, ordinary glass does not form ionic bonds as readily.

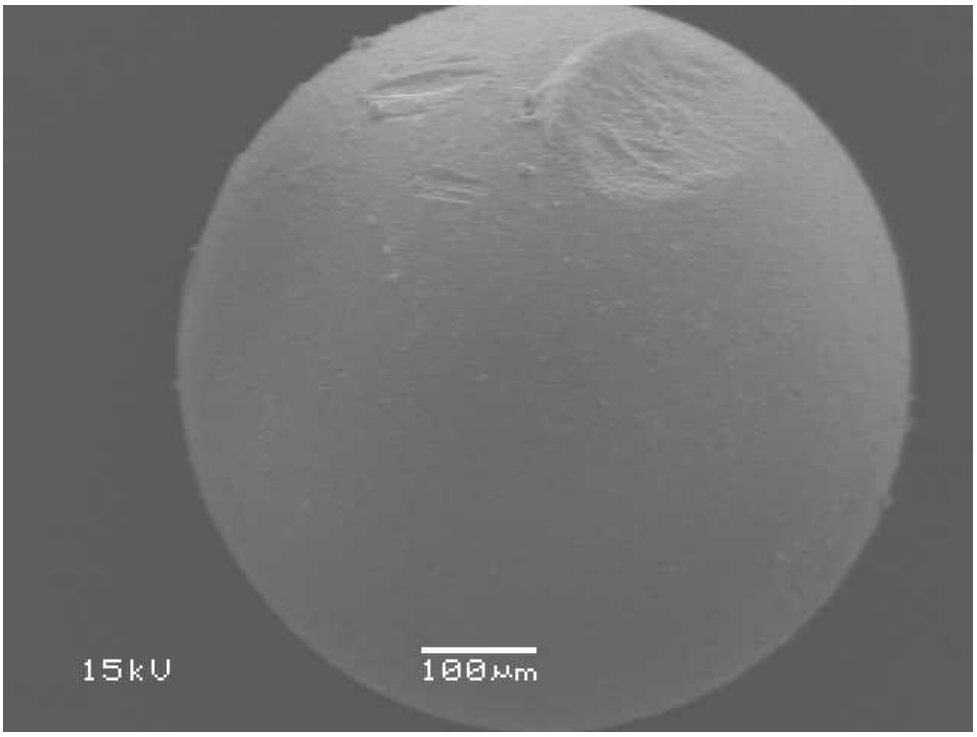

Figure 32. Alumina particle at low magnification.

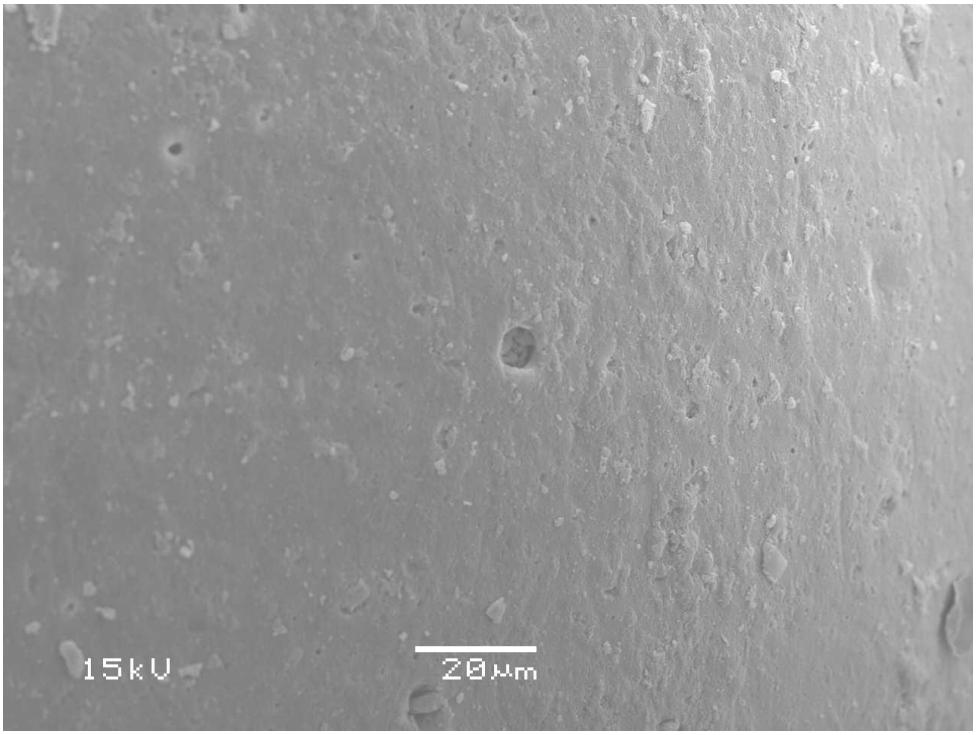

Figure 33. Surface of the Alumina particle

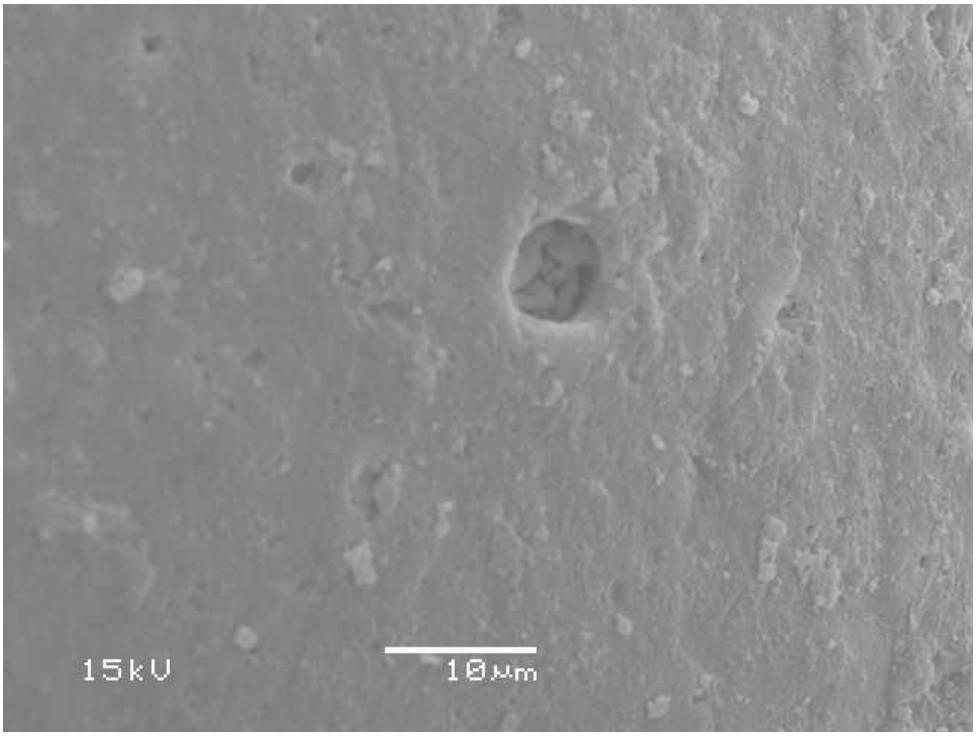

Figure 34. Close up of the surface of the Alumina particle

The alumina spheres were made of γ phase material and are said by their supplier (Alfa Aesar) to be porous as may be inferred by the surface features seen in figs 32, 33 and 34. They had a measured density 2873.5 kgm^{-3} with a standard deviation of 8.8 kg/m^3 for 0.0396g the 200μm particles, this being the true or absolute density. These measurements were made by the School of Chem. Eng. at Birmingham University using a micrometrics™ AccuPyc II™ 1340 gas displacement pycnometry system. In the pycnometry system a gas displacement system is used to measure volume accurately, the sample to be measured is sealed in a compartment of known volume, and helium is then introduced into the compartment which is then expanded into a second precision internal volume. The pressure of the helium before and after expansion is then used to compute the volume of the sample. Once the volume is known the density can be found by dividing the sample mass (measured using a precision balance) by the volume. The values found can be compared to the value of 3650 kg/m^3 reported by Inframat Advanced materials for 99.9% pure γ phase alumina[112] this gave a closed porosity value of 21.27% for the 200μm particles. The particles are less dense than pure alumina but the 200μm particles are still significantly more dense that molten aluminium at its melting point, this being around 2375 kg m^{-3}.

The porosity of the 600μm particles was found by sectioning (polishing though) the particle recovered from the particle tracking experiment using A20X alloy (see figs 91,92,93), and observing its internal structure, using a Jeol 6060 electron microscope. The images from the microscope were processed by applying a threshold to display the pores in a back and white image. The black pixels, (of the pores) were counted to give a porosity percentage by area relative to the whole image, The figure of 4.866% by area was recorded, this giving 4.866% by volume (Delesse's Principle) and the particles had a density of 3650-(0.04866*3650), 3472 kg m^{-3} denser than molten aluminium. The same technique was used to estimate the

open porosity. Using a part from the image shown in fig 33, this gave an area of 0.612% of the particles surface area which was used as the estimate the surface porosity. It was estimated given the low amount of closed porosity that 0.24% open porosity exists by the interconnectivity of pores then it is possible to estimate the envelope density of a particle.

Using the International Standard Atmosphere ISO 2533:1975 (air at sea level and 15^{o}C), the density of this air is 1.225 kg m^{-3}. The volume of a 600µm particle is 1.1309 x 10^{-10} m^3 giving an estimate of the mass of air within the open porosity of a particle of (0.0024 x 1.1309 x 10^{-10} m^3 x 1.225 kg m^{-3}) 3.3248 x 10^{-13} kg. (3.3248 x 10^{-10}g) When the mass of the alumina 0.999 x 1.1309 x 10^{-10} m^3 x 3472 kg m^{-3}) 3.922558 x 10^{-7} kg and the air is combined it gives a total mass of 3.922561 x 10^{-7} kg and an envelope density of (3.922561 x 10^{-7} kg/1.1309 x 10^{-10} m^3) 3468.5306 kg m^{-3}. The effect of temperature on the density of the solid alumina was assumed to be negligible, however the effect of temperature upon the gaseous air was significant, using an absolute pressure of 101000 Pa, a gas constant for air of 287 $J.kg^{-1}.K^{-1}$ [113] and the pouring temperature of 1023.15^{o}K (750^{o}C) using density = pressure/(Specific gas constant x Temperature) the density for air becomes 0.34388 kg m^{-3}, this gave an expansion in volume of 3.5623 times. The original volume of the gas within the particle remained unchanged and hence an additional volume of gas (3.5623 – 1), 2.5623 times the original volume of the air originally contained within the open pores of particle was expected to extend the envelope of the particle (the particle being contained within an oxide layer within the melt). The maximum pressure supplied by the melt resisting this expansion is small (2375 kg/m^3 x 9.81m/s^2 x 0.05m) 1.1649 Pa compared to the atmospheric pressure of 101000 Pa and is neglected here. The additional envelope volume created by the expanding air was given by the additional volume of the air added to the original particle volume. The new “envelope” had a volume of 1.13792 x 10^{-10} m^3 giving a temperature corrected density

of (3.922558 x 10^{-7} kg / 1.13792 x 10^{-10} m^3) 3442.52 kg m^{-3} , high compared to the density of liquid aluminium. When the 200µm particles were considered, it was not practical to count the number of particles used in the pycnometer, and an. open porosity of 20% of the closed porosity, (as was estimated for the 600µm particles was assumed) and 4.2% open porosity was used in the calculations. The envelope density was estimated to be 2752 kg m^{-3} and after allowing for the expansion of the air in the open porosity this became 2485 kg m^{-3}again denser than liquid aluminum. The 200µm particles would require an open porosity in excess of 7.3% in order for the particles to be positively buoyant in liquid aluminium, since the closed porosity was ~21% it was assumed that it was unlikely this level of connection between pores was present. The 600µm particles had a higher true density and would require even more open porosity and both sizes of particle were expected to be negatively buoyant and hence sink in liquid aluminum.

The particles are radioactively labeled using the ion exchange/surface adsorption technique outlined in 2.5.2.3, this is performed by immersing the particles in water containing ^{18}F ions created by ^{3}He bombardment of the purified water in the cyclotron. Bombarding water with high energy ^{3}He causes some of the oxygen atoms present in the water to transmute into negatively charged ^{18}F ions . During the adsorption phase of the process the water is evaporated leaving just the ^{18}F ions attached to the surface of the particles. To accelerate the evaporation, an infrared lamp heated the water, whilst a stream of nitrogen was directed over its surface.

3.2 Experiments conducted

Experiments were conducted to explore the use of the PEPT and PET techniques in conjunction with metal casting. The experiments investigated the temperature range, particle paths taken and final particle locations for several casting geometries, and also in a launder.

3.2.1 Low Melting point Alloy Experiment

It was unknown if the particles created by the ion exchange/surface adsorption process could be tracked by a PEPT camera at elevated temperatures, in liquid metals. The exact method by which the radioactive fluorine attaches to the particles is not currently known. It is believed to be by surface adsorption, involving van der Waals forces, or in some cases (when an ion-exchange resin particle was used, but this may possibly also be the case for γ phase alumina) by ionic bonding. The force binding the fluorine to the surface of the particle, and any force which would cause it to separate, are therefore not quantifiable as the ratio of the ^{18}F bound particle by ionic bonds and the ^{18}F bound to the particle by surface adhesion is not known and this could have an enormous effect. As the temperature rises in a system, the energy available increases, and as it is unknown what, if any, mechanism would cause the ^{18}F to separate from the particle and pass into the liquid metal. There is reason to believe that any such mechanism would be temperature related, in order to investigate the possibility that the particles could be tracked at elevated temperatures several preliminary experiments were conducted.

In the initial experiments an ADAC^{TM} positron camera was used to track radioactive particles placed in an apparatus between its detector faces. The relevant section of the cameras description from the Birmingham University Positron Imaging website is given below.

"The Positron Camera is a Forte dual-headed gamma camera manufactured by Adac Laboratories (California). It consists of two heads on a motorised gantry which permits rotation about a horizontal axis, and adjustment of the face-to-face separation of the detectors from 250 to 800 mm. Each head contains a single crystal of NaI(Tl) scintillator, 500x400mm2 and 16mm thick, optically coupled to an array of 55 photomuliplier tubes. The dead-time per pulse is approximately 170 ns and each head can operate at a singles rate of over 2M cps. The detectors have an energy resolution of better than 15% (FWHM of the 511 keV photopeak), sufficient to discriminate against photons scattered by more than 30°. The quantum efficiency of each head for detecting 511 keV photons is approximately 23% (full spectrum) or 16% using just photopeak pulses, while the coincidence resolving time is 7.5 ns. The spatial resolution of the camera (FWHM of the back projected image of a point source) is approximately 6 mm." [114]

A hot plate was used to melt a low melting point alloy, Lens alloy 136, which was contained within a 600ml glass beaker. In all the experiments K type thermocouples were used to track the temperature. Particles of glass, resin and γ phase alumina were used in the experiments.

In the first series of experiments a radioactive particle was held under the surface of the liquid metal using a steel mesh (Fig 36). The metal used was Lens alloy136, this is an alloy of 49%Bi , 21% In, 18% Pb and 12% Sn, by weight, it has a density of approximately 0.30 lb/in^3 (8304 kg/m^3) [115] and attenuates γ-rays appreciably compared to most other metals. It has a melting point of 58^oC which allowed experiments to be performed at relatively low temperature using a hot plate as the heat source. The intention was to investigate if sufficient radioactivity from a particle transfers, "leaches", into the surrounding molten metal so as to interfere with the particle tracking system. Had this happened the

apparent particle location would have shifted during the experiment so each experiment was conducted over a considerable time in excess of 25 minutes each.

The particle was observed using PEPT, experiments were conducted with both γ phase alumina, ion exchange resin and glass particles, each activated by the ion exchange/surface adsorption process.

Initially a 600 ml beaker was used to contain the Lens alloy metal, this having a diameter of 82mm, this diameter determined the attenuation of the emitted γ rays in the system as a particles at one edge of the beaker would emit γ-rays which would possibly have to travel through the metal for the entire diameter of the beaker (and its glass wall) before it could strike a PEPT detector. After it was found to be impossible to track the particle (using two different particle types) a calculation for the attenuation was performed for 82mm of Lens alloy and 1.5mm of glass (the beaker wall).

The γ ray attenuation was calculated for the system, using the equation

$$I_d = I_o . e^{-lt} \qquad \text{Eq. 26.}$$

where
I_d = transmitted radioactivity
I_o = Intial radioactivity
l = linear attenuation coefficient (quoted by NIST as a value per cm)
t = thickness of material (in cm)

e^{-lt} gives a transmission coefficient the attenuation coefficient is given by $1- e^{-lt}$.

The transmission coefficient may be multiplied together for a parallel combination of materials of differing thickness to give the combined transmission. The linear attenuation coefficient for lensalloy at 500KeV was given as 1.17cm^{-1} by Beshay [116] and the linear attenuation for silica (Glass) at 500KeV is given by NIST as 0.218cm^{-1} [117]

	Lensalloy		Glass
$I_d = I_o . e^{-1.17 * 8.2}$		*	$e^{-0.218 \times 0.15}$
$I_d = I_o . 0.00006814$		*	0.9784
$I_d = 0.00006666\ I_o$			

1 - 0.00006666 =

99.99993% Attenuation

In the experiment 99.99993% of the emitted γ-rays was absorbed by the metal and glass of the apparatus, therefore the experiment was modified to use a flat bottomed test tube to hold a lower volume of metal to reduce the attenuation, by reducing the thickness of the metal which the γ rays had to penetrate. In addition a steel tray to contain any potential spills was included as the calculated worst case attenuation only changed by 1% when this was factored in, the modified apparatus is shown in Fig 37.

When the new configuration of the experiment with 16mm of Lensalloy, 1mm of Glass and 1mm of steel tray was considered it gave the following equations for γ ray transmission and attenuation.

With steel tray included in experimental apparatus (See Fig 35).

Lens alloy Glass Steel

$Id = Io.\ e^{-1.17 \times 1.6} \times e^{-0.218 \times 0.1} \times e^{-0.655 \times 0.1}$
$Id = Io.\ 0.1538 \times 0.9784 \times 0.9366$
$Id = 0.1409\ Io$

$1 - 0.1409 = 0.8591$

86% γ ray attenuation within the apparatus

Without steel tray included in experimental apparatus (See Fig 35).

Lensalloy Glass

$Id = Io.\ e^{-1.17 \times 1.6} \times e^{-0.218 \times 0.1}$
$Id = Io.\ 0.1538 \times 0.9784$
$Id = 0.1504\ Io$

$1 - 0.1504 = 0.8496$

85% γ ray attenuation within the apparatus

The attenuation coefficient for Iron from NIST [117] was used as an approximation for the attenuation for steel as the carbon content is low enough to be neglected for γ-ray attenuation considerations.

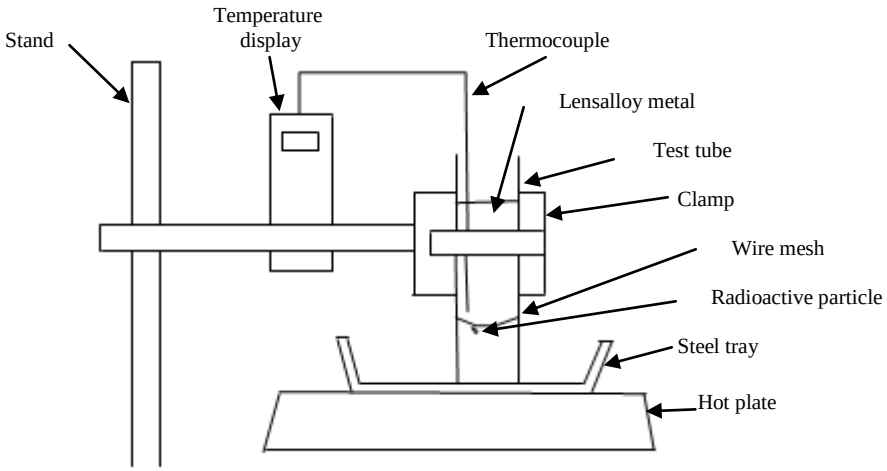

Figure 35. Apparatus used for the initial experiments

The apparatus was moved during the experiment to determine if the motion could be detected. At the end of the experiment, after the radioactive particle had been removed from the liquid metal, the metal was tested for radioactivity with a Geiger counter.

3.2.2 Low Melting point alloy and Sn Experiment

As some radioactivity dispersion was observed by the Geiger counter in the previous experiments, a further set of experiments was conducted, these used pure Sn as well as Lens alloy136, the experiments were used to determine if the dispersion of radioactivity in the metal, significantly affected the ability to track a particle by PEPT.

The experiments were conducted, so that movement of the particle could be induced, by mechanically pushing the particle down within the melt and allowing it to rise again. This was done to rule out the possibility that the initial set of experiments had been tracking the centre of a spread of radioactivity. Another issue the initial experiments had highlighted was the heat loss from the test tube, which caused a thermal gradient to occur with the metal at the top of the test tube being considerably cooler than that at the bottom, this could have caused abnormal radioactivity dispersion, by convection within the liquid metal.

The second series of experiments was performed to address the issues arising from the first experiment and also to increase the maximum temperature used. The test tube was placed in a copper sleeve, with a copper base, to conduct heat from the hot plate to the top of the test tube.

A small glass rod with an inverted test tube attached, was used to contain the particle during each experiment. This was half-filled with metal, the particle inserted - and additional liquid metal poured in at a temperature just above its liquidus such that the particle became trapped, when the metal solidified. The rod-tube combination was then inserted into the main test tube of liquid metal such that the solid metal it held at this point would melt releasing the particle (Fig 36). The temperature used in these experiments started at 70^{o}C for the Lens alloy and was gradually increased to just over 400^{o}C and was then started at 240 ^{o}C for the Sn and increased to a final temperature of 411^{o}C. Since all the particles used were less dense than the Lensalloy136 and Sn used in the experiments, the particle would always rise up inside the inverted tube until it met the glass rod. Pressing down or lifting the rod whilst keeping the bottom of the attached inverted tube section under the level of the liquid metal allowed a vertical motion of the particle within the liquid metal to be obtained and recorded.

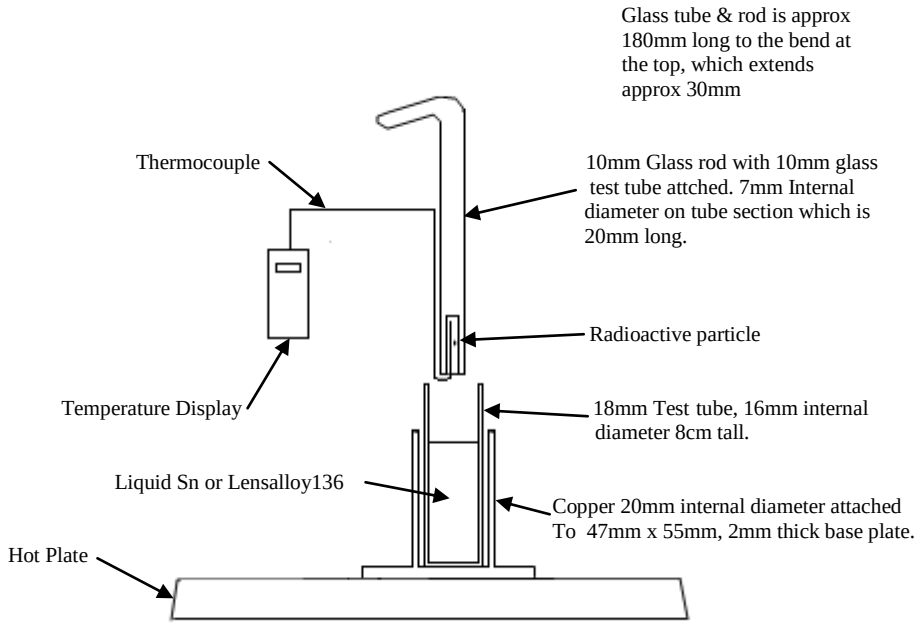

Figure 36. Apparatus used in the second series of experiments

3.2.3 Particle tracking experiment in Aluminium.

A modular positron camera already existed at Birmingham University as described in section 2.5.1.3. To carry out a casting experiment the encased detector modules were positioned in a square pattern around a resin bonded sand mould, the mould was positioned diagonally within this square. The outer dimensions of the mould were nominally 460 mm x 275 mm 110 mm, consisting of two halves.

The two co-incident back to back γ-rays, created with each positron annihilation were detected by this positron camera, it was constructed using components from a standard medical PET scanner, it had in total sixty four detector blocks, four in each module, with four modules in each bank on each side of the detector configuration. The moulds used in the experiments were made of resin-bonded silica sand, with the mould cavity itself being a simple plate 200 mm in length, 100 mm in height and 15 mm in depth, with a bottom-filled

running system with a cross section of 20mm. To introduce the radioactive particle into the mould the particle was placed inside a 3mm diameter aluminum rod (the particle was held in a 1mm diameter 5mm deep blind hole, crimped closed at around 2mm from the open end) which was inserted through a hole formed in the mould so that it protruded into the top of the downsprue at a known initial position. (See Fig 37).

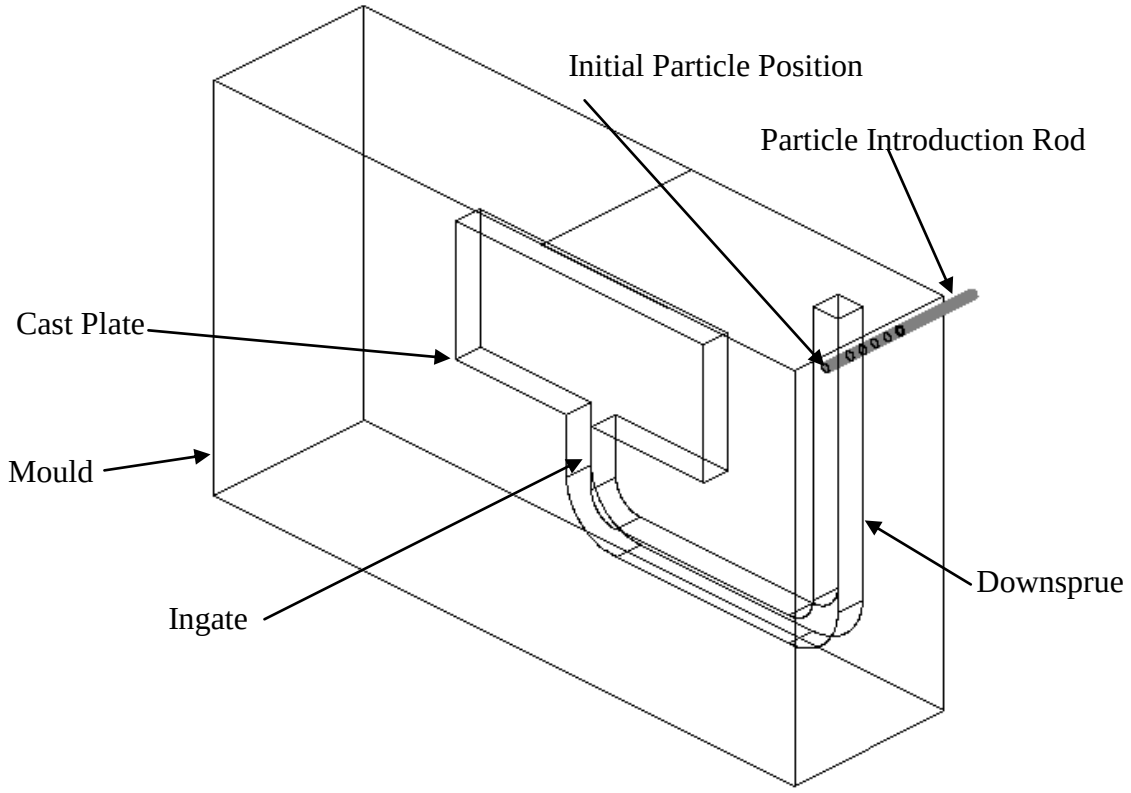

Figure 37. Mould cut away showing downsprue, plate and particle introduction rod

In order to protect the positron camera from a possible liquid aluminum spill a 26mm thick aluminum chill plate was placed on a bed of sand, around this a row of insulating bricks was laid and bonded together with silicone, the gap between the chill plate and the bricks was filled with sand. Outside the insulating bricks and wedged in position by the positron camera modules, MDF panels were set to protect against liquid metal splashes (Figs 38 and 39)

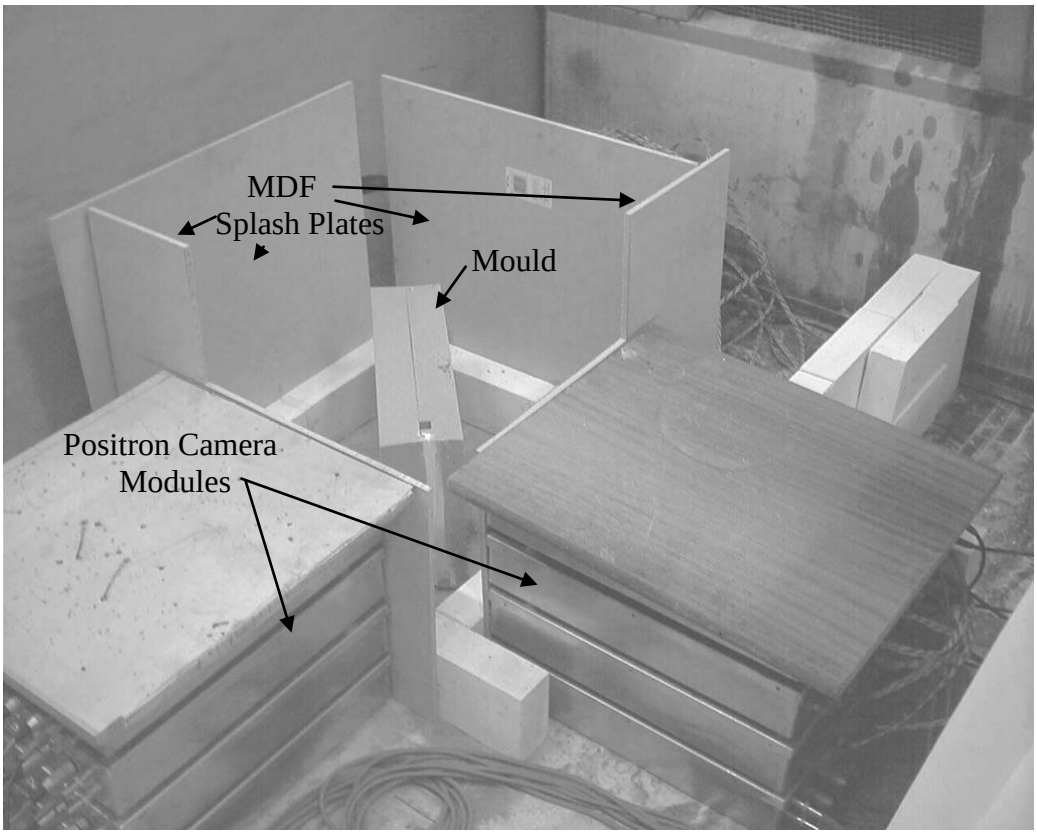

Figure 38. The Mould position within the modular positron camera

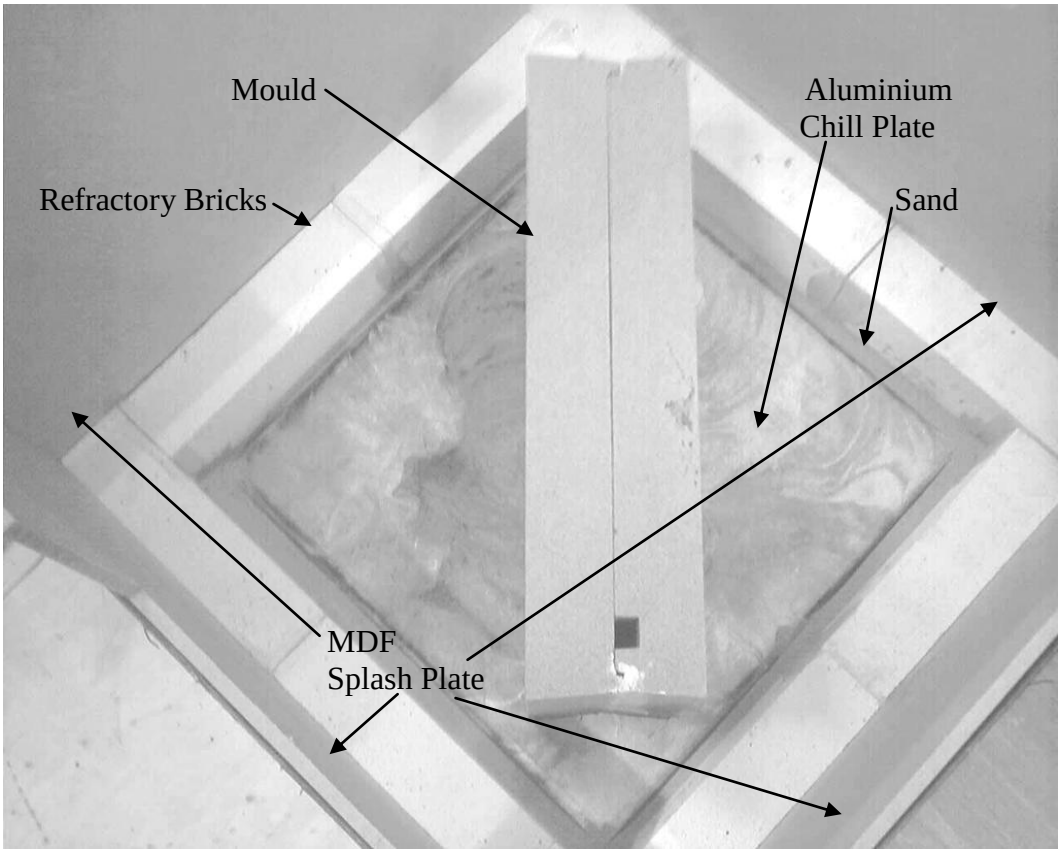

Figure 39. Overhead view of the Mould

Once the mould had been set up inside the detector geometry, a radioactive tracer particle was positioned at several reference points around the first mould, such that these could be used to give known locations within the three dimensional space observed by the positron camera, Fig 40, These were later used to correct alignment errors between the mould and the co-ordinate system when plotting particle tracks.

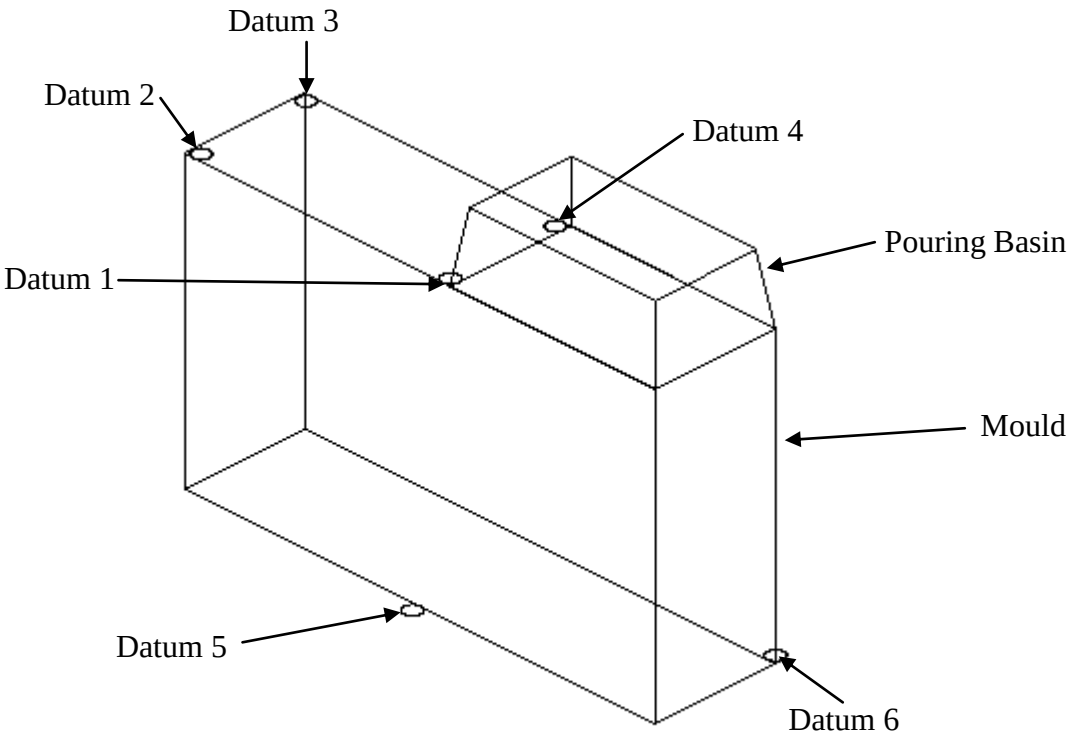

Figure 40. Datum positions recorded around the mould.

The particles were sufficiently small that it was difficult to place them inside the hole in the introduction rods. These handling problems with the smallest of the particles were solved by transferring them to the cavity in the rod using a pin coated with cyanoacrylate glue, the contact area between the pin and the particle was minimized as much as possible to reduce contamination.

The moulds were cast at 750°C and in order to ensure that the liquid metal flow was as consistent as possible a graphite stopper blocking the entrance to the downsprue was used. Once the pouring basin was filled, the stopper was removed and liquid metal was released into the downsprue, causing the 3mm Al rod to melt, releasing the radioactive particle into the metal stream.

Twelve moulds were cast containing radioactive particles of γ-alumina and glass (i.e., predominantly SiO_2), these were of three different nominal sizes, 600 μm alumina, 300 μm glass and 110 μm alumina. The range of activity associated with the particles was from a maximum of 780 μCi down to 26 μCi, at the time they were used in an experiment. The activity at the time of use was calculated from the measured radioactivity at the time of the particle production, the half-life of ^{18}F (109.77 minutes [118]), and the time elapsed between particle production and use. Since the cast plate was only 15 mm thick, and the positron camera had a resolution of 4 to 8mm in each axis, only plan views of the particle tracks within the castings were considered.

The attenuation in the experiment was analysed, the mould was placed at 45^o to the faces of the positron camera and the γ-ray attenuation considered should also take this into account. Assuming a γ-ray takes the most direct path to the positron camera detector face, the worst case occurs if the particle travels to the side of the aluminum plate such that one of the γ-rays emitted, has to travel through the full depth of the cast plate and the thickest section of the resin-sand mould (both at 45^o to the detectors). The γ-ray then also has to travel through the 9mm MDF splash protection board (See Fig 43). This represented the average attenuation that the most affected γ-rays of a pair might experience when the particle was at this point. A 20% porosity value was used for the attenuation calculation to represent the air gaps between the AFS 60, 60μm sieved sand.

Positron Camera Detectrors

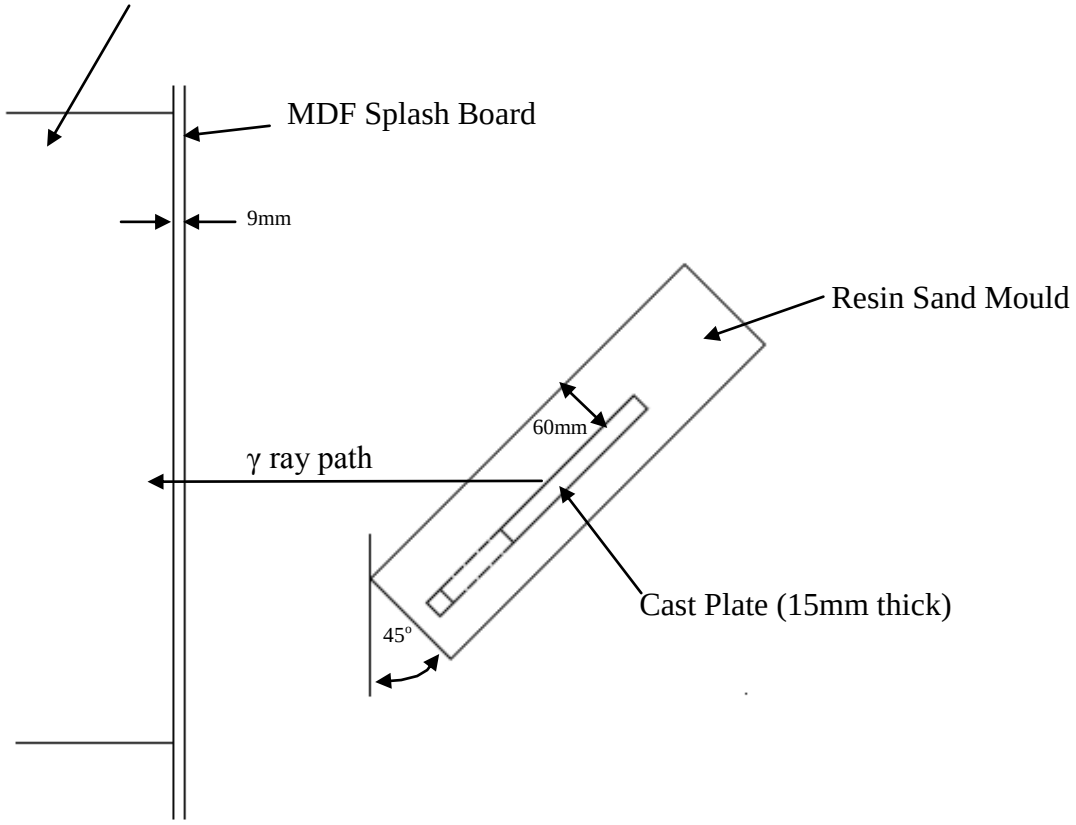

Figure 41. Path of γ ray for worst case direct path attenuation considered.

As the γ-ray is at 45° to the mould material and the cast metal, as is the case for the aluminium and the silica sand in the experiment , the distance it travels though these two materials can be determined by Pythagoras theorem. At 45° the sum of the square of the two sides which are not the hypotenuse becomes a fixed ratio of 1.41 times the length of the side. So taking the square root of 1.41 times the material thickness directly yields the thickness of material the γ-ray has to travel through.

The γ-ray absorption is calculated by

$$\gamma \text{ absorption } = e^{-(\gamma \text{ absorption coefficient } \times \text{ material thickness})} \qquad \text{Eq. 27.}$$

The γ-ray absorption for each of the materials used in the experiment is considered in turn.

Aluminium
Max thickness → 1.5 cm @ 45 degrees = $\sqrt{1.41 \times 1.5}$ = 2.12
γ absorption coefficient→ 0.228 [117]
γ absorption $= e^{-0.228 * 2.12} = 0.6167$
attenuation = 1- γ absorption
(1-0.6167) = 0.3833 38.3% attenuation

Silica (AFS 60 60um sieved sand.)
γ absorption coefficient → 0.218 [117] * 0.8 (for 20% porosity) = 0.174
Max thickness 6 cm @ 45 degrees = $\sqrt{1.41 \times 6}$ = 8.46
γ absorption $= e^{-0.174 * 8.46} = 0.2294$
attenuation = 1- γ absorption
(1-0.2294) = 0.7706 77.1% attenuation

Wood (MDF)
γ absorption coefficient → 0.024 [119]
Max thickness 0.9cm
γ absorption $= e^{-0.024 * 0.9} = 0.9786$
attenuation = 1- γ absorption
(1-0.9786) = 0.0214 2.1% attenuation

The total attenuation is given by multiplying the absorption figures for the three materials together and subtracting this value from 1.

0.6167 * 0.2294 * 0.9786 = 0.1384
(1-0.1384) = 0.8616 86.2% attenuation.

The radioactivity levels of the particles used in each of the experiments was considered, this allowed for the decay of the ^{18}F tracer isotope, after the production of the active particle before its use in an experiment. The effective radioactivity at the time the particle was used but after the effect of attenuation was also calculated, this is not a true radioactivity level, but can be used as a guide as to the intensity of γ-rays the positron cameras detectors experience.

$$A_t = A_i - (A_i\left(\frac{t}{halflife}\right)0.5) \qquad \text{Eq. 28.}$$

where A_t is the Activity at the time of use (of the radioactive particle)
A_i is the Initial Activity (of the radioactive particle)
t is the Time (between production and use of the radioactive particle)
halflife is radioactive half-life of the isotope (109 mins for ^{18}F)

Experiment Number	Particle Size	Particle Type	Initial Radioactivity (Ai)	Time between production and use (t)	Calculated Radioactivity at time of use (At)	Effective Radioactivity after attenuation
1	600µm	γ Alumina	1067µCi	60 m	773µCi	107
2	600µm	γ Alumina	887µCi	90 m	520µCi	72
3	600µm	γ Alumina	967µCi	120 m	434µCi	60
4	600µm	Glass	200µCi	30 m	172µCi	24
5	600µm	Glass	196µCi	60 m	142µCi	20
6	110µm *	γ Alumina	492µCi	40 m	401µCi	55
7	110µm *	γ Alumina	132µCi	85 m	51µCi	7
8	110µm *	γ Alumina	105µCi	120 m	47µCi	7
9	300µm	Glass	48µCi	35 m	40µCi	6
10	300µm	Glass	92µCi	42 m	74µCi	10
11	300µm	Glass	75Ci	75 m	49µCi	7
12	300µm	Glass	50µCi	105 m	26µCi	4

Table 6. Particle tracking experiment in aluminium radioactivity levels

*particles in experiments 6,7 & 8 were from a batch of 110 µm γ Alumina powder, these were quoted as being 110 µm average size by the supplier but some variation in size was observed, the particles ranged from 70 µm to 140µm.

An additional experiment was performed using an aluminium alloy called A20X, this used a 600 µm aluminina particle of 392 µCi at the time of production. The plate casting made was sectioned so that the particle was contained within a 28 mm x 24 mm x 15 mm block of metal.

A Geiger counter was presented to both cast faces of the block, this indicated which side of the block the particle resided in. The block was marked up with the predicted location of the particle and X-Ray images were made, in an attempt to locate the particle. A dark shadow on the X-ray images was present at the expected location of the particle around 6mm depth from the side of the highest reading on the Geiger counter. The particle would have been expected to have made a area on the X-ray lighter than the background. The block was machined by dry cutting with a milling machine, using a 20 mm milling cutter, to a depth of 5 mm from the cast face of the block which had been the most active. Then 100 µm cuts were taken with visual inspections with a USB microscope in between. When pores opened up, they were examined by use of a Jeol 6060 electron microscope, with an EDS spot used to identify the material of the features found. This process continued until the particle was found.

3.2.4 Particle tracking in Steel and Aluminium

It had been found that it was possible to track particles in aluminium at a temperature of 750 ^{o}C, an experiment was conducted to test if particles could be tracked at even higher temperatures.

Due to these higher temperatures an investment mould was used, rather than a sand mould, the new mould had two layers of zircon amounting to a thickness 1.5 to 2mm and five layers of mullite of around 4.5 to 5mm thick, giving a total shell thickness of around 7mm. Despite being more highly attenuating materials, this arrangement gave a lower overall attenuation figure than that of the resin-bonded sand moulds. This was due to the reduced amount of material the γ-rays have to penetrate.

The mould (See Fig 42) consisted of an upper and lower ring, of 100mm internal diameter and 130 mm external diameter, 25 mm in height. The lower ring had four radial 15 mm diameter arms at 90^{o} to each other rising at 45^{o} until they met a central boss of 50mm diameter which was 25 mm deep. The two rings were linked together by four 10mm diameter connecting rods each 200 mm long, the connecting rods were immediately adjacent to the radial arms. A 225 mm long tapered downsprue was positioned in the centre of the upper ring, being 30 mm diameter at the top and 15 mm at the bottom where it met with the upper face of the boss. A 110 mm x 60 mm pouring basin 70 mm deep was positioned on top of the downsprue. 160 mm from the base of the downsprue and at a rotation of 45 degrees from the orientation of the pouring basin, there protruded a tubular support, this was used to allow the use of a 3mm radioactive particle introduction rod.

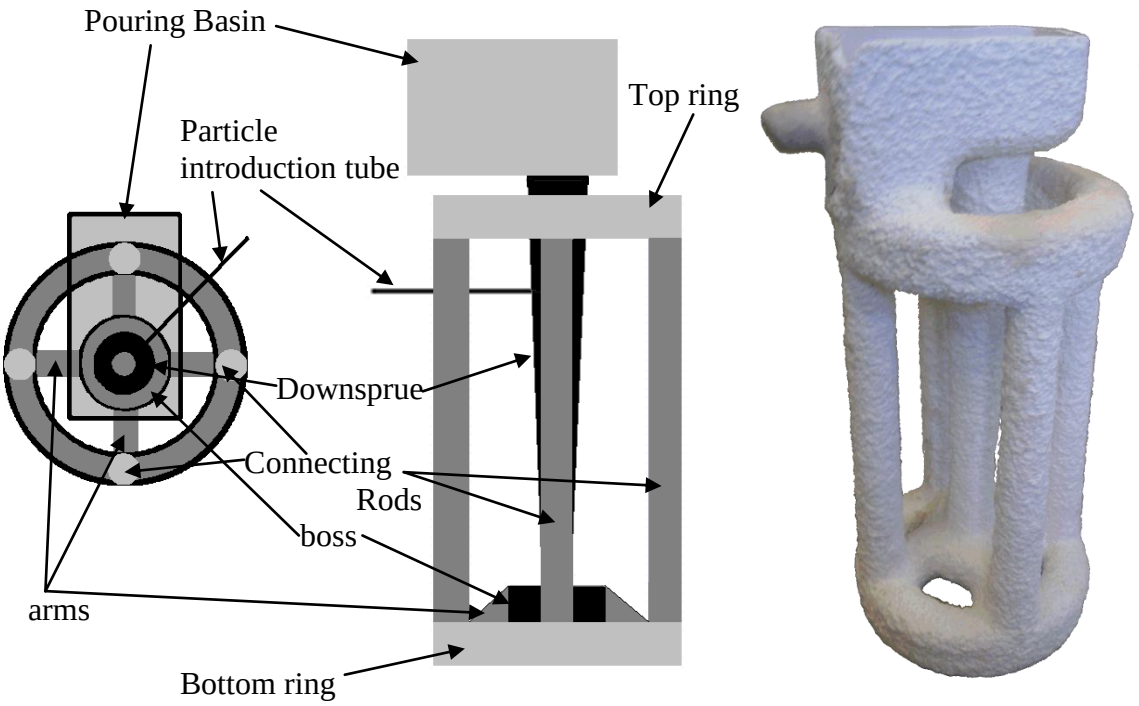

Schematic of mould Physical mould

Figure 42. The design of mould for tracking in Al and Steel

The thermal protection arrangement was the same as the experiments in section 3.2.3 except for the MDF boards. The higher temperature used to cast steel meant the detector modules needed more protection from heat and the board thickness was increased to use two 9mm thick boards on each side separated by a 9mm air gap, this allowed additional heat to escape by convection.

Each of the moulds intended to be cast using steel, was preheated to 900^{o}C , while for the experiments using aluminium, the moulds were not preheated. The mould was aligned within the casting area at an orientation relative to the PEPT modular detector banks. This was not square on but had a 12^{o} offset so that it would obvious from the initial data examination

(using Microsoft™ Excel™) from the x, y and z plots of the collected data, which if any, of the connecting rods the particle had travelled into.

The particle introduction rods were identical to those used for experiment 3.2.3.

Ten castings were made in total, 5 in steel and 5 in aluminium and these ranged in temperature from 748°C to 757°C for the aluminium experiments and 1574°C to 1582°C for the steel experiments, an example casting in steel is shown in Fig 43.

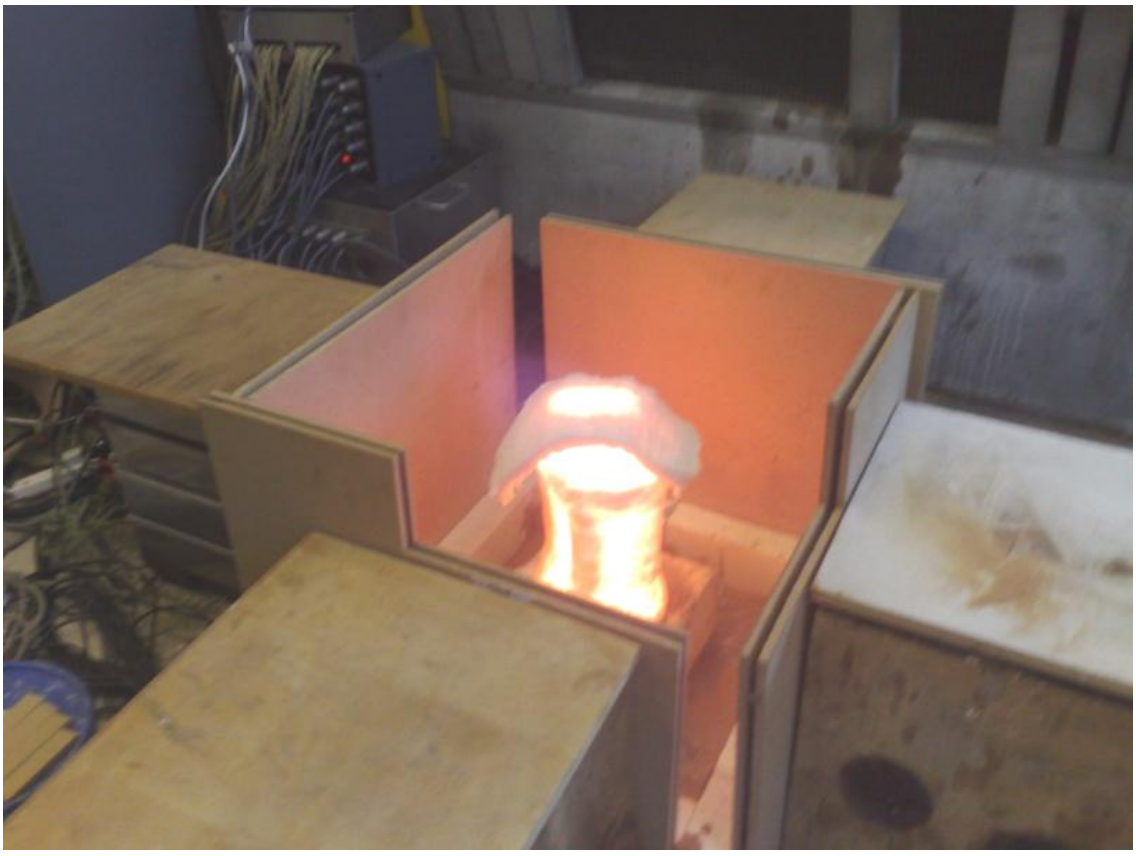

Figure 44. Particle tracking in steel

The γ-ray absorption for each of the materials used in the experiment is considered in turn.

Aluminium
Max Thickness considered → 2 x 1.5 cm = 3cm
γ absorption coefficient→ 0.228
γ transmission → $e^{-0.228*3}$ = 0.5045
attenuation = 1- γ transmission
(1-0.5045) = 0.4954 49.54% attenuation

Steel (Calculated using data for Iron)
Max Thickness considered → 2 x 1.5 cm = 3cm
γ absorption coefficient→ 0.663
γ transmission → $e^{-0.663*3}$ = 0.1368
attenuation = 1- γ transmission
(1-0.1368) = 0.8632 86.32% attenuation

Zircon
$ZrSiO_4$
Average mass attenuation coefficient : Use mass attenuation coefficient for
(1 Zirconium atom, 1 silicon atom, 4 Oxygen atoms) / total atoms in compound
(0.08693 + 0.08748 + (4 x 0.08729)) / 6 = 0.08726
Density for Zircon 4600 .. 4700 kg/m^3 use 4.65 g/cm^3 [120]
Linear attenuation = Average mass attenuation coefficient x Density
Linear attenuation = 0.08726 x 4.65 = 0.405759
Max Thickness considered → 3 x 0.2 = 0.6 cm
γ absorption coefficient→ 0.406
γ transmission → $e^{-0.406*0.6}$ = 0.7838
attenuation = 1- γ transmission
(1-0.7838) = 0.2162 21.62% attenuation

Mullite
$3AL_2O_3\ 2SiO_2$
Average mass attenuation coefficient : Use mass attenuation coefficient for
(6 Aluminium atom, 2 silicon atom, 13 Oxygen atoms) / total atoms in compound
((0.08445 x 6) + (0.08748 x 2) + (13 x 0.08729)) / 21 = 0.08473
Density for Mullite 3110 .. 3260 kg/m^3 use 3.18 g/cm^3 [121]
Linear attenuation = Average mass attenuation coefficient x Density
Linear attenuation = 0.08473 x 3.18 = 0.26944
Max Thickness considered → 3 x 0.5 = 1.5 cm
γ transmission → $e^{-0.270*1.5}$ = 0.6669
attenuation = 1- γ transmission
(1-0.6669) = 0.3331 33.31% attenuation

Wood (MDF)
γ absorption coefficient → 0.024
Max Thickness 1.8cm
γ absorption $= e^{-0.024*1,8} = 0.9577$
attenuation = 1- γ absorption
(1-0.9577) = 0.0423 4.23% attenuation

The Total attenuation is given by multiplying the transmission figures for the four materials (Metal, Zircon , mullite and MDF) together and subtracting this value from 1.

For casting using aluminium
0.5045 * 0.7838 * 0.6669 * 0.9577 = 0.2526
(1-0.2526) = 0.7474 74.74% attenuation.

For casting using steel
0.1368 * 0.7838 * 0.6669 * 0.9577 = 0.0685
(1-0.0685) = 0.9315 93.15% attenuation.

A table of activity levels for this experiment given in appendix B1.1

All attenuation coefficients for the materials used are the quoted values at 500KeV obtained from the NIST database [117] except for that for wood (MDF) which used the value from a forestry journal paper [119]

3.2.5 PET experiment using a filter in aluminium

This experiment was conducted to find the final locations of a group of radioactive particles after they have passed through an industrial ceramic foam filter, to assess the effectiveness of these filters at removing inclusions. Ceramic foam filters have been used in casting for some time and the improvements in metal quality have been ascertained by LimCa (Liquid Metal Cleanness Analyzer) [122] which is a system using a small orifice in a glass tube and a pair of electrodes, one in the glass tube and one nearby, all immersed in the liquid metal. These electrodes measure the change in conductivity caused by inclusions in the tube. Another method is called PoDFA (POrous Disc Filtration Apparatus) [123], PoDFA is a system in which a liquid aluminum sample is taken and poured into a special PoDFA crucible, then put on a small portable PoDFA sampling station. This station creates a vacuum to force the aluminum through the filter. The metal is frozen, then the filter, along with the residual metal, is cut, mounted and polished before being analyzed under a microscope by a trained PoDFA metallographer. Both of these methods cannot identify where the inclusions removed traveled from and do themselves interact directly with the metal stream, the PET process allows a less intrusive of the final particle locations.

The mould used was a plate 187 x 193 x 20mm with a running system of dimensions approximately 20 x 23mm, (see Fig. 45), with a 22mm filter, (see Fig. 44).

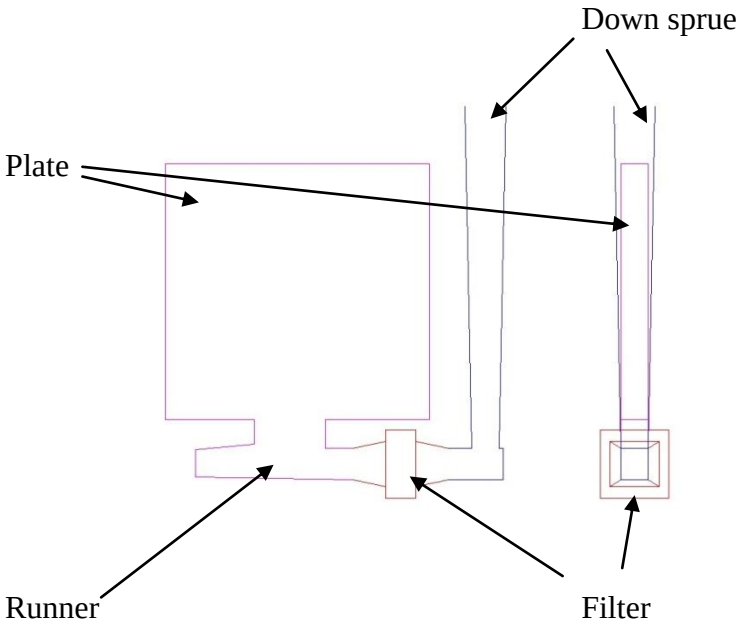

Figure 44. Filtered mould design , showing plate, filter, downsprue and running system.

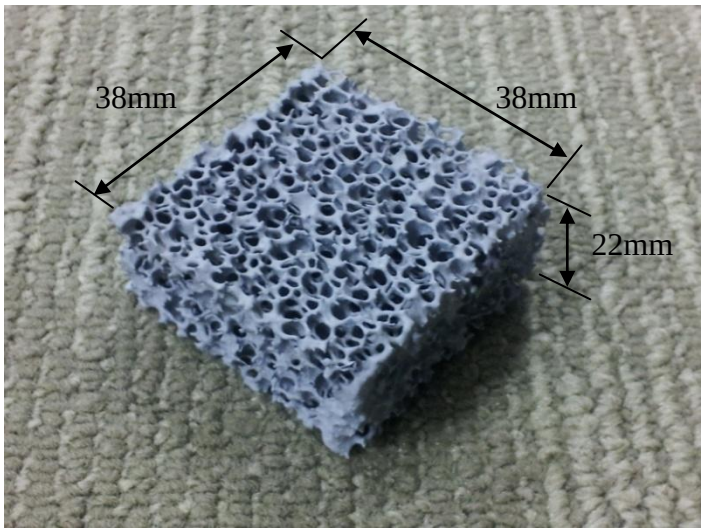

Figure 45. Example ceramic foam filter used in the experiments

At the top of the downspue a 2mm thick plate of high purity Al was positioned, this had a 6 x 5 matrix of 1mm deep blind holes, (see Fig 46). Into each of these holes a radioactive particle was positioned (ideally one per hole, although in practice occasionally two would be placed in a single hole because of the difficulties of particle transfer).

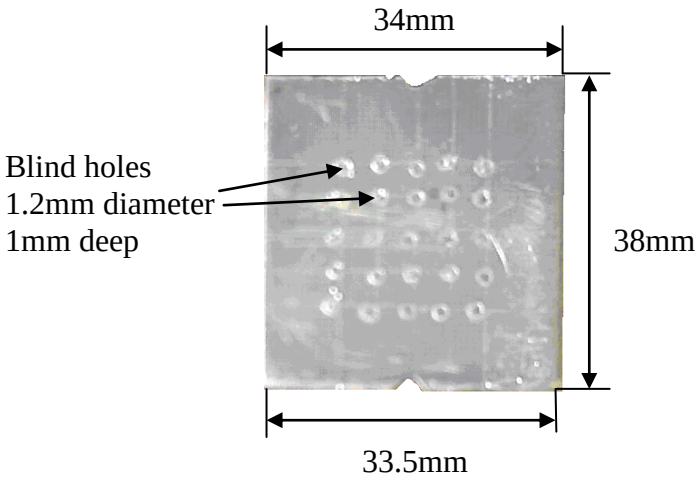

Figure 46. Example 2mm thick plate used to introduce particles into casting.

A second 0.5 mm thick high purity Al plate was positioned over the first place to keep the particles in place. The activity of the whole assembly was recorded, in a Capintec™ calibrated ionisation chamber (calibrated using a set of industry standard reference sources) and then positioned in the downsprue of the mould such that the taper on both the downspue and the plates allowed the assembly to be wedged into position with no additional clamping or glue, see Fig 47.

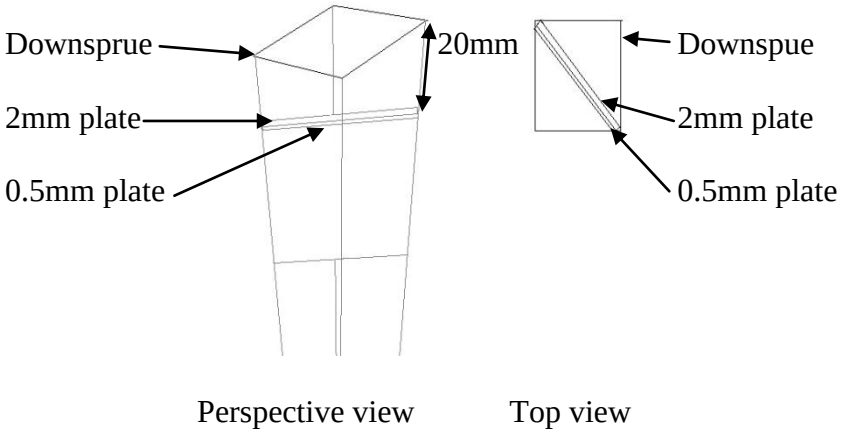

Figure 47. Multiple particle introduction plate location in downsprue

Liquid aluminium was then poured at a 900^{o}C into the pouring basin, it melted the plates as it flowed down the downspue and released the particles into the metal flow. Three such experiments were carried out. One experiment used a 10ppi Foseco^{TM} ceramic filter and used a set of 33particles, of 200 µm size with a total activity of 4.96 mCi (at the time of production), they were cast into the mould 13 minutes later, when they had a calculated activity of 4.57 mCi. A second experiment used a 20ppi filter, Fig 45, with 22 particles, of size 200 µm having an activity of 3.27 mCi at the time of production, these particles were used just 6 minutes after production and therefore had a calculated activity level of 3.15 mCi. A third experiment utilised a 30ppi filter with 33 particles, of size 200 µm having an activity of 2.13mCi. These were used after 24 minutes and had a calculated activity of 1.83mCi at the time of use.

The metal was poured and allowed to solidify, and was then sectioned into downsprue, filter and plate sections (the plate section retained its ingate).

The filter sections were then scanned in an Siemens ECAT® EXACT™ 47 PET scanner (full 3D scan mode).

"The Siemens ECAT® EXACT™ 47 scanner is a whole body positron emission tomography (PET) system. Simultaneous acquisition (2D or 3D), image reconstruction, processing and data analysis can be performed. It features Bismuth Germanate (BGO) Detector Material, 47 Contiguous Image Planes, 16.2 cm field of view and has a Patient Portal: 56.7 cm" [124]

While the plates and the running system (running system from first experiment only) were scanned in an ADAC PET scanner. A back projection algorithm was then applied to the data to create PET images. The PET images were visually inspected to count the particles present.

The ADAC PET images were also then processed, each radioactive particle created a hotspot within the image, the brightest hotspot was removed from the image, and the contrast increased to allow weaker hotspots to be displayed. This process was repeated until visually the hotspot no longer looked like the bright circle recognisable as a particle image. A count was kept of the number of particles processed, this being the minimum number of distinct particles in each plate and in the one recorded running system. The 3D ECAT images were manually inspected and a count made of image hotspots which represented particles, a count of the hotspots represented the minimum number of particles within the filter. It is possible that several particles could be close enough, on either of these scanners, that they would appear as a single particle due to the low, 4 to 8 mm, spatial resolution of a positron imaging scanner .

In addition an attempt was made to gauge the total amount of radioactivity in each part of the mould system, namely the downsprue, the filter and the cast plate. A ^{22}Na source was positioned at various locations within the viewable area of the PET scanner and the location and count rate recorded. Knowing the original activity when the ^{22}Na source was produced and the time between the production and the use of the source, for this purpose it was possible to calculate the activity of the source, this was also directly measured for confirmation. Having a known activity and PET count rate, an attempt was made to correlate the count rate and the activity to arrive at an approximate activity level based upon the observed count rate.

The images were all processed with the same acceptance angle, that being the maximum angle from being perpendicular to the detector faces at which the LORs defined by the γ-ray strikes are accepted. Any LOR's outside of this angle were rejected from the event count. The acceptance angle used was 20^{o} for generating images as this gave a sufficient LOR count within each pixel, to give a high contrast image, without excessive blurring and 1^{o} for count rates indicating overall activity levels to reduce the counts from random events. A count of the number of LOR's at the plane of the backscatter projection, corresponding to each pixel in the image was made, each pixel being 1mm square in real space. The image was then processed so that the contrast was effectively reduced and the pixel data was also scaled so that it could be displayed on a screen. In order to reduce the contrast so that more features, other than the pixel count hotspots, could be seen, all pixel count values were replaced with the $\log_{10}$ value of the originally collected pixel data count. In order to convert the image to something that could be displayed on a computer screen a scan of the pixel values was performed to find the highest pixel value, this value was then divided by 256, (the number of grey values available in most modern computer systems), to yield a scaling factor. The

calculated scaling factor was then applied to each pixel in turn by dividing the count value by the scaling factor. In order to generate clear images the backscatter distance (the distance from the detectors to the plane at which an image in the backscatter algorthm is reconstructed) in the backscattering algorithm was adjusted until visually the particles observed were not blurred, in the images created, this gave a backscatter distance of 391mm.

3.2.6 Tracking experiment using a launder in aluminium with 600 µm particles

3.2.6.1 Particle Tracking

This experiment used a preformed launder made from Insural™ 140, the main constituent of this being calcium silicate. The launder was 1.1 m long having a cross-section which presented a channel 73mm wide at the top and 70mm wide at a depth of 30mm blending with a radius of 36mm channel to the lower section (Fig 48, Fig 49).

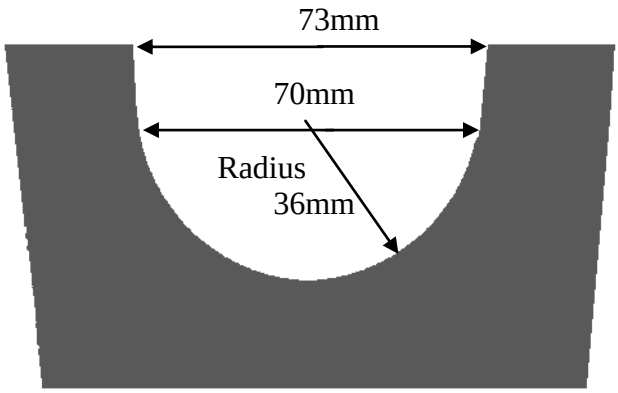

Figure 48. Launder cross section

Within this channel an obstruction, a baffle 20mm high at the centre and 20mm wide, was positioned to affect the flow of the metal as it ran down the launder, Fig 49.

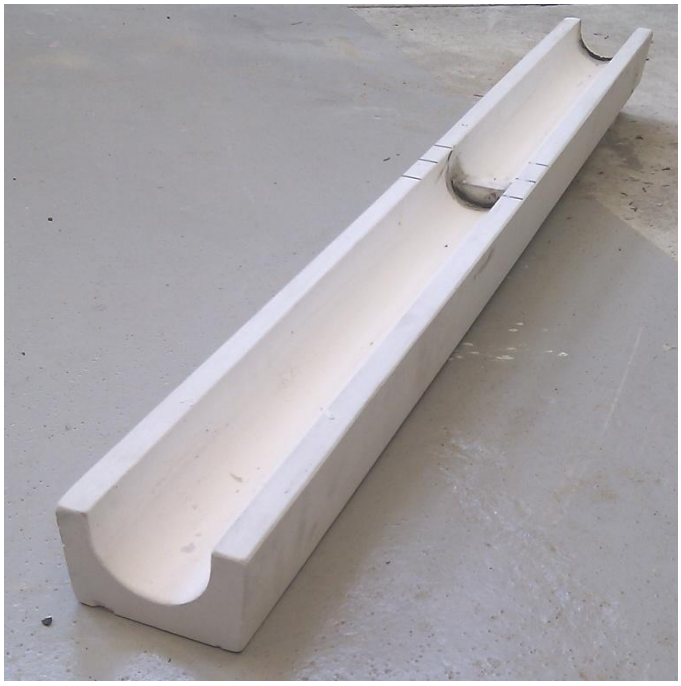

Figure 49. Launder showing baffle in situ

In order to track the radioactive particles as they traversed the launder the modules of the positron camera previously used were re-arranged into a new configuration, so that they surrounded a thin (0.5mm x 203mm) stainless steel tube with a clearance of 10mm at the closest point of the detector face and the tube, giving a distance between opposing detector faces of 223mm.

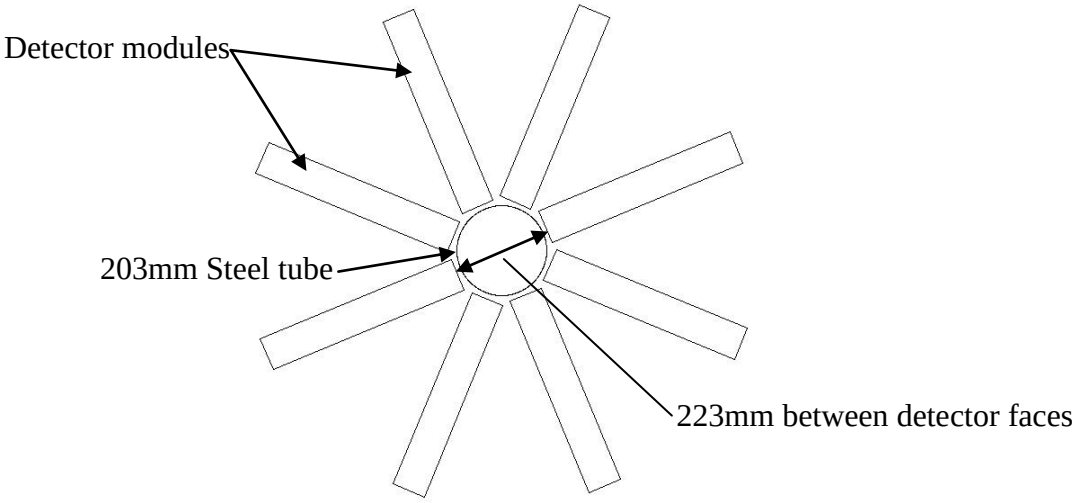

Figure 50. Radial position of PEPT detector modules around steel tube

The detector modules were arranged radially with an angular displacement of 22.5^{o} (see Fig 50) arranged in banks of two to give a total length of view of 700mm. This meant that the total viewable volume consisted of a cylinder 150mm diameter x 700mm long, of which the sensitivity map had a complete overlap for the inner 100mm diameter positioned on the tube centerline (Fig 51).

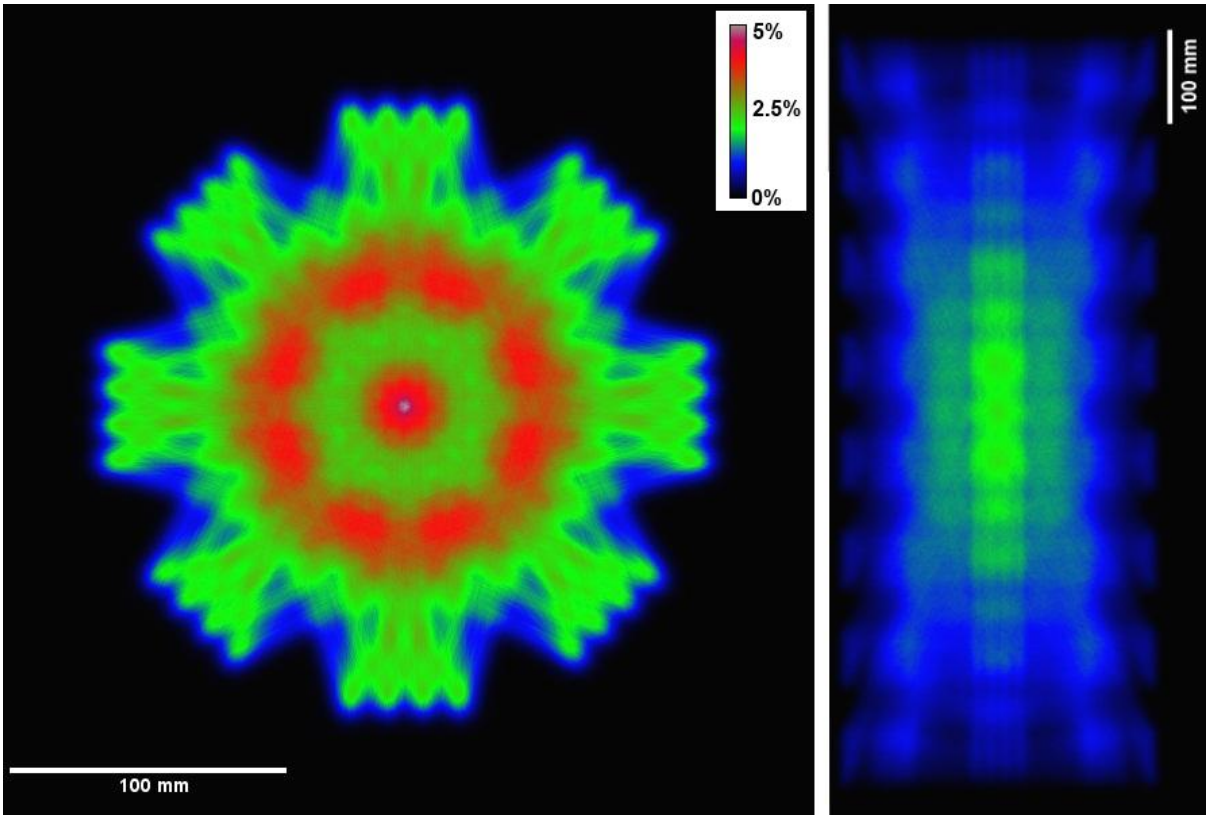

Front view Top View

Figure 51. Sensitivity map for 223mm separation between detectors

The sensitivity map (Fig 51) displayed is the result of a Monte Carlo simulation of positron camera sensitivity in the cameras XZ plane, with the peak in the centre representing approximately 5% sensitivity (The sensitivity is the percentage of γ-ray pairs emitted that are recorded and used for PEPT at any point within the volume of the positron camera). A larger apeture ~270 mm tube resulted in dead zones within the viewable area, hence the tighter 223 mm configuration was used, despite this limiting the working room for experiments.

Figure 52. Positron camera configured for tracking particles in a launder

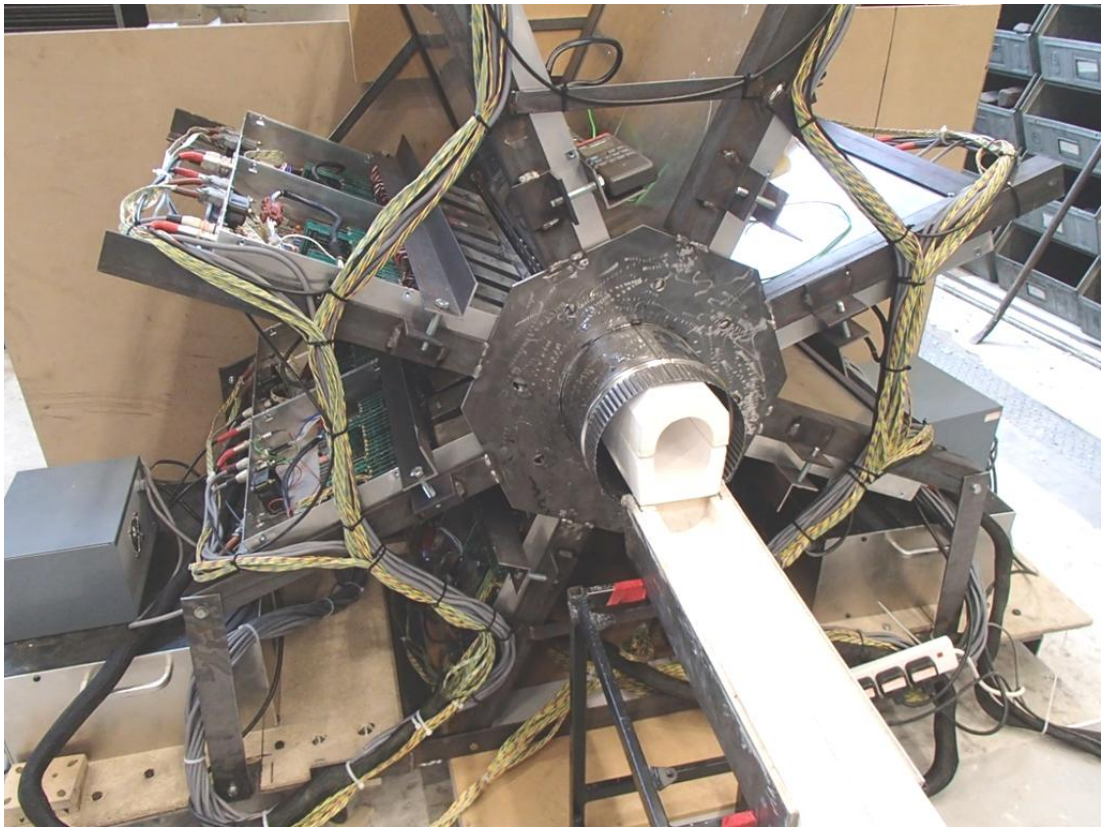

Figure 53. Front view of positron camera, showing thermal protection

The launder with the baffle was positioned within the viewable volume of the positron camera. It was positioned so that the channel was central in the 203 mm tube. A second launder section was positioned above the first to provide insulation and thermal protection for the detectors (Figs 52, 53). The launder had a baffle positioned at a distance of 350mm from the end face of the detector array, such that the baffle face fell at the centre position of the last set of detectors from the first bank.

The launder was arranged such that it had a slope of 1^{o}, it being higher at the end closest to the furnace, the surrounding detector rig had a matching displacement. There was an additional 0.25^{o} of slope due to a slight taper of the launder itself.

At end of the launder closest to the furnace, a particle introduction block (Fig 54), was positioned this allowed aluminium bars to be inserted to a known depth.

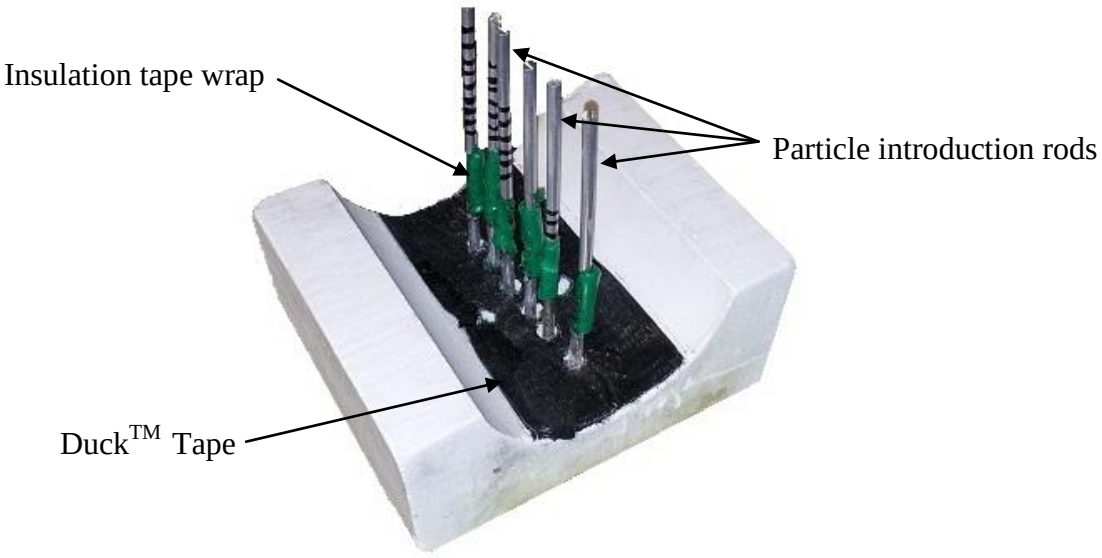

Figure 54. Particle introduction block

The block had 3mm holes through it on its centerline, with 10mm spacing between each hole and the next, these were taped over with "Duck^{TM}" tape so that a rod pushed through the tape was held in position by friction, until it was later pushed down into the melt. The depth of insertion was set by placing a "wrap" of insulation tape at a measured position on the insertion bar to act as a stop, as the tape made the rod too thick to pass any further through the hole in the block, when the bar reached the required depth. The depth of insertion ranged from 15mm to 45mm below the insertion block. 600µm alumina particles labeled with radioactive ^{18}F were sealed into 5mm long, 0.8 mm diameter holes in the end of 3 mm diameter Al rods. These holes were crimped closed within 3mm from the bar end sealing the particle into the rod. The rods were then introduced into the metal stream at a known depth, set by the insulation tape wrap at the other end of the rod. With the molten metal flowing from the furnace down the launder, the rod melted, releasing a particle, which was then carried by the metal stream down the launder and over the baffle, down the rest of the launder, to a large (200kg capacity) ingot mould.

The furnace used was a Ramsell Naber K110/S furnace, with a capacity of 220kg of liquid aluminium, of which some 180kg could be effectively utilised for a single pour. The metal used was primarily made up of re-melted 2L99 aluminium alloy, and other re-melted aluminium alloys of unknown composition. The use of large amounts of re-melted alloy was driven by cost. The first experiment gave an ingot of 72kg over a pouring time of 40 seconds (1.8 kg/s), the second pour gave 112kg in 60 seconds (1.86 kg/s), This suggested a mean flow rate, expressed as a volume of liquid aluminium of density 2345 kg m^{-3}, of 0.000788 m^3 s^{-1}.

The aluminium in this experiment was subject to considerable superheat, It was therefore concluded that the density of the metal would reduce from the figure of 2375 kg m^{-3} at the metals melting point. Figures ranging from 2324 kg m^{-3} to 2592 kg m^{-3} where quoted by one journal paper for wrought Al alloys at this temperature [125], in this context a value of 2345 seems reasonable.

The experiment was repeated four times, with metal temperatures ranging from 757^{o} to 764^{o}C (measured in the furnace). A temperature of 747^{o}C was measured in the pouring basin, when the temperature in the furnace was 764^{o}C. Six to eight radioactive particles were released with each casting process, with activities ranging from 472 μCi to 1346 μCi, (achieved by the ion exchange/surface adsorption method).

For the first experiment the metal temperature was recorded in both the furnace and the pouring basin, at 764^{o}C and 747^{o}C respectively. The radioactive particles were introduced into the metal stream immediately before a joint between the launder section and the spout of the pouring basin (this spout was constructed from another section of launder). The particles had differing levels of radioactivity and were introduced one at a time, the rods closest to the furnace, generally with the highest activity (Appendix B1.2 Table B2), introduced first. For the second experiment the furnace temperature was measured at 764^{o}C, the temperature in the pouring basin was not measured, it would again be expected to be around 747^{o}C as found in the first experiment. The activity levels for this experiment are given in (Appendix B1.2 Table B3). In the third experiment the furnace temperature was measured at 757^{o}C and the introduction point was moved to just after the joint between the launder leaving the pouring basin and the main launder, as the compound Insural^{TM} 700, used to seal the joint may have released moisture, affecting the metal flow in the area of the launder where the particles were

inserted into the metal stream. The activity levels for this experiment are given in (Appendix B1.2 Table B4). For the 4th experiment, with a temperature in the pouring basin of 763^{o}C, the introduction block was modified in order to accommodate an additional two rods, making eight in total. The additional introduction holes were at the mid position (lengthwise) of the block, but offset to either side by 15mm, as there was not enough room to place extra holes in line with those already existing. In addition excess radioactive particles were introduced after the rods had been inserted in an attempt to determine the position of the free surface of the metal. Four additional small rods were introduced (by dropping them onto the surface of the melt). All the particles were introduced seven seconds apart from each other. The activity levels for this experiment are given in table (Appendix B1.2 Table B5).

The particle positions from these experiments were determined from the raw line of response (LOR) data produced by the positron camera, using the tracking algorithm developed in the School of Physics and Astronomy at Birmingham University [126]. The particle locations determined were then overlaid upon a computer simulation of the launder.

The γ-ray attenuation for this experiment was derived, as an indication as to the ability of the PEPT positron camera to detect particles in these experiments. This was determined by the materials between the detector faces and the radioactive particle, it consists of up to 73mm of aluminium, the launder (made primarily of calcium silicate) and the steel of the detector protection tube, each matererial was considered in turn.

Aluminium
Max Thickness considered → 7.3 cm
γ absorption coefficient→ 0.228
γ transmission → $e^{-0.228*7.3}$ = 0.1893
attenuation = 1- γ transmission
(1-0.1893) = 0.8107 81.07% attenuation

Calcium Silicate
Ca_2SiO_4 Assumed for Insural 140
Average mass attenuation coefficient : Use mass attenuation coefficient for
(2 Calcium atom, 1 silicon atom, 4 Oxygen atoms) / total atoms in compound
((0.08851 x 2) + (0.08748) + (4 x 0.08729)) / 7 = 0.08767
Density for Insural 140 → 1.4 g/cm^3
Linear attenuation = Average mass attenuation coefficient x Density
Linear attenuation = 0.08767 x 1.4 =0. 1227
Max Thickness considered → 4 cm
γ transmission → $e^{-0.1227*4}$ = 0.6121
attenuation = 1- γ transmission
(1-0.6121) = 0.3879 38.79 % attenuation

Steel (Calculated using data for Iron)
Max Thickness considered → 0.06 cm
γ absorption coefficient→ 0.663
γ transmission → $e^{-0.663*0.06}$ = 0.961
attenuation = 1- γ transmission
(1-0.961) = 0.039 3.90 % attenuation

Combining the effect of each of the materials into an overall attenuation figure gives

Total Transmission → 0.1893* 0.6121* 0.961 = 0.11135
Total Attenuation → (1-0.11135) = 0.88864 88.86 % attenuation

This 88.86% attenuation figure is applicable to all four experiments.

3.2.6.2 Calibration of 600µm launder experiment

In order to align the particle data with the mesh from a computer simulation and the physical lauder a ^{22}Na source in the form of a 5mm sphere was placed at the bottom edge of the baffle face on the furnace side of the baffle, the data collected for this static position was then used to align the computer generated mesh geometry with reality. A rotation (22.5^o to allow for the

fact that the detectors were offset by this amount from the vertical) was applied and translational offsets in x, y and z were adjusted manually until the position of the baffle was determined, as shown in Fig 55, this procedure was performed prior to the experiments being carried out and the x,y,z offsets were used to align the particle track data from the experiments.

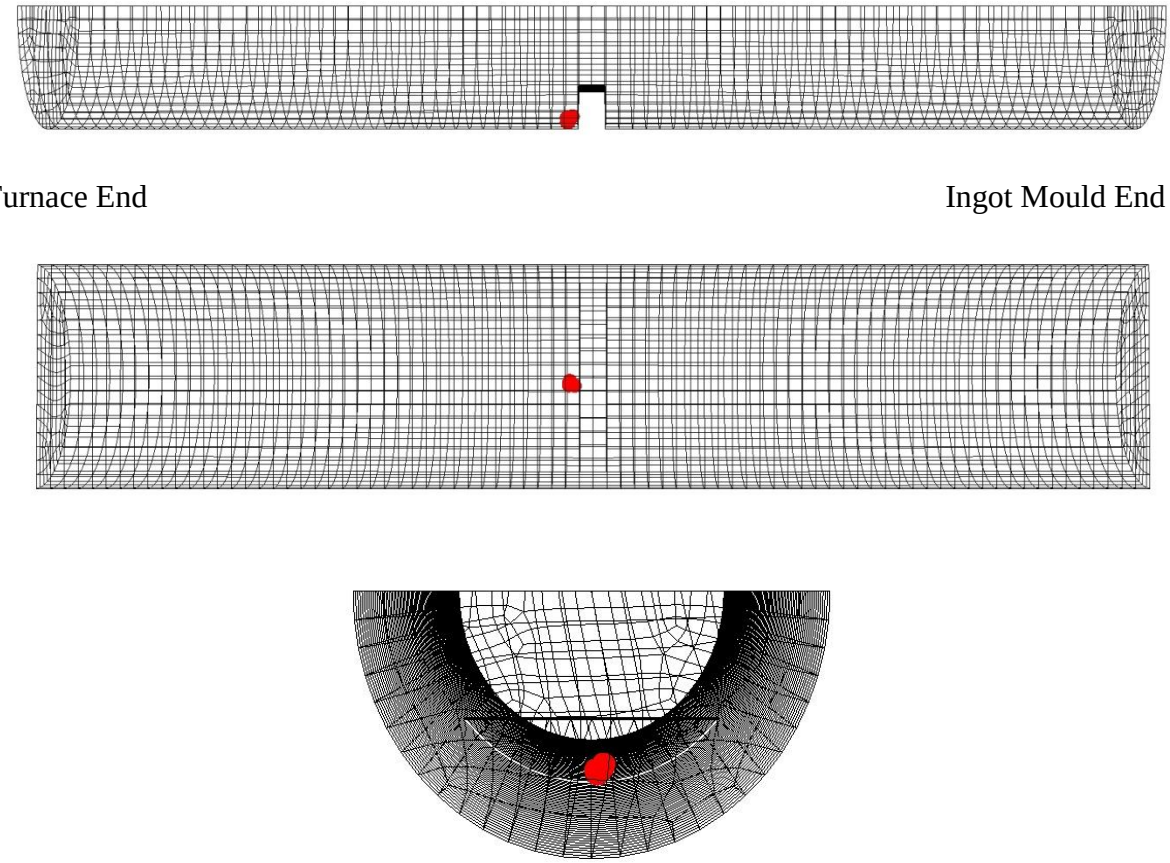

Figure 55. Baffle location calibration for 600µm particle experiment

3.2.7 Tracking and PET experiment using a launder in aluminium with 200 µm particles

3.2.7.1 Particle Tracking

The tracking experiment was repeated a second time, but on this occasion the particles were 200µm in diameter. After a rearrangement of the apparatus the launder was levelled with a slope of 1^{o} again, this matched the detector apparatus which had not been adjusted.

The experiments were conducted as they were for the 600µm particle experiments, all eight of the particle introduction points were used in this new set of experiments. The introduction depth was adjusted during the course of the first three experiments, gradually increasing the depth, from 15mm below the introduction block to the final value 45mm below the block (The insertion depth used in experiments four and five).

A total of five experiments were conducted to track individual particles and tables (Appendix B1.3 Tables B6 to B10) detail the radioactivity levels used in these experiments, an additional experiment to find the end location of a large number of particles, released simultaneously was also performed.

3.2.7.2 Calibration of the 200µm particle tracking experiment

The launder position within the positron camera was determined using a Na^{22} source bead of 5mm diameter. To improve upon the calibration from the previous experiment, this was attached to a rod in order that it could then be manipulated within the volume of the launder. The rod was inserted into the launder from the ingot mould end until the bead contacted the face of the baffle. The face of the baffle was then traced out, this was repeated several times. The procedure was then repeated from the furnace end of the launder, this gave the position and profile of the baffle. The computer model mesh (see section 3.2.9) was then overlaid upon the data this generated and this was then manually adjusted with x,y,z offsets inserted into the particle position generating code until the mesh and the data, overlapped as below in Fig 56. The final x,y,z offsets were then applied to the data from the particle tracks generated in the experiment.

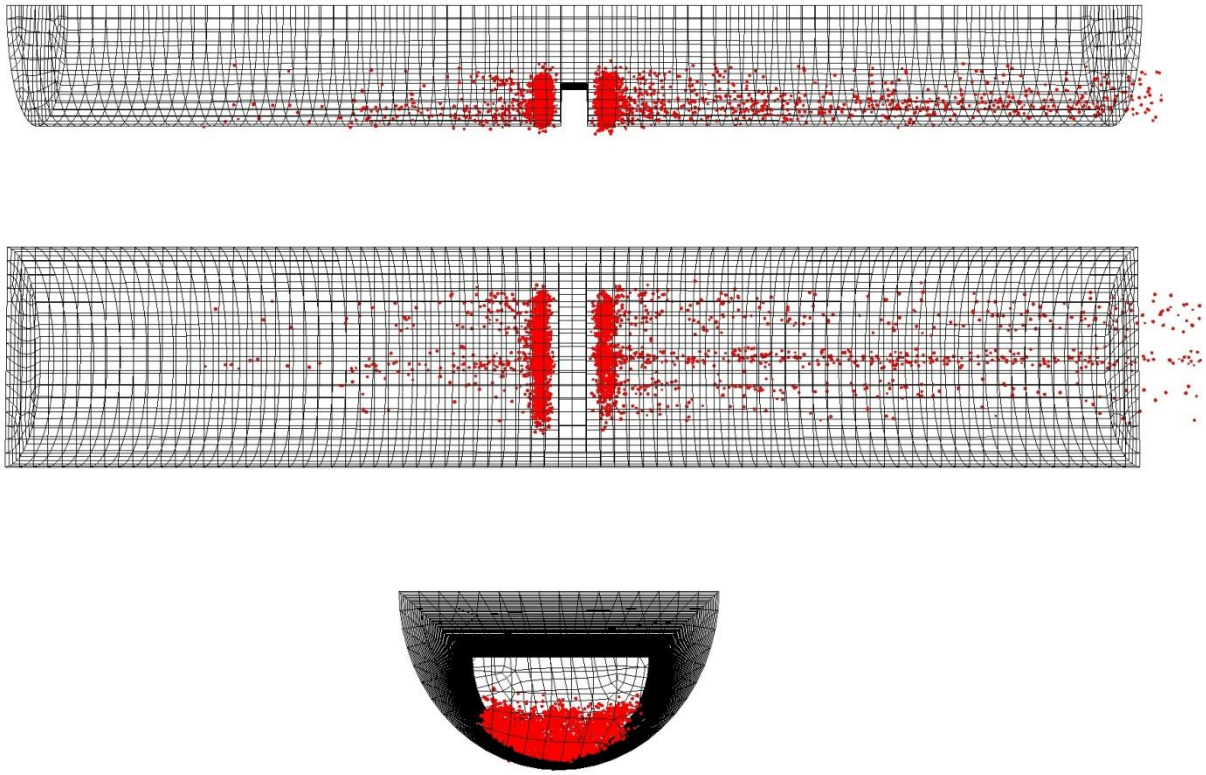

Figure 56. Calibration images for 200µm particle tracking experiment.

3.2.7.3 Particle Cloud Experiment

The final experiment was a departure from the previous method of introducing particles into the melt, for this experiment the particles were introduced all at once. A steel bar was bent so as to have a loop 40mm diameter at its one end, see Fig 57.

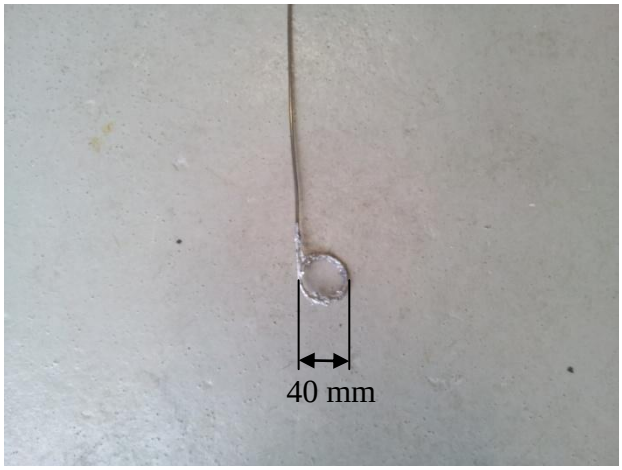

Figure 57. 40mm hoop used to introduce a cloud of particles into the metal stream.

The loop was then covered in aluminium foil so that it formed a flat surface. Solid glue was then applied to the foil and radioactive particles distributed randomly on this surface, (safety concerns regarding losing radioactive particles drove the decision to use glue). A second layer of aluminium foil was then placed on top of the first and wrapped over the ring edges to form a seal. The activity of the particles within the foil layers was measured at this point to be 17mCi and there was visually observed to be in excess of 35 particles.

The experiment was started, 21 minutes after the creation of the radioactive particles by pouring liquid aluminium down the launder as it was for the previous experiments, but instead of introducing the particles one after another, the ring was inserted into the metal stream, this was after around 20 seconds of pouring the metal. The 40mm loop was

submerged below the surface of the liquid metal with the foil covered face of the ring at 90^{o} to the metal flow, the foil melted releasing the particles nearly simultaneously. The PEPT tracking was active during this time, but was used merely to confirm the passage of particles down the launder system. Once the particles had been released and no further motion was seen on the PEPT positron camera, the pouring of the metal was concluded after a further 20 seconds. A Geiger counter indicated significant activity within the Ingot mould which was used to collect the runoff from the launder.

The aluminium remaining in the launder was allowed to solidify and cool for approximately one hour. The launder was then removed and taken to the ECAT 3D PET scanner where it was scanned in overlapping sections such that the entire volume of the metal remaining could be inspected for the presence of any radioactive particles.

Figure 58. The launder used for the multiple particle experiment

Figure 59. The launder used for the multiple particle experiment (front view)

The launder was scanned in sections, the overlapping sections were physically marked on the launder edges as can be seen in Figures 58 and 59, these were arranged to have ~20mm overlap between one section and the next. The length of each set section was 155mm, each consisting of 47 tomographic “slices” giving a gap between each slice of 3.3mm and 6 slices from each section covering the 20mm overlap. A tomographic representation of the full length of the launder was created by linking the scanned sections together. This involved discarding three tomographic slices from the end of each section preceeding an overlapping area and discarding three slices from the beginning of next section which followed an overlapping area.

Emission scans of the entire launder length were made at this point, then 24 hours later matching attenuation maps were made using the ECAT scanners ^{137}Cs 662KeV source, and the resultant images were then overlaid. The energy release from ^{137}Cs is close to 511keV annihilation photons and is commonly used in medical scanners for generating attenuation correction maps.

4.1 Simulation

In order to simulate particles flowing in a launder many factors regarding what should be simulated need to be considered. One of the main considerations is whether one way or two way momentum transfer is required. Two way transfer makes a simulation much more complex to implement and slower in operation. One way coupling is not suitable for solids and liquids where the density difference, or volume fraction is large [48]. However if it is assumed that the worst case to be considered is that of a dirty melt, this is defined by Campbell [58] to be a volume fraction of 0.0001 inclusions, most of these inclusions will be alumina bubble trail defects, 80% [58] and the density difference between molten aluminium and alumina is around 1.5 (3650/2375 kg m^{-3}). At a volume fraction of 0.0001 the inclusions will represent less than 0.16% of the momentum in the flow system, ignoring the additional momentum of the particles, this will introduce an error of 0.06% into the momentum calculations. The extra speed and simplicity of one way coupling can therefore be justified due to the small error introduced.

4.1.1 Simulation of fluid flow in a launder.

A simulation of the particle tracking experiments in sections 3.2.7 and 3.2.8 was performed; this modeled the same launder geometry as the physical experiments. The geometry was

recreated in ICEMCFD™ from ANSYS™, this allowed for an inlet, outlet and for the open top to allow bidirectional flows into and out of the model see Fig. 60.

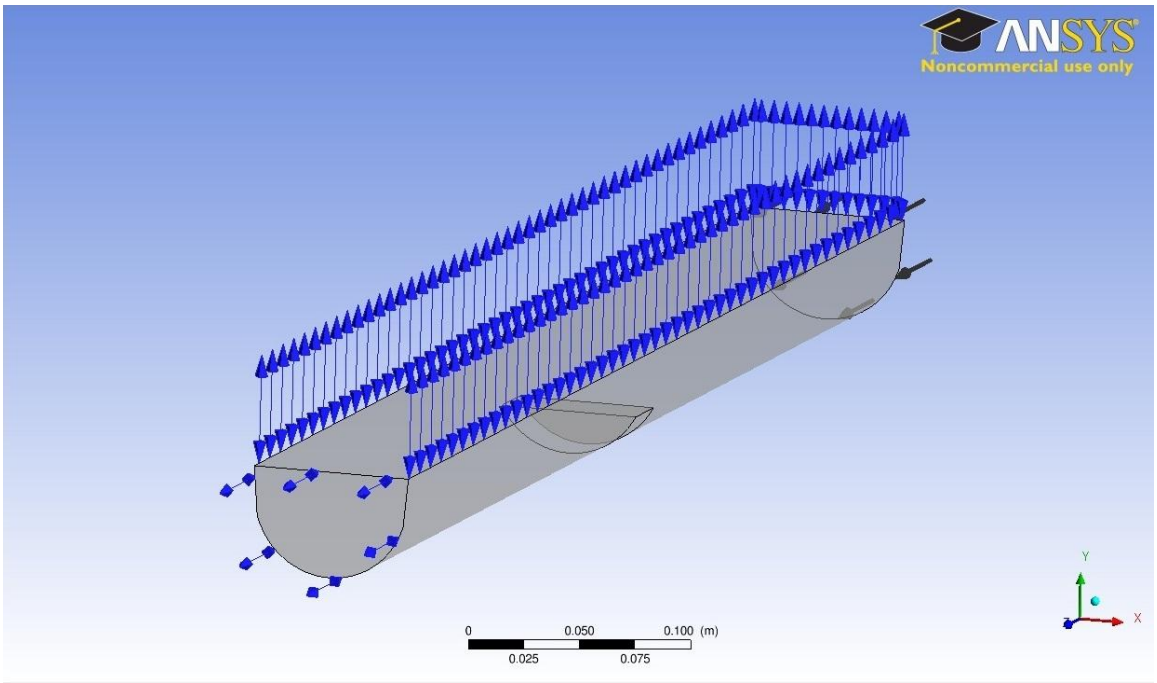

Figure 60. Launder simulation geometry

The launder volume was filled with a Cartesian mesh 1 mm in height, width and depth, this was later changed to 2-2.5mm in each axis, due to processing constraints, the cartesian mesh cells were distorted at the boundary in order to meet the edges of the geometry, the mesh was constructed completely of Hexa – Quad elements (each element has six sides and each side has four edges). The mesh cells were chosen so that they could fully enclose the largest particles simulated whilst not being so large as to overly degrade the accuracy of the fluid simulation. No free surface mesh refinement was applied as this would have made the mesh elements size, be uncomfortably close to the diameter of the largest particles simulated. In addition free surface refinement would also have introduced pyramids and tetrahedral elements into the mesh which the particle simulation code was not written to handle. The mesh extended to 700 mm to represent the full viewable volume of the positron camera, see Fig 61.

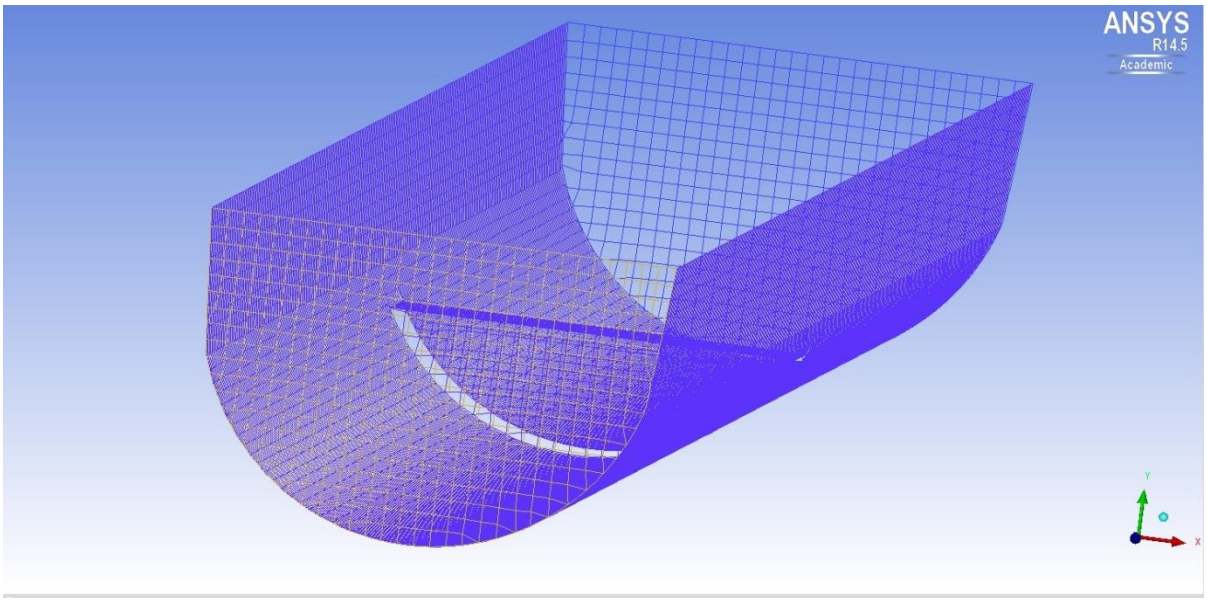

Figure 61. 2-2.5mm Mesh of launder geometry

The mesh geometry was exported from ICEMCFD™ into ANSYS™ CFX™ a computational fluid dynamics package. The geometry was used to simulate a free surface model of molten aluminium. The following material values were used in the free surface simulation, the density of molten aluminium, 2345 kg m^{-3} with a dynamic viscosity of 0.0013 Pa s. The standard CFX supplied value for the density of air at 25 ^{o}C of 1.185 kg/m^3 was also used.

The free surface position was determined based upon the pressure within the fluid, so starting with a rough position for the height of the fluid at the inlet and outlet, taken from the 'tide mark' measured from the corresponding experiment, the CFD package can repeatedly adjust the pressure at all points along the simulated geometry until the pressure at all points in the simulation is consistent with the dynamic behaviour of the fluid.

The expressions used in the simulation are shown in appendix C and the terms used are defined below.

The ‘OffsetY’ variable re-aligns the depth calculation for the fluid to allow for the fact that the launder geometry was defined from the Y axis, thus the launder channel itself starts 26mm above the Y axis, this value was assigned to the variable ‘LaunderBottom’.

The ‘UpH’ and ‘DownH’ values were the initial height of the metal upstream and downstream, in absolute terms, referenced from the Y axis and not from the bottom of the launder channel. For the value from the bottom of the launder subtract 26mm (OffsetY) as the channel was raised above the Y axis within the model.

‘UpPres’ and ‘DownPres’ are used calculate the upstream and downstream pressure respectively.

The ‘OffsetX’ variable shifts the X calculation for the launder tilt, from the X axis origin to the start of the launder.

The ‘AdjustHeightForSlope’ variable reduces the effective height of the fluid by product of the sine of the slope (in this case 1.25^{o}) and the length along the launder, which accounts for the slope of the launder on the shape of the free surface and the pressure within the liquid aluminium flow.

The variable ‘UpVFLiquid’ provides a step function to determine a Boolean value to decide whether to provide a pressure value for the liquid aluminium based on the volume fraction of

aluminiym relative to air, 'UpVFAir' is the equivalent for air in the simulation and is used as part of the calculation of UpVFLiquid.

Gravity for buoyancy effects was offset at 1.25^{o} using g*0.021815 in Z axis and –g * 0.0999762 in the X axis, representing a tilt of the launder geometry of 1.25^{o} to the horizontal plane in the basic settings for the fluid cell domain.

A simulated molten aluminium fluid flow of 1.85kg/s was implemented at the inlet boundary, as a flow rate given by, the bulk mass flow rate / density of aluminium (whilst molten) divided by the Inlet area. The volume flow rate is given by ;

$1.85\ kg\ s^{-1} / 2345\ kg\ m^{-3} = 0.00078891257\ m^{3}\ s^{-1}$

The inlet area was given as 0.002886 m^2 however the upper 15mm of this area was not actually used by the metal in the experiments, as the free surface must be below the launder walls at its highest point, ~14mm higher than where it enters the launder. The launder at this height is approximately 72mm wide, so the unused area was subtracted from the inlet area

$0.002886m^2 - (0.010m \times 0.07m) = 0.002186m^2$

So dividing the volume flow rate by the effective inlet area gives

$0.00078891257\ m^{3}\ s^{-1} / 0.002186\ m^{2} = 0.360893\ m\ s^{-1}$

This value of $0.360893\ m\ s^{-1}$ was representative of the true velocity at which the metal was poured during the physical experiments, calculated from the mass of metal poured and the time taken to pour the metal.

The turbulence model was set with an intensity and length scale of 0.05 fractional intensity with a eddy length scale of ‘UpH’.

The initial conditions were set to a Cartesian velocity of 0.360893 m/s in the z axis and a static pressure of ‘UpPres’ and a kε Turbulence model, this created a starting point for the simulation to progressively correct from.

The simulation was run and computation fluid dynamics CGNS data was created, which defined, both the launder mesh, (see Fig 62) and the fluid flow (see Fig 63). The free surface, was represented as a changing volume fraction from one fluid (molten aluminium) to another (air), typically over several (3 to 5) fluid cells, a volume fraction 0.5 was used to indicate the actual free surface. Fluid cells with a molten Al volume fraction less than 0.5 were set to have the fluid density of air and no fluid flow within them, when imported into the particle simulation model.

The CGNS library was built from source code, using Microsoft visual C++ 2012, this was used to import the data describing the mesh geometry and the fluid flow data into a bespoke C++ program. The mesh walls were described in this data as Quad-4 elements, these represented the launder walls as well as the inlet and outlet vents for the simulation. The program dynamically allocated memory for the data of these structures, so as to be able to handle a larger simulation, with smaller fluid cells at a later date.

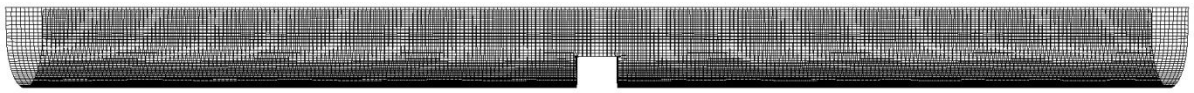

Figure (62) Launder geometry, with the baffle at the midpoint of the launder

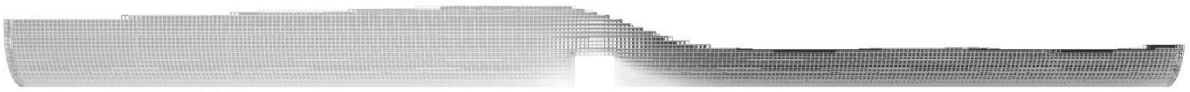

Direction of fluid flow →

Figure (63) Free surface fluid velocity map. Dark = High velocity. Light = low velocity.

4.1.2 Particle Simulation

The particle simulation was run using the CGNS data generated by CFX for the free surface model. The particle sizes in the simulation ranged from 200 µm to 600 µm, the size for each particle was selected using a pseudo random number generator. The starting location for each particle was also generated using the random number generator. The simulation time step was dynamically changed, initially a minimum particle movement parameter allowed the first particles to begin their simulated motion. The timestep was then adjusted for each iteration until such time as the velocity of the fastest particle caused a particle movement of less than the radius of the smallest particle in the simulation per timestep. Using this system, particle motion could be simulated under the influence of the fluid motion and gravity quickly and efficiently, in addition collisions between particles were detected at the end of each timestep, only the most glancing of contacts would thus be missed, those that make and break contact

in a distance smaller than the radius of the smallest particle in the simulation. Upon a particle to particle or particle to launder wall contact being detected the simulation of the affected particles was rolled back to the start of the timestep, the timestep was then reprocessed with a much smaller stepsize. The smaller timestep size is again calculated dynamically but is based upon the Rayleigh wave propagation within the solid material of the colliding spheres. During the smaller timesteps the contact mechanics of the colliding spheres was also accounted for.

The simulation itself starts by introducing a particle at each timestep (subject to the volume fraction of particles in the metal being less than a preset value, this being 0.0001 as stated as a dirty melt by Campbell [58]) at a pseudo random location calculated to be somewhere on the inlet face of the launder in the simulation, In the free surface simulation the particle selected is only introduced if it falls below the height of the free surface (Al volume fraction of the fluid cell the particle is introduced into must be 0.5 or greater). Then at this and subsequent timesteps the particle centre is used to calculate the fluid cell in which the particle resides, the fluid cell is always a convex planar hexahedron, so determining if a point is inside its volume can be achieved by dot product vector mathematics, using the sign of dot product from the vertices to the particle. Once the fluid cell is known, the fluid flow within the cell can be retrieved, this is assumed to surround the particle. The fluid flow is defined by CFX at the vertices of the fluid cell and so these values were averaged to ascertain its effect upon a particle.

The individual forces acting upon a particle were calculated and the net motion of the particle due to these forces, for each timestep, calculated. The forces involved cause an acceleration which in turn results in a displacement. The forces considered were forces from particle

contacts, the force due to interaction the particle and the fluid, and the force from the effect of gravity. These forces were calculated for each particle in turn, such that particle motion relative to each other was derived Eq. 29.

$$m_i \frac{\mathrm{d}\mathbf{v}_i}{\mathrm{d}t} = \mathbf{F}_{ci} + \mathbf{F}_{fpi} + m_i\mathbf{g} \qquad \text{Eq. 29}$$

Where
m_i = mass of particle i
$\mathbf{v}_i$ = velocity of particle i
$\mathbf{F}_{ci}$ = contact force acting on particle i
$\mathbf{F}_{fpi}$ = fluid particle interaction force acting on particle i
m_i = mass of particle i
$\mathbf{g}$ = acceleration due to gravity.
t=time

In addition to these linear displacements, rotational motion due to contact interactions was also considered. Contact between particles results in the creation of a torque which in turn results in a change to the rotational moment of inertia of a particle, by a change in the angular velocity (see Eq.30). The new angular velocity of each particle was calculated for each timestep and a new angular displacement derived. The rotational damping effect of the metal was not considered.

$$I_i \frac{\mathrm{d}\boldsymbol{\omega}_i}{\mathrm{d}t} = \mathbf{T}_i \qquad \text{Eq. 30.}$$

where
T_i = The torque acting upon particle i
I_i = the moment of inertia of particle i
$\boldsymbol{\omega}_i$ = the angular velocity of particle i
t=time

The metal flow was the main cause of the motion of the particles, this was set to be 0.36 ms^{-1} at the inlet face. This provided the initial inflow, from which the flow in each fluid cell was calculated. In order to calculate the force pushing on the particle from the fluid, the Reynolds

number of the fluid flow with respect to the particle was calculated (Eq. 31), this was later used in the calculation of the drag force;

$$\mathrm{Re}_{pi} = \frac{\rho_f d_{pi} \varepsilon_j \left|\mathbf{u}_j - \mathbf{v}_i\right|}{\mu_s} \qquad \text{Eq. 31}$$

Where
Re_{pi} = Reynolds Number for superficial fluid slip around particle i
ρ_f = Density of the fluid (Molten Aluminium)
d_{pi} = Diameter of particle i
ε_j = Void Fraction of fluid cell
$\mathbf{u}_j$ = Fluid velocity vector within fluid cell
$\mathbf{v}_i$ = Velocity vector of particle i
μ_s = Shear viscosity

The drag force Eq. 33 was calculated as in Guos thesis [26] but with an additional element, the virtual mass force (Eq. 32), to account for the additional force provided by the displacement of the Al by the alumina particle which Guo neglected as for air (which he used) it is negligible.

The additional virtual mass of a sphere is given by:

$$\frac{2}{3}\Pi r_i^{\,3} \rho_f \qquad \text{Eq. 32}$$

Where

r_i = radius of particle i
ρ_f = density of fluid (molten aluminium)

The drag force the particle experiences is complex, and was modeled as the drag for a sphere. This has many approximations and the one adopted for this simulation was that of Guo and Thornton, Eqs (33,34,35). The drag force was calculated for a Newtonian fluid using the

empirical correlation of Di Felice (1994) which gave a continuous variation of drag force over a practical range of flow regimes based upon the difference between the fluid and particle velocities and the density of the fluid, it also took into account particle porosities (void fractions) within the fluid [26].

$$\mathbf{F}_{di} = \frac{1}{2} C_{di} \rho_f \frac{\Pi d_{pi}^2}{4} \varepsilon_i^2 \left|\mathbf{u}_j - \mathbf{v}_i\right| \left(\mathbf{u}_j - \mathbf{v}_i\right) \varepsilon_j^{-(\chi-1)} \qquad \text{Eq. 33}$$

$\mathbf{F}_{di}$ = Drag force acting on particle i
C_{di} = Fluid drag coefficient for particle i
P_f = Density of fluid
d_{pi} = Diameter of particle
ε_j = Void Fraction of fluid cell j
$\varepsilon_i^{-(\chi+1)}$ = Porosity function to correct for the presence of other particles in fluid cell j.
$\mathbf{u}_j$ = Velocity of fluid in fluid cell j
$\mathbf{v}_i$ = Velocity of particle i
χ = Porosity correction term

This is an approximation for the drag of a sphere as it passes through its different flow to drag regimes.

The drag coefficient for a particle is given by

$$C_{di} = \left[0.63 + \frac{4.8}{\sqrt{\mathrm{Re}_{pi}}}\right]^2 \qquad \text{Eq. 34}$$

The term χ in the porosity function is given by

$$\chi = 3.7 - 0.65 \exp\left[-\frac{(1.5 - \log_{10}\mathrm{Re}_{pi})^2}{2}\right] \qquad \text{Eq. 35}$$

The effect of gravity causes an acceleration (**g**) to act upon the mass of a particle, and the same effect causes the mass of the fluid to accelerate. The displaced fluid providing a buoyancy effect, the effective mass of the particle due to this buoyancy is the true mass of the particle minus the mass of the displaced fluid, gravity then acts upon effective mass to give a downwards acceleration (or for fluids denser than the solid particle an upwards acceleration) acceleration Eq. 36.

The term $m_i\mathbf{g}$, is given by;

$$m_i\mathbf{g} = (m_i - m_{fd})\ \mathbf{g} \qquad \text{Eq. 36.}$$

where

$m_i\mathbf{g}$ = the force from the mass of the particle and the effective gravitational force
m_{fd} = the mass of the fluid displaced
m_i = the mass of the particle
g = accrleration due to gravity

Since particles move relative to each other under the influence of forces acting upon them from the fluid they, are therefore prone to collision with each other and with the launder walls. The simulation uses a modified Johnson, Kendall and Roberts (JKR) model, this was presented by Guo [26], and which incorporates modifications from Thornton.

In the model a contact initiates a reaction force. This is normal to the surfaces in collision and unless the direction of the impact passes through the particle centre(s), a tangential displacement occurs. When a tangential displacement occurs it creates a traction which causes a tangential force to act.

The combined effect of these forces is to cause each particle to accelerate which in turn causes rotational and linear movement of the particles. Any rotational displacement at the point of contact during a collision also reduces the particles' normal displacement relative to the contact point of the two (or more) particles involved. The effect is to change the normal direction that is applied at the next time step in the model and this alters the path of the particles after a collision. For large particles this effect is negligible but for smaller particles it can be significant.

The motion of the particles due to elastic reaction forces continue to change until either they bond together or separate. This is dependent upon whether the combination of the particles momentum and its reactive normal force exceed the necessary "pull-off" force to separate the particles. This pull-off force is created by the particles surface energy of the particle [51].

The "pull-off" force was described by Johnson, Kendal and Roberts as;

$$F_c = 3\Pi\gamma R^* \qquad \text{Eq. 37.}$$

And by Dejugarin as

$$F_c = 4\Pi\gamma R^* \text{ (the JKR derived value was used in the simulation)} \qquad \text{Eq. 38.}$$

Where

F_c = the force needed to break contact,
γ = surface energy
R^* = the effective radius, as defined by Eq. 42

Collisions during contact, according to Thornton [26] pass through several stages:
These being

(i). initial contact
(ii) peeling
(iii) microslip
(iv) sliding

These stages are occur in order but are dependent upon the balance of force from the particle surface energy, preventing slipping and sliding, and the momentum of the particles producing forces that overcome the bonding action of the surface energy.

Solid materials under a load less than that needed to exert a force which exceeds the materials yield strength, so that they deform elastically during a collision (plastic deformation from large loads are not considered in this model), causing reaction forces to occur, as the particles try to return to their original shape. The contact force between the particles, $\mathbf{F}_{ci}$, Eq. 37, is not directly predictable by integration as it relies in part upon the loading and unloading history of the particles involved in the collision. It can, however, be calculated numerically over very small timesteps. The timesteps need to be smaller than the Rayleigh wave propagation within the most compliant of the solid materials in contact. The Rayleigh wave propagation function therefore defines the critical timestep, and is given by;

$$\Delta t_c = \frac{\Pi d_p^{\min}}{2\lambda}\sqrt{\frac{\rho_s}{G}} \qquad \text{Eq. 39}$$

where

$\lambda = 0.1331\nu + 0.8766$ [26].

ν = Poission ratio of the smallest particle
G = Shear modulus
d_p=Particle diameter of the smallest particle
ρ_s =density of the solid

The contact force is given by a modification of the normal force (F_n) as defined by Hertzian contact mechanics Eq. 40

$$F_n = \frac{4}{3} E^* R^{*1/2} \delta_n^{3/2} \quad \text{Eq. 40}$$

where

$$\frac{1}{E^*} = \frac{1 - \nu_1^2}{E_1} + \frac{\nu_2^2}{E_2} \quad \text{Eq. 41}$$

$$\frac{1}{R^*} = \frac{1}{R_1} + \frac{1}{R_2} \quad \text{Eq. 42}$$

E_n = Young‘s modulus of particle n
E^* = the Effective Young‘s modulus as defined by Eq. 41
R_n = the radius of particle n
R^* = the effective contact radius as defined by Eq. 42
δ_n = the displacement in the normal direction.

The displacement in the normal direction is dependent upon the loading history, because the current normal and tangential loading are also dependent upon the loading history and the displacement is derived in response to these loadings.

4.1.3 Particle Simulation Implementation

The particle simulation was coded in Microsoft™ Visual C++ 2012 (64bit) and included multi threading to improve calculation times on multi core processors, the fluid flow data from CFX was imported using the CGNS library [127] and stored in memory.

Each particle was modeled individually and was represented in the model as an C++ object, and a C++ particle class was developed in which the parameters for an individual particle were stored. For each large timestep, (defined as the time taken of the fastest particle in the

simulation to travel a fraction of the radius of the smallest particle in the simulation), the force acting upon the particle was calculated. This consisted of the force from the particle and fluid interactions, and the force from gravity, calculated for each of the x,y and z vector components.

The components of the two vectors were subsequently added to give a resultant force vector, and the components of this force vector were then divided by the combined particle mass and virtual mass (the simulated additional mass to account for the mass of displaced fluid) of the particle, to yield an acceleration. The acceleration across the timestep was assumed to be constant and hence the velocity was derived by the classical formula Eq. 43.

$$\mathbf{v} = \mathbf{u} + \mathbf{a}t \qquad \text{Eq. 43.}$$

where

v = new velocity
u = original velocity
a = acceleration
t = time step

And the new position by Eq. 44

$$s' = s + 1/2\ (\mathbf{u} + \mathbf{v})t \qquad \text{Eq. 44.}$$

Where

s' = new positon
s = old position
v = new velocity
u = original velocity
t=time

The acceleration formulas are applied to each of the x,y and z vector components for acceleration, velocity and position to derive a new location of a particle.

Should the new position of the particle bring it into contact with another particle the position of the two particles involved is ‘unwound’ to the end of the previous timestep. The timestep was then split into smaller steps, (the timestep based on Rayleigh wave propagation within the particles), and the timestep reprocessed, taking into account not only the fluid particle forces and the gravitational force but also the particle contact forces.

Should the particle contact the launder wall it is stopped at that point and considered captured.

Particle locations predicted by this model were displayed and manipulated using the open GL Graphics Library and the graphics library utility toolkit (GLUT).

Chapter 5
RESULTS

The results consist of four sections, the first is concerned with the effect of temperature upon the ^{18}F particles during the PEPT process. The second section was to track particles in cast aluminium plates , assessing the motion of the particles and the effectiveness of ceramic foam filters. In the third section particles were tracked along the length of a launder and the path taken by the particles recorded. The fourth section was to generate a simulation of the particles and compare it to the physical results.

5.1 The effect of increasing temperature upon the PEPT technique

PEPT has previously been demonstrated in various industrial processes, but tracking in liquid metals was a particular challenge, as the density of metallic materials causes problems with γ-ray attenuation. The temperatures needed to keep the metal in the molten state causes the BGO detectors to suffer an efficiency drop and they need to be protected from heat. PEPT cannot therefore be performed as easily as with cooler low density materials. Particularly active tracers are required, due to high levels of γ-ray attenuation and furnaces are needed to generate the high temperatures required. Particles with higher radioactivity levels are created by the ion exchange method, but the stability of a tracer created by this method at elevated temperatures was unknown. Experiments in which the temperature was progressively increased were used to show the stability of the ion exchange ^{18}F tracer particles at elevated temperatures.

5.1.1 Lensalloy experiment

Initial experiments were conducted using a low melting point alloy, Lensalloy 136, which has a melting point of 136^{o}F (67^{o}C). This meant that the initial experiments could be conducted in relative safety at low temperatures.

The first three experimental attempts were marred by flaws in the experiment, one of these being an excessive thickness of metal. The Lensalloy is very dense and attenuates γ-rays greatly and this prevented the detection of radioactivity, (except when particles were on the surface of the metal). In addition there was a lack of any method to indicate that the centre of the particle was being tracked, rather than the geometric centre of radioactivity, which could possibly have been the case if the radioactive fluorine had been transferred into the liquid metal. The last experiment in this series was modified to account for these deficiencies by replacing the large beaker (600 ml ~85 mm diameter) of Lensalloy with a smaller diameter test tube (10mm diameter). The whole test tube assembly containing a radioactive particle was then moved so that some motion could be tracked. The experiments showed that PEPT could follow the position of an indirectly labelled particle whist immersed in liquid Lens alloy136. The particles were tracked for a period in excess of 20 minutes at 270 ^{o}C through 16mm of Lens alloy with a particle activity of 220 μCi, (measured at the start of the experiment). Some dispersion of the radioactivity did occur, as this was detected by a Geiger counter, indicating that some residual radioactivity was present in the metal after the particle had been removed, upon completion of the experiment. It was observed that there was a thermal gradient from the top to the bottom of the test tube, of around 30^{o}C, which meant the temperature at the position of the particle itself was not known precisely. This may have been important as the temperature may have been the driving force for the dispersion of ^{18}F ions.

Since the particle was static, as was the temperature measurement location, the temperature of the particle was directly related to the temperature recorded by the thermocouple.

An example particle track of a resin bead (initially 220 µCi) has been shown , the apparatus was moved early in the experiment, then again, just after ten minutes into the experiment and these movements are indicated in Fig 64.

Time	Temperature (degrees C)		
180	101		
200	107		
220	110		
240	114		
260	119		
280	122		
300	126		
320	137		
340	141		
350	145		
360	141		
390	139		
420	150		
460	150		
500	156		
520	158		
540	159		
580	160		
610	162	Baking Tray removed	
790	180		
835	182		
920	186		
975	186		
1000	185		
1060	189		
1143	189		
1193	192		
1235	194		
1564	201		
1758	203		
1984	208		
2090	210		

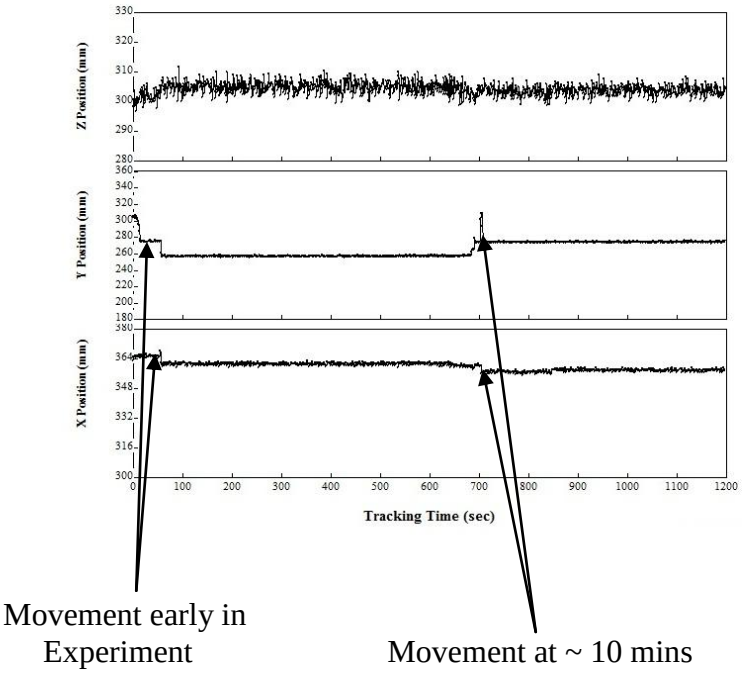

Figure 64. A particle track from the final run of the initial experiment.

5.1.2 Increased temperature experiment in Lensalloy and liquid Sn

A second set of low melting point alloy experiments were performed in which the apparatus was modified to allow forced movement of a radioactive particle. The example particle track,

shown in Fig 65, was of a 600 µm glass bead (initially 100µCi). The glass rod was used to force vertical motion of the particle, which was successfully tracked.

In addition the motion of the entire apparatus horizontally, (moved to the left), was recorded. The motion of the particle was also tracked as the hot plate was exchanged for another capable of generating higher temperatures, this resulting in a new higher base y location. Further motion was tracked up to a temperature of 400 ^{o}C for 4000 plus seconds (1.1 hours).

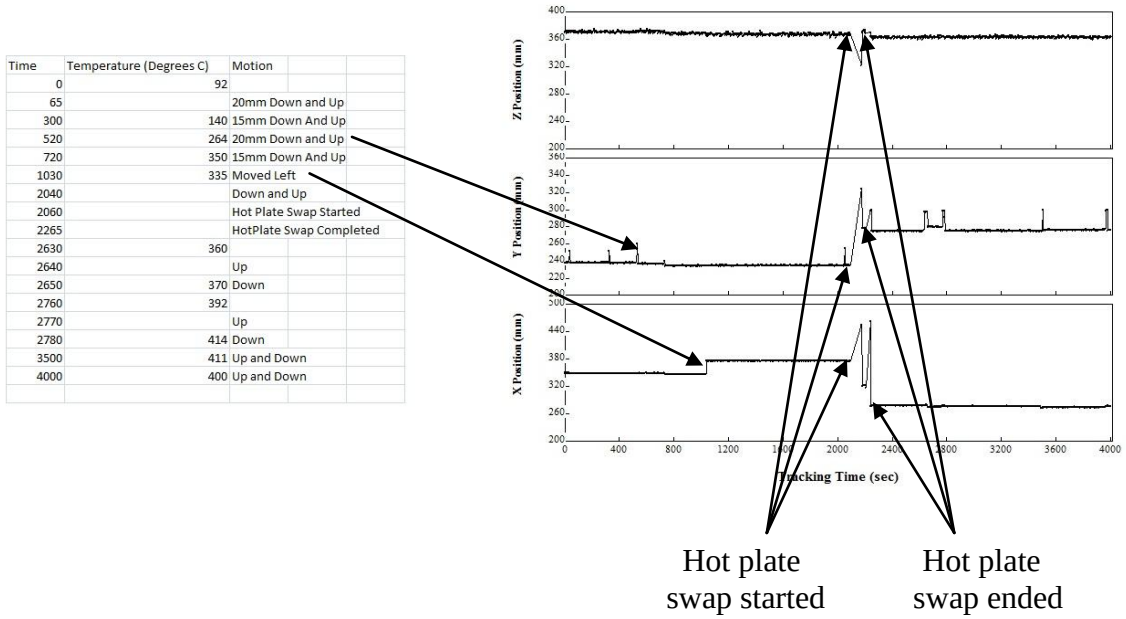

Figure 65. A particle track (particle movement record) (600µm glass particle)

The PEPT traces followed the position of the particle within the liquid Lensalloy, the particle was still able to be tracked after 20 minutes at over 270 ^{o}C. The glass rod (with some attached Lensalloy retained 29 µC of residual radiation and the test tube 9µC due to the manner in which these measurements were taken (being lowered into a radiation meter) these values cannot be taken to be definitive.

The experiment 672µC was repeated using a 600γm gamma alumina particle, the motion of which matched with the actions recorded at the time of the experiment using temperatures up to 400^{o}C (see Fig 66 and Table 7).

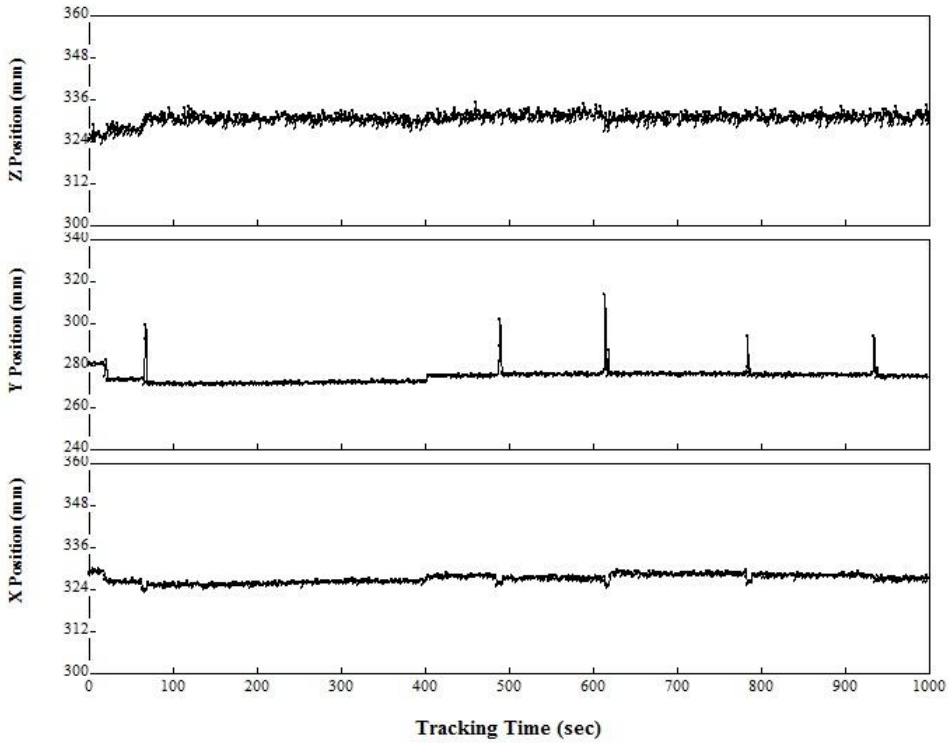

Figure 66. A particle track (600µm γ-alumina particle)

Time s	Action	Temperature ^{o}C
70	Move Up then Down	124
500	Move Up then Down	305
610	Large Move Up then Down followed by small Move Up then Down	350
780	Move Up then Down	390
930	Move Up then Down	400

Table 7. Movements recorded for 600µm γ-alumina particle experiment using Lensalloy

The experiment was repeated again using a 400µm resin bead of 410 µCi activity, the motion was recorded along with the temperature and the time, the maximum temperature was 414^{o}C (see Fig 67 and Table 8).

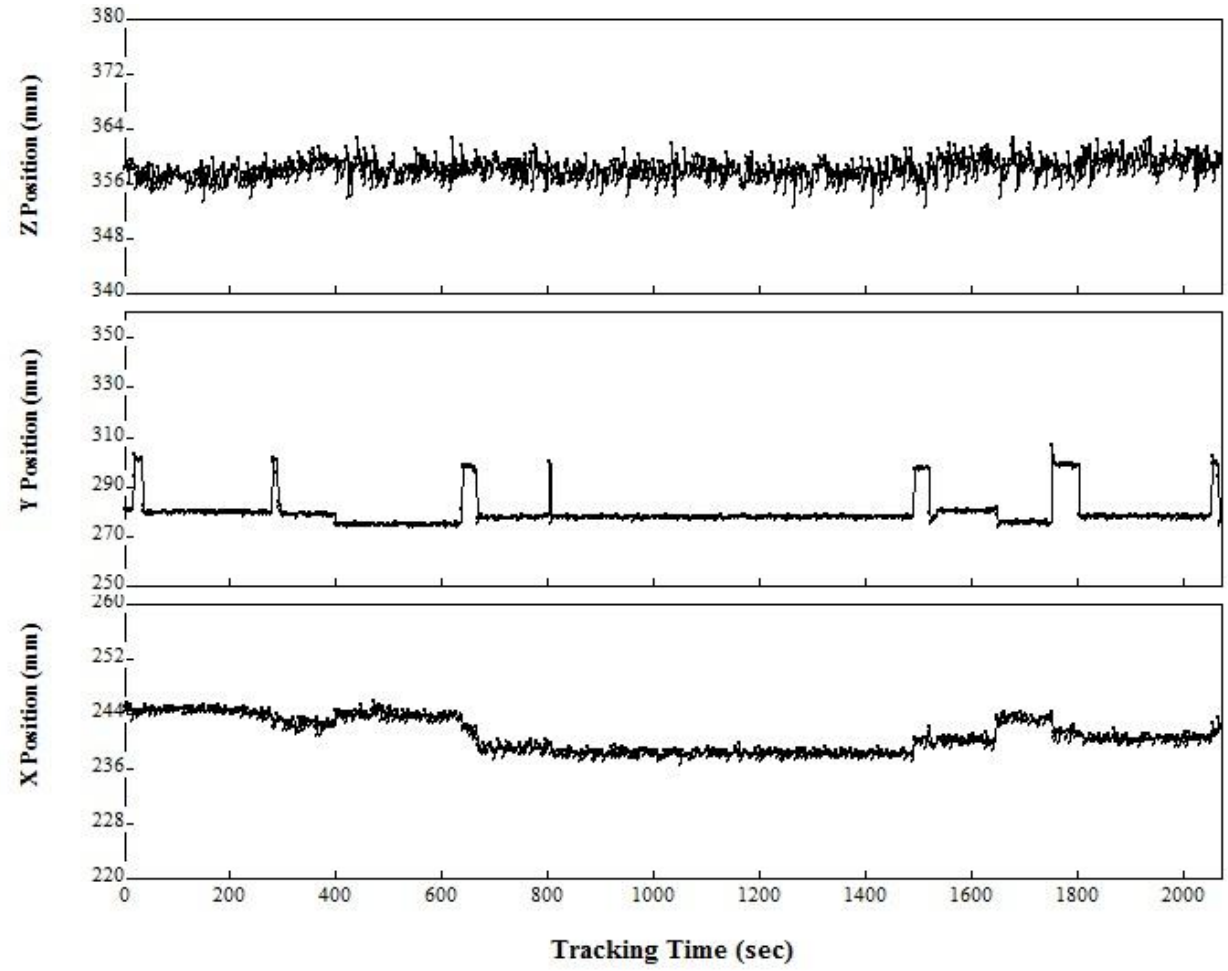

Figure 67. A particle track (600µm resin particle)

Time s	Action	Temperature ^{o}C
10	Move Up	167
30	Move Down	183
300	Move Up then Down	Not Recorded
630	Move Up	398
680	Move Down	398
800	Move Up	408
810	Move Down	408
1490	Move Up	408
1510	Move Down	418
1650	Small Move Up then Down	418
1750	Move Up	414
1800	Move Down	414
2050	Move Up	414
2060	Move Down	414

Table 8. Movements recorded for 600µm Resin particle experiment using Lensalloy

Glass, alumina and resin particles could all be tracked, however as the resin started to decompose and vapourise it was deemed potentially hazardous and all further experiments used only glass or γ alumina particles. A Geiger counter indicated some radioactivity present in the metal after the particle had been removed at the end of each experiment. The residual radioactivity in the metal suggested that there had been some transfer of radioactivity from the particles during the course of the experiments.

The experiment was also conducted using pure Sn, which allowed tracking of an alumina particle, until the experiment was discontinued after the apparatus failed (the test tube cracked, releasing the tin into the copper tube at 310 ^{o}C). At the point of the test tube's failure the PEPT camera was still tracking the particle movement.

5.1.3 Particle tracking in Al in a thin section mould

An experiment was conducted to ascertain if indirectly labelled particles could be tracked inside the body of a high temperature liquid, such as aluminium alloy (2L99). In this series of experiments 600 μm alumina particles were utilised as they gave the highest activity, with indirect activation, of any of the particles used to date. The mould shown in section 3.2.4., Fig 42, was used in these experiments.

The first Al casting in the series of experiments was performed using molten Aluminium alloy (2L99) at 750^{o} C. In this experiment, a particle was successfully tracked into and down the length of the downsprue. It then travelled into the fourth of the arms at the lower extremity of the mould, connecting the boss at the bottom of the downsprue to the lower collar (see Fig 68). The particle was seen to move in an erratic motion within the boss, before entering the connecting arm.

The next casting made, allowed the particle to be tracked down the downsprue, into the boss, through the second of the arms and up through the nearest associated rod connecting the lower and upper collars (see Fig 69). Unfortunately, as the mould was set at a position that was high in the volume observable by the positron camera (72mm), the particle position was lost due to an excessive amount of scatter in its reported location, as it entered the upper ring

of the mould, This was believed to be due to sensitivity issues caused by the geometry used in this region of the positron camera. At the top and bottom of the positron camera geometry fewer opposing detector modules are available to co-incidence match with the top (or bottom) row of detectors, which results in reduced sensitivity at the top and bottom extremities of the cameras viewable volume. This issue meant the particle final location could not be reported in this case.

The casting in Fig. 70 showed a particle that travelled the length of the downsprue, with a swirling motion towards the bottom before it entered the boss. It then travelled through it and into the third arm, where it came to rest.

Fig 71 shows a particle that was tracked to a location some 50mm lower down in the downsprue than the particle introduction location. The particle had moved to a position which appeared to be against the downsprue wall.

The final casting in this series of experiments, Fig 72, showed a particle which travelled the length of the downsprue, through the boss and into the fourth connecting arm then through the lower collar and into the bottom of the fourth connecting rod, where it came to rest after a short upwards motion.

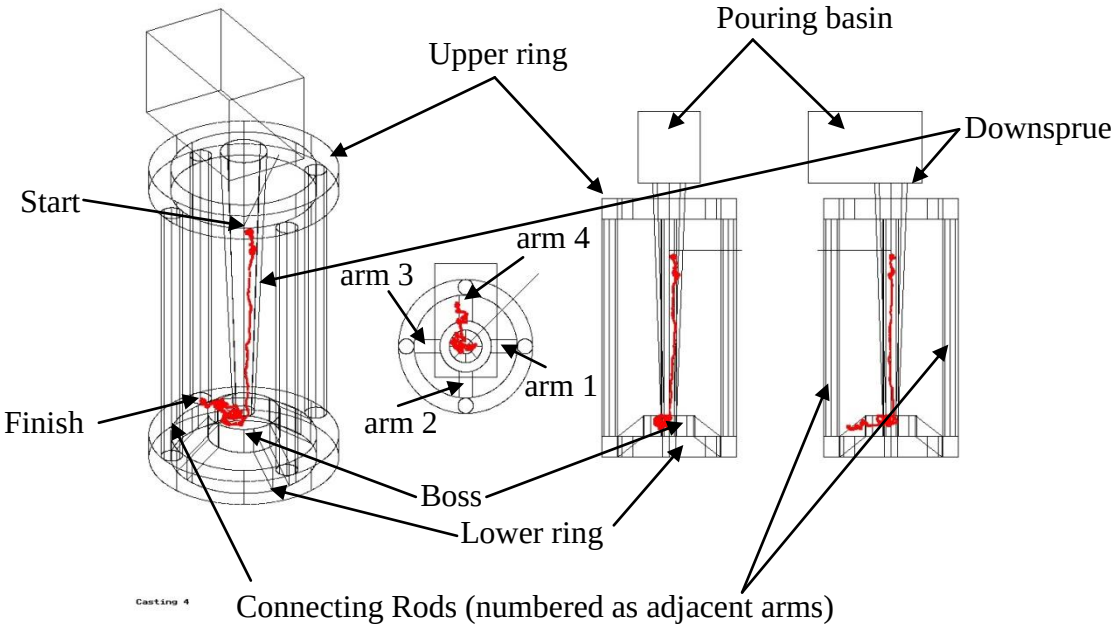

Figure 68. Diagram of mould and particle track (in red) for the 1st experiment in Al (The arms from the boss at the base of the downsprue to the lower collar are numbered, This numbering is applicable to all diagrams in sections 5.1.3 and 5.1.4) See fig (42) in section 3.2.3 for a full description of the mould.

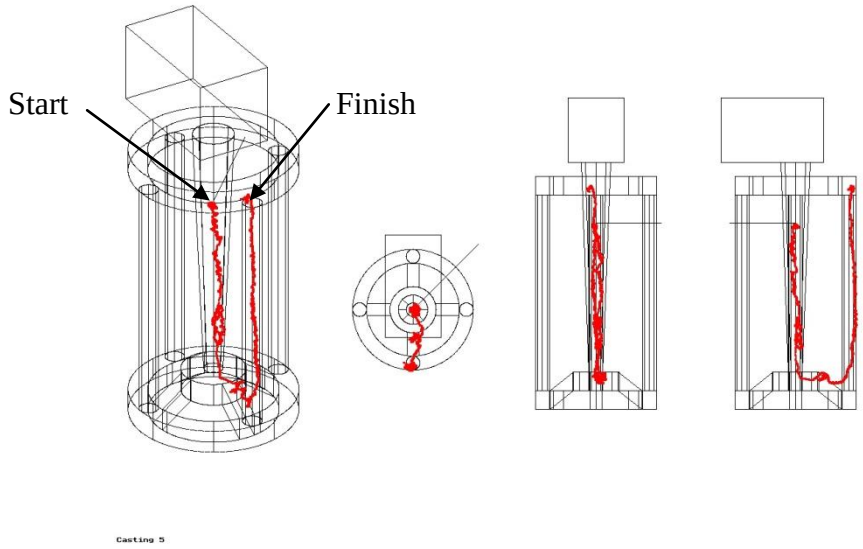

Figure 69. Diagram of mould and particle track for the 2nd experiment in Al

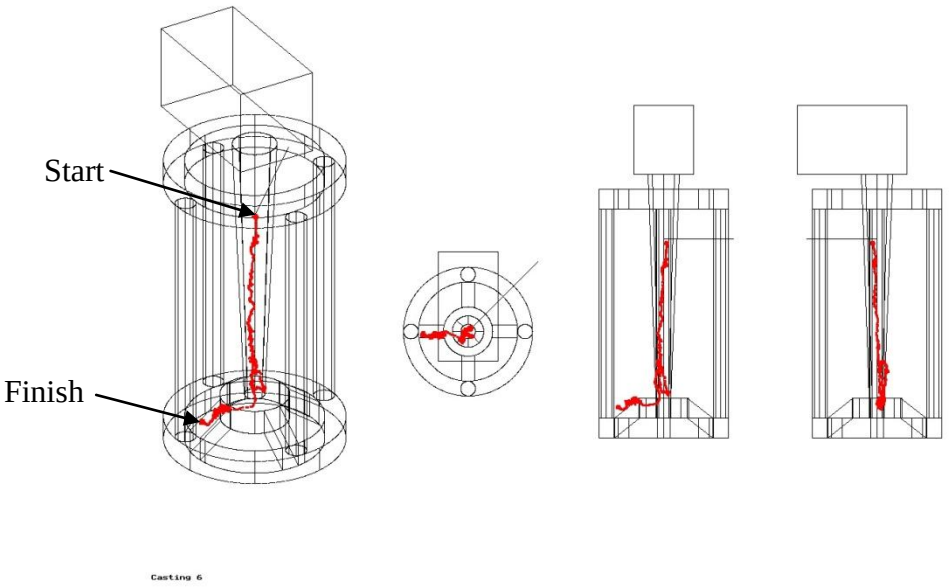

Figure 70. Diagram of mould and particle track for the 3rd experiment in Al

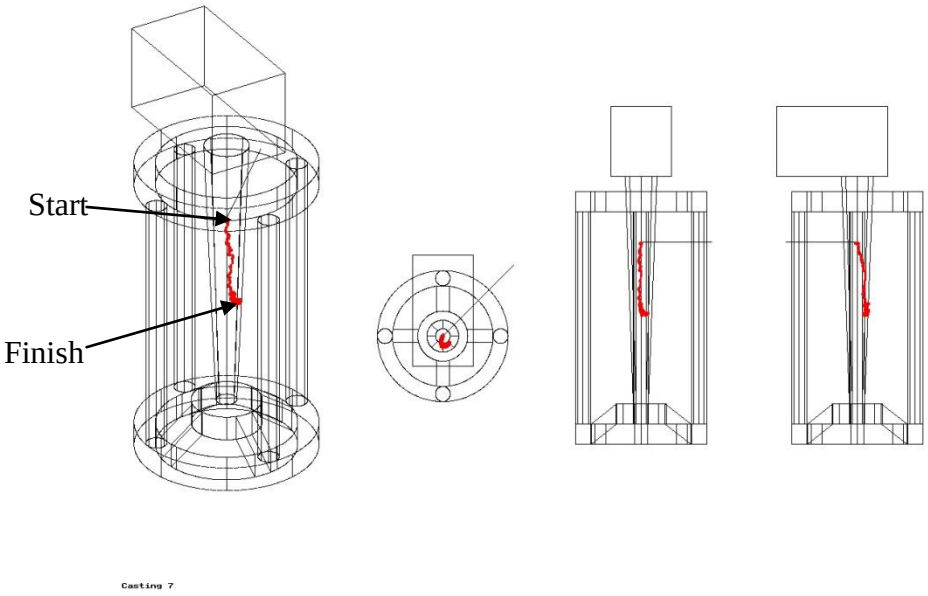

Figure 71. Diagram of mould and particle track for the 4th experiment in Al

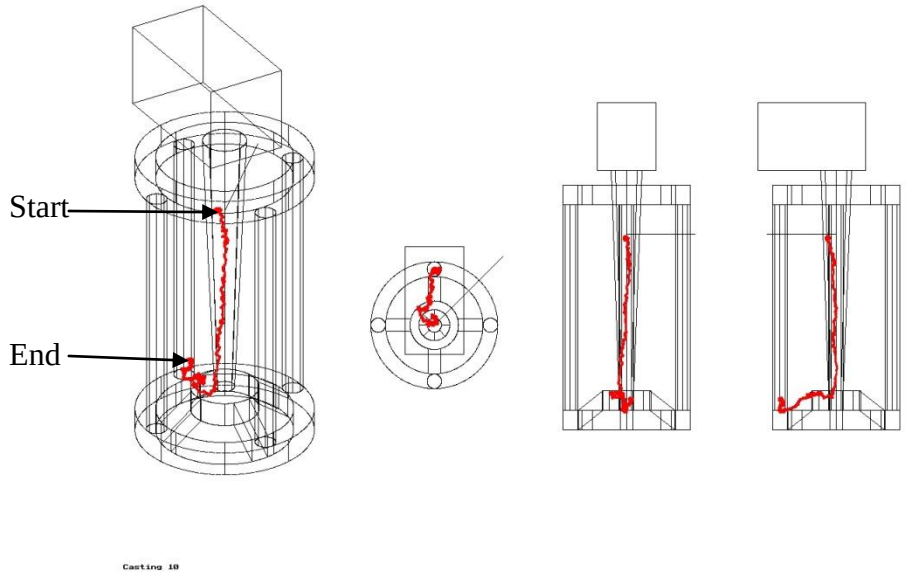

Figure 72. Diagram of mould and particle track for the 5th experiment in Al

5.1.4 Particle tracking in Steel in a thin section mould

Particle tracking in liquid steel was attempted using the same investment mould used for the experiments in aluminium, (the mould had been designed with the use of liquid steel as a consideration). The investment mould was capable of surviving temperatures in excess of 1500°C.

The first of the experiments using liquid steel, shown in Fig .73, produced a particle track that began at the introduction point in the downsprue to a point 10mm above the boss, alongside arm four, but still within the downspue. The second experiment, see Fig. 74, showed the same pattern, where again the track stopped just short of the boss. A closer examination of the data collected showed that, below this point, a very considerable scatter in the reported particle location was observed and the error in the location reported was too high to give a definitive

particle track. It was felt that this was due to the lower sensitivity of the positron camera at the lower part of its viewable volume, as described in section 5.1.3. A reference particle without any additional attenuation from the mould and the metal could be tracked in this region, but a particle subject to significant attenuation could not be tracked. The mould was therefore raised by 72 mm, by placing it on an insulation brick before the next experiment. The third experiment, see Fig. 75, tracked the particle into the boss, where it came to rest at the entrance to the 2nd arm, below the point in the mould where the particle tracking had failed in the previous two experiments. In the fourth experiment, see Fig. 76, the particle travelled the length of the downsprue and into the 3rd arm, where it came to rest, following a very similar path as that shown in Fig 70, (one of the experiments using aluminium), but the particle travelled a little further along the arm and possibly into the lower ring.

A fifth and final casting was made in steel, see Fig 77, in which the particle travelled the length of the downsprue and into the second arm; it then travelled through the arm into the adjacent lower collar where it finally came to rest at the base of a connecting rod.

Dispersion of radioactivity within the mould could not be checked with a Geiger counter in both the Al and steel experiments as it was not possible to remove the particles from the castings.

Despite some issues with the geometry of the positron camera it was evident that radioactive particles could be tracked at high temperatures, up to and including the temperature of molten steel (> 1500^{o}C).

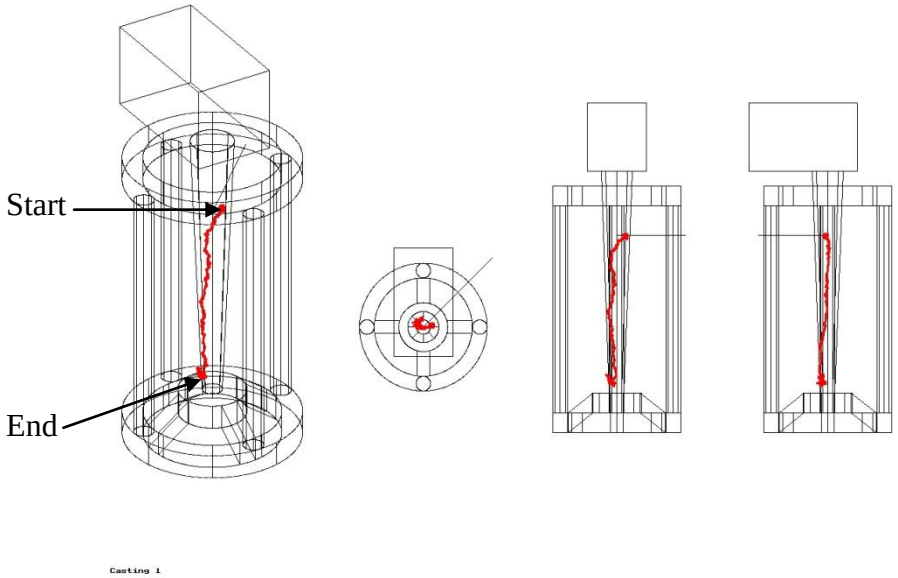

Figure 73. Diagram of mould and particle track for the 1st experiment in Steel

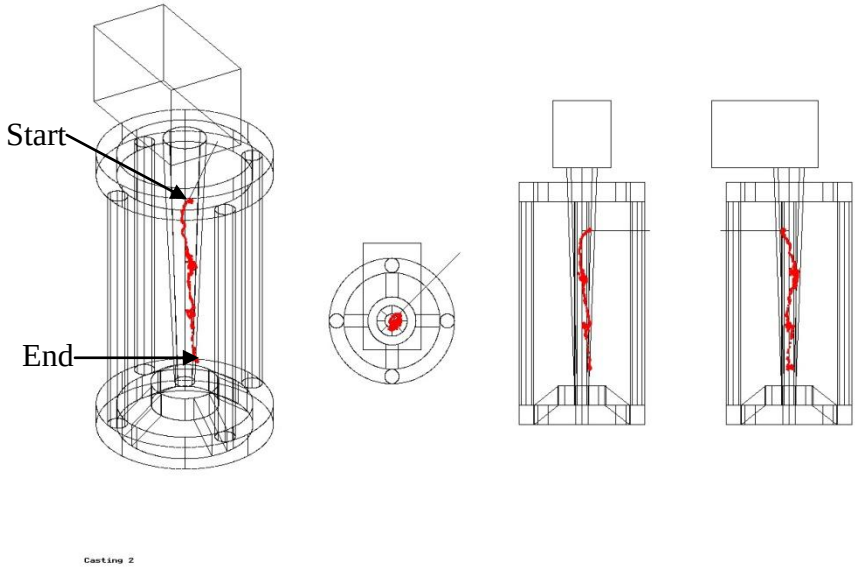

Figure 74. Diagram of mould and particle track for the 2nd experiment in Steel

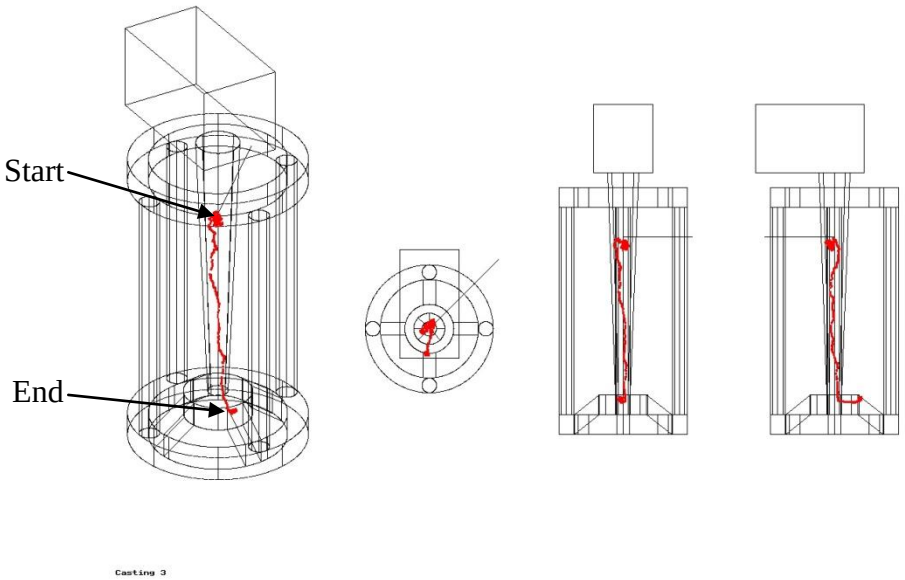

Figure 75. Diagram of mould and particle track for the 3rd experiment in Steel

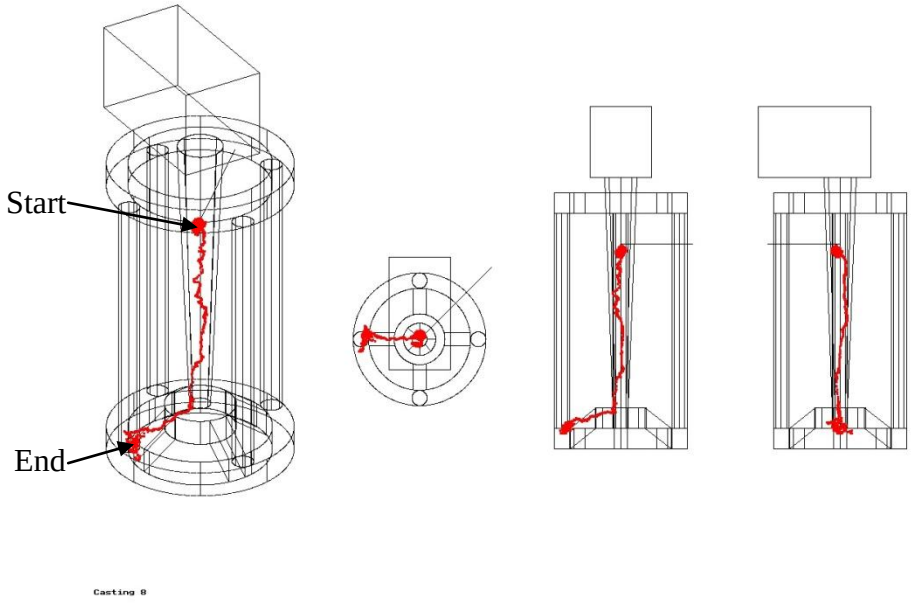

Figure 76. Diagram of mould and particle track for the 4th experiment in Steel

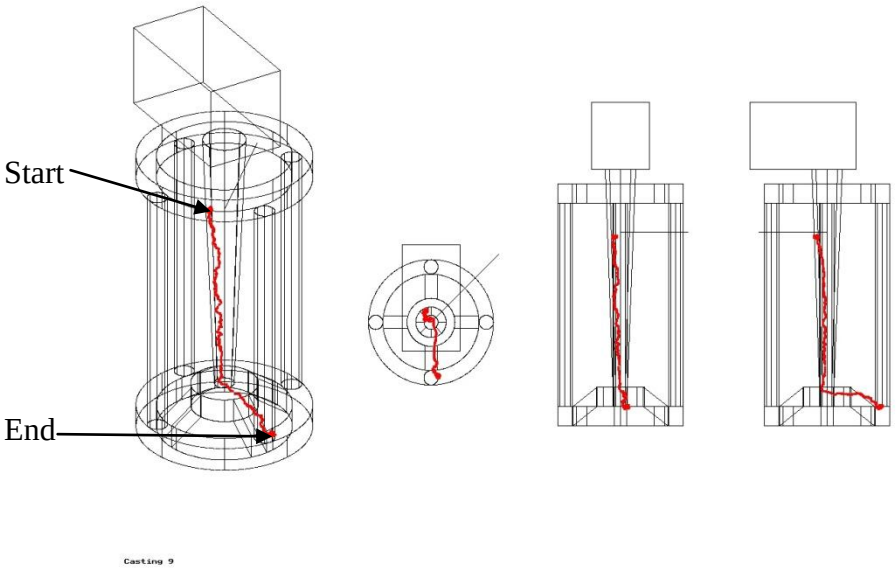

Figure 77. Diagram of mould and particle track for the 5th experiment in Steel

5.2 PEPT and PET of particles in Al plates cast with and without a filter

Radioactive tracer particles were tracked in an aluminium plate casting using PEPT without a filter. In addition final particle locations were determined by PET scans in a plate casting experiment with a filter.

5.2.1 PEPT tracking of particles in Al plates without a filter

A series of 12 experiments were conducted to track radioactive particles in a liquid aluminium alloy (2L99). Both γ-alumina and glass particles of sizes nominally 600 μm and 110 μm for the alumina particles, and nominally 600 μm and 300 μm for the glass particles were used. All experiments were conducted with a pouring temperature ~750^{o}C. The figures shown (Figs 78-90) are all displayed in an orientation where the running system is to the right of the cast plate, when viewed from the front of the plate, the description in the experiments also follow this convention.

Figs. 78 and 79 show the particle tracks of two 600μm γ-alumina particles of activity 773 μCi and 520 μCi, respectively. These particles were introduced in the downspue at a known location. Upon the metal being poured, in both cases, the particle travelled through the running system, stopping just short of the ingate. There was some scatter in the predicted locations and some of the positions were reported as being outside the mould cavity. Fig 83 used a 401μCi 110 μm γ-alumina particle. This particle travelled into the plate cavity having traversed the running system. It adopted a circular motion to the right hand side of the ingate, before stopping just short of and to the right of the plate centerline near the top of the plate. Scatter caused some locations above the final particle location outside the plate to be reported. The particle in Fig. 80, a 434 μCi 600μm γ-alumina particle was tracked, but

stopped in the downsprue after travelling about 160mm. In Fig. 84, a 110 μm alumina particle of 51 μCi activity rose slightly in the downsprue but did not show any other movement, this was not expected particle behaviour given the downwards flow of the molten aluminum. In Fig 86 μCi, 110 μm, alumina particle produced a track that was obtained despite its low activity, relative to other experiments. Very few data points were recorded in the running system and in the plate itself and all the reported locations suffered from considerable scatter in the data. The start and end location of this particle reported in the data had considerable scatter with some of the data inside the mould cavity and some of the data outside.

Fig. 81 showed a particle track produced with a 600μm glass particle being tracked into the cast plate itself, although scatter in the data caused the indicated end location of the particle to be outside the casting. This particle, with 172 μCi activity had a considerably lower level of radioactivity than the particles used for Figs 78 and 79, as is typical when activating glass particles using the ion exchange/surface adsorption process. It can be inferred from the degree of scatter that this particle was not sufficiently active to track well in a metal thickness of 15mm. Fig. 82 shows a result using a 142μCi 600 μm glass particle which travelled through the running system before rising into the cast plate, where it moved in a circular motion before coming to rest, just below the horizontal centre line of the plate and towards the left hand side of the plate. In Fig. 86, a 40 μCi, 300 μm glass particle was tracked. This particle, like the alumina particle in Fig. 85 had a lower activity compared to other particles in these experiments and as in the experiment with the 47 μCi alumina particle this 40 μCi particle was tracked quite poorly with a large degree of scatter in the statistical data from which the particle locations are derived, relative to more active particles. Fig. 87, shows the track of a 74 μCi 300μm glass particle. This rose slightly in the downsprue but as with the alumina particle in Fig. 84 did not show any other movement. Fig. 88 shows a 300μm 49μCi

glass particle. With its relatively weak level of radioactivity the start and end locations for this particle were detected, but no locations were found whilst the particle was in motion. The particle used in Fig. 85 was a 47μCi alumina particle and this level of activity appears to define the lower limit for successful tracking. Fig. 89 showed a track produced with a 300um 26μCi glass particle and this was the lowest activity level of any of the particles in these experiments. It showed a particle so weakly radioactive that it appears to have ceased being tracked as soon as the aluminium was poured, and it displayed an abnormal amount of scatter prior to the casting operation.

An additional casting was made using the alloy A20X, (see Fig 90), In this case the particle was poorly tracked down the downsprue, as the particle would have been moving quickly, but then in the runner the particle track was temporarily lost. The track resumed after the final bend before the ingate to the plate, where the metal slowed down. The particle was tracked to an end location after having made a figure of eight motion.

The end location given by the tracking system was 186 mm in the X direction, -39 in the Y direction and 3 mm in the Z direction. The particle position was confirmed by machining away the aluminium to reveal the particle. Its true location was measured to be 191 mm in X, -42 mm in Y and 6mm in Z. Thus the error along the X axis was 5mm and 3mm in the Y axis. The Z axis measurement was absolute from the face of the downsprue when measured, but relative to the introduction point within the downsprue when tracked and both values matched within 3mm.

Once revealed the particle was inspected by optical and electron microscopy and the image from the optical microscope, Fig 91, shows the circular arc of the particle's spherical shape,

which was discoloured by its passage through the metal, now appearing dark, as opposed to the almost white colour of a pristine particle.

The electron microscope image in Fig 92, showed the particle much more clearly; the particle being lodged in the side of a ~1.7 mm pore. EDS analysis, Fig 93, was carried out on the particle and the pore. The three readings from the particle indicated approximately 62% Aluminium and 36% oxygen by weight. The two readings from the pore showed the aluminium and A20X alloying elements, but very little oxygen, suggesting that the pore had not entrained in air, and consumed oxygen.

An area analysis of the particle surface, Figs 94 and 95, showed that there was almost a 50:50 ratio (Table 9), between oxygen and aluminium in the particle, showing it to be alumina and it is therefore concluded that the particle found was the once radioactive alumina particle that was previously tracked.

Particle Tracks

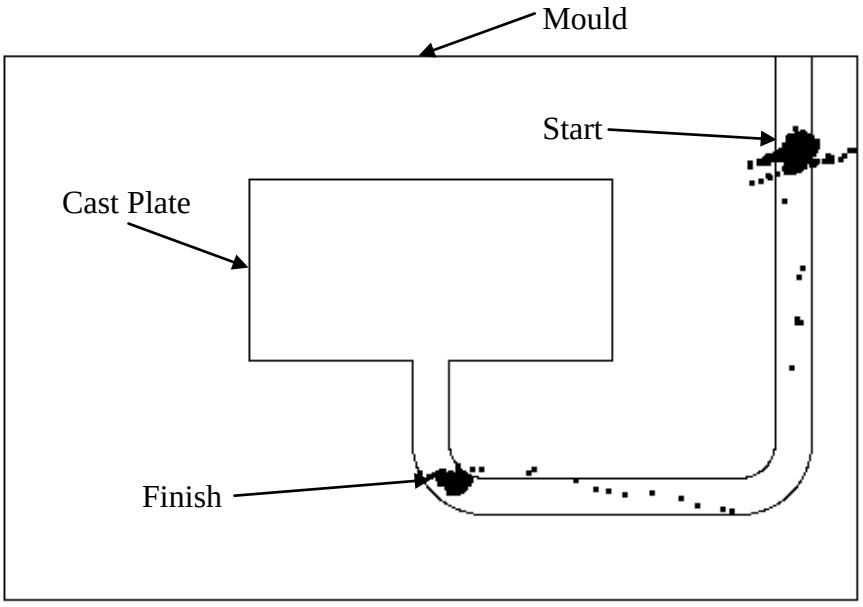

Casting 1
Alumina - 773uCi

Figure 78. 1st 600µm γ alumina particle track in a cast plate

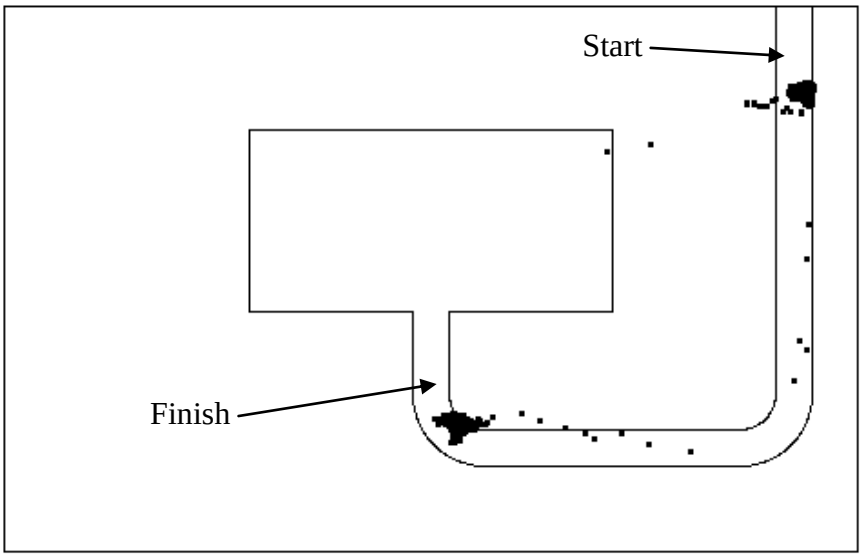

Casting 2
Alumina - 520uCi

Figure 79. 2nd 600µm γ alumina particle track in a cast plate

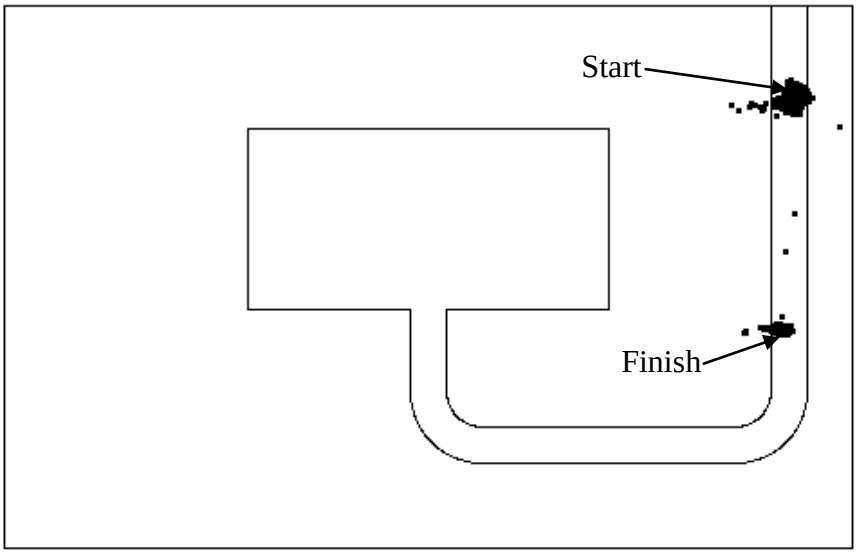

Casting 3
Alumina - 434uCi

Figure 80. 3rd 600µm γ alumina particle track in a cast plate

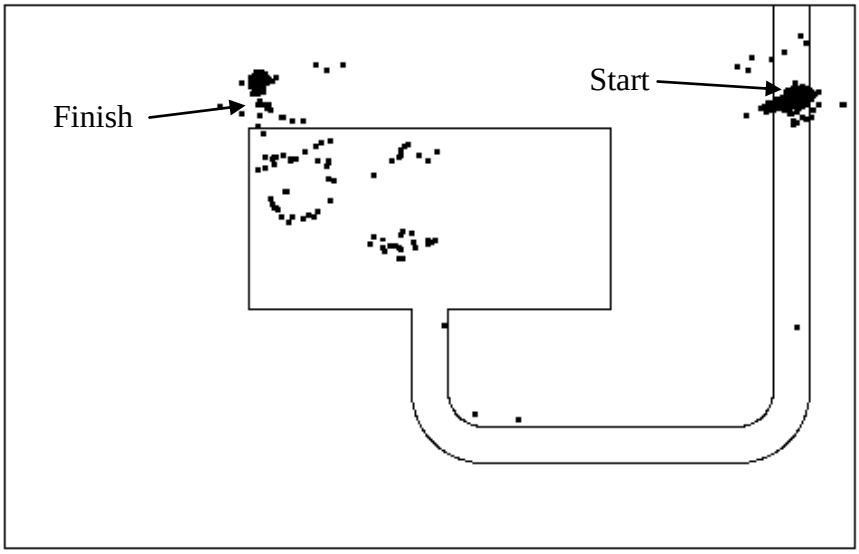

Casting 4
Glass - 172uCi

Figure 81. 1st 600µm glass particle track in a cast plate

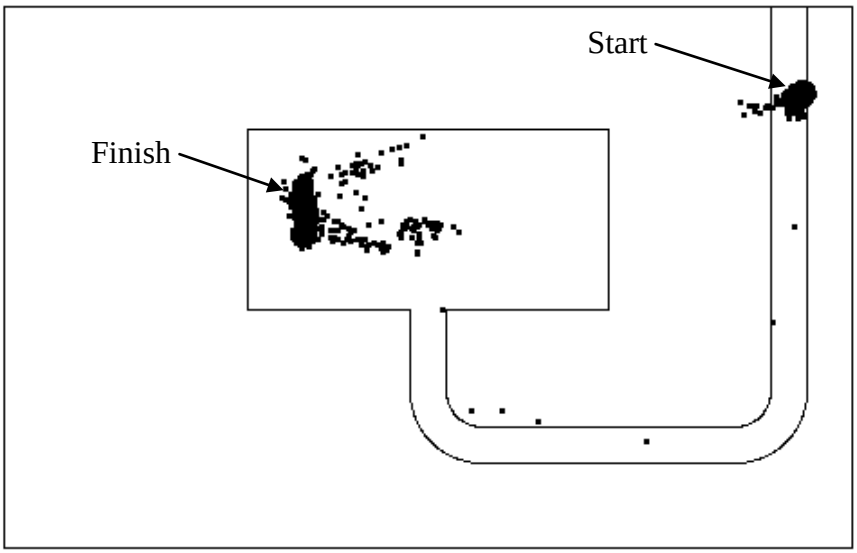

Figure 82. 2nd 600µm glass particle track in a cast plate

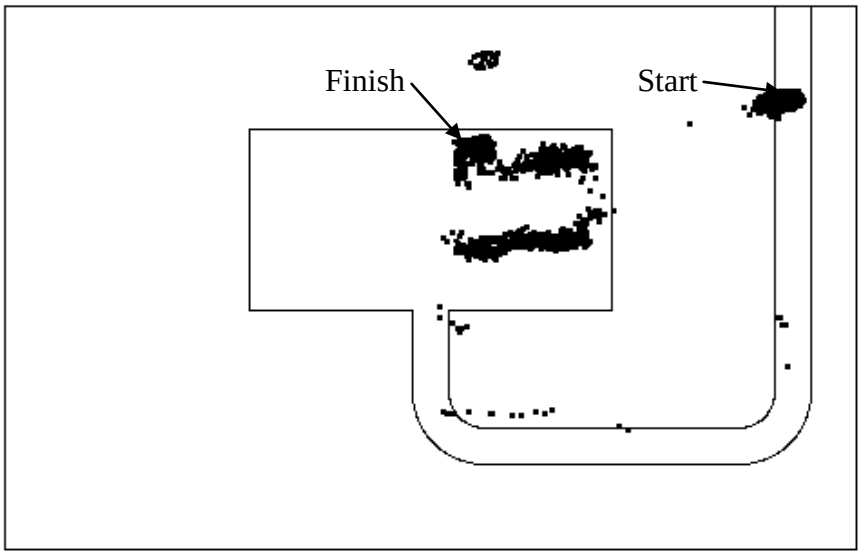

Figure 83. 1st 110µm γ alumina particle track in a cast plate

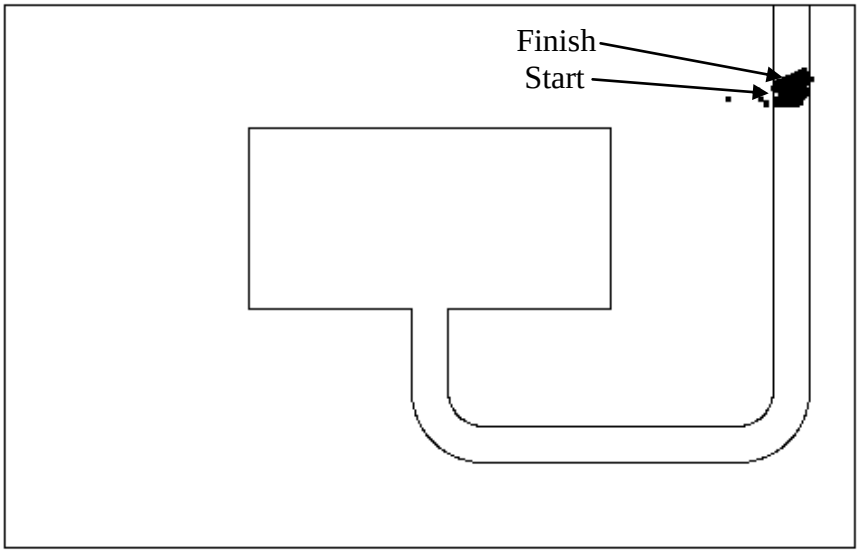

Figure 84. 2nd 110µm γ alumina particle track in a cast plate

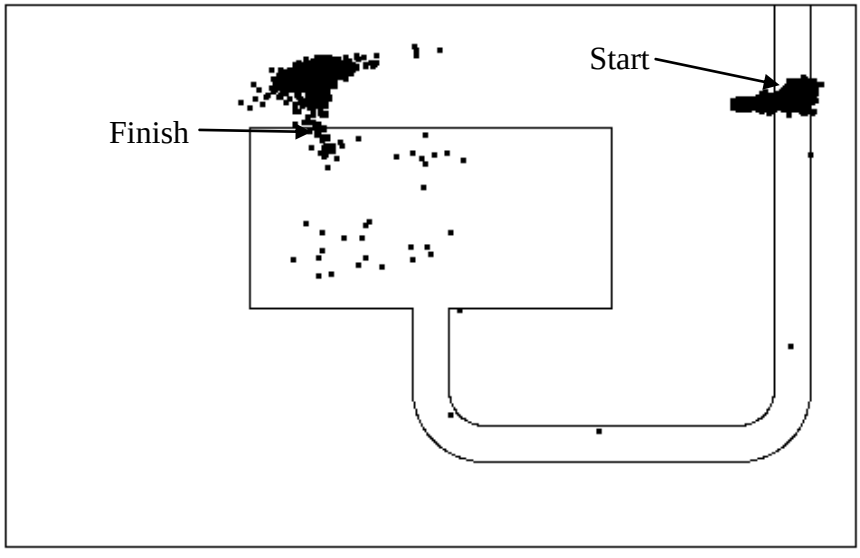

Figure 85. 3rd 110µm γ alumina particle track in a cast plate

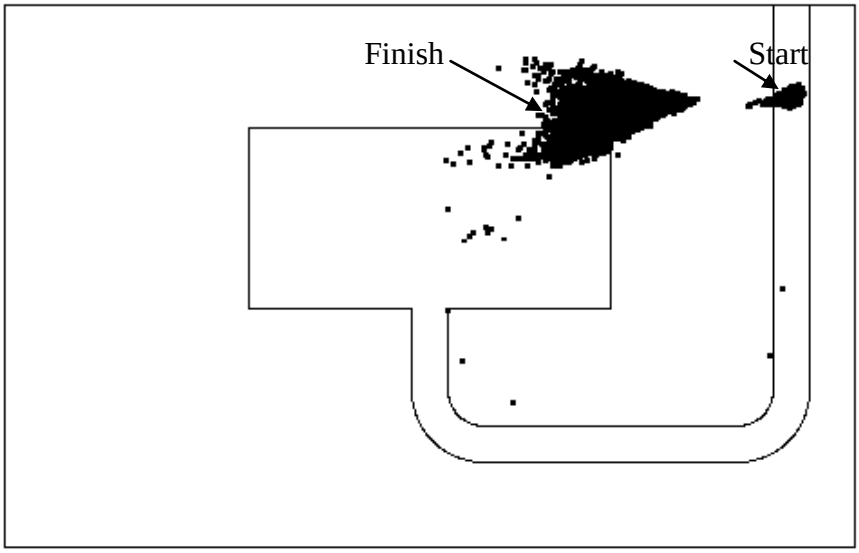

Figure 86. 1st 300µm glass particle track in a cast plate

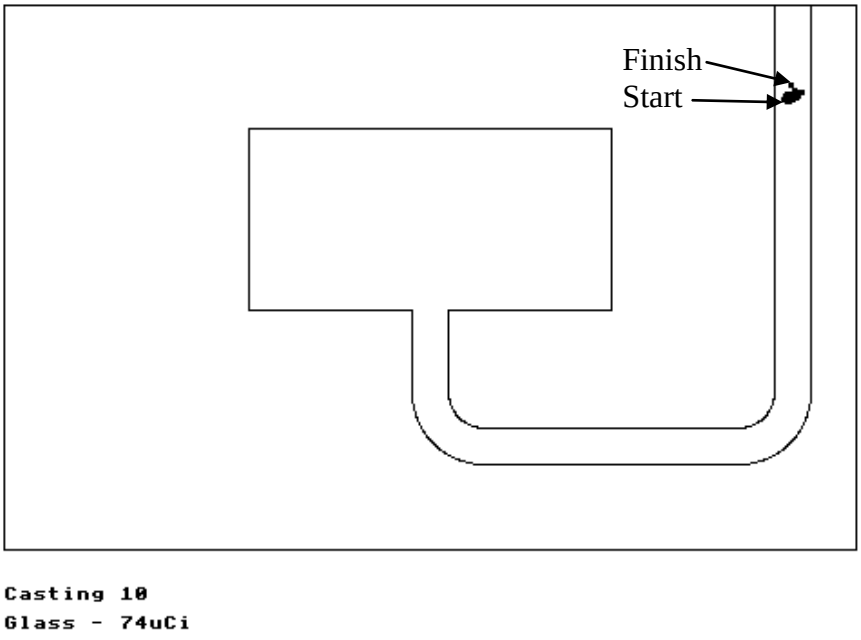

Figure 87. 2nd 300µm glass particle track in a cast plate

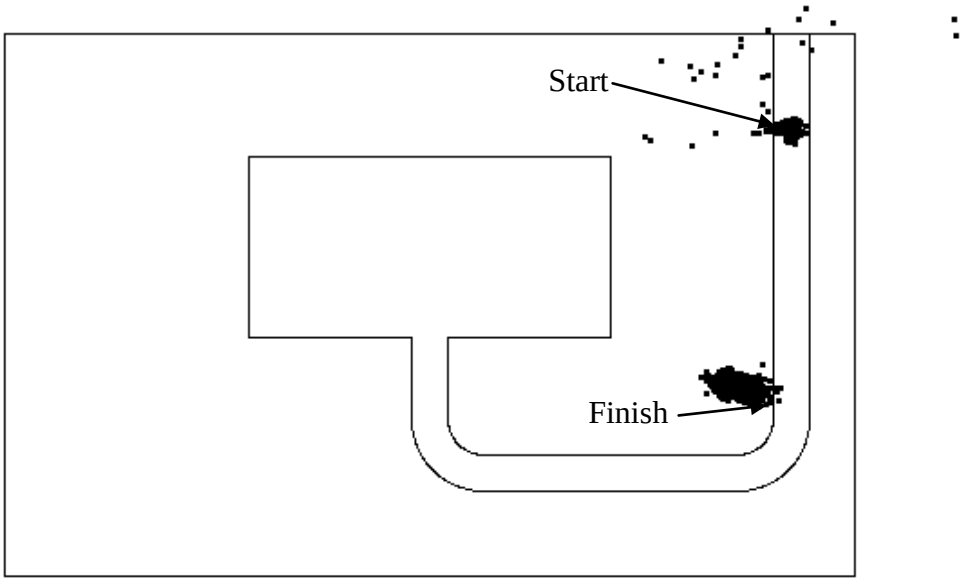

Figure 88. 3rd 300µm glass particle track in a cast plate

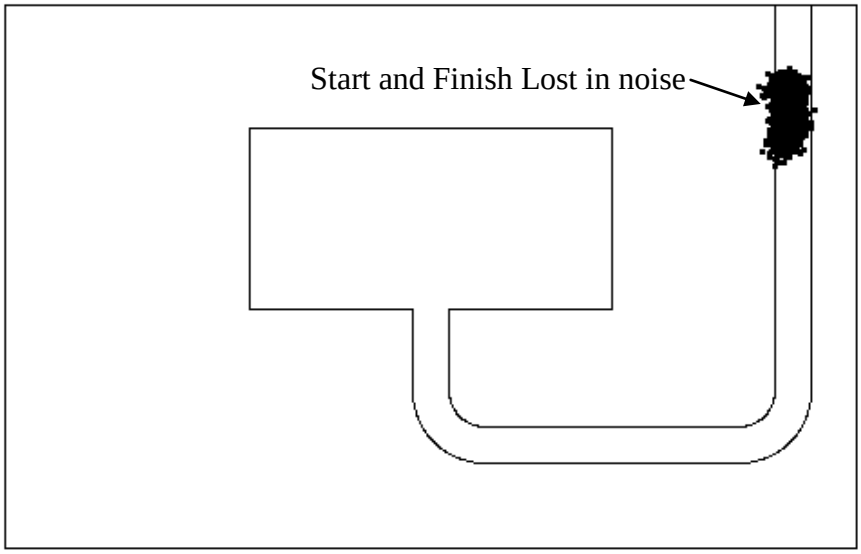

Figure 89. 4th 300µm glass particle track in a cast plate

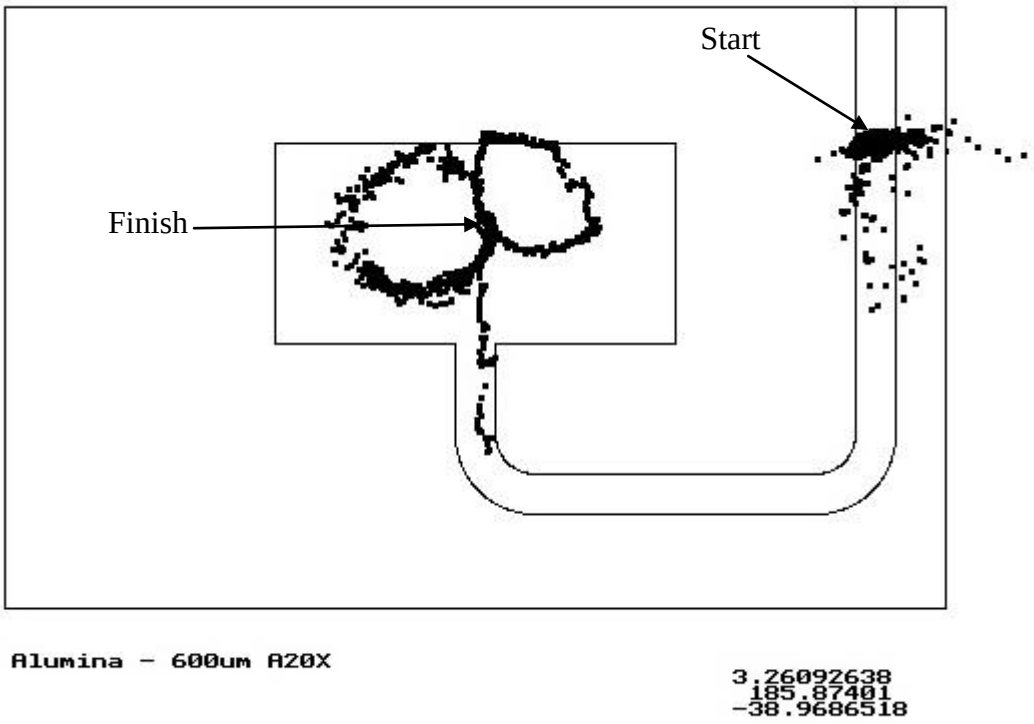

Figure 90. 600 µm particle path showing particle end position in A20X

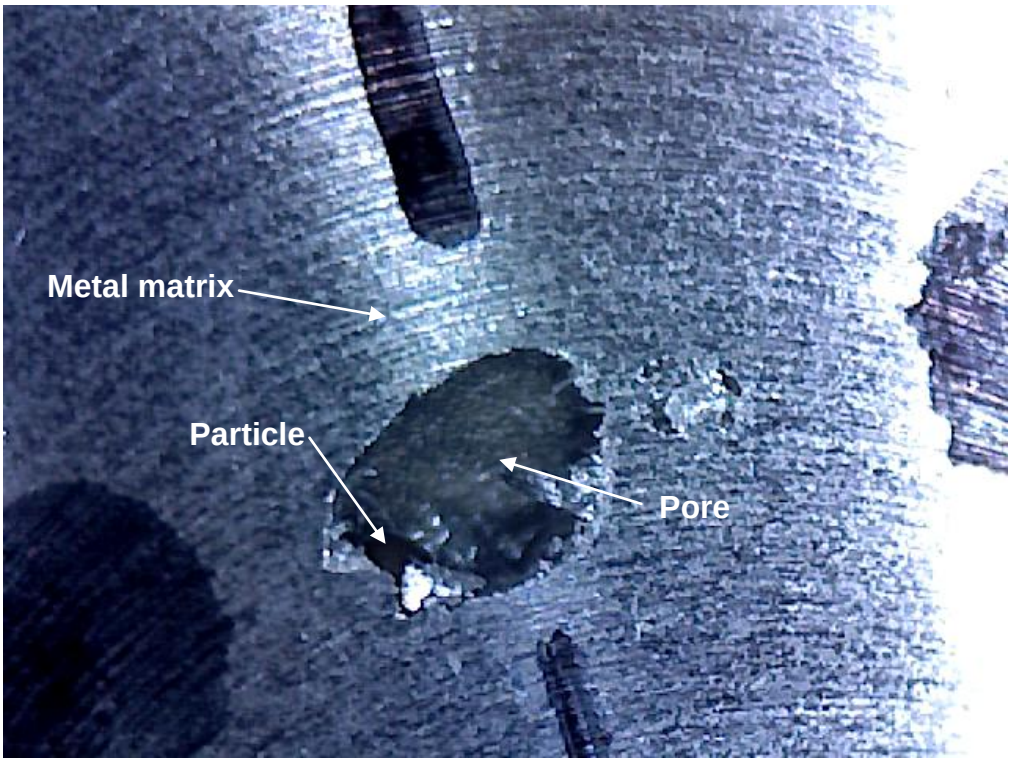

Figure 91. 600 µm particle attached to pore – Optical image

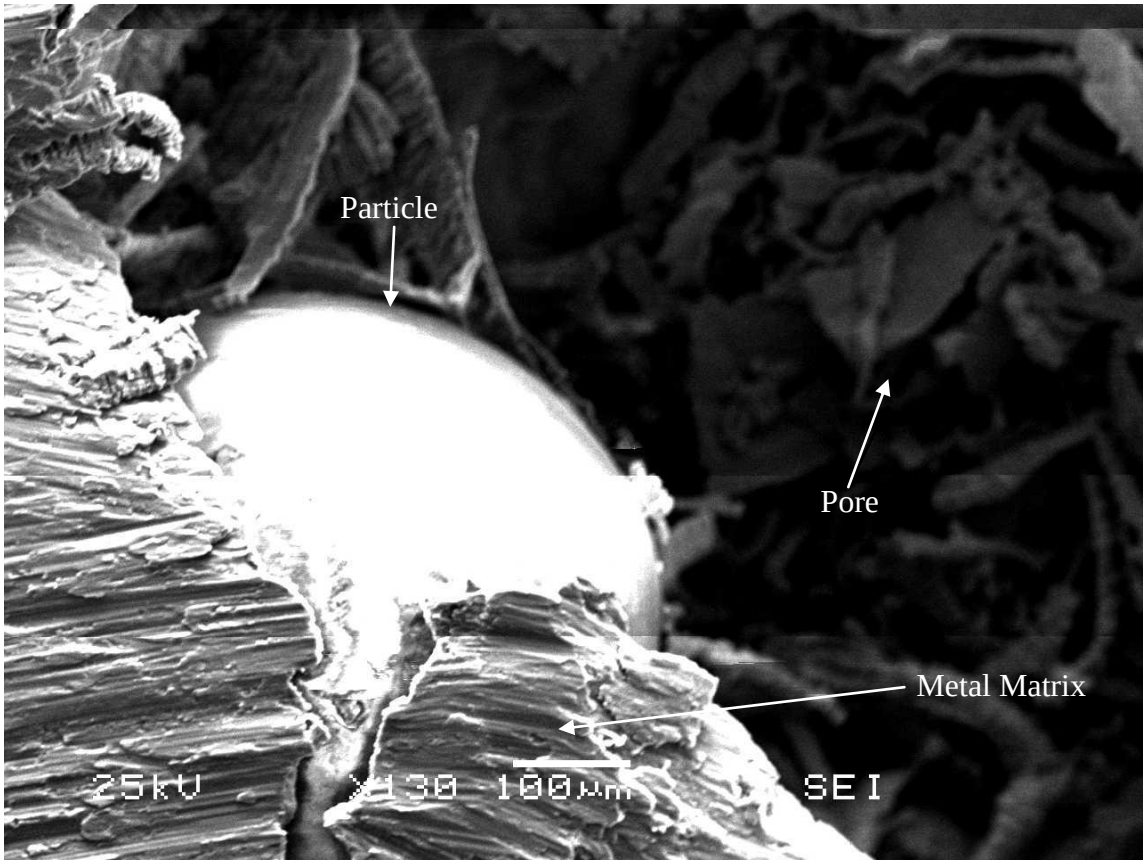

Figure 92. 600 µm particle attached to pore – Electron microscope image

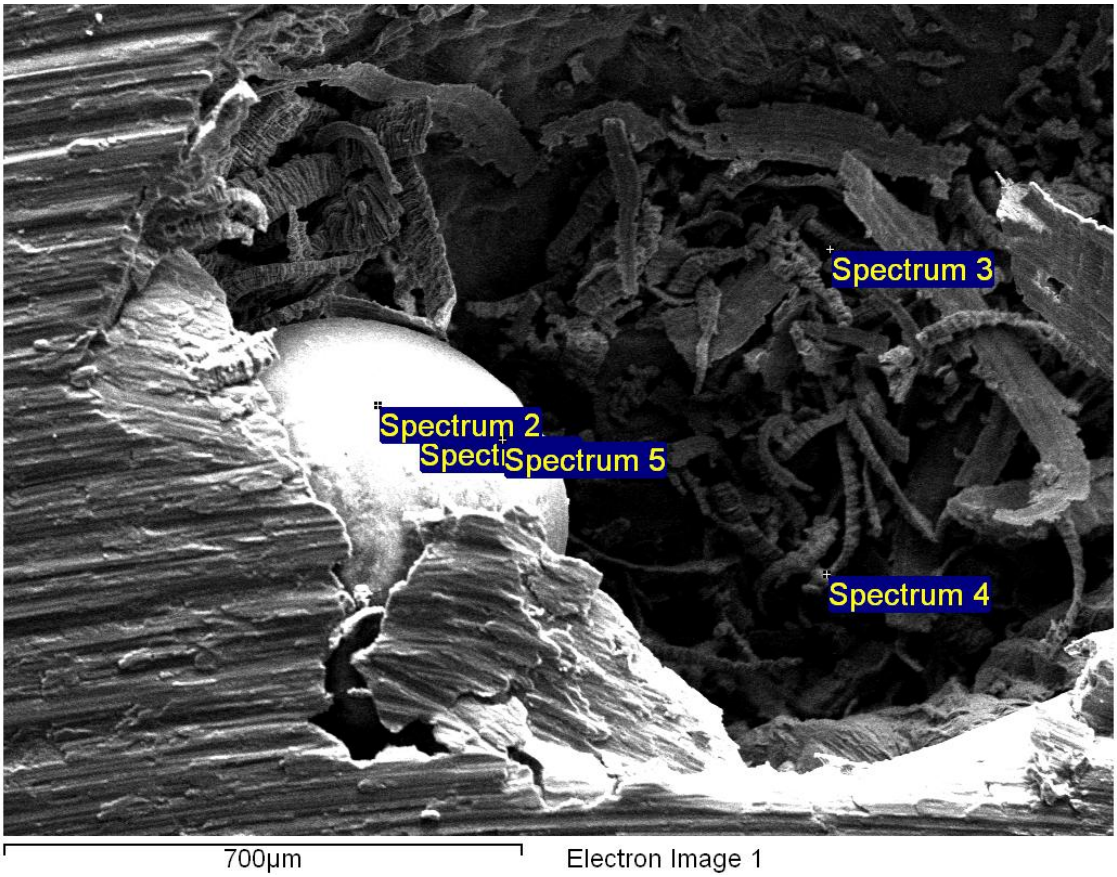

Figure 93. 600 µm particle attached to pore – EDS analysis sample points

Processing option : All elements analysed (Normalised)

Spectrum	In stats.	O	Mg	Al	P	Ar	Ti	Cu	Zn	Ag	Total
Spectrum 1	Yes	35.65	1.00	62.99		0.20		0.16			100.00
Spectrum 2	Yes	35.95	0.98	61.81	0.15		0.10	0.18		0.82	100.00
Spectrum 3	Yes	7.00		82.42			3.72	6.87			100.00
Spectrum 4	Yes			95.04			0.97	2.03	0.00	1.96	100.00
Spectrum 5	Yes	35.79	1.44	61.26	0.16		0.09	0.23		1.04	100.00
Max.		35.95	1.44	95.04	0.16	0.20	3.72	6.87	0.00	1.96	
Min.		7.00	0.98	61.26	0.15	0.20	0.09	0.16	0.00	0.82	

All results in weight%

Table 9. 600 µm particle attached to pore – EDS analysis by weight

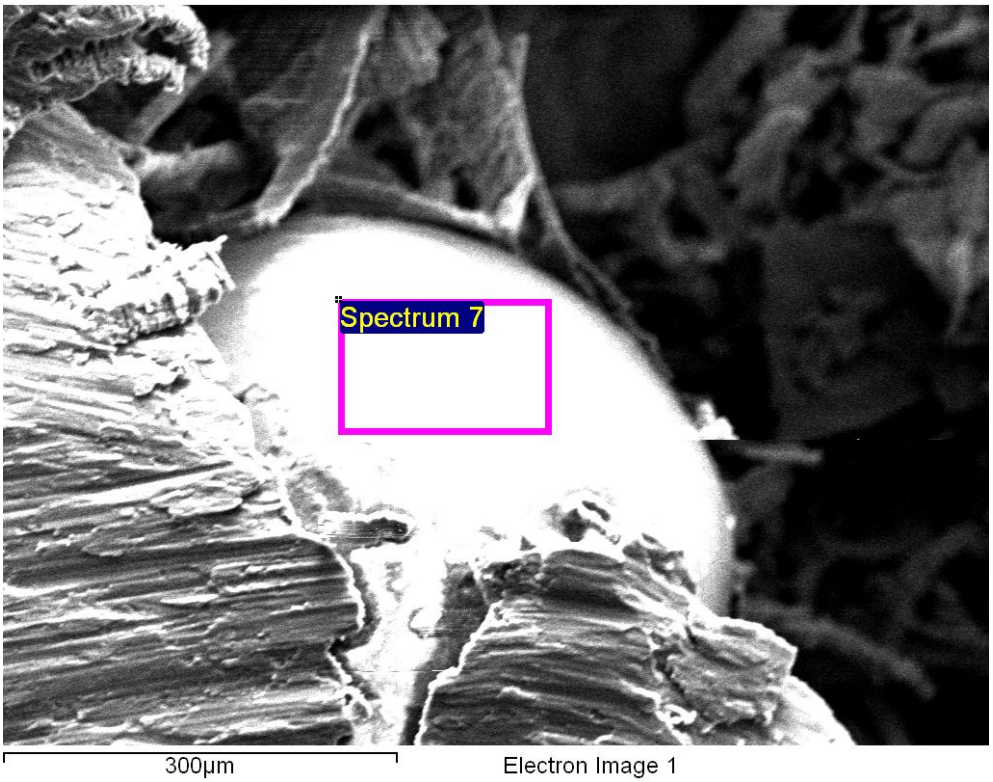

Figure 94. 600 µm particle attached to pore – Area for EDS analysis by %

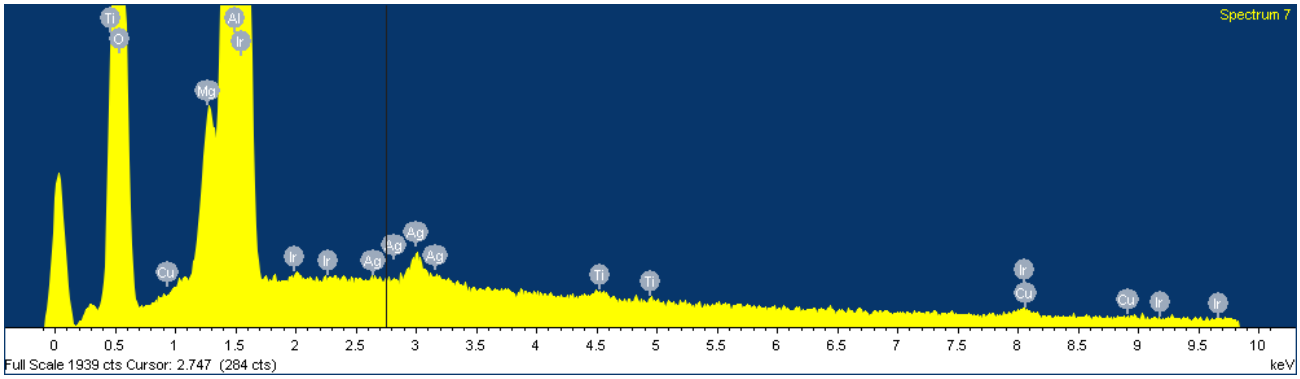

Figure 95. EDS analysis of 600 µm particle

Spectrum processing :
No peaks omitted

Processing option : All elements analyzed (Normalised)
Number of iterations = 5

Standard :
O SiO2 1-Jun-1999 12:00 AM
Mg MgO 1-Jun-1999 12:00 AM
Al 15KV-AL2O3 23-Jan-2012 03:39 PM
Ti Ti 1-Jun-1999 12:00 AM
Cu Cu_20kvpfs 15-Jun-2009 11:42 AM
Ag Ag_20kv pfs 15-Jun-2009 11:37 AM
Ir Ir 1-Jun-1999 12:00 AM

Element	Weight%	Atomic%
O K	35.91	48.86
Mg K	1.48	1.33
Al K	61.33	49.48
Ti K	0.13	0.06
Cu K	0.31	0.11
Ag L	0.84	0.17
Ir L	0.00	0.00
Totals	100.00	

Table 10. EDS analysis of 600µm particle

5.2.2 PET particle distribution in Al plates, cast with a ceramic foam filter

The results of the particle tracking experiment in plate moulds gave some indication of the general path taken by an unhindered particle in a casting utilising a simple running system. Ceramic foam filters are used in industry to regulate the metal flow rate and to remove inclusions, and these are typically located in the running system. An experiment was performed as described in section 3.2.5 to verify the effectiveness of these filters. The experiment consisted of releasing a number of particles, 22 to 33, nearly simultaneously. These were then allowed to travel within the casting and PET scans were made to find the particle's final positions after the metal had solidified.

The first experiment was performed using a 10ppi ceramic filter, this was carried out, 13 minutes after a batch of 33, 200 μm radioactive γ alumina particle's were created. The activated particles had a total radioactivity level of 4.96 mCi at the time of production. After introduction of the particles the casting was allowed to freeze and was then sectioned into its downsprue, filter and cast plate, as shown in Fig 44 from section 3.2.5. The cast plate was scanned in an ADAC positron camera, one hour and ten minutes after the particle's had been created.

At the time of the start of the scan 30399 Line Of Response (LOR) events occurred per second at a calculated activity level of 3.569 mCi. At the end of the scan 1 hour 23 minutes (5000 seconds) later, this had dropped to 21114 events per second at a calculated activity level of 2.108 mCi. Given the time difference the radioactivity will have decreased significantly (0.76 of a halflife) during the time taken to perform the PET scan and it was anticipated that the count rate measured by the ADAC camera would drop to (30339 counts * 0.5^0.87) = 16594 events per second.

It was thought that the radioactivity in each of the sections of the casting could be determined by observing the LOR event rate, if this were true, the LOR event rate would track with the activity level and it would be possible to calculate the time taken for the scan from the LOR event rate at the start of the scan and the end of the scan which should match with the measured time to make the PET image.

The time taken from the start and end count rates was calculated;

$t = t_{half} /(Ln(2)/Ln(No/Nt))$ Eq. 45.

where

t = time
t_{half} = halflife of isotope (109.77 Minutes for ^{18}F)
No = Initial value of LOR Events
Nt = Final value of LOR Events

t=6586.2/(0.6931/Ln(30339/21114))
t= 3445 s
t = 57 Min 25 Sec

From the calculation, the scan took just under one hour, where in reality it was over an hour and twenty minutes (5000) seconds, this indicates that there is a poor correlation between the LOR event rate and the real activity level.

The side profile image of the downsprue (Fig. 97) gave 3616124 events, a total of 12013.701 events per second.

The data from the plate in experiment 1 was re-processed with an acceptance angle of 20 degrees in order to yield an image allowing the radioactive particles to be manually counted.

Twelve particles can be seen in Fig. 96, which indicates the number of particles discernible from the image, it may be possible that more than one particle was located at an image radioactivity hot spot. It must therefore be taken that the count of particles is the minimum number present and cannot be taken as a definitive value. The same process was then applied to the downsprue, both in side profile and from the front.

The image from the side view shown in Fig. 97, was generated from a scan taken over a period of five minutes, 153 minutes after the particle's creation and gave the following statistics : 12122 events per second at the start of the scan and 11696 events per second at the end of a five minute scanning period. Using the same method to predict the scanning period from the start and end count rates gave a time of five minutes and thirty nine seconds which was 39 seconds longer than the actual time taken for the scan.. Manually counting the particle's in this image gave a minimum of nine particles which could be observed.

The process was repeated for a second scan of the same downspue (Fig 98), and this time the scan performed was the front elevation. This second scan of the downsprue was performed over six minutes and had a count rate of 11323 events per second at the start of the scan and a count rate of 10856 events per second at the end of the scan, giving a calculated scan time of 6 min 40 seconds. It was not possible to determine the number of particles in image Fig. 98 due to blurring of the image, as some of the particles were offset from the 491 mm backscatter plane, but from the other view of this part, there were at least 9 particles present.

The filter section of the casting was scanned in the ECAT 3D PET scanner and this was performed approximately two hours and forty minutes after particles were created. This created a series of 47 tomographic images. Each image represented 256mm x 256mm of space in the XY plane. Each image was separated from the next by 3mm in the Z direction. The XY images were then combined with data displayed in the ZX and ZY planes, the ZX data was positioned above the XY image and the ZY data to the right of the main XY image. The scaling of these ZY and ZX images is 3:1. The separation between pixels in the Z

direction was 3mm, but was 1mm in both the X and Y directions. Forty seven images were created for each filter scan with the XY plane image replaced for each image in the series. Fig. 99 shows just one of these images from the first scan., The scam duration was 10000s, and showed particle positions within the filter. The scan in Fig 99, was taken from a series of scans, which when stepped through one by one, showed at least 9 particles to be present in filter.

A second experiment using a 20ppi filter was performed using a set of 22, 200μm activated alumina particles with a total radioactivity level of 3.27 mCi at the time of their creation. The casting was made six minutes after the production of the particles at which time they had a calculated activity level of 3.148 mCi.

The first scan from this casting (Fig. 100) was made 11 minutes later (17 minutes after particle production) with a calculated activity of 2.937 mCi. The plate imaged in Fig. 100 showed at least 8 radioactive particles and had an initial event count of 14888 events per second and this dropped to 11934 events per second forty four minutes (2600s) later, with a calculated activity for all 22 particles of 2.22 mCi. When the decay time was calculated back from the count rates it was found that the decay was predicted to have taken 35 minutes.

A second scan, see Fig. 101, was performed immediately after the first, (61 minutes after particle production). The radioactivity had decayed somewhat and this scan showed the plate itself in more detail, allowing its edge to be detected within the image. The scan was performed to determine if rotating the sample had any effect upon the image generated, and the plate was rotated 90^{o} before the scan was performed (It did not need rotating prior to reporting here, unlike the other scans in this section). This scan took seventy four minutes but

was calculated to have taken almost seventy one minutes, the error in the calculation seems to decrease with the decreased activity of the sample and may represent the “dead time” of the detectors.

A scan was made in the ECAT scanner of the filter from this second experiment (Fig 102), this was performed 17 minutes after particles were produced and was carried out over 300 seconds. It showed at least 9 particles lodged in the filter. A second scan was made immediately after the first (22 minutes after particle production) for the shorter duration of sixty seconds (Fig. 103). In Fig. 102, recorded over 300 seconds it was possible to discern 9 particles, in Fig. 103 recorded over 60 seconds it was only possible to make out 7 particles clearly.

The third and final experiment was performed using a 30ppi ceramic foam filter and used a set of 33 - 200μm activated alumina particles of total activity 2.13 mCi. The PET scan of this experiment (see Fig 104) was made 58 minutes after the particles had been created and had a duration of 67 minutes. The count rate at the start of the scan was 1675 events per second and had dropped to 1159 events per second at the end of the scan. The expected duration of the scan calculated using the start and end counts was just over 58 minutes giving a less significant error compared to PET scans performed earlier after particle production.

It was possible to identify 12 particles in the plate shown in Fig. 104, 11 along the top edge of the plate and one lying against the top edge of the running system overshoot. The plate itself was visible (probably due to scattering at a lower total activity level). The particles were weakly radioactive compared to the scans from the previous two experiments which gave a better signal to noise ratio.

Scans were made of the filter from this third experiment in the ECAT 3D PET scanner. The first of these was performed one minute after the PET scan of the plate from the experiment (~ 2 hours after particle production). Two scans were made, the first of 300 seconds duration and the second immediately afterwards of 500 seconds. The first scan, see Fig. 105, showed 6 (possibly 7) particles in filter, the second scan see Fig. 106 which was of a longer duration showed the 'possible' seventh particle in more detail, Fig. 106 shows the frame from the second set of 47 images in which this particle (near the centre of the XY image) is visible.

Five PET scans were made using the same ^{22}Na particle in order to provide a reference count rate at a known activity level, so that the radioactivity levels of the previous scans could be determined. The first of these was at the back right of the scanned area at the location 281,378 in XY co-ordinates (see Fig. 107). This scan showed almost no change in the count rate during the scan. It recorded 21.822 events per second on average, which was 0.122 events per second at a one degree acceptance angle. An image with the particle at the back right, (Fig. 108), at XY location 179,374, gave 25.59 events per second average with 0.176 events per second at one degree acceptance angle. When the particle was moved to the front left of the viewing area (176,235), (Fig. 109), 35.783 events per second average were recorded which corresponded to 0.129 events per second at one degree acceptance angle. At the front right (284,232), (Fig. 110), gave counts of 21.822 events per second and 0.139 at one degree acceptance angle were found. Finally the ^{22}Na particle was positioned near the centre of the viewing area (231,308) (Fig. 111), and gave an overall reading of 91.026 events per second and 0.254 at one degree acceptance angle.

Knowing the activity of the reference particle, it is possible to calculate a radioactivity level for the images recorded based upon the count rate. Due to the variation in the count rate from the reference images a maximum and minimum activity level were calculated. A small acceptance angle (1^o) was used to filter the count prior to calculation to minimise the effect of errors in the count rate due to the geometry of the detectors.

The reference ^{22}Na particle was measured to have an activity of 0.70 μCi (0.26 mBq), (however the Capintec^{TM} ionisation chamber which was used to measure this activity is prone to error at very low activity readings). The Na^{22} source was originally produced on January 1st 2006 when it was measured to have an activity of 4.59 μCi (170 kBq). There were 2147 days between the production of the source and when it was used as a reference for these experiments. ^{22}Na has a half life of 951 days so this represents 2.26 half lives, meaning that 0.208 ($0.5^{2.26}$) of the original 4.59 uCi of ^{22}Na remained, this means the activity of the reference source was 0.95 μCi. Since the calculated value was measured in a manner less prone to measurement error, it was this value that was used in the calculations of the activity levels for the PET scans.

The count rate value at 1^o acceptance angle therefore varied from 0.122 to 0.254 events per second average depending upon where on the scanning table the ^{22}Na particle was placed, It is therefore only possible to use this reference to provide a worst case and a best case possible for the activity of a PET scan. The lowest count value from the reference source was 0.122 counts per second, the maximum was 0.254 counts per second, both at 1^o acceptance angle, these correlating to 0.95 μCi, If the low value was 0.122 events per second then one event per

second is equivalent to 7.786 μCi. Conversely, a high value of 0.254 counts per second means one event per second was equivalent to 3.74 μCi. The count rate average of 134.823 counts per second from the first scan (Fig. 96) was then used to calculate a maximum and a minimum of the activity from the particles that had collected in the plate. A program using a numeric integration of the decay exponential was used to convert from the average value of 134.823 counts per second to the value at the start of the scan, 227.6 counts per second at 1^{o} acceptance angle. This corrected value was used to calculate the maximum and minimum possible activities at the start of the scan, being {227.6 * 7.786} 1772.1 μCi and {227.6 * 3.74} 851.2 μCi, respectively. The scan had been performed 70 minutes after the particles creation (coincidentally almost exactly a ^{18}F half life) so these figures double to 3544 μCi and 1702.4 μCi respectively. This implies that between {3544/4960 * 100} 71.4% (maximum and {1702.4/4960 * 100} 34.3% (minimum) of the tracer had made its way into the cast plate.

There were two scans of the running system, the first gave an average count rate of 50.628 and the second 45.293 at 1^{o} acceptance angle. After correction to give the count rate at the start of the scan, The error caused by using a direct average of the total event count can then be compensated for, again using a numerical integration for F18 decay which was adjusted until the average count rate matched. The values become 52.25 and 47.05, respectively at the start of the scans. Converting these count values to activity levels gives {52.25 * 7.786} 406.82 μCi (maximum) and {52.25 * 3.74} 195.42 μCi (minimum) for the 1^{st} running system scan and {47.05 * 7.786} 366.3 μCi (maximum) and {47.05 *3.74} 176.0 μCi (minimum) for the 2^{nd} running system scan. These activity values were then adjusted to give the activity of the particles in the running system at the time the particles were created. The first running system scan was performed 2 hours and thirty three minutes after the particles

were created, giving a maximum activity of 1069 µCi and a minimum of 513.5 µCi. The 2nd running system scan was performed 2 hours and thirty eight minutes after particle creation and gave a maximum activity level of 993.4 µCi and a minimum of 477 µCi. The results from the two running system scans were both close to a minimum of 500 µCi (10.1% of the total tracer) and a maximum of 1000 µCi (20.1% of the total tracer).

It should be possible to find the minimum initial activity for the particles trapped in the filter by subtracting the maximum activity of the plate and the running system from the initial total activity { 4960-(3544+1000) } 416 µCi, (8.4% of the total tracer activity) . The same can method can be used to find the maximum initial total activity of the particles by subtracting the minimum plate and running system activity from the initial overall activity { 4960-(1702+500) } 2758 µCi, (55% of the total tracer activity)

Due in large part to the large variation in the measurement of the count rate for the ^{22}Na source, the activity values derived, did not accurately predict the distribution of the particles in the different sections of the casting. However when combined with the manual count of the particles from the PET images it was possible to say that some particles were trapped in each section. The particle counts indicated roughly that 1/3 of the activity was split between the plate, filter and running system. In any case the filter efficacy at removing inclusions, was shown to be less than 60% even for these large (600 µm) particles, with little variation seen for the filter pore sizes used.

At a backscatter distance of 391mm, as used in the scans from these experiments, a 2^{o} acceptance angle will, for a point source give a circle with a maximum radius on the generated PET image of 13.65 mm, in which the endpoints of the lines of response were expected to occur, this being the worst case expected. So for an image processed with a 2^{o} acceptance angle it should be able to remove any point source by finding the pixel with the most events, then setting it and all other pixels within a 13.65 mm radius to zero. This removed the brightest pixels and reprocessing the contrast of the image using the next brightest pixel as the maximum and scaling all remaining pixels to the new value was intended to allow difficult-to-see particles to come into view. By successively repeating this process the particles were removed until a threshold value for the brightest remaining pixel was breached and the process ended.

In practice it was observed there was an increased sensitivity of the PET scanner at the position of the photo multiplier tubes (Fig. 112). The method did not work well as the sensitivity disparity at the photomultiplier tubes made it difficult to detect particles as the ‘contrast’ at low activity levels was increased.

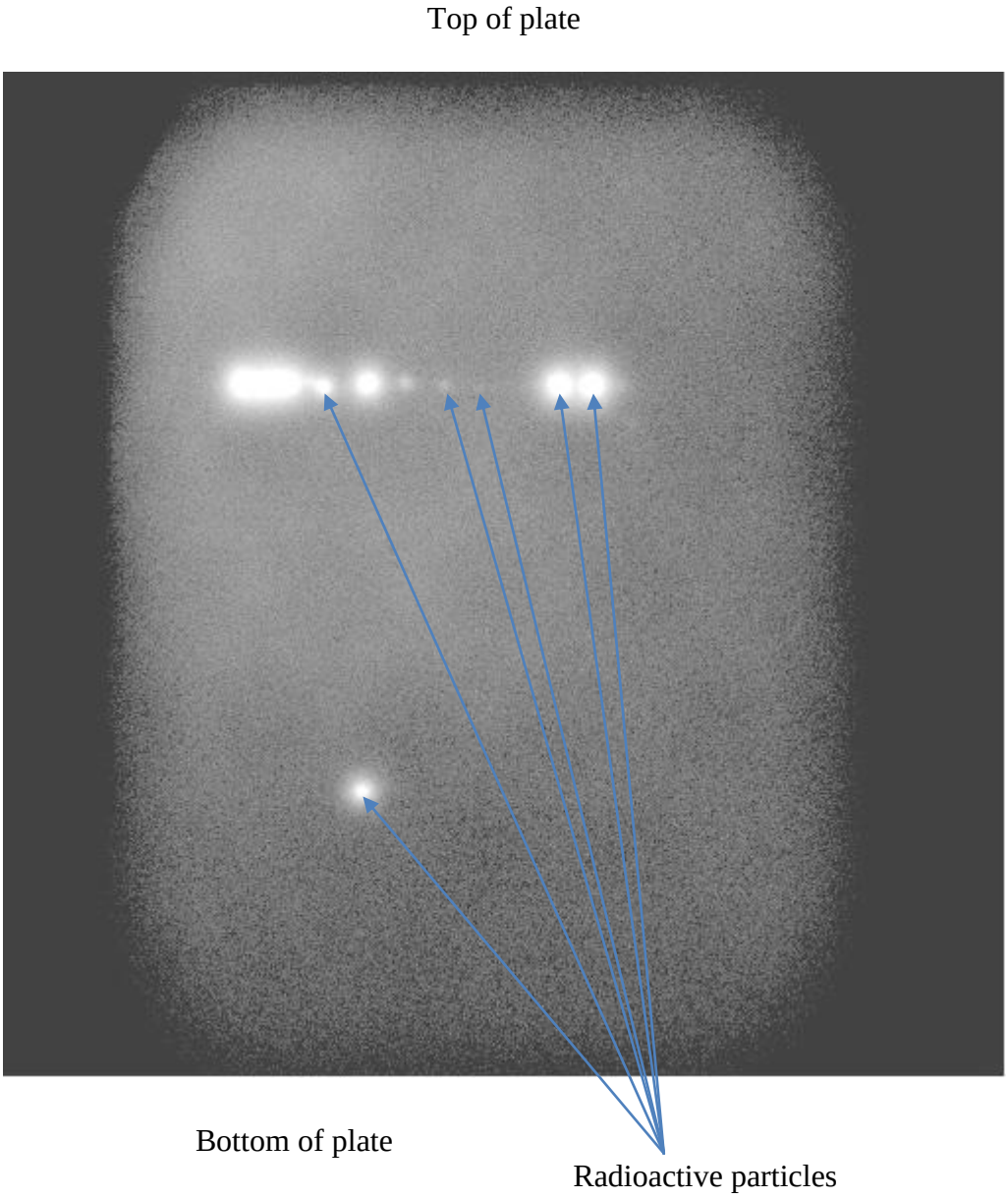

File – cast.da01

Figure 96. PET scan from the first filter experiment, minimum count of 12 particles in casting.

Top of downsprue

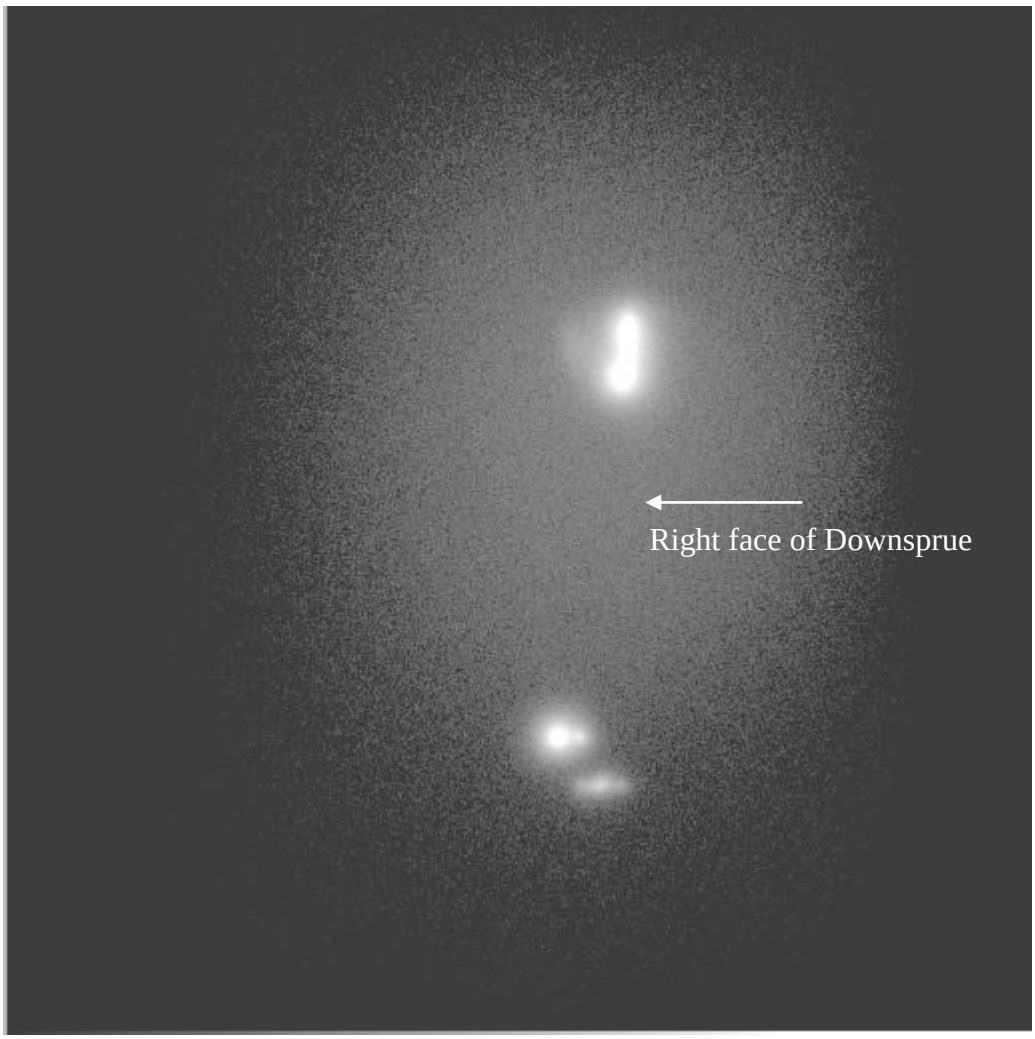

Bottom of downsprue

File – cast.da02

Figure 97. Downsprue Side view (1st Experiment)

Top of Downsprue

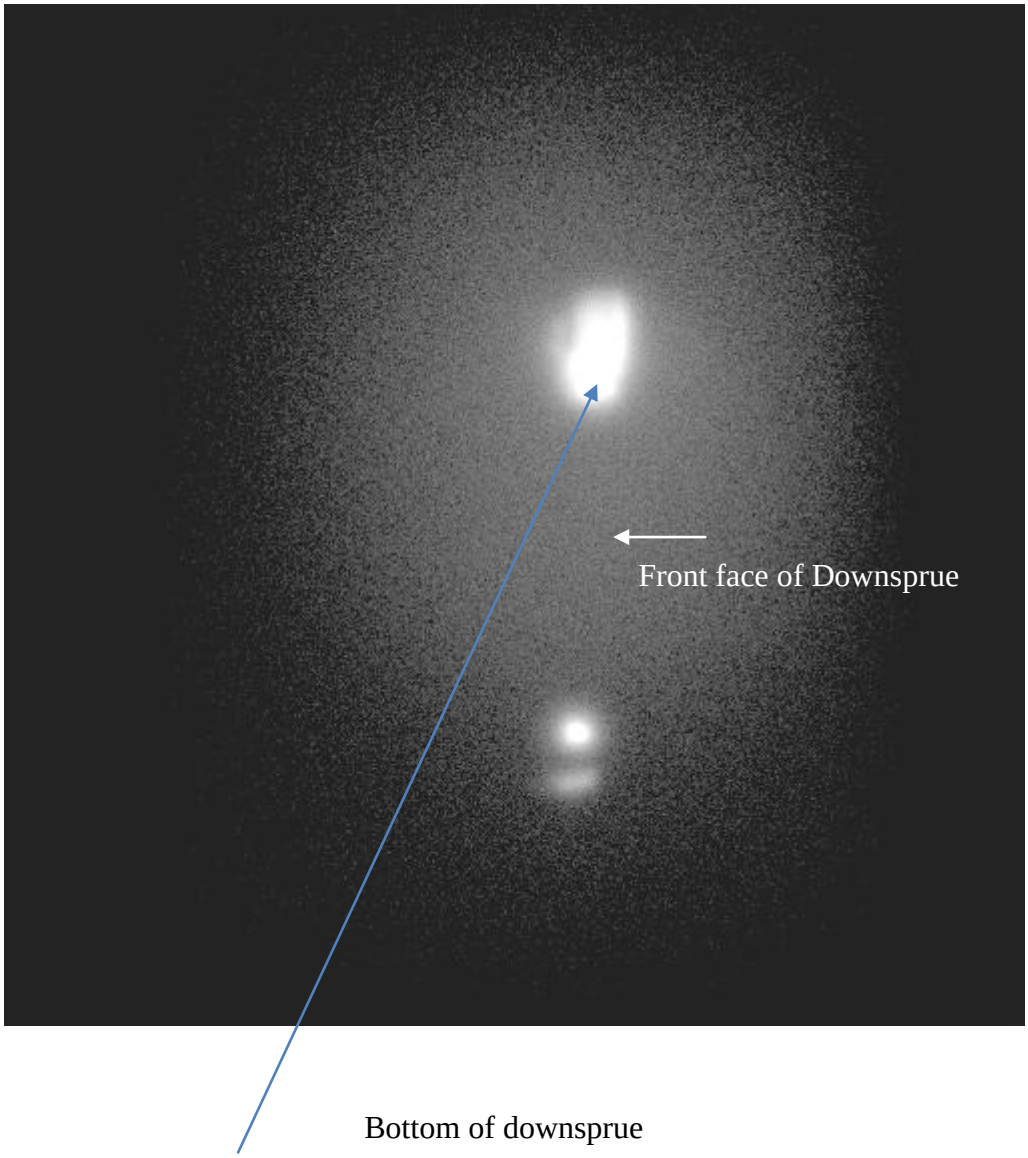

File – cast.da3

Figure 98. Downsprue top view (1st Experiment)

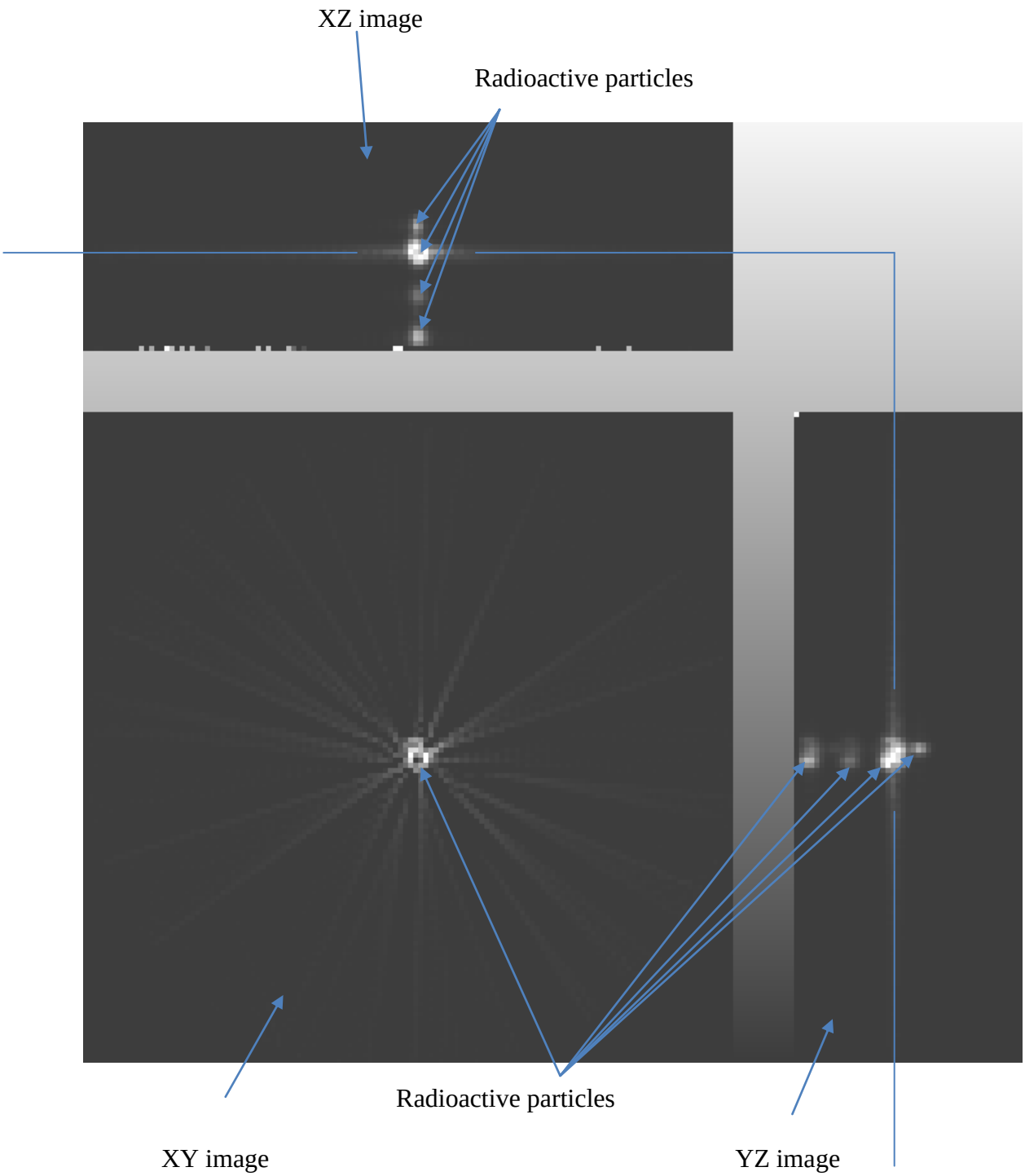

Burnard_23_111_de3 (2nd Experiment) (10000s)

Figure 99. (35) Scan of the filter from the 1st Experiment showing particle locations

Top of Plate

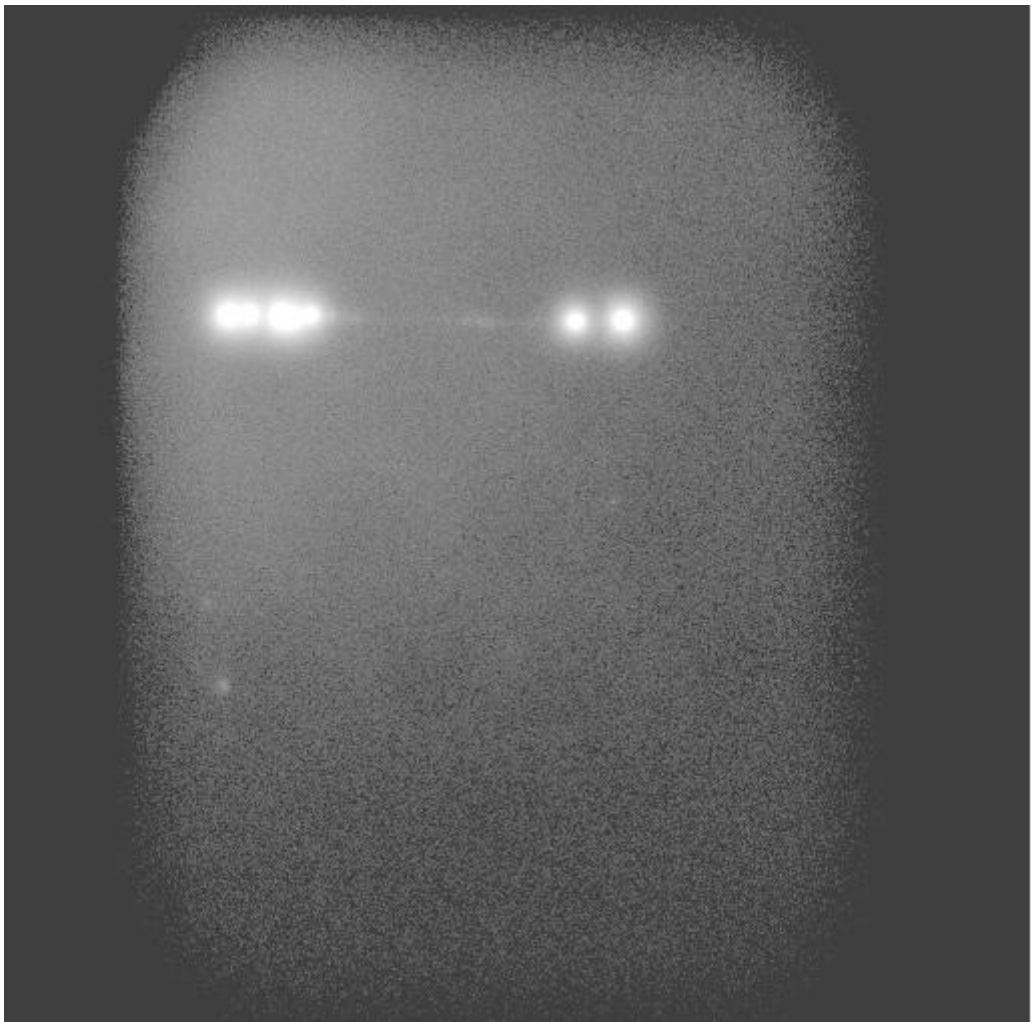

Bottom of plate

File – cast.da4

Figure 100. Scan of plate for 2nd experiment, minimum 8 particles in plate

Top of plate

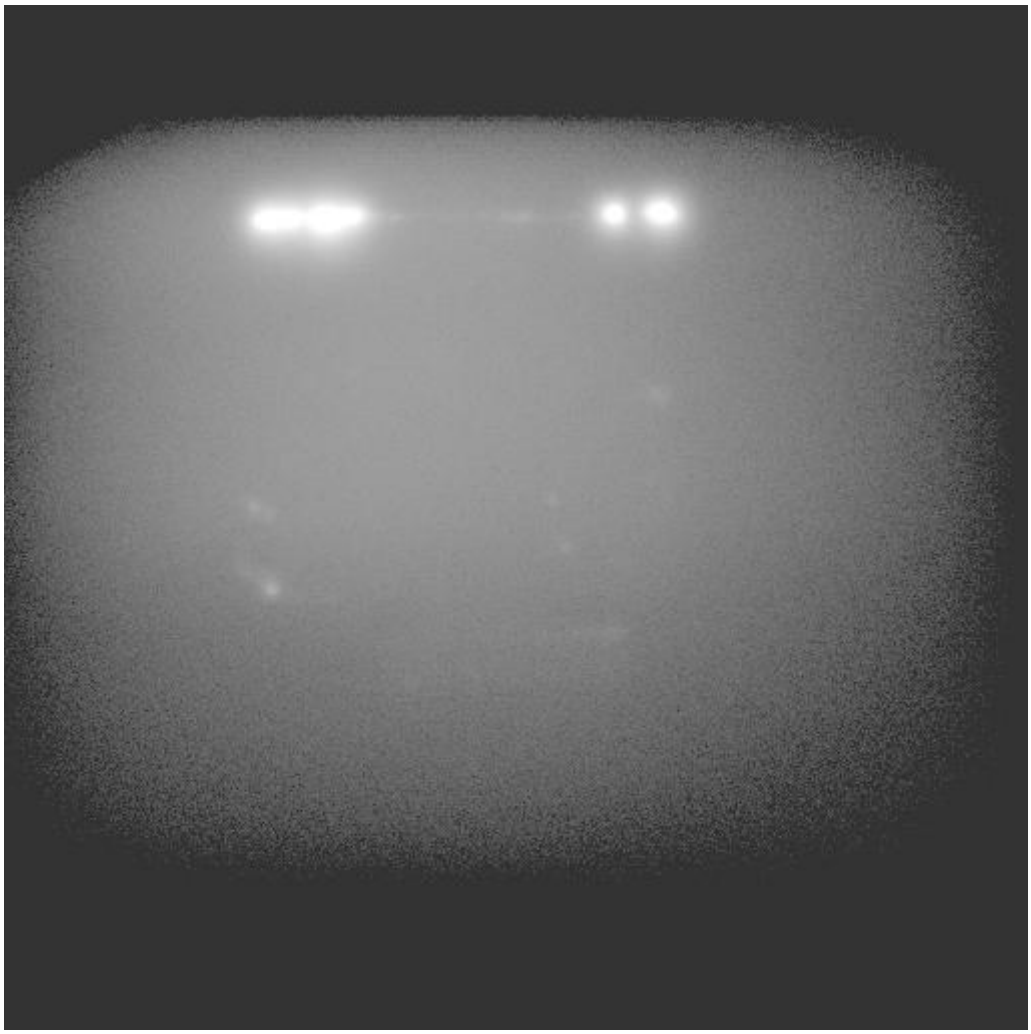

Bottom of plate

File – cast.da5

Figure 101. Later scan of plate from 2nd experiment, miniumum 8 particles in plate

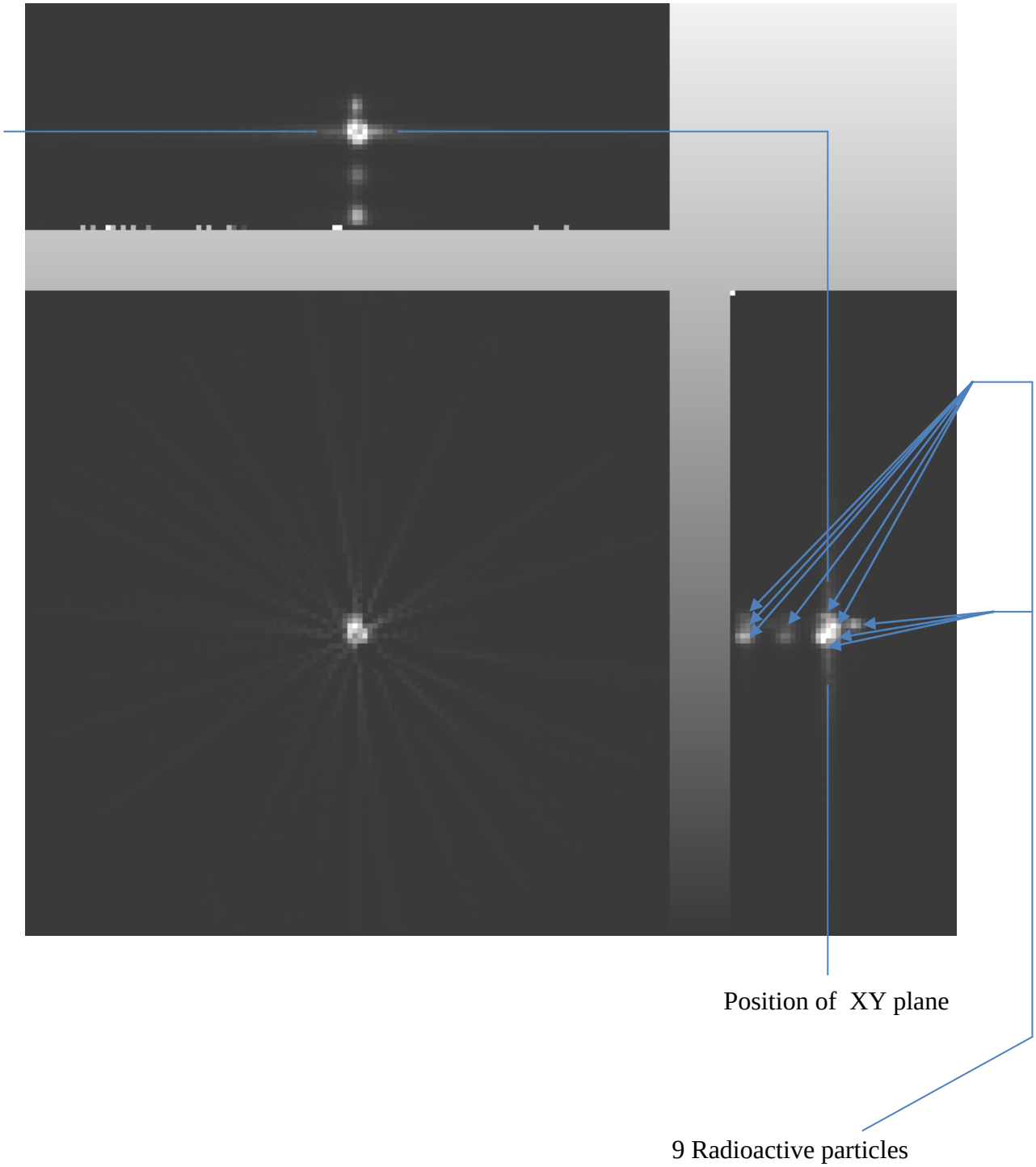

Burnard_23_112_de3.v (300 s)

Figure 102. Filter (2nd Experiment) showing a minimum of 9 particles

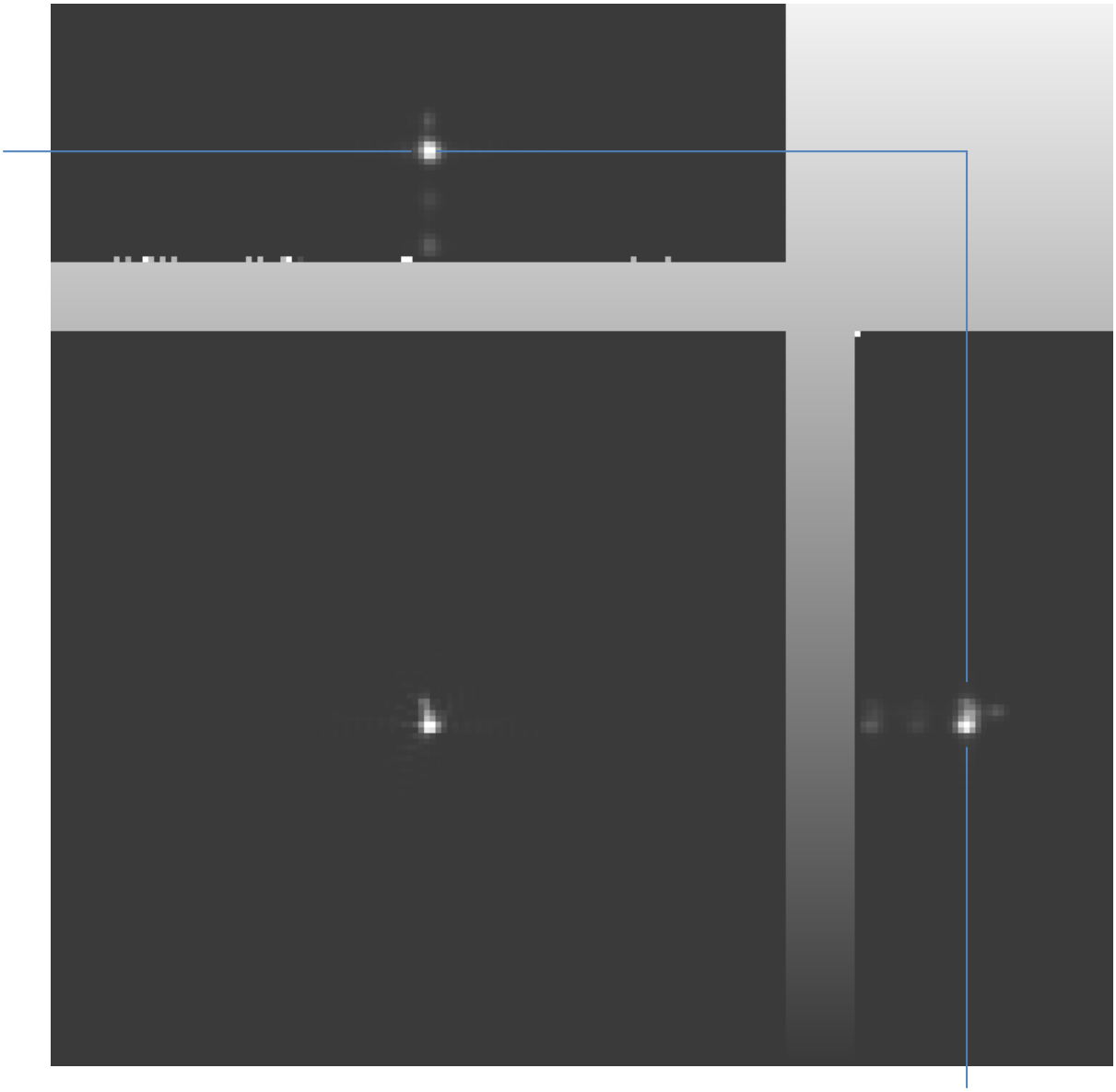

Burnard_23_114_se6.v (60s)

Figure103. Filter (2nd Experiment) shorter scan time, minimum 7 particles

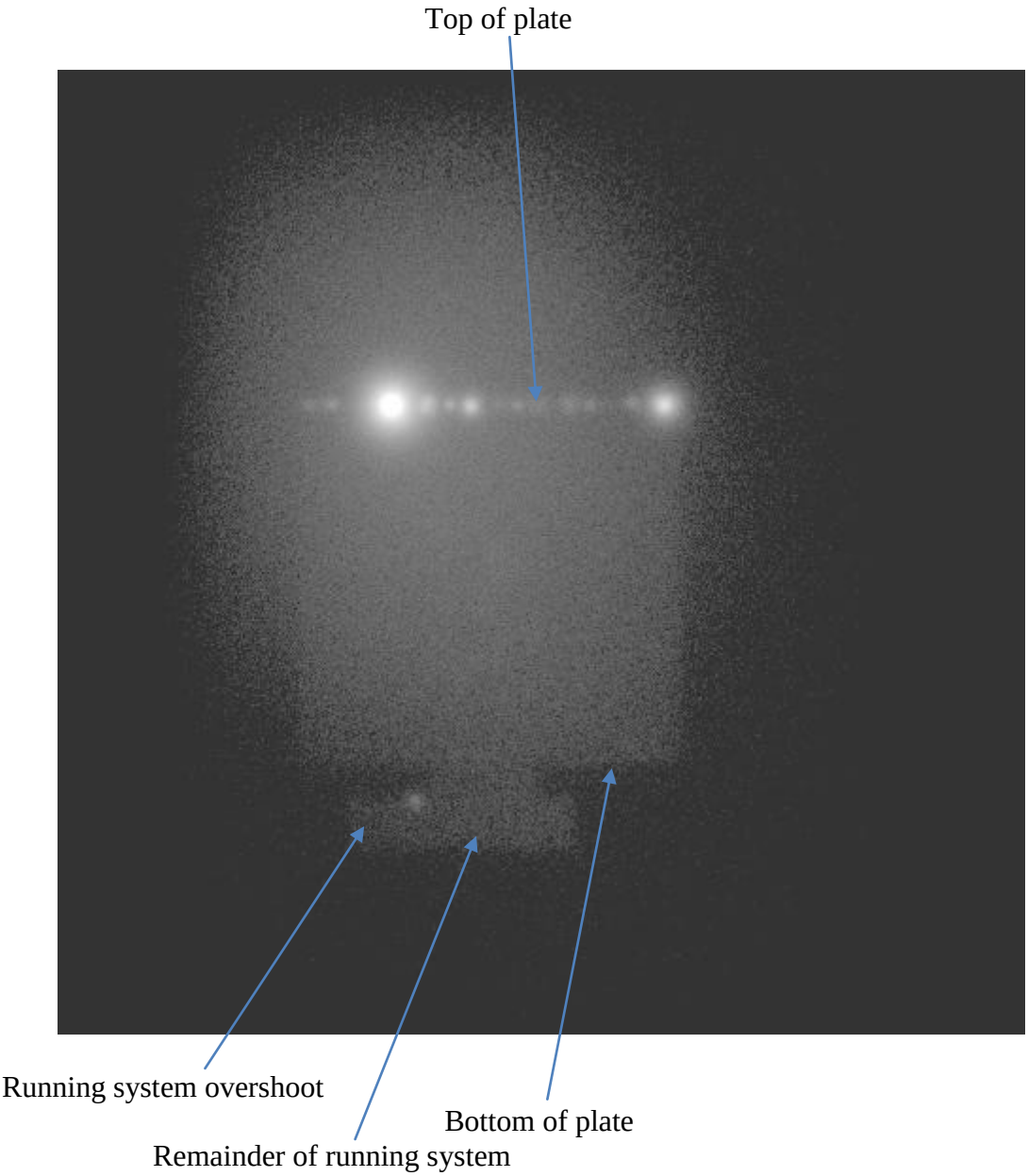

File – cast.da6

Figure 104. PET scan of plate from 3rd experiment.

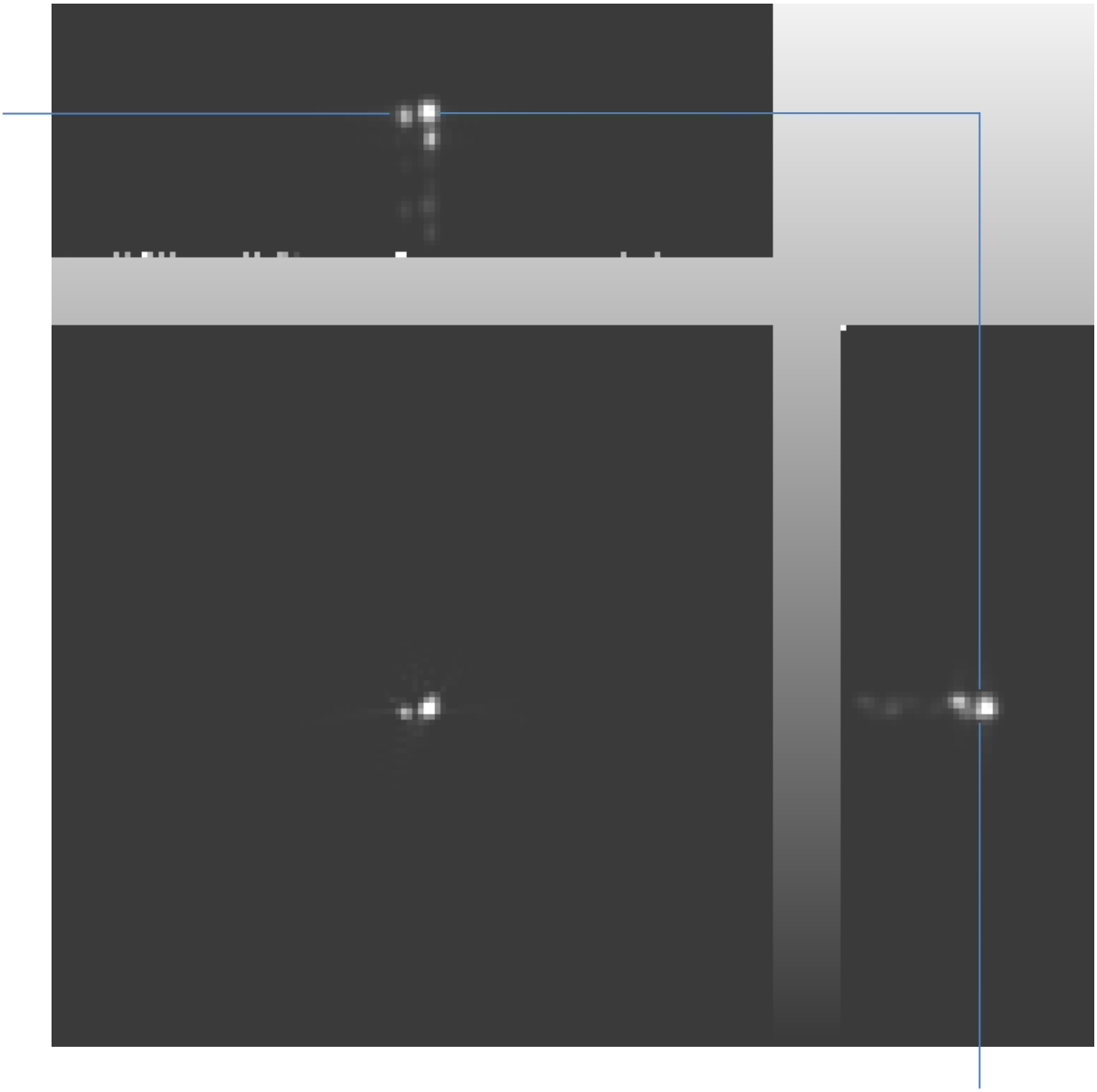

Burnard_23_118_se10.v

Figure 105. 300 second scan of the filter from the 3rd experiment.

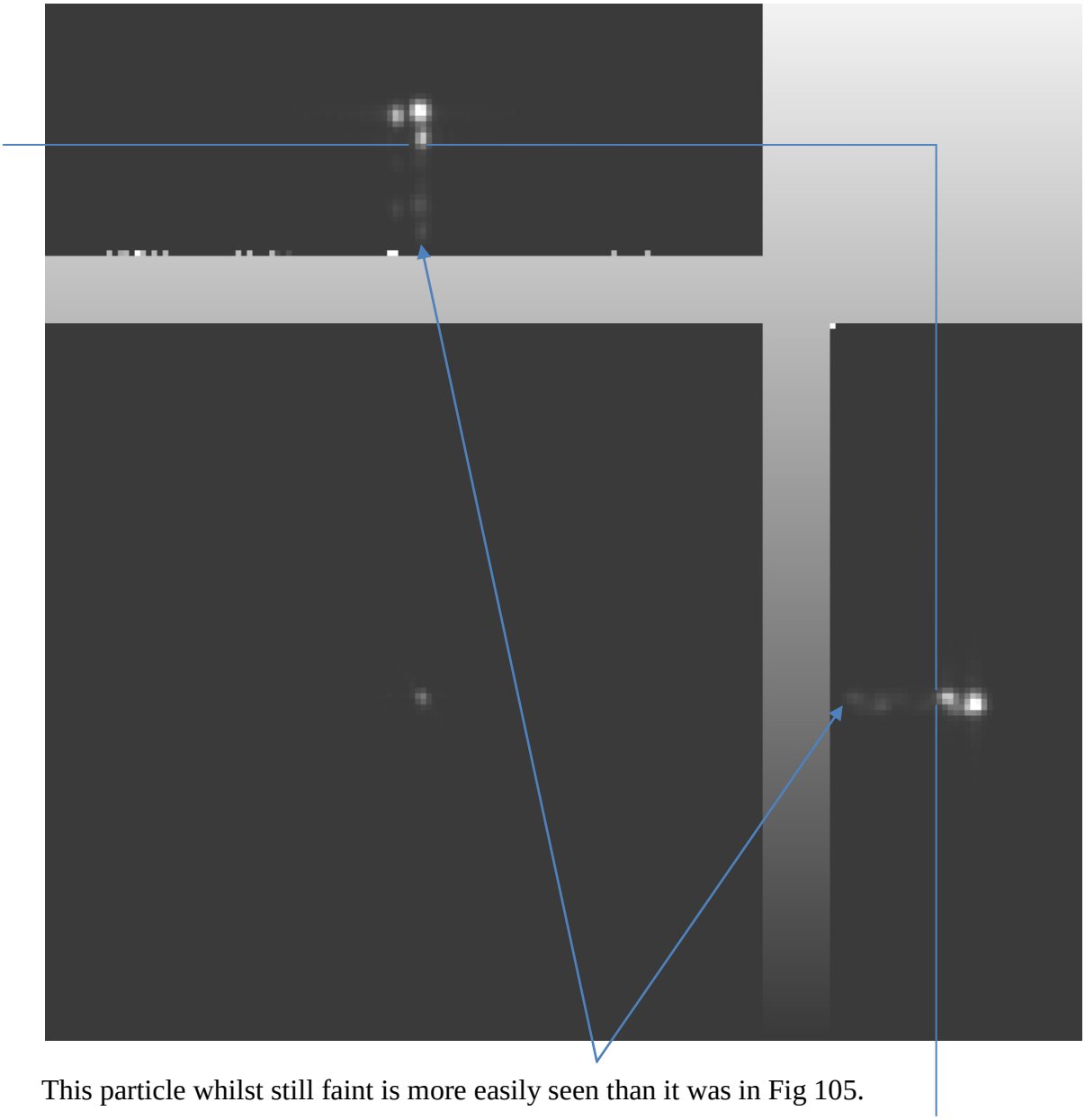

This particle whilst still faint is more easily seen than it was in Fig 105.

Position of XY plane

Burnard_23_11a4_se12.v

Figure 106. 500 second scan of the filter from the 3rd experiment.

Reference scans for calculating activity levels

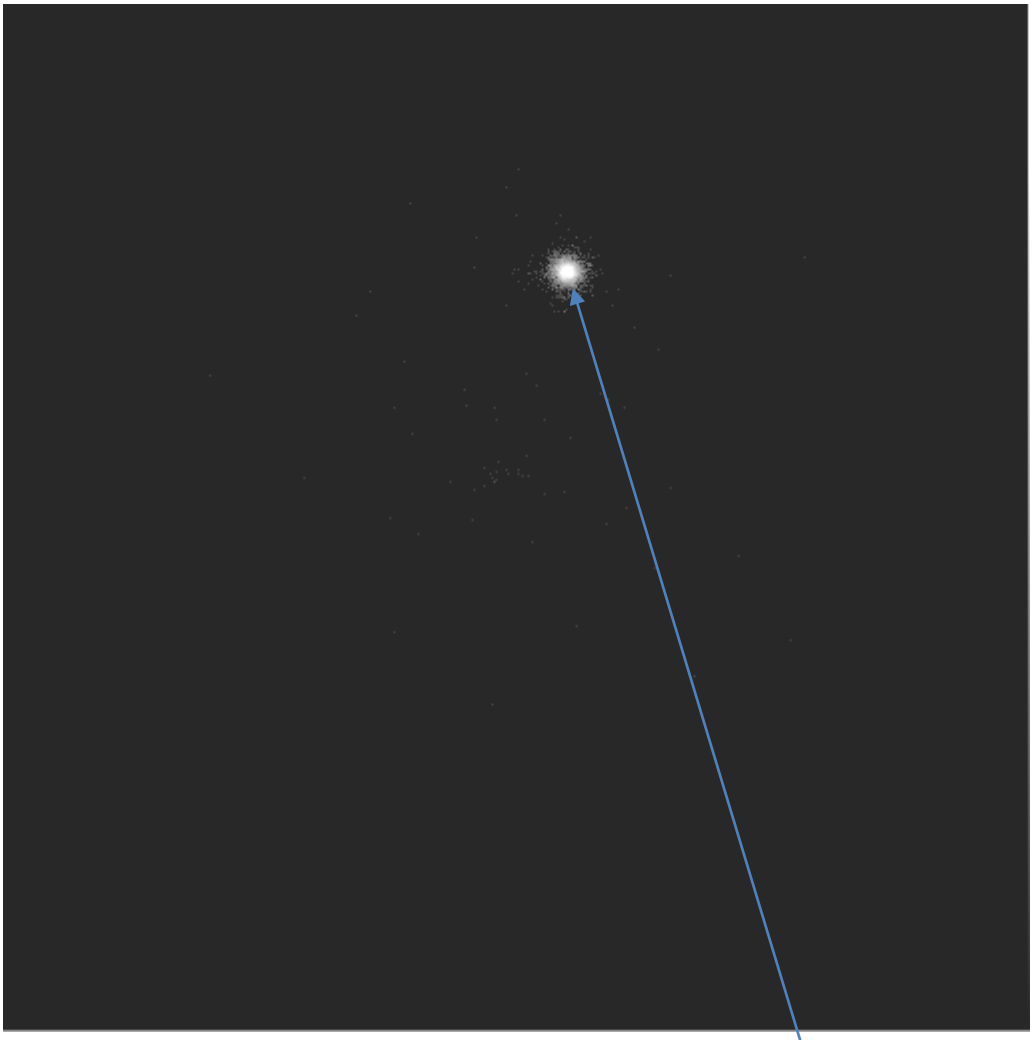

cast.da07 Reference single Na^{22} Particle

Figure 107. Back Right reference position

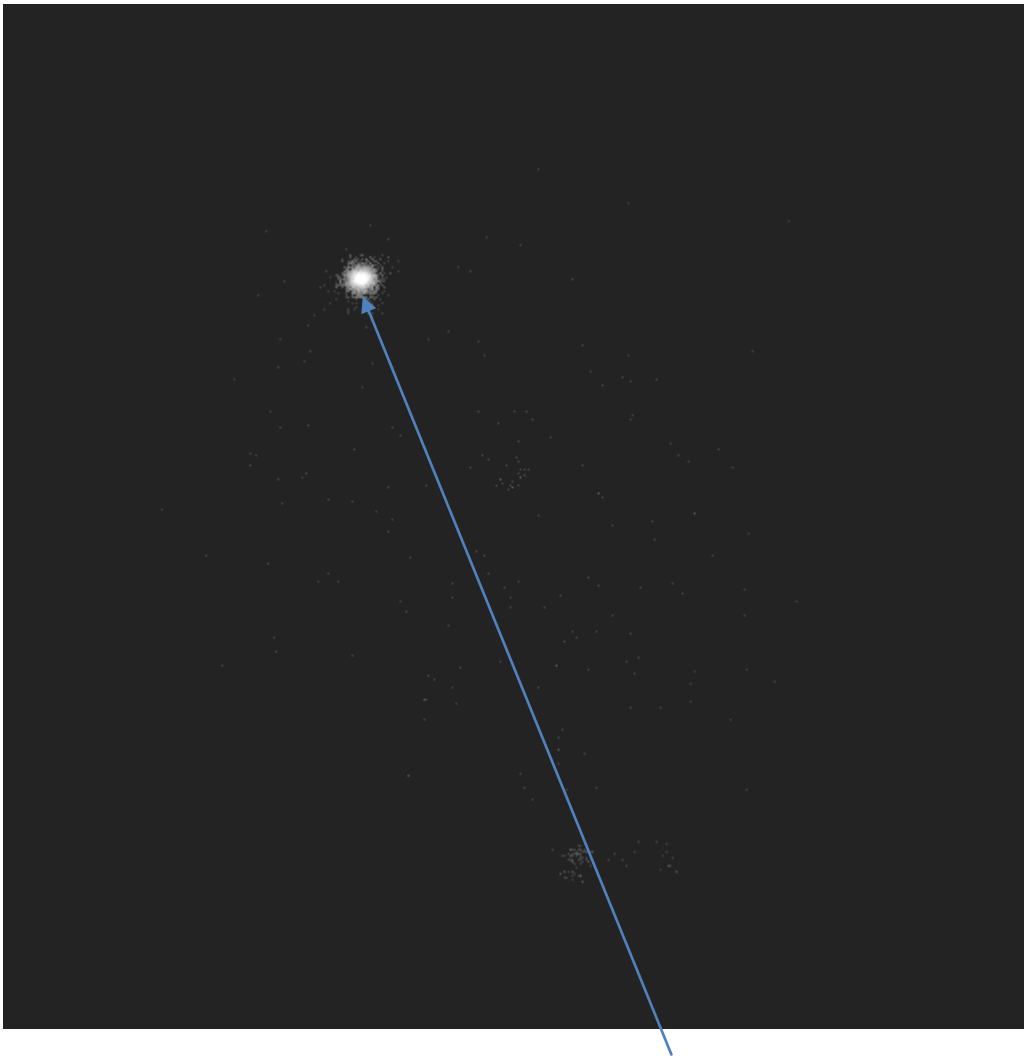

cast.da08 Reference single Na^{22} Particle

Figure 108. Back Left reference position

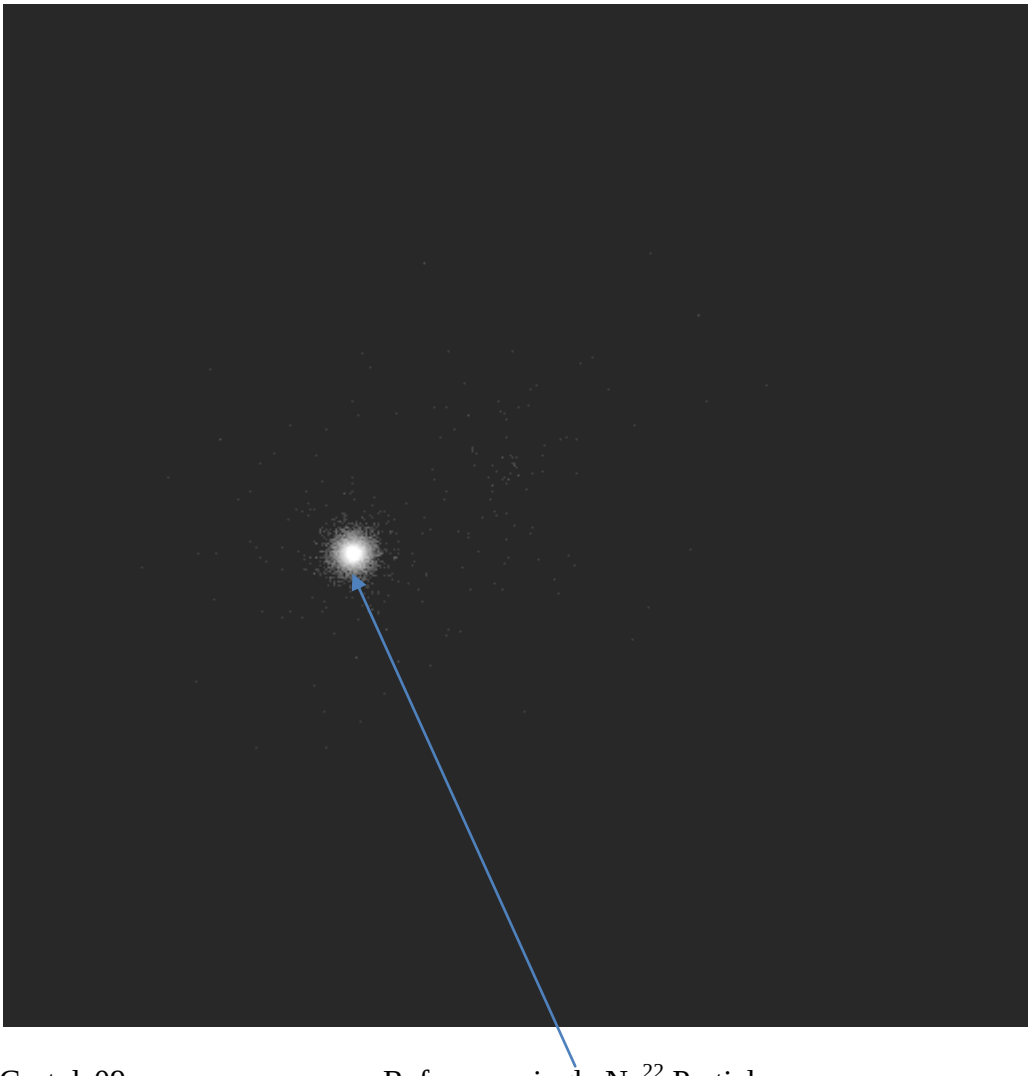

Cast.da09 Reference single Na^{22} Particle

Figure 109. Front Left reference position

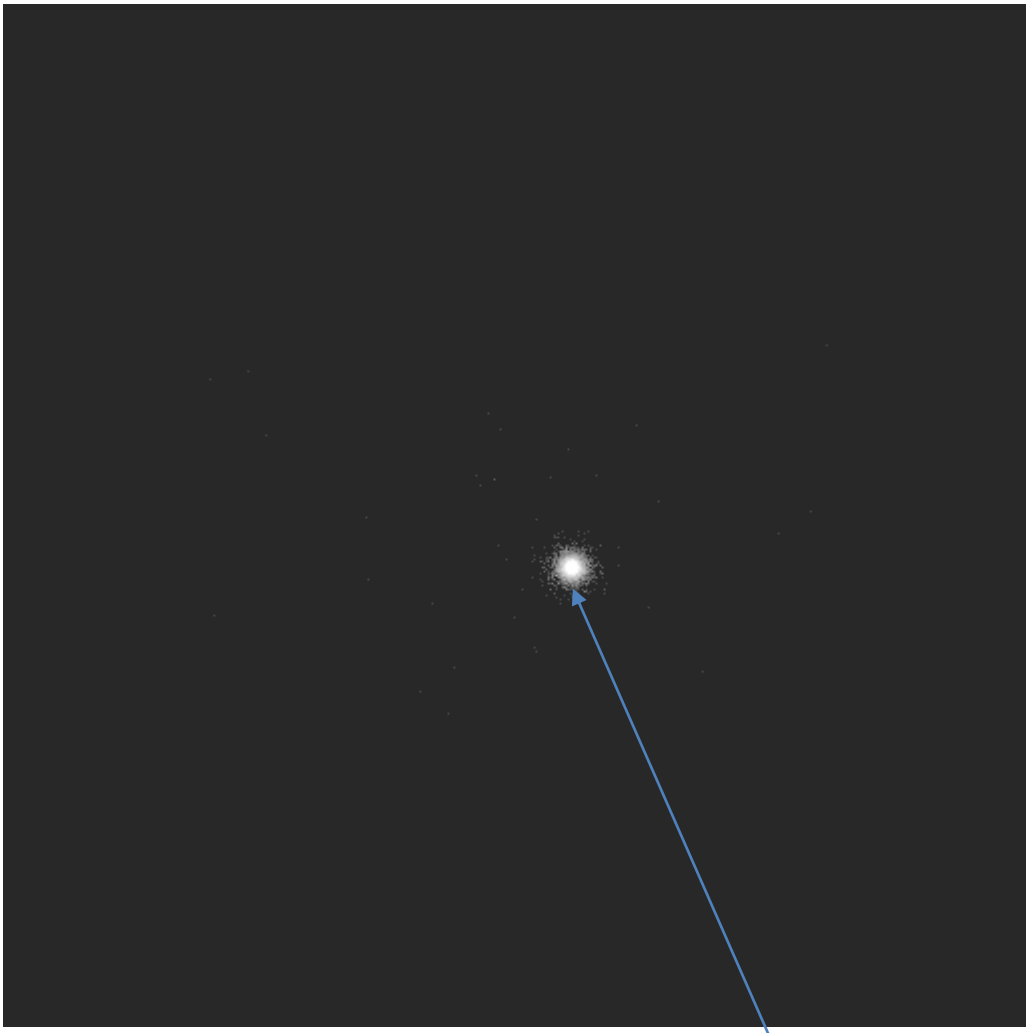

Figure 110. Front Right reference position

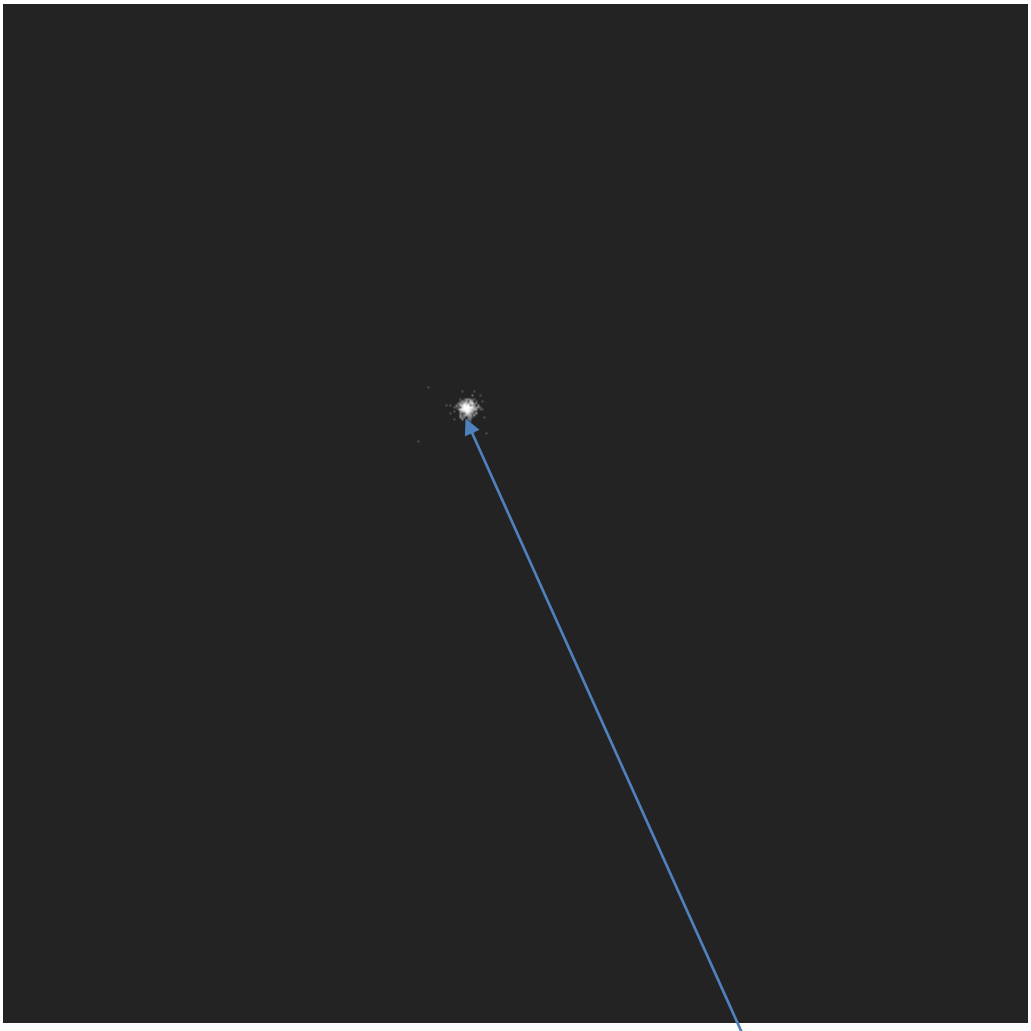

Alplate.da10 Reference single Na^{22} Particle

Figure 111. Centre reference position

Bottom of Plate

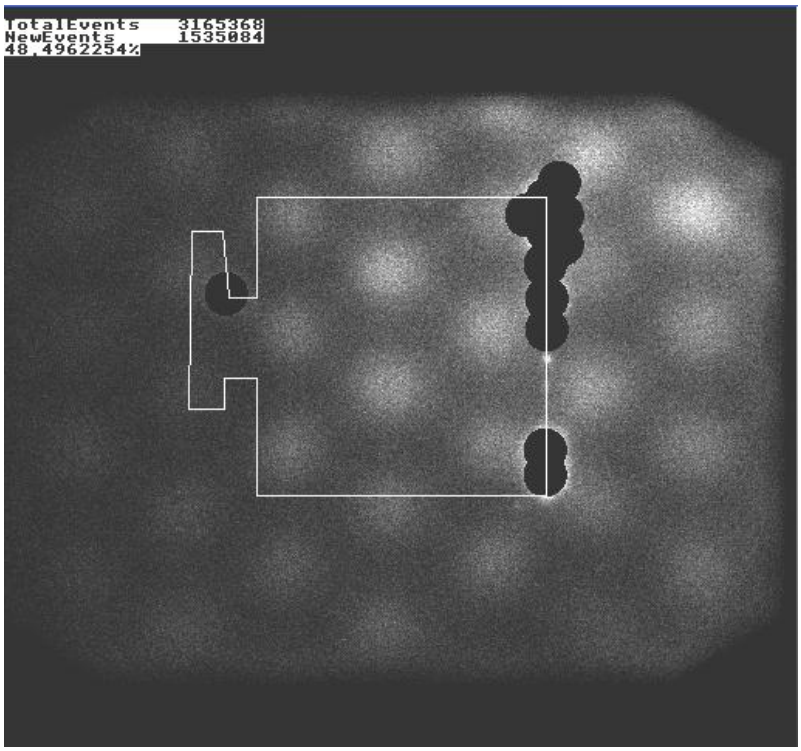

Top of plate

Figure 112. Image from cast.da05 processed by removing particles

5.3 Particle Tracking experiment within a launder

An experiment was performed which used a new geometry for the modular positron camera, in which the modules were arranged in a circle, giving a field of of view up to 223mm diameter. The inner 55mm was continuous, and the camera had a longitudinal view of 700 mm. A launder was placed inside this positron camera and radioactive particles placed inside liquid aluminium were observed as the liquid metal flowed through the apparatus (section 3.2.6. Figs. 48-53).

5.3.1 Tracking 600µm particles in a launder

The objective of the experiment was to track radioactive particles in liquid aluminium and show how inclusions move within the metal. The particles were released into the metal stream as described in section 4.2.6. In the first experiment, the particles were introduced at a depth of 10 to 15mm below the liquid metal surface, which itself was 15 mm below the top of the launder at the point of introduction. This resulted in two out of six radioactive particles successfully being tracked as they moved down the launder.

The first particle tracked, Fig. 113, followed a path which was very high in the metal stream, and it travelled in almost a straight line along the length of the launder, rising as it passed over the baffle. It was noted that there was a short break in the track of the particle between the introduction point and where the particle track was first seen to show particle motion. It was assumed that at least one of the two previously released particles was lodged upstream of the detectors adding to the random events recorded in that area, causing the tracking algorithm difficulties in resolving an accurate location in this area of the launder.

The second successful particle track, Fig. 114, appeared to start some way along the launder, It was assumed that, as for the previously tracked particle, the parameters for the tracking algorithm necessary to display the particle while it was moving were such, that an activity contribution from other particles, which lay upstream of the positron camera, disrupted the tracking algorithm, due to the manner in which invalid lines of response were rejected. The particle path took it from left to right as it approached the baffle, then straight along the longitudinal (z) axis. Again the particle took a path which appeared high in the metal stream and was possibly at the top, on the surface of the metal.

A further four particles were not tracked in the melt as they were not seen to enter into the viewable volume of the positron camera. PET scans were subsequently made of the metal at the end of the launder closest to the furnace, to determine the location of the particles which did not traverse the length of the launder. In order that the particles' locations could be determined relative to the launder itself, the radioactivity from the ^{18}F was allowed to decay for over twenty four hours, such that only a negligible amount of activity from this source remained. The PET scanner was then used with its ^{137}Ce source (662 KeV emissions from its decay product ^{137m}Ba) in order to determine an attenuation map. Since the launder had not been moved between each scan, it was then possible to overlay the images from both scans to form a combined image. The scans for the first two experiments were performed together (Fig. 116) by placing one launder on top of the other. The image from the scan showed particle(s) from the first experiment resting near the bottom of the solidified melt.

The second experiment, with a particle introduction depth of 30mm below the top of the launder (see Fig. 115), resulted in none of the particles, out of the six introduced being tracked through the length of the launder. The tracking image showed many possible particle locations at the furnace end of the launder, most probably the result of a large number of random LOR events with no 'real' events recorded to correct the erroneous particle location.

The scan of the particle introduction area for both experiments was conducted as a single 141mm long 3D scan (see Fig. 116), consisting of 47 images with the launder from the first experiment placed on top of the launder from the second experiment. This indicated at least some of the particles had adhered to the launder wall, in both cases, prior to entering the field

of view of the positron camera, presumably whilst the metal was flowing as some of the particle(s) were above the height of the solidified metal.

A third experiment, with particles at release depths of from 20 mm to 40 mm below the particle introduction block (see section 3.2.6. Fig 54), resulted in a single particle track being observed, from the last particle released at a depth of 40mm. This track was again broken at the beginning near the furnace end of the launder. The particle was seen to rise quite sharply from its introduction location, about 150mm before the baffle, before travelling high in the metal stream, exiting the launder ~15mm to the right of the centreline.

The fourth and last experiment had all the particles released at 40 mm depth (from the top of the launder) and six out of eight particles released traversed the launder length. It was not clear exactly when the particles were released from their host aluminium rods, as they were pushed into the melt. The success rate of the release mechanism increased with increasing insertion depth, possibly due to particles rising as was suspected in the previous tracking experiment in section 5.2.1. When a particle did not successfully enter the main bulk of the metal stream it was found that it was trapped at the same end of the launder as where it was introduced. The particle release area was outside the viewable volume of the positron camera and the particles' behaviour could not be observed in this region.

The first particle in this experiment, (Fig. 118), started on the left hand side and made its way to the centre of the metal stream as it traversed the length of the launder. The initial data showing the particle moving to the left hand side of the channel may be slightly misleading as the particle was emerging from the radioactive noise from other particles in the introduction

area. This motion to the left occurred, but whether the particle took the sharply angled path shown is debatable. The 2nd particle introduced, (Fig. 119), followed a similar path to the first with the same caveats and possible errors, and both followed a path very high in the metal stream, despite the lower depth that the particle introduction rods were pushed into the metal. The third particle, (Fig. 120), introduced, traversed along the centerline of the launder, high in the metal, before its track was lost about 75mm in front of the baffle. The fourth run was again very similar to the first two and this particle was again close to the surface of the metal. The fifth particle tracked was another which failed to track further than 100mm from the baffle face, and appeared to stop mid-stream, in a similar manner to the third particle. The sixth particle tracked was another which failed to track further than 75mm from the baffle face, along the launder, and the path taken was not very clear and was possibly due to a particle stuck in the melt from an earlier run (possibly particle 5). Particle 7 (Fig. 121) did not show a trace until it had passed the location indicated as the final location for particle 6, after this position it tracked along at a high level, passing over the baffle and dropping with the level of the metal stream. Particle 8 behaved as particle 7 did, and did not show a trace until it had passed the location indicated as the final location for particle 6. After this position it was tracked in a similar manner as particle 7, except for some small deviations to its path as it approached the baffle.

After all the available insertion rods had been used from the introduction block, some additional rods were still available. These had been shortened so that they could be deposited on the top surface of the metal stream and would not foul on the sides of the launder. Three out of the four particles inserted in this manner were tracked as they travelled down the launder. (Fig. 122), the rods being placed on the surface of the melt. Hence, other than the intial dip as one particle was presumably pushed under the surface by turbulent flow in the

introduction area, after which it resurfaced, introduced one at a time, they followed a path tracing out the level of the surface of the metal in this experiment. In all cases when tracking was successful the particles took approximately 1.7 to 2 seconds to traverse the 1m long launder.

The particle positions from this last experiment show the introduced particles were initially near the top of the metal stream, with some possibly dropping below the surface closer to the bottom of the metal stream, after the baffle. The simulation of fluid flow in this launder predicted that particles would generally rise slightly before the baffle, but then sink, slowly, following it. This effect was observable but appeared to have been affected by other phenomena acting upon the particle immediately following its introduction into the metal. The particle's travelled from their introduction position to the volume covered by the positron camera, and during this time they had made their way towards the top of the metal stream. The simulation did not take into account the mechanism by which this happened.

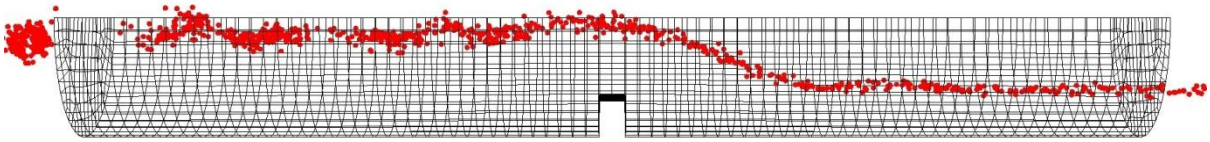

Figure (113a) 600µm particle, launder experiment 1, first particle tracked – Side view.

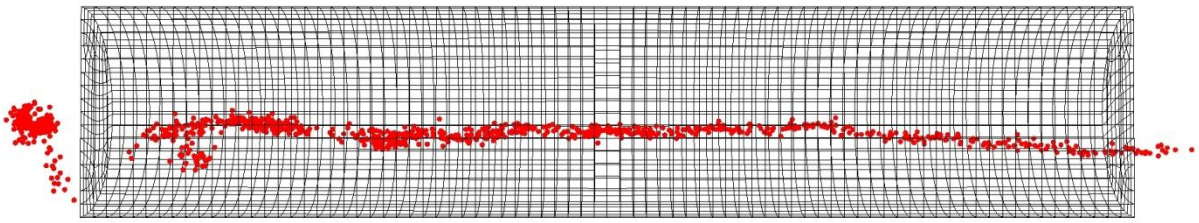

Figure (113b) 600µm particle, launder experiment 1, first particle tracked – Top view.

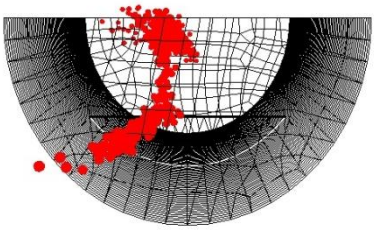

Figure (113c) 600µm particle, launder experiment 1, first particle tracked – End view.

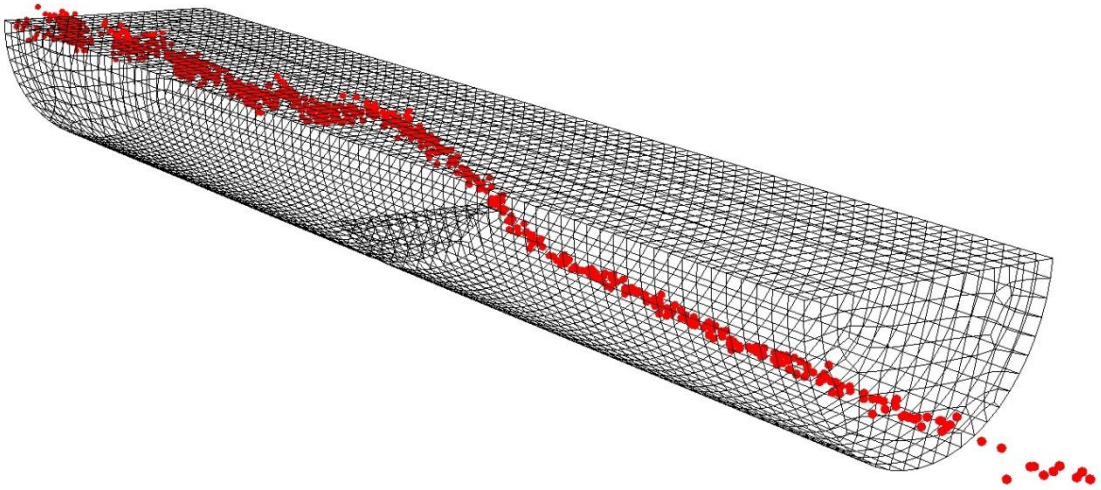

Figure (113d) 600µm particle, launder experiment 1, first particle tracked – Angled view.

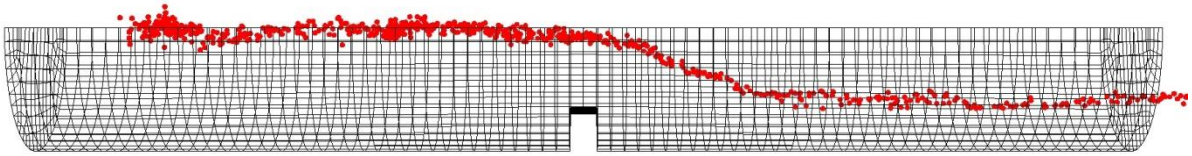

Figure (114a) 600µm particle, launder experiment 1, second particle tracked – side view.

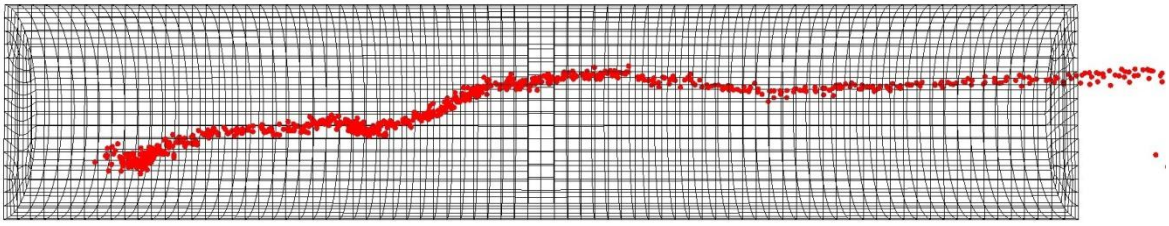

Figure (114b) 600µm particle, launder experiment 1, second particle tracked – top view.

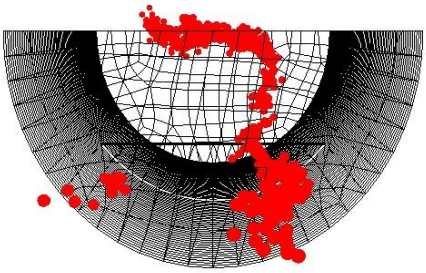

Figure (114c) 600µm particle, launder experiment 1, second particle tracked – front view.

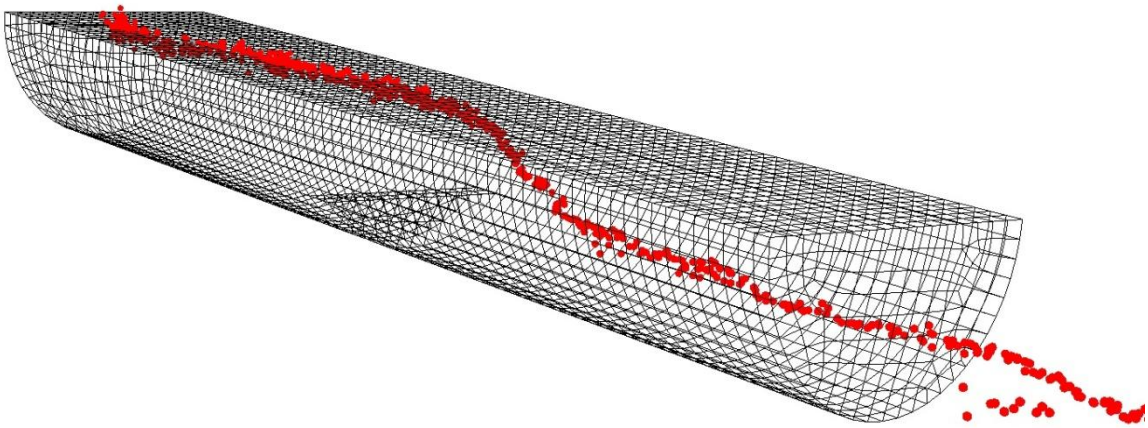

Figure (114d) 600µm particle, launder Experiment 1, second particle tracked – Angled view.

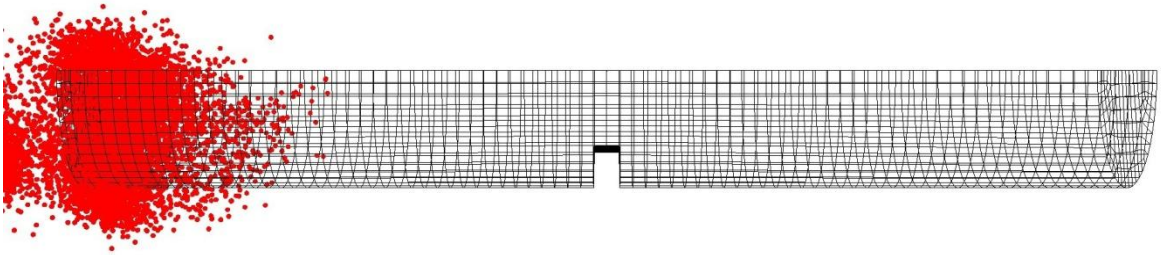

Figure 115. 600 µm particle, launder experiment 2 – all particle tracks

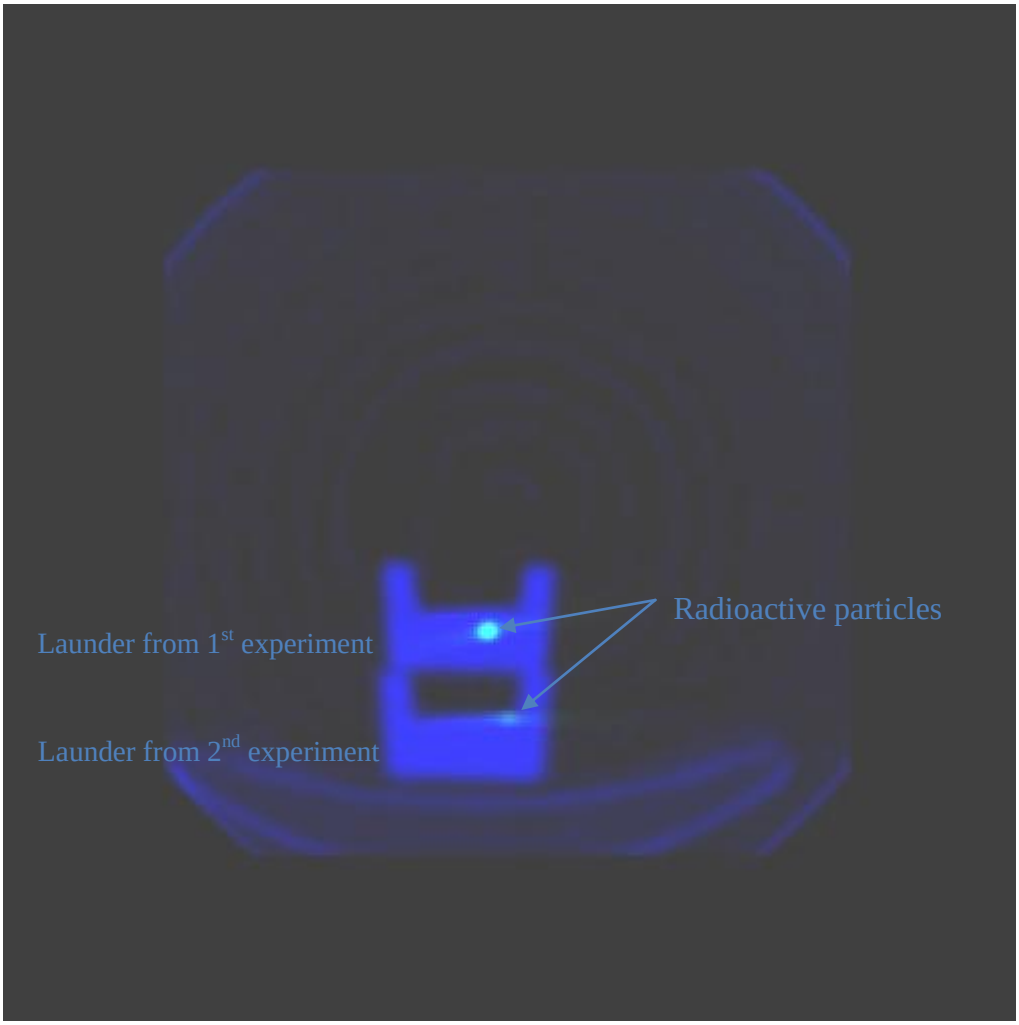

Figure (116) Example combined attenuation and transmission scans from the first two (600µm) experiments, launder from the first experiment on top of the launder from the second experiment.

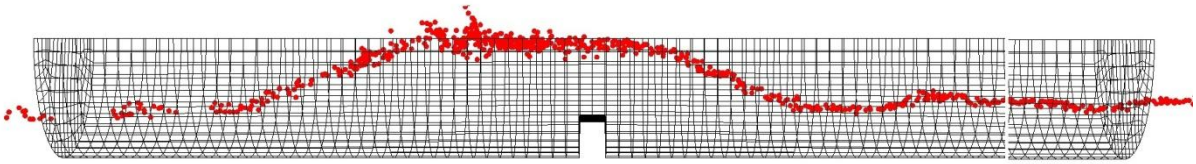

Figure 117a 600µm particle, launder experiment 3, particle 6 – side view

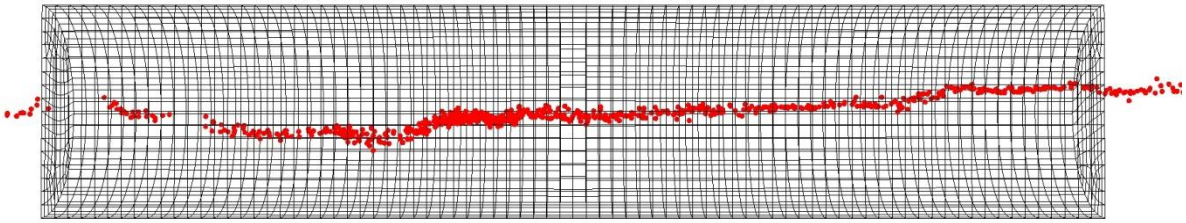

Figure 117b 600µm particle, launder experiment 3, particle 6 – top view

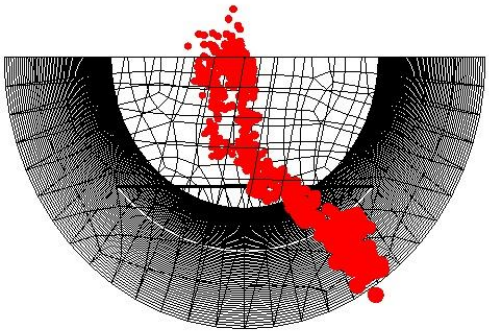

Figure 117c 600µm particle, launder experiment 3, particle 6 – front view

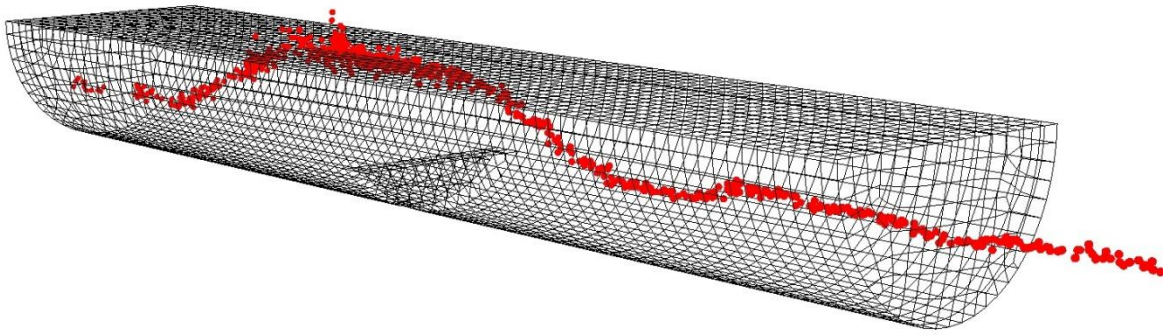

Figure 117d 600µm particle, launder experiment 3, particle 6 – angled view

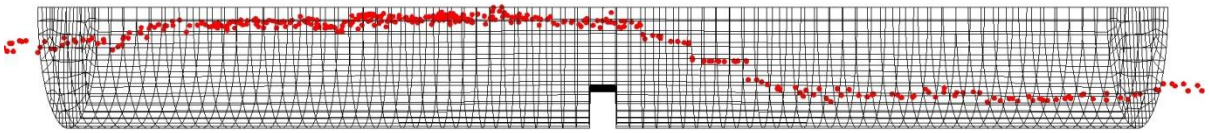

Figure 118a 600µm particle, launder experiment 4, particle 1 – side view

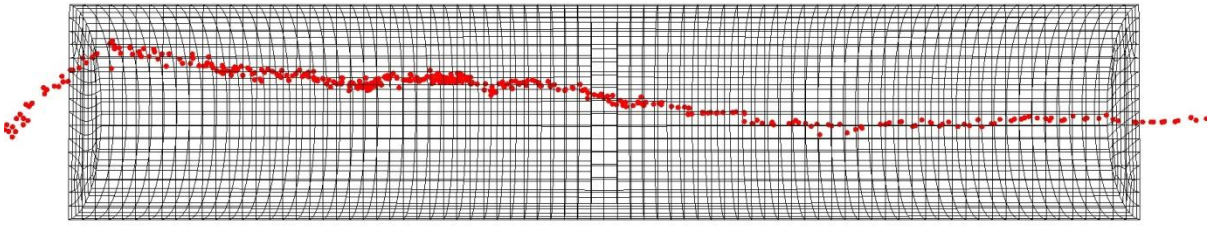

Figure 118b 600µm launder particle, experiment 4, particle 1 – top view

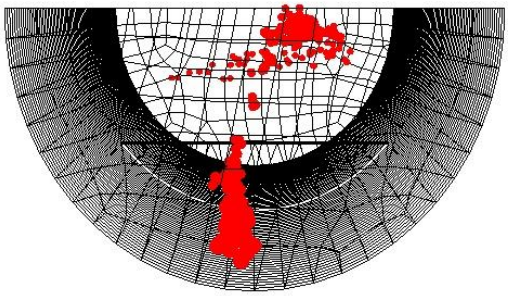

Figure 118c 600µm particle, launder experiment 4, particle 1 – front view

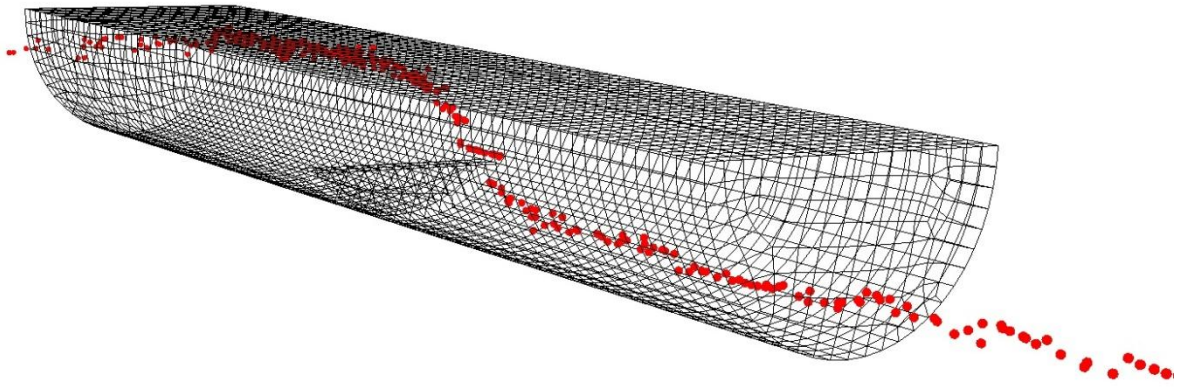

Figure 118d 600µm particle, launder experiment 4, particle 1 – angled view

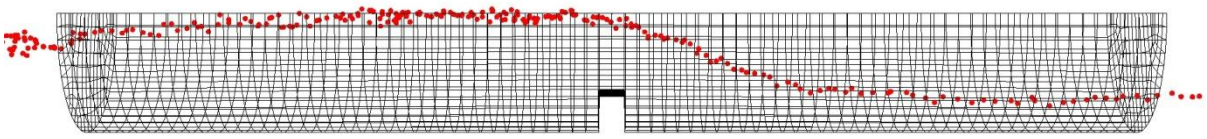

Figure 119a 600µm particle, launder experiment 4, particle 2 – side view

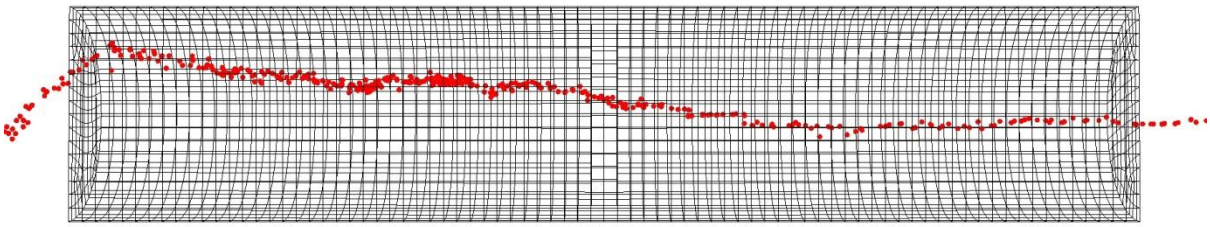

Figure 119b 600µm particle, launder experiment 4, particle 2 – top view

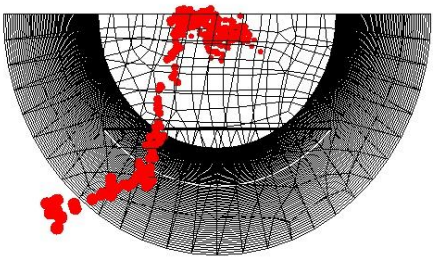

Figure 119c 600µm particle, launder experiment 4, particle 2 – front view

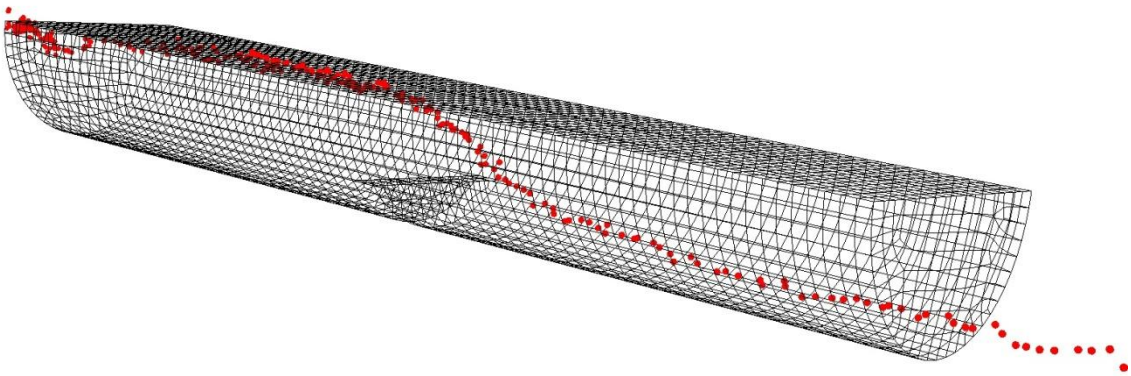

Figure 119d 600 µm particle, launder experiment 4, particle 2 – angled view

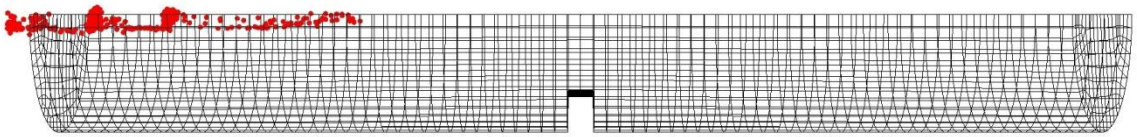

Figure 120a 600µm particle, launder experiment 4, particle 3 – side view

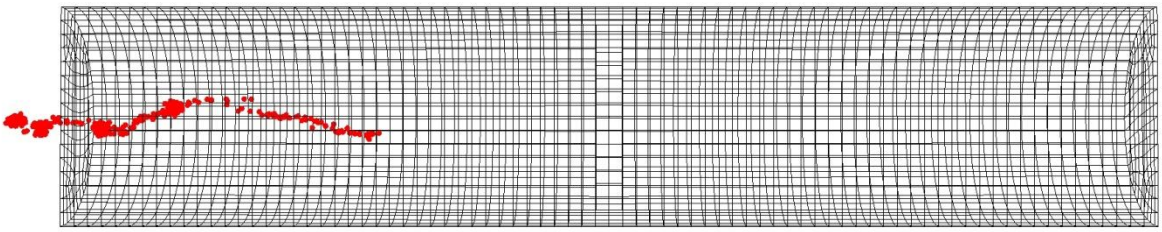

Figure 120b 600µm particle, launder experiment 4, particle 3 – top view

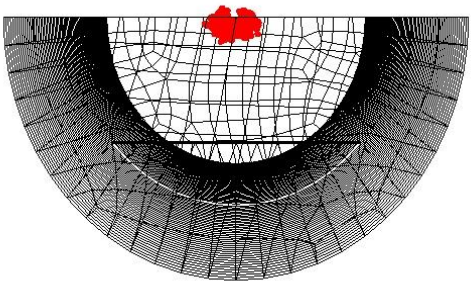

Figure 120c 600µm particle, launder experiment 4, particle 3 – front view

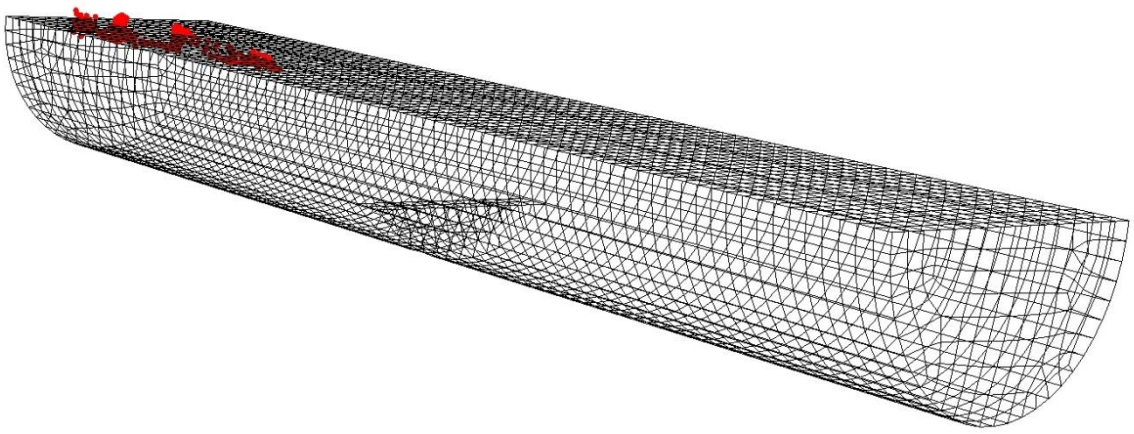

Figure 120d 600µm particle, launder experiment 4, particle 3 – angled view

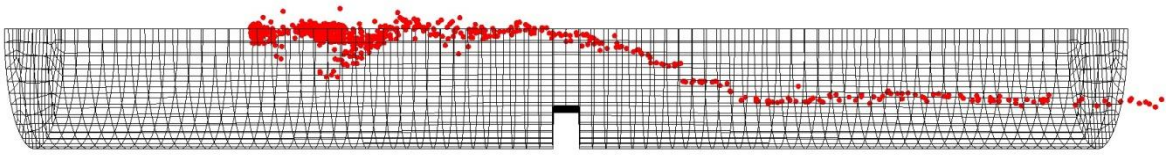

Figure 121a 600µm particle, launder experiment 4, particle 7 – side view

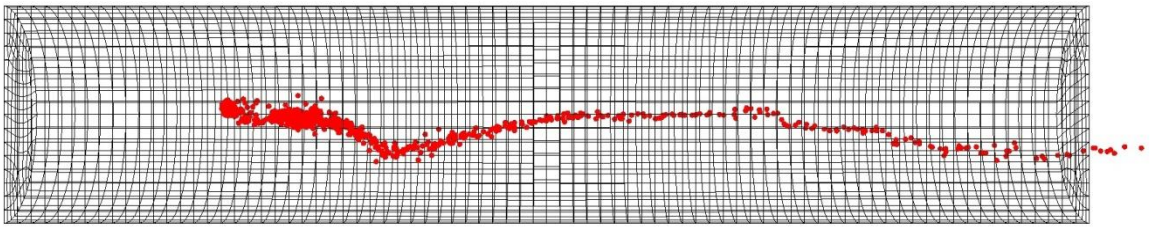

Figure 121b 600µm particle, launder experiment 4, particle 7 – top view

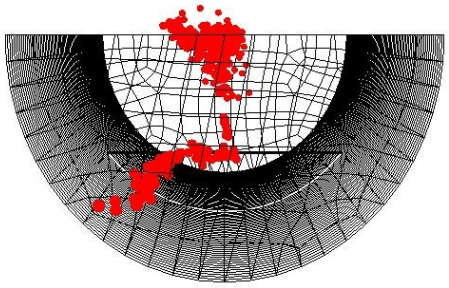

Figure 121c 600µm particle, launder experiment 4, particle 7 – front view

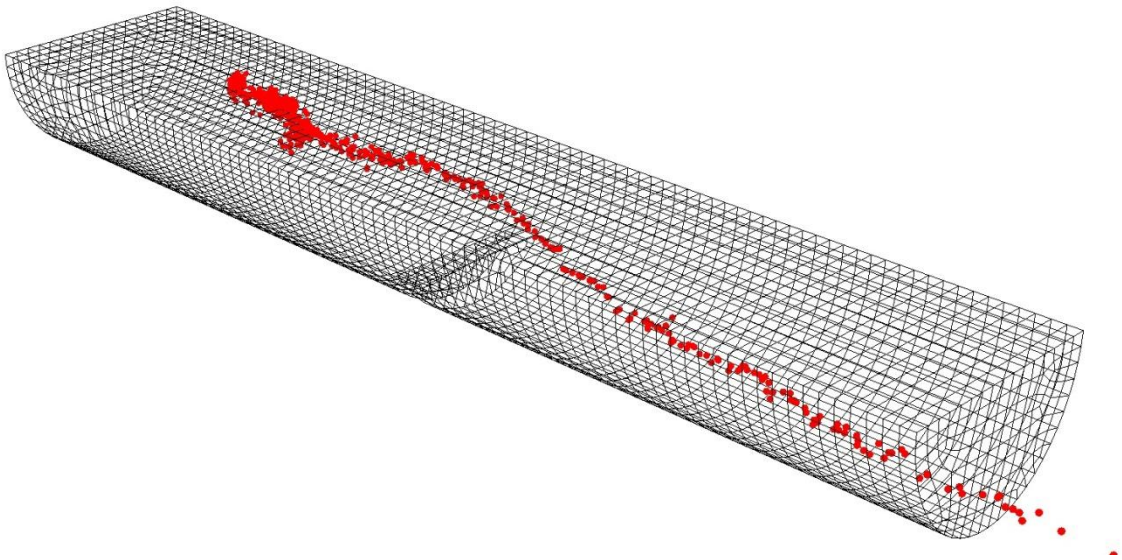

Figure 121d 600µm particle, launder experiment 4, particle 7 – angled view

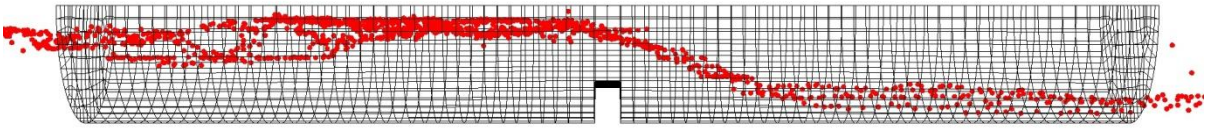

Figure 122a 600µm particle, launder experiment 4, particle 9 (bars) – side view

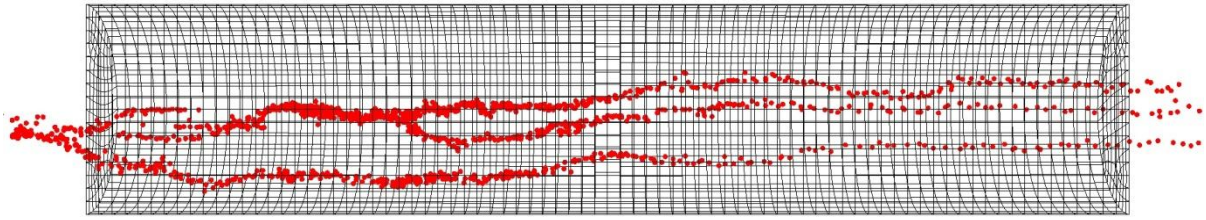

Figure 122b 600µm particle, launder experiment 4, particle 9 (bars) – top view

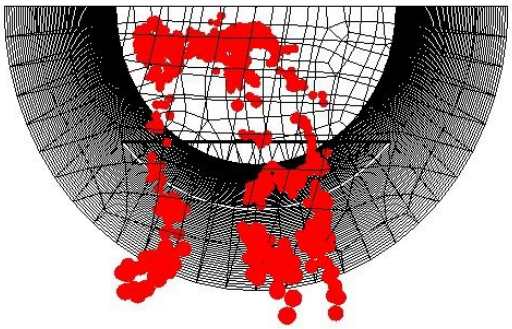

Figure 122c 600µm particle, launder experiment 4, particle 9 (bars) – front view

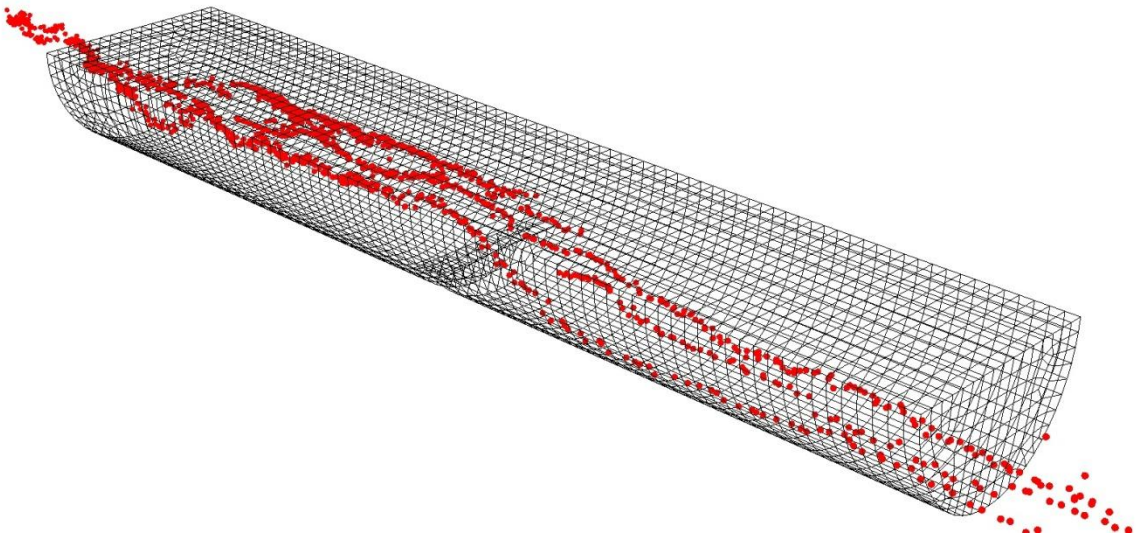

Figure 122d 600µm particle, launder experiment 4, particle 9 (bars) – angled view

5.3.2 Tracking 200μm particles in a launder

The first experiment did not yield any particle tracks and it appears that the data collected Fig. 123, represents noise from outside the field of view of the positron camera This was also probably true for the second experiment performed. In the fourth experiment, the second particle (Fig. 126) and the third, fourth and sixth particles gave very similar results, again with no trace from the particles themselves. In the third experiment (Fig. 124) a clean particle track was not obtained, however it appears that there was much data collected from the area 60mm in front of the baffle, it is notable that a proportion of this data was above the top of the launder. A particle track was generated, emerging from the noise about 100mm in front of the baffle, however this was elevated above the position expected in the metal stream and was in fact higher than the launder sides, so this must be an artifact of the tracking process, possibly caused by particle(s) on the metals' surface, but these were not seen as distinct particle tracks. The depth at which the particles were introduced was adjusted during the first three experiments, (section 3.2.7.1). One hypothesis is that particle(s) on the surface of the melt give off γ-rays in all directions, and that the detectors at and below the height of the liquid surface see an attenuated signal from the particle(s) whereas those above the height of the liquid see a signal which is not attenuated. The effect upon the tracking algorithm of this, would be to provide a higher percentage of LOR's above the fluid surface than below, consequently the position of the particle determined would be higher than in reality. If this is true, then it may be assumed that anywhere there is a disparity in attenuation due to the geometry of dense materials surrounding a particle, then any particle locations predicted by the PEPT tracking algorithm will be distorted. Any such density driven distortions in reported positions in dense and hence highly attenuating materials will add to the errors already identified for the PEPT process.

The first particle released in the fourth experiment (Fig 125), traversed the launder first sinking in the melt before rising 60mm before the baffle, travelling over it before dipping again, exiting the launder less than10mm above the launder floor. It travelled side to side, this motion started at the centerline moved about 30mm left as it approached the baffle (10 mm before the baffle) and then moved over again, around 40mm to the right, over the remaining length of the launder, exiting the field of view 10mm to the right of the centerline.

The particle illustrated in Fig. 127, the fifth from the fourth experiment, was unusual as it was the only particle to interact with the metal flow immediately following the baffle. It travelled longitudinally along the launder lower in the metal stream than had been observed with other particles. It rose upon the approach to the baffle, travelled over it, and was then seen to display a horizontal swirling motion in which the particle travelled in an elliptical motion with just a 5 to 7 mm vertical rise. The particle made two elliptical loops, then continued lengthways along the launder, rising about 15mm, after the loops, before doing so.

The fifth experiment generated three successful particle tracks, which were similar to each other, the first of these, (fig 129) shows 200µm particle taking a path, very similar to that of an earlier experiment using 600µm particles, (Fig 121), it even started part way down the launder in a similar location, suggesting something was interfering with the data collection mechanism, as this was seen on the three tracks from this experiment.

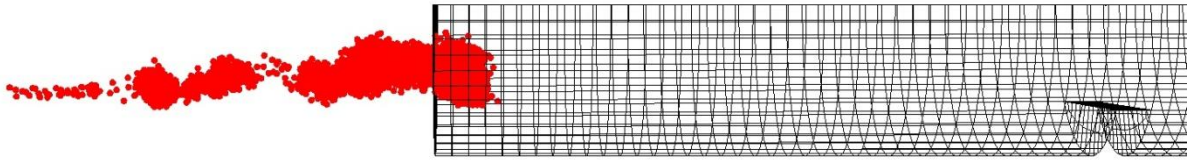

Figure 123a 200µm particle, launder experiment 1, all particles – side view

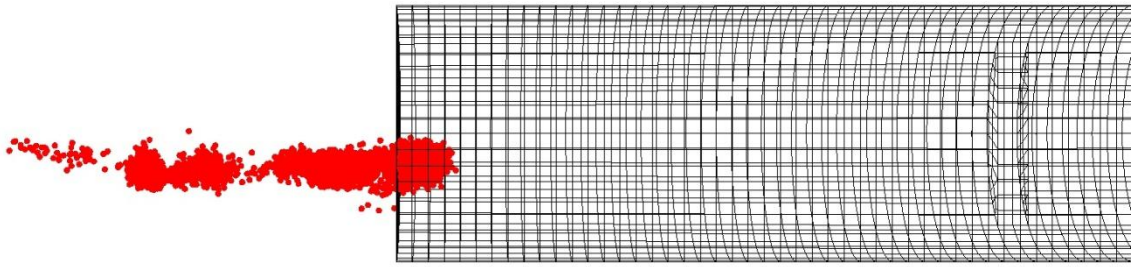

Figure 123b 200µm particle, launder experiment 1, all particles – top view

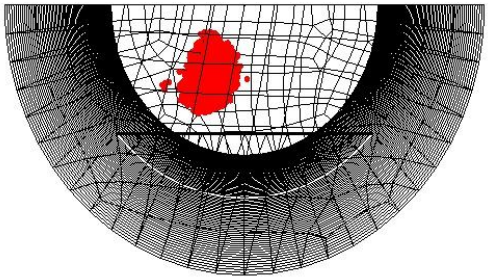

Figure 123c 200µm particle, launder experiment 1, all particles – front view

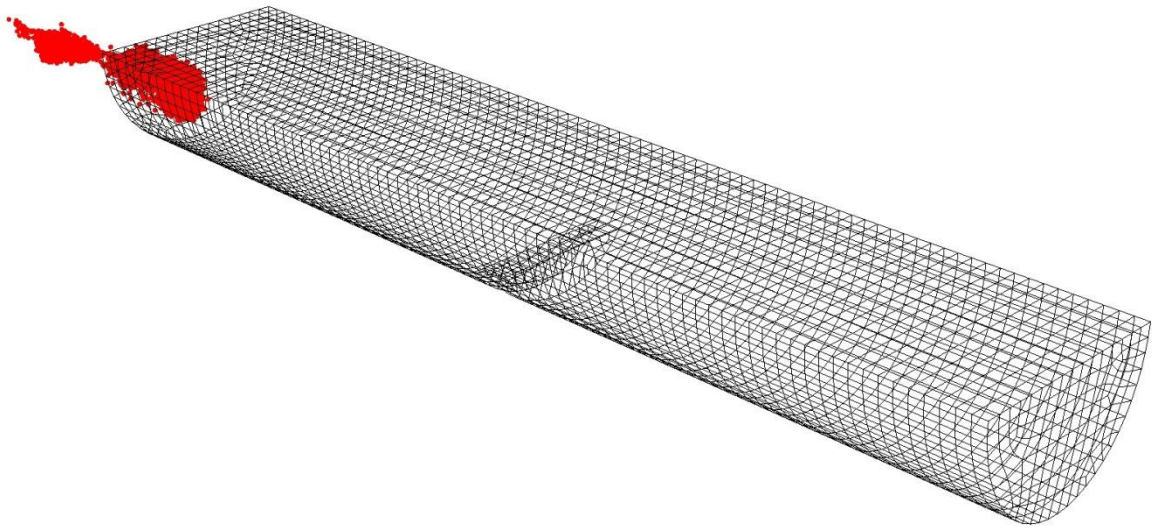

Figure 123d 200µm particle, launder experiment 1, all particles – angled view

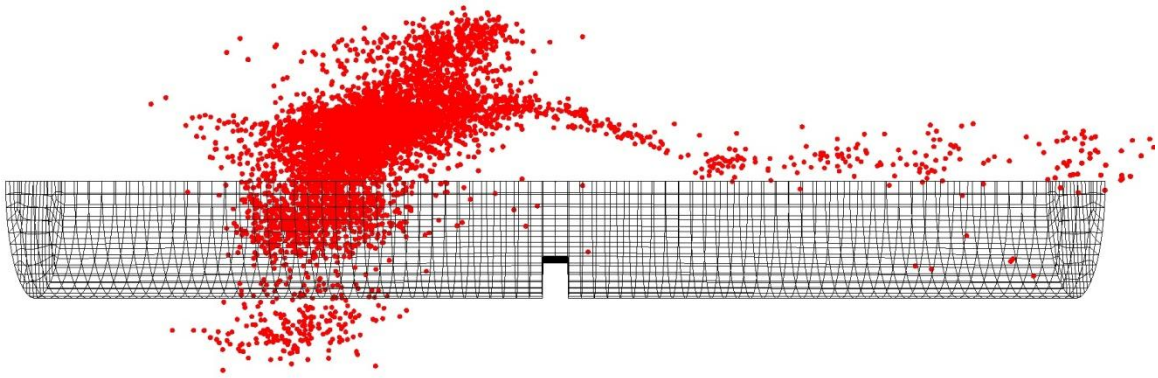

Figure 124a 200µm particle, launder experiment 3, all particles – side view

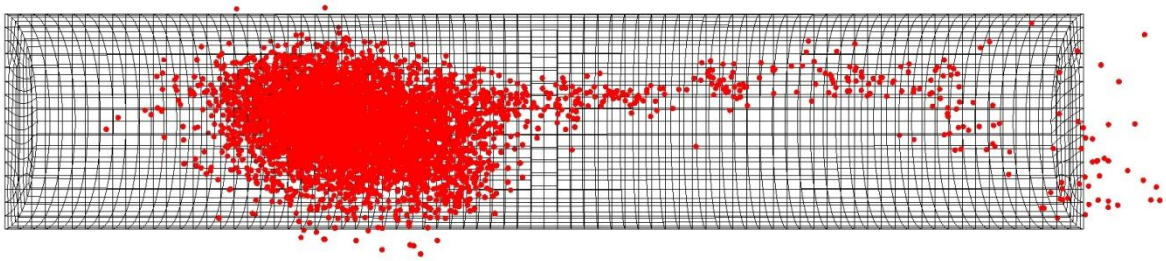

Figure 124b 200µm particle, launder experiment 3, all particles – top view

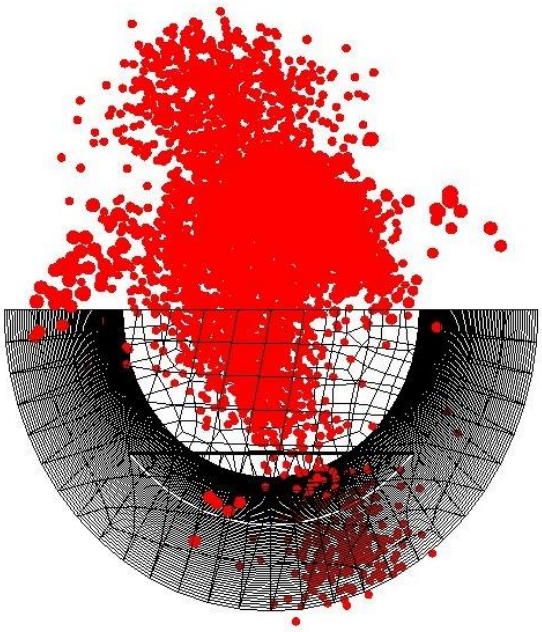

Figure 124c 200µm particle, launder experiment 3, all particles – front view

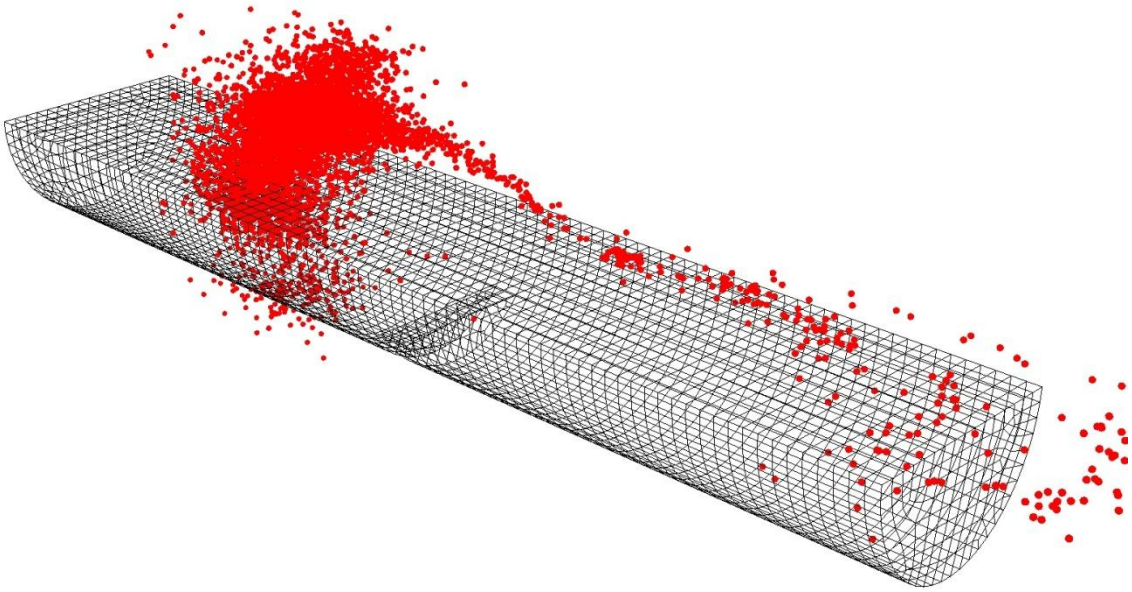

Figure 124d 200µm particle, launder experiment 3, all particles – angled view

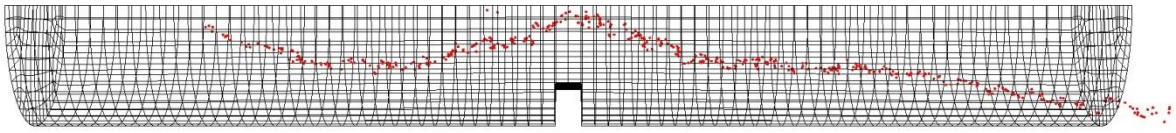

Figure 125a 200µm particle, launder experiment 4, particle 1 – side view

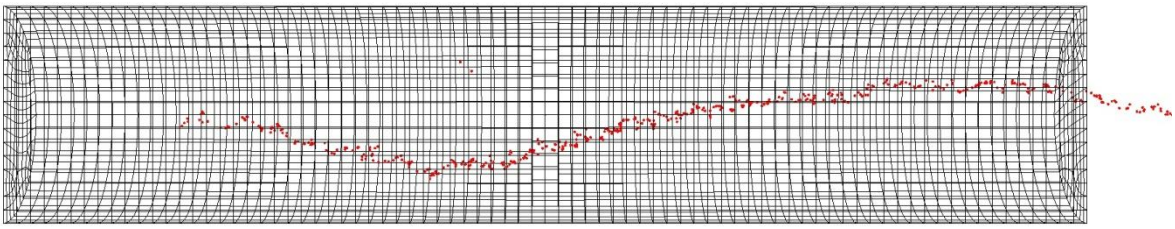

Figure 125b 200µm particle, launder experiment 4, particle 1 – top view

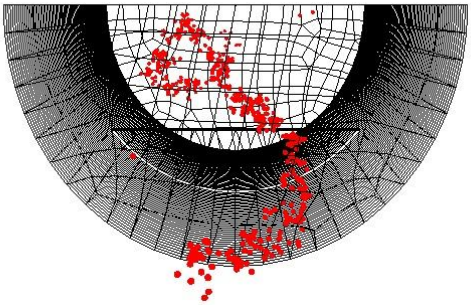

Figure 125c 200µm particle, launder experiment 4, particle 1 – front view

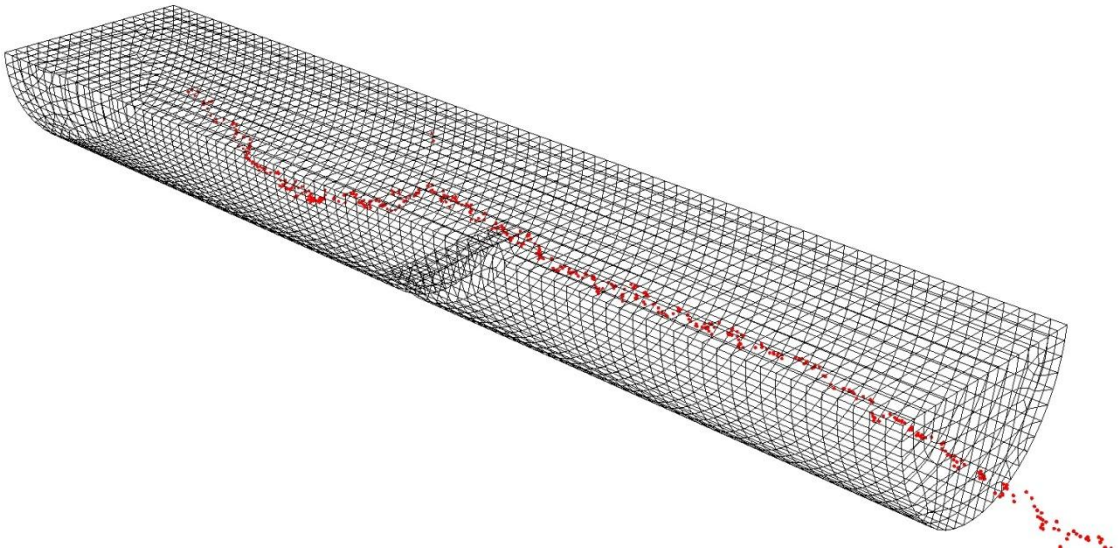

Figure 125d 200µm particle, launder experiment 4, particle 1 – angled view

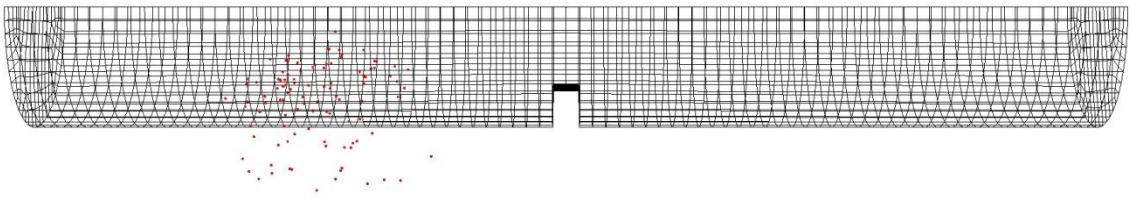

Figure 126a 200µm particle, launder experiment 4, particle 2 – side view

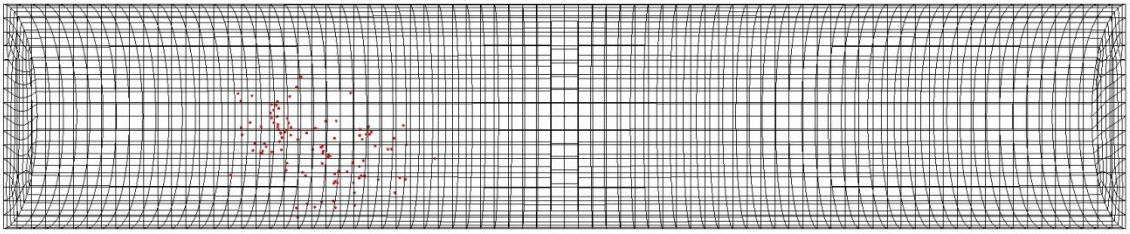

Figure 126b 200µm particle, launder experiment 4, particle 2 – top view

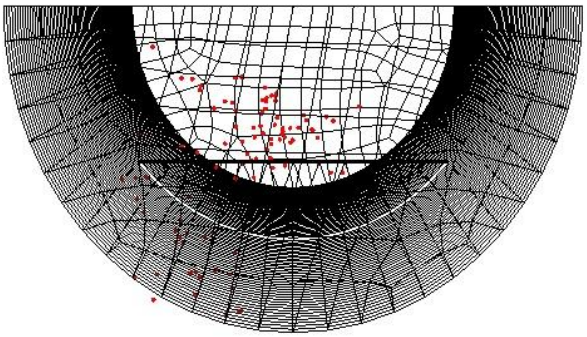

Figure 126c 200µm particle, launder experiment 4, particle 2 – front view

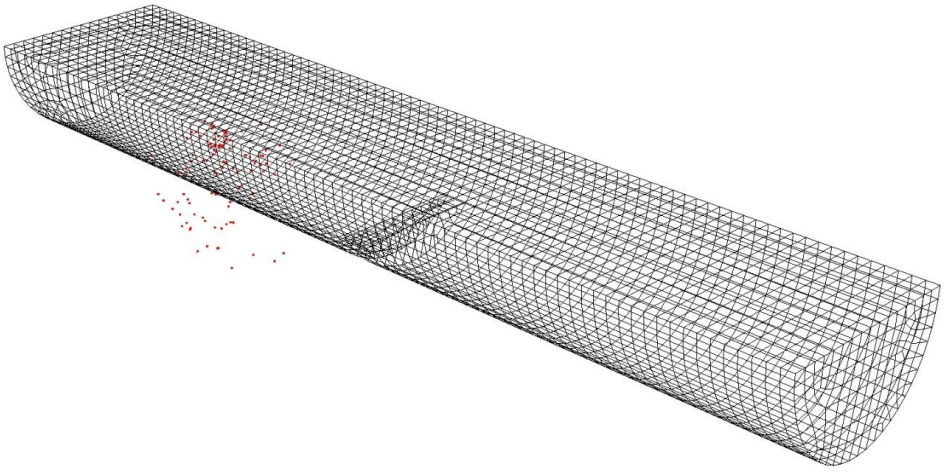

Figure 126d 200µm particle, launder experiment 4, particle 2 – angled view

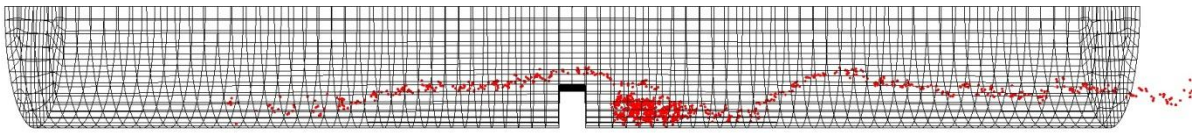

Figure 127a 200µm particle, launder experiment 4, Particle 5 – side view

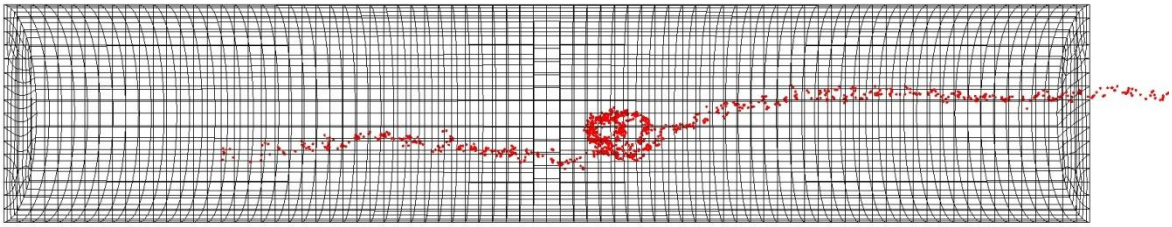

Figure 127b 200µm particle, launder experiment 4, Particle 5 – top view

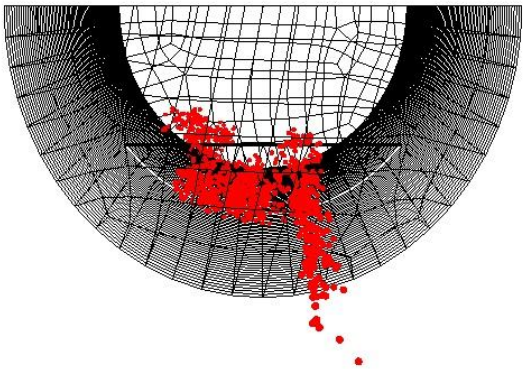

Figure 127c 200µm particle, launder experiment 4, Particle 5 – front view

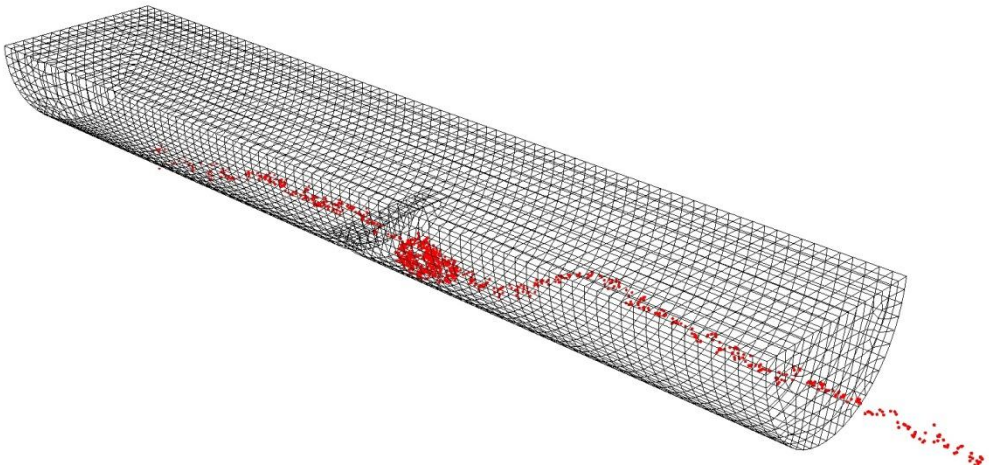

Figure 127d 200µm particle, launder experiment 4, Particle 5 – angled view

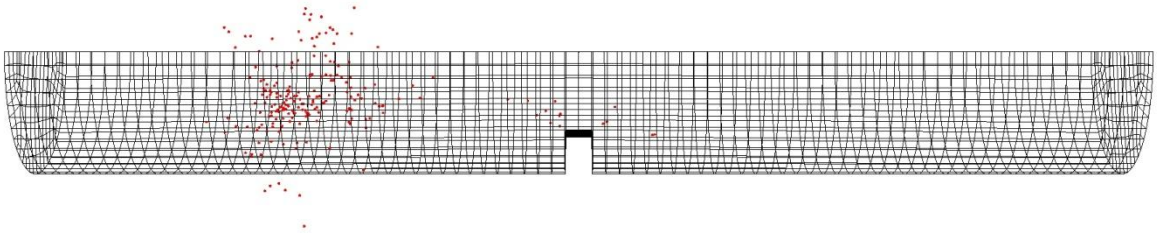

Figure 128a 200µm particle, launder experiment 4, Particle 6 – side view

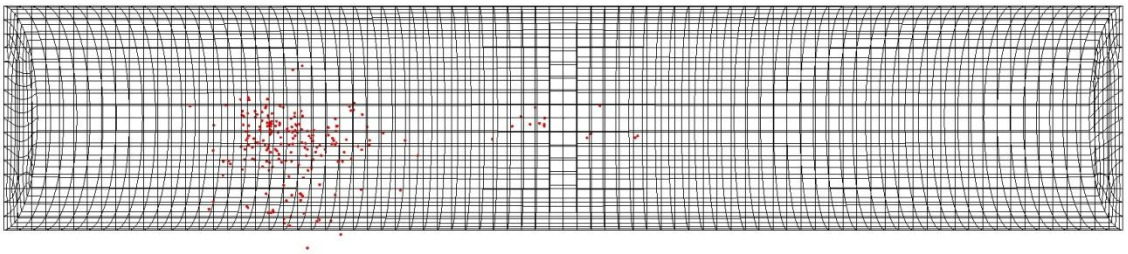

Figure 128b 200µm particle, launder experiment 4, Particle 6 – top view

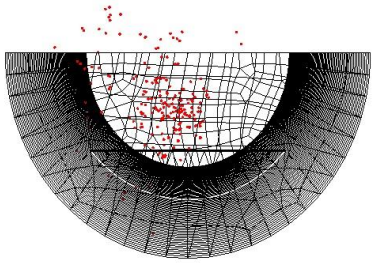

Figure 128c 200µm particle, launder experiment 4, Particle 6 – front view

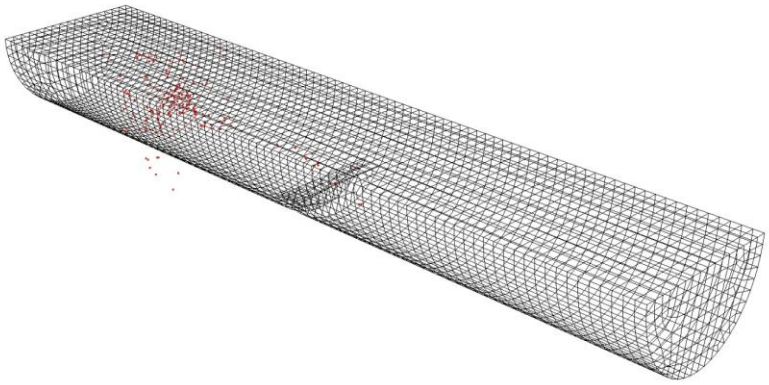

Figure 128d 200µm particle, launder experiment 4, Particle 6 – angled view

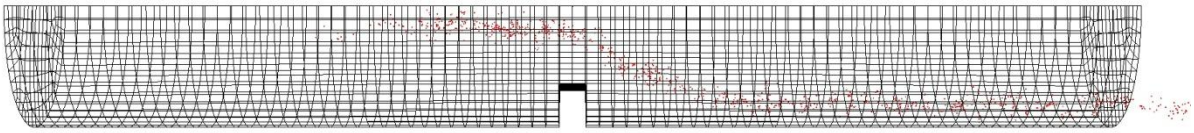

Figure 129a 200µm particle, launder experiment 5, Particle 1 – side view

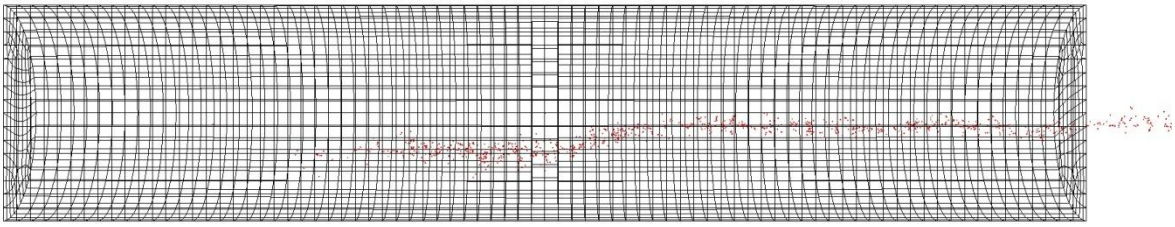

Figure 129b 200µm particle, launder experiment 5, Particle 1 – top view

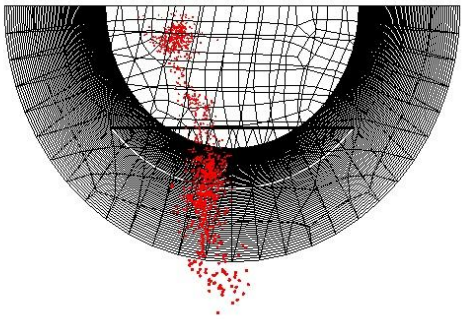

Figure 129c 200µm particle, launder experiment 5, Particle 1 – front view

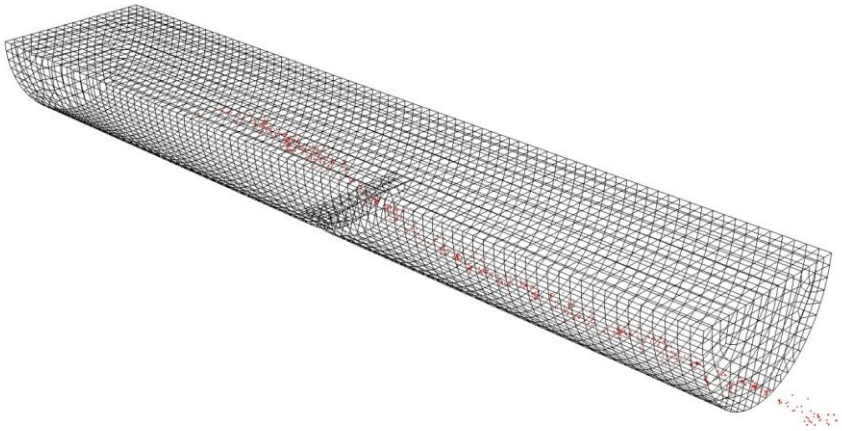

Figure 129d 200µm particle, launder experiment 5, Particle 1 – angled view

5.3.3 200 µm particle cloud experiment

An experiment was conducted using the 200µm particles, in which a large number of particles (35+) were released simultaneously into the metal stream, these were carried with the metal, and some radioactivity was observed by a Geiger counter in the large ingot mould used to catch the liquid metal from the experiment. This radioactivity indicated that at least some particles had passed completely through the apparatus. The tracking system was not designed or intended to track many particles (Maximum of 3) and it was observed that the overall tracking "signal" was elevated above the level of the launder, with excessive random LOR events being confused by the tracking algorithm with true events from multiple particles.

Some particles did become trapped within the metal in the launder (see Fig. 131). The metal remaining in the launder experienced a hot tear during solidification, which occurred approximately 600mm along the launder (measured from the end which had been closest to the furnace). This feature was static during the positron imaging process and gave a clear indication of position for correlation with the images generated by the PET scanner, which were combined together as described in section 3.2.7.3. to represent the launder. The tear did appear at its correct location on the scans giving some confidence that the images are in their correct position along the entire length of the scanned launder.

The first observable particle, (see Fig. 132), was seen almost 74mm from the furnace end of the launder, close to the launder wall. This appeared to be more than the point source expected for a single particle and hence an agglomeration of particles cannot be ruled out. The next particles were detected at a distance of 96mm from the end of the launder (see Fig.

133) and the shape of the emissions suggested that multiple particles were attached to the right hand wall of the launder, with a smaller signal suggesting a single particle had attached to the left hand wall. The image at 160mm along the launder (see Fig. 134), clearly showed a particle off centre and on the surface of the metal. In addition careful examination indicates a second particle part way down the right hand wall of the launder channel. There were no more particles detected for a considerable distance, the next particle being found at a location of 227mm. This was found on the surface of the metal, roughly at the centre of the channel, (see Fig. 135). A particle at 256mm, Fig. 136, was positioned at the top of the metal on the left hand side, near the wall of the launder. A single particle was seen at 333mm on the top surface of the metal, to the left hand side of the centerline. The next collection of particles were situated at around 406mm, the particle images extended over several frames. The image at 403mm (Fig. 138) showed two particles. As the frames progressed it was clear that the left most particle was considerably more active than the right hand particle and also that it was positioned some millimeters behind at around 406 to 409mm (Fig. 139). This may possibly have been a collection of several particles.

No further radioactive particles were found within the launder, however the baffle itself was visible in the images at its correct location (see Fig. 140). About 80mm behind the baffle, a hot tear had occurred and the metal on the baffle side of the tear had lifted showing a clear gap between the launder and the metal, this was seen in the images approaching the tear (Fig 141 and Fig. 142), followed by a gap in the metal, where only the cross section of the launder could be seen (Fig 143). This feature was physically measured to be in the same position on the scans as it was in reality. The remainder of the metal was seen as a small strip at the bottom of the launder (Fig 144). This strip continued all the way to the end of the launder (Fig 145).

Out of the 35 plus initial particles at least 10 seem to have collected on the surface of the metal and within it against the launder walls. No particles were observed mid stream in the metal. The images in Figs 132,133,136,138 and 139 show particles attached to the metal surface, in the area where the oxide film had apparently thickened, (see Fig. 146), possibly due to the velocity gradient at the edge of the launder due to the metal flows boundary layer.

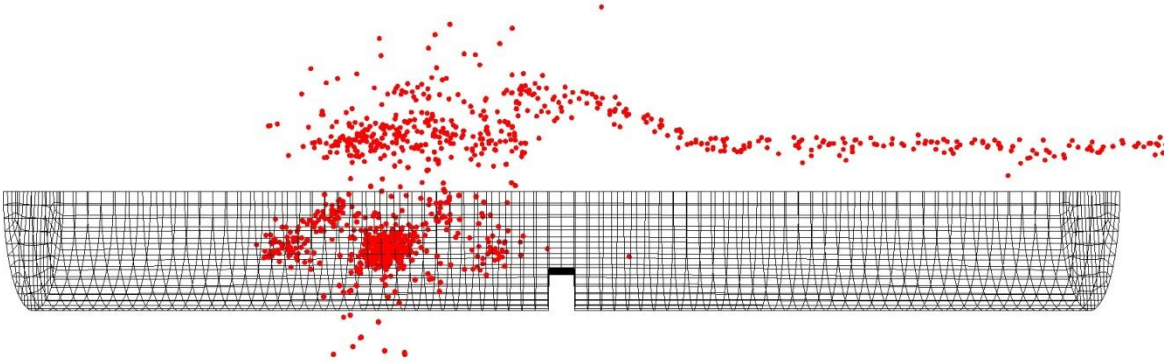

Figure 130a. 200µm particle, launder experiment 6, Multiple Particles, side view

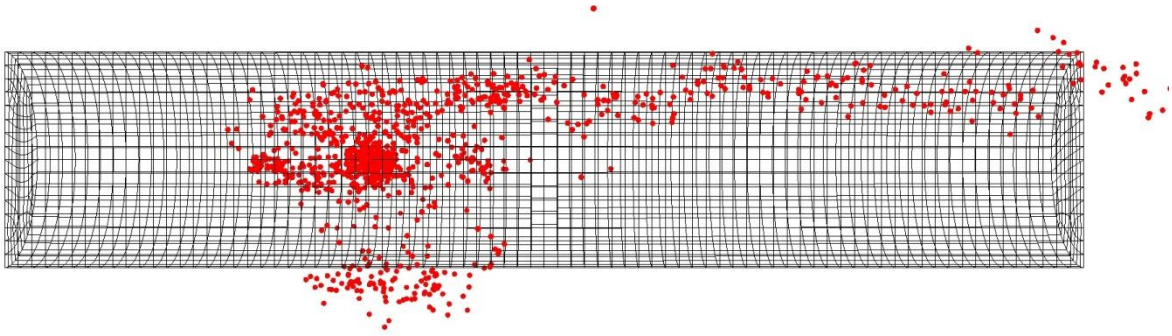

Figure 130b. 200µm particle, launder experiment 6, Multiple Particles, top view

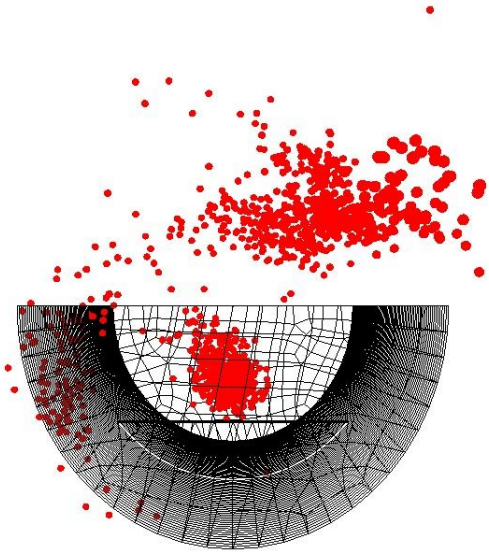

Figure 130c. 200µm particle, launder experiment 6, Multiple Particles, front view

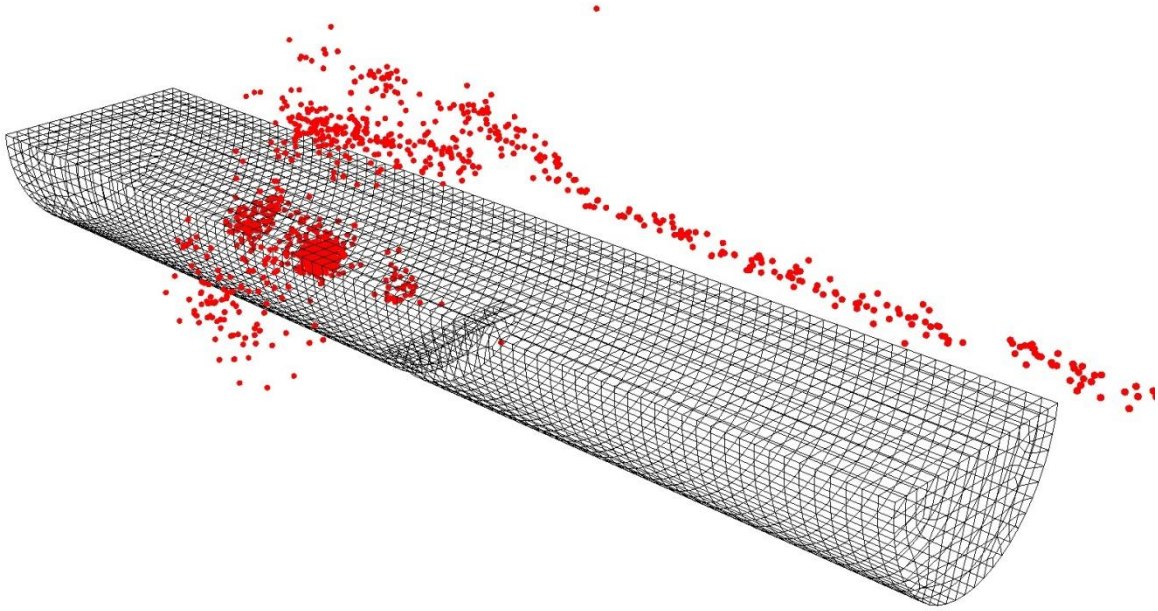

Figure 130d. 200µm particle, launder experiment 6, Multiple particles, angled view

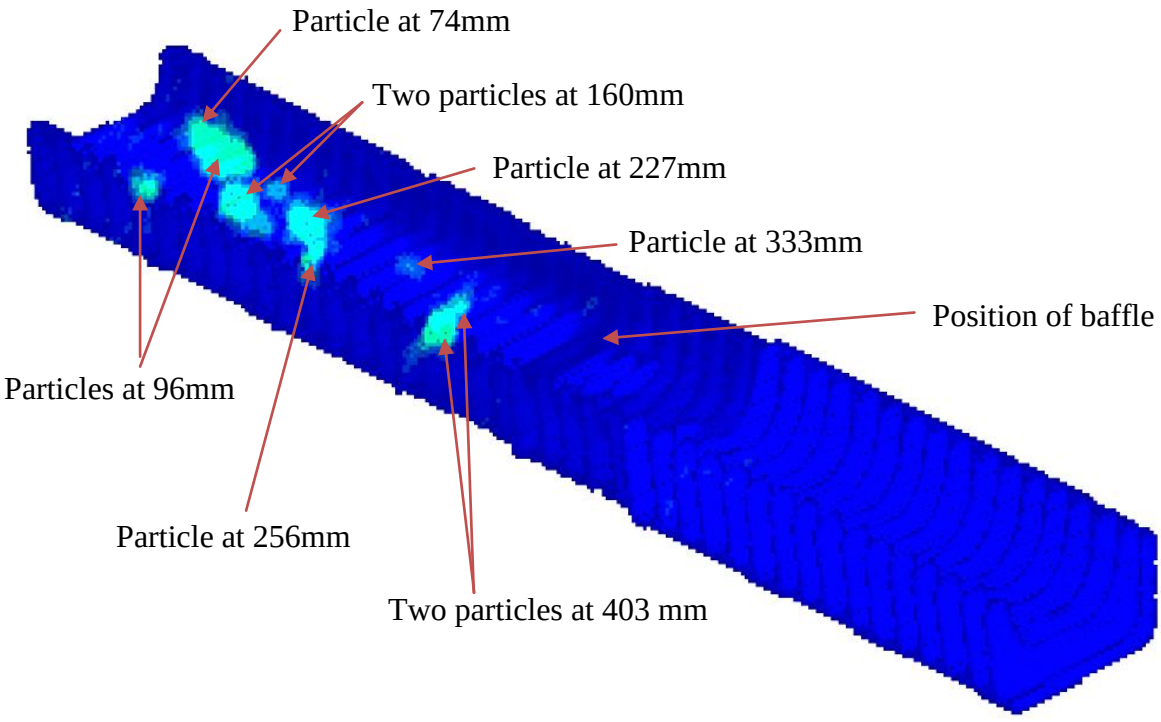

Figure 131. Isometric view of tomographic reconstruction of launder

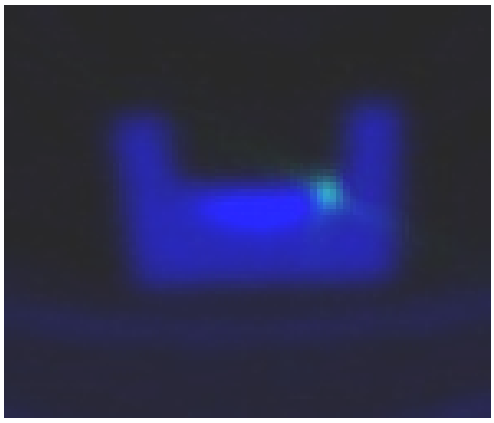

Figure 132. Particle on right hand edge of the launder at 73.6mm

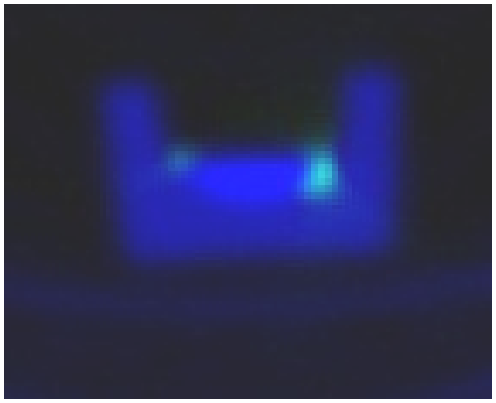

Figure 133. Multiple particles at 96mm along launder

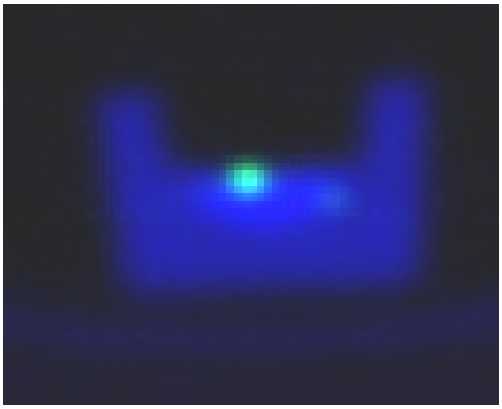

Figure 134. Particles at 160mm along launder

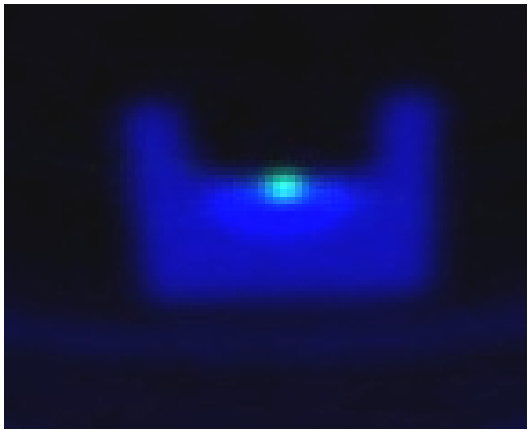

Figure 135. Particle at 227mm along launder

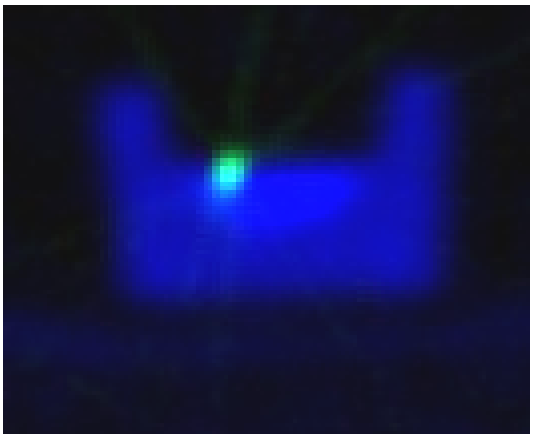

Figure 136. Particle at 256mm along launder

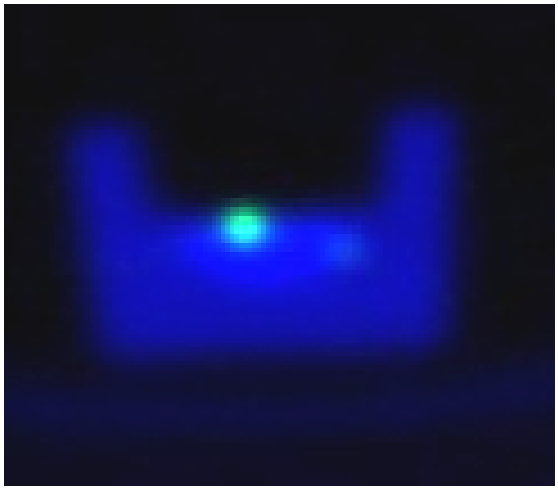

Figure 137. Particle at 333mm along launder

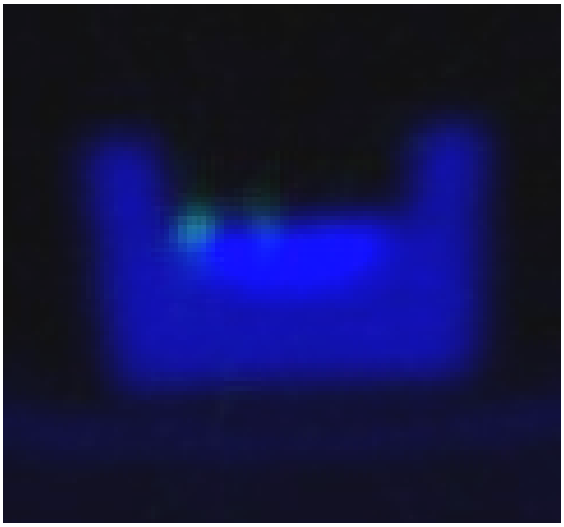

Figure 138. Two particles visible at 403mm along launder

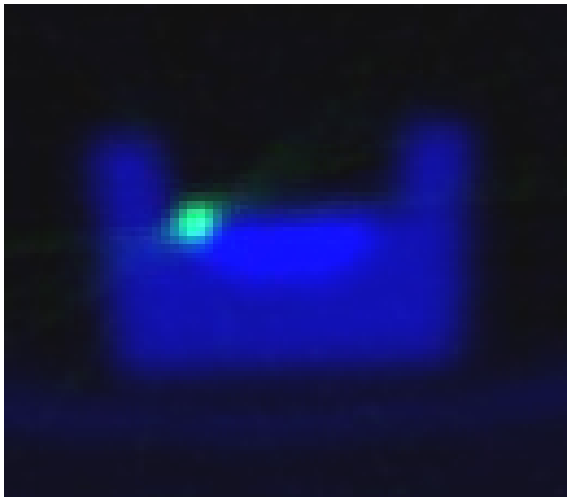

Figure 139. Left hand particle still visible at 409mm along launder.

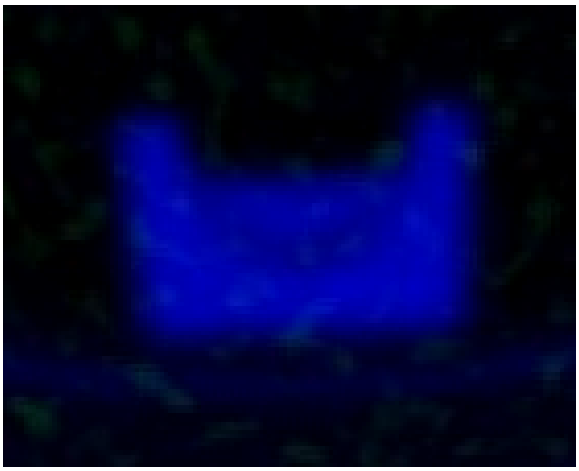

Figure 140. Cross section through baffle at 506mm

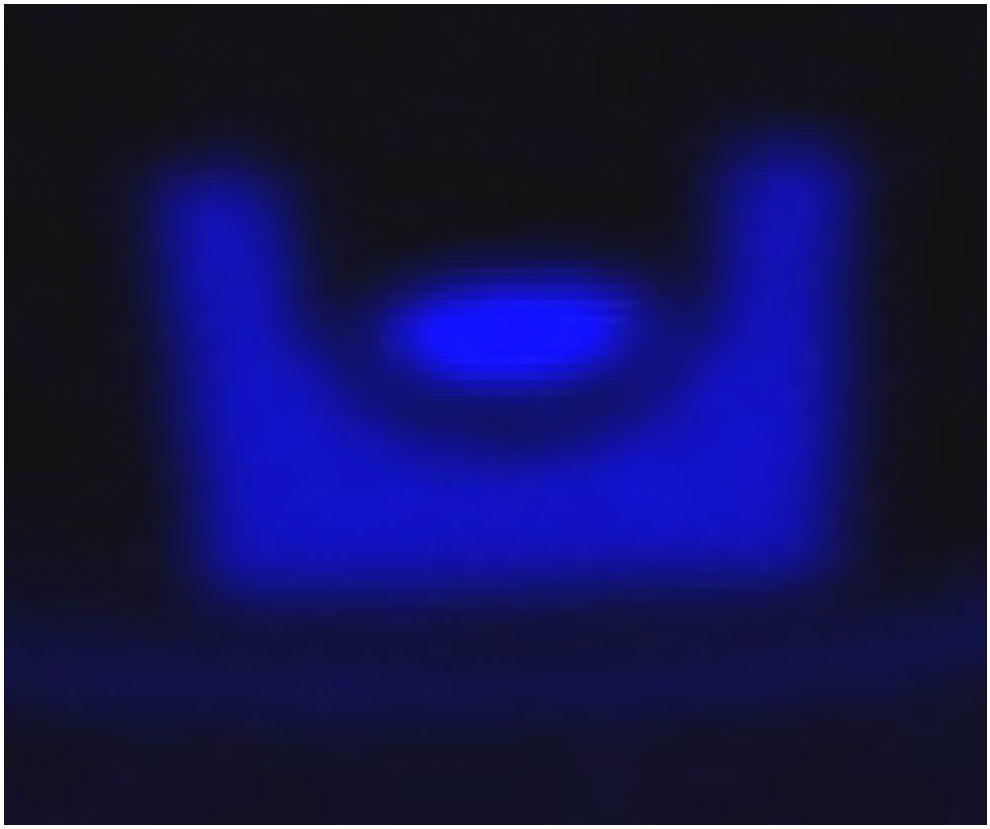

Figure 141. Metal lifted after hot tear at 556 along launder

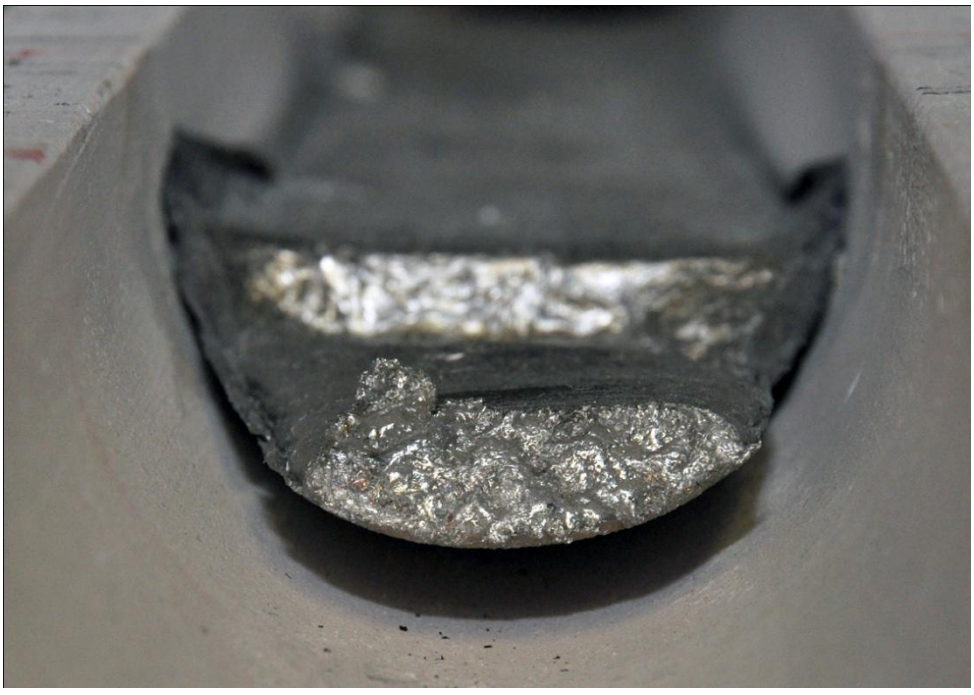

Figure 142. Photograph of metal lifted after hot tear

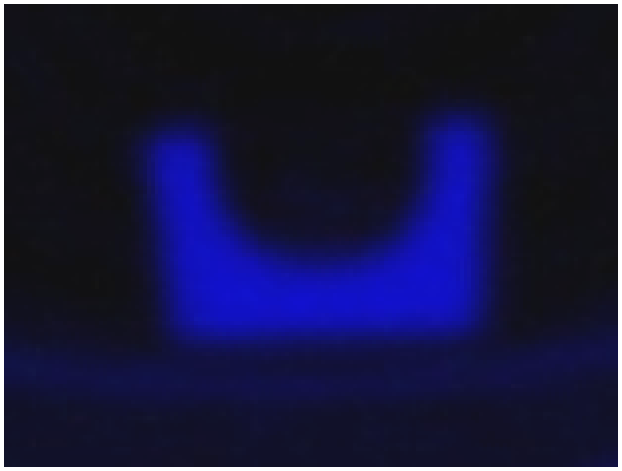

Figure 143. Launder cross section in the break in the metal caused by the hot tear at 604mm

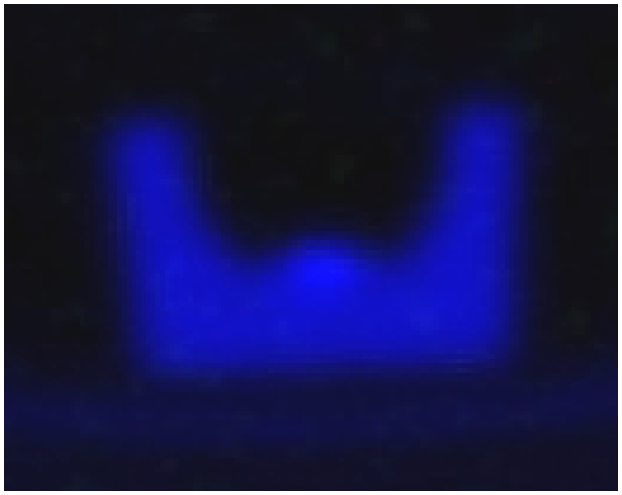

Figure 144. Launder cross section after the break,caused by the hot tear at 630mm

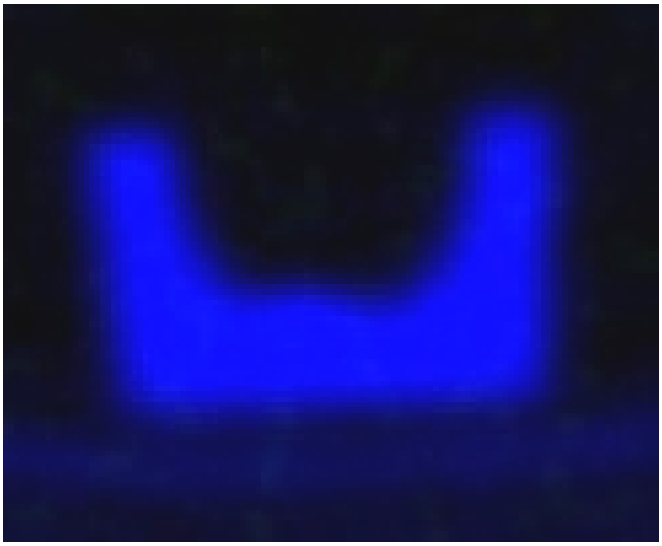

Figure 145. Launder cross section very near to the far end of the launder at 1001mm

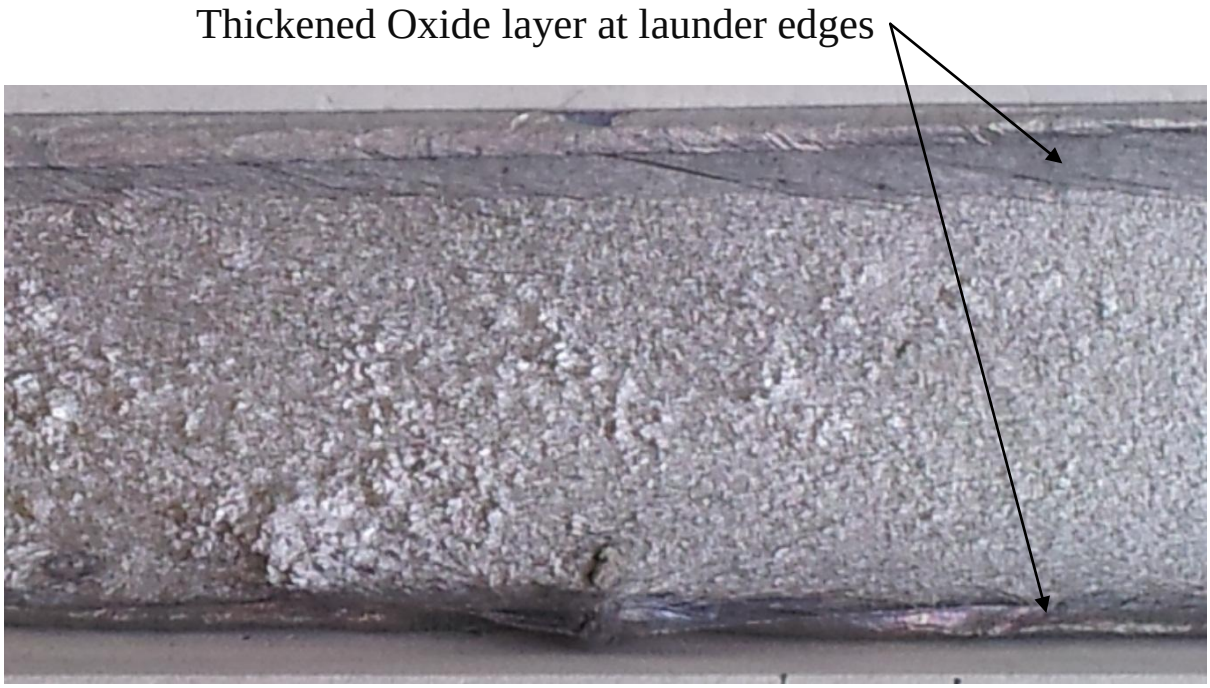

Figure 146. View from above launder, after solidification, showing thickened oxide layer at launder edges

5.4 Simulation results

5.4.1 Validation of model

The simulation was implemented using a free surface, using the simulation data from section 4.1. A velocity of 0.845 ms^{-1}, (Figs.148,149,150 and 151) was calculated exiting the launder with a free surface shape that was comparable to the mark left at the maximum level of the flow within the launder.

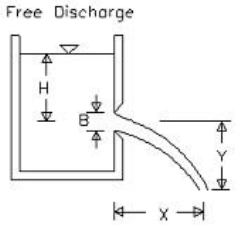

Figure. 147. Diagram of free discharge from an orifice

Confirmation of the real velocity of the metal flow exiting the end of the launder, (see Fig 147), was determined by the following formulas Eqs 1 and 2 [128]

$$V=X*SQRT(g/2y) \quad \text{Eq. 46.}$$

And

$$V=Cv*SQRT(2gH) \quad \text{Eq. 47.}$$

Where

V = Velocity at orifice
X = Horizontal displacement from orifice
Y = Vertical displacement from orifice
G = Acceleration due to gravity
H = Head of fluid
Cv = Velocity coefficient

The velocity coefficient was not used in this case as the outlet was an unusual geometry, however the X and Y displacements were 170mm and 200mm respectively. This gave a calculated launder exit velocity of 0.170*SQRT(9.81/2*0.200) = 0.842 ms^{-1} , in good greement with the simulated figure of 0.845 ms^{-1}. The mark from the metal flow on the launder also showed good agreement with the free surface from the model, being within 5mm for the whole 700mm length of the launder.

The simulated velocity before the baffle was around 0.35 ms^{-1} after the metal had entered the launder, at a preset velocity of 0.37ms^{-1} (the real inlet velocity). The velocities following the baffle were seen to be significantly higher at between 0.45ms^{-1} and 0.84ms^{-1} (see Figs 148, 149,150 and 151) with the fastest velocity being 0.845ms^{-1}.

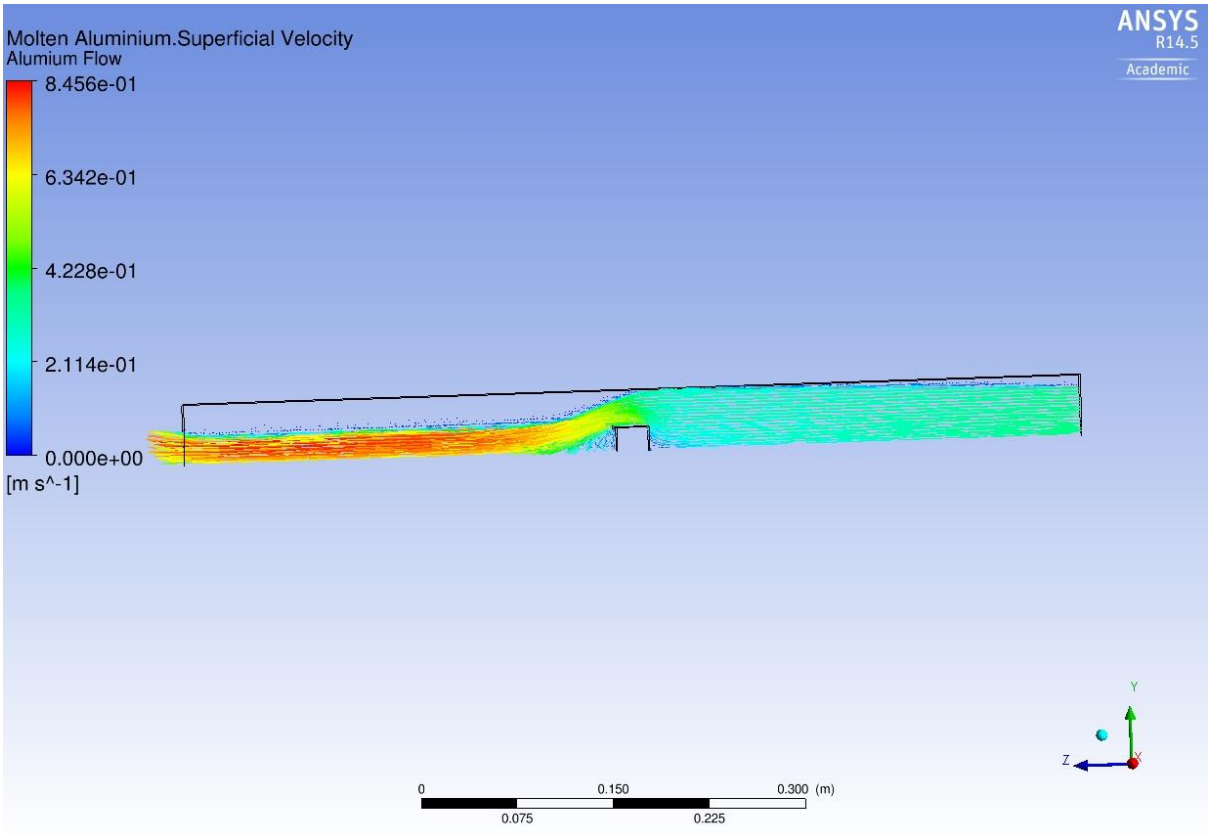

Figure 148. Flow Vector within Molten Al (side view)

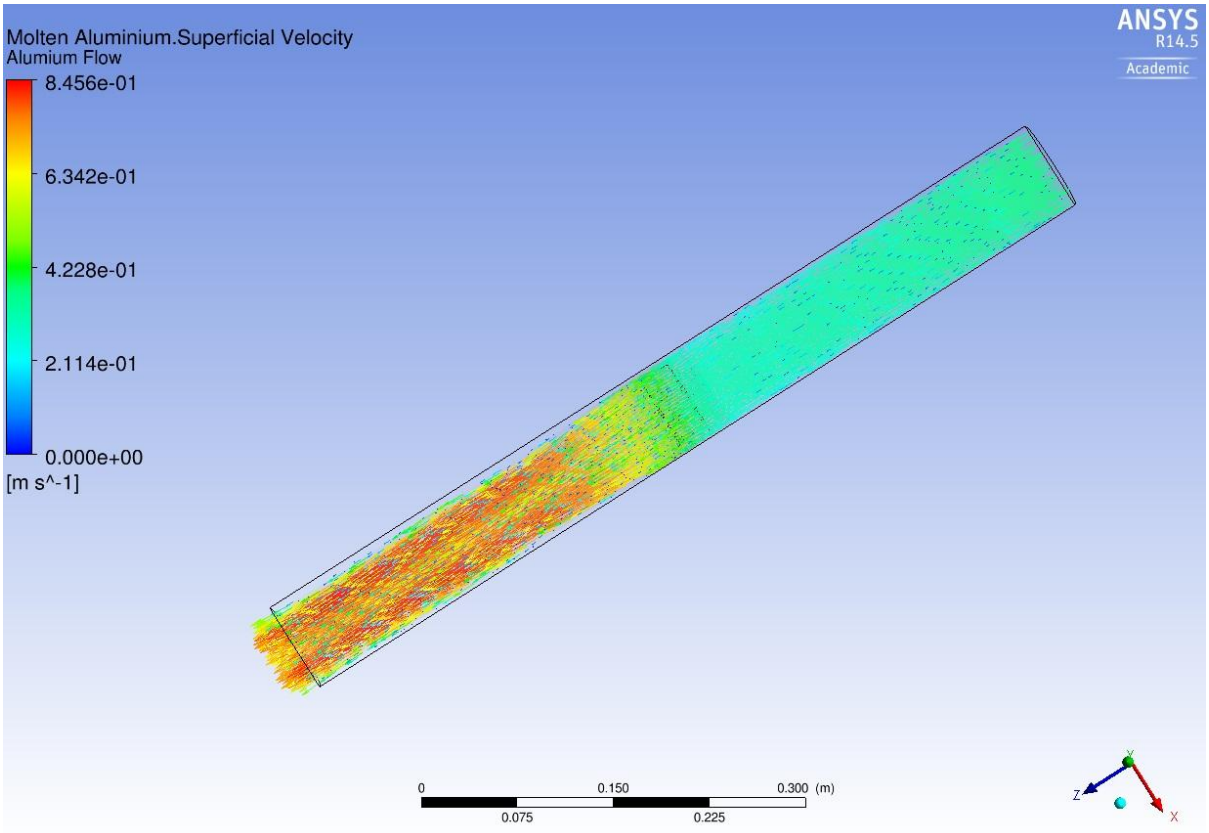

Figure 149. Flow Vector within Molten Al isosurface (top view)

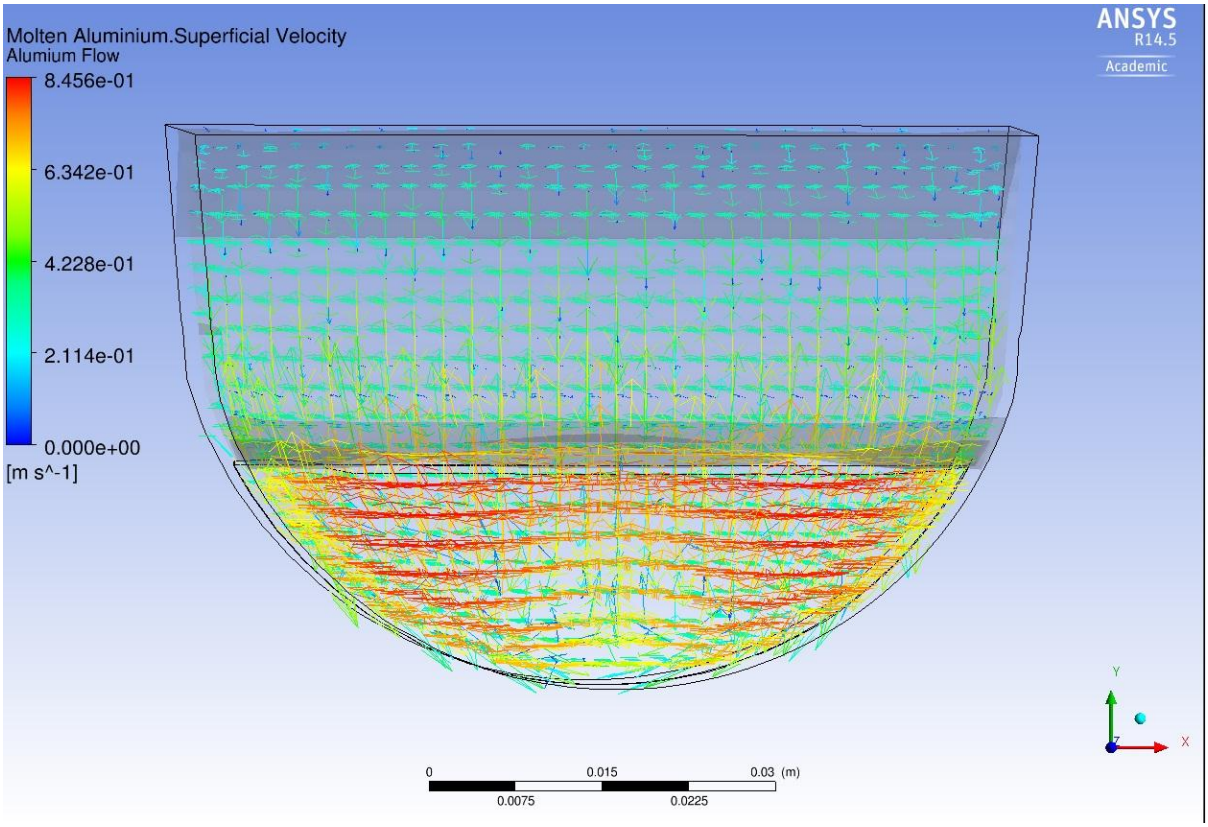

Figure 150. Flow Vector within Molten Al (front view)

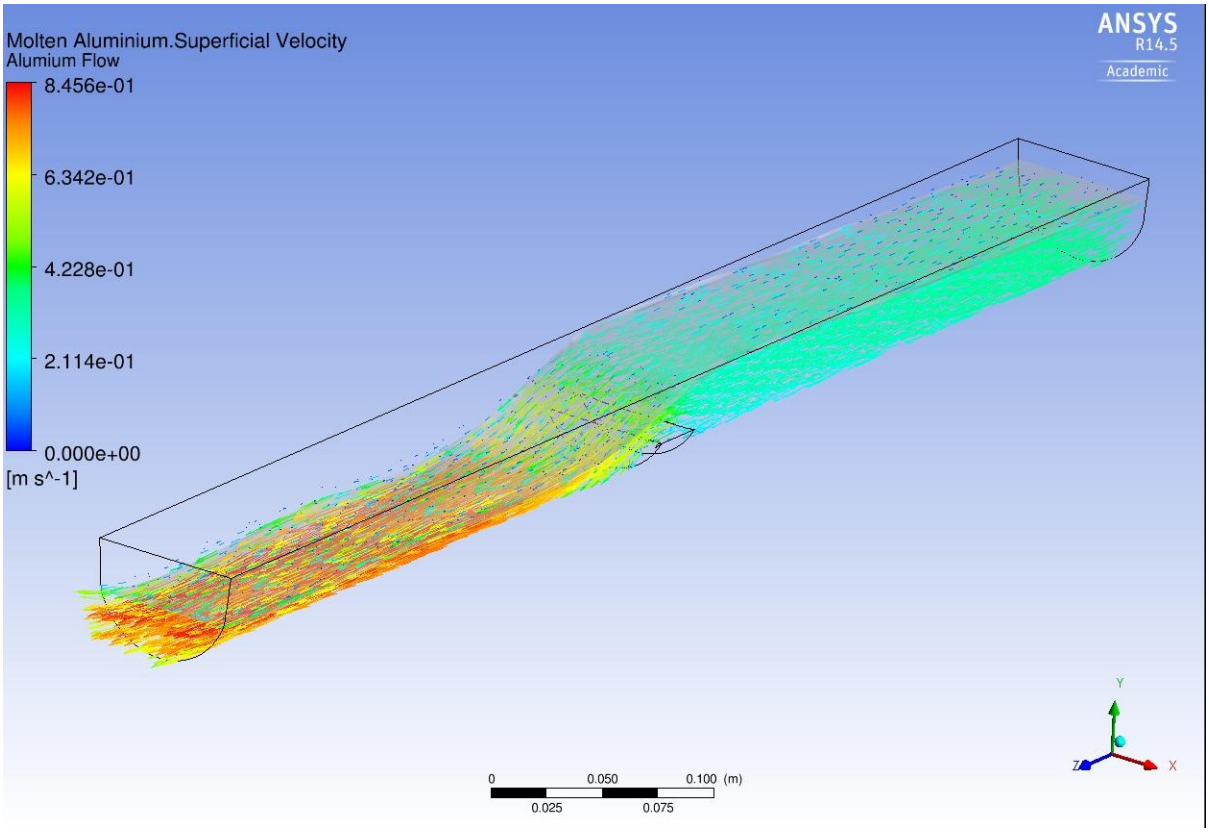

Figure 151. Flow Vector within Molten Al (angled view)

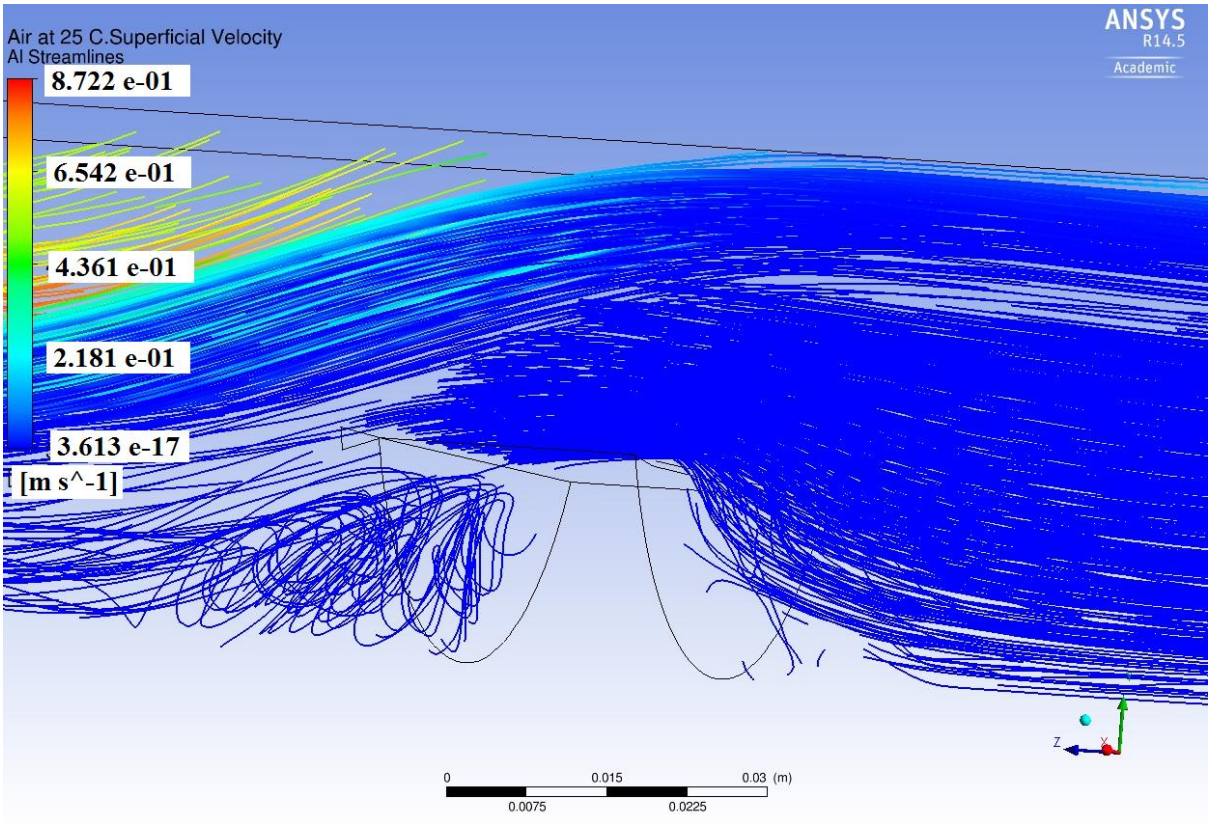

Figure 152. Baffle closeup (streamlines)

Close examination of the area immediately after the baffle showed that flows of less than 0.1 ms^{-1} were expected in this region (see Fig. 152).

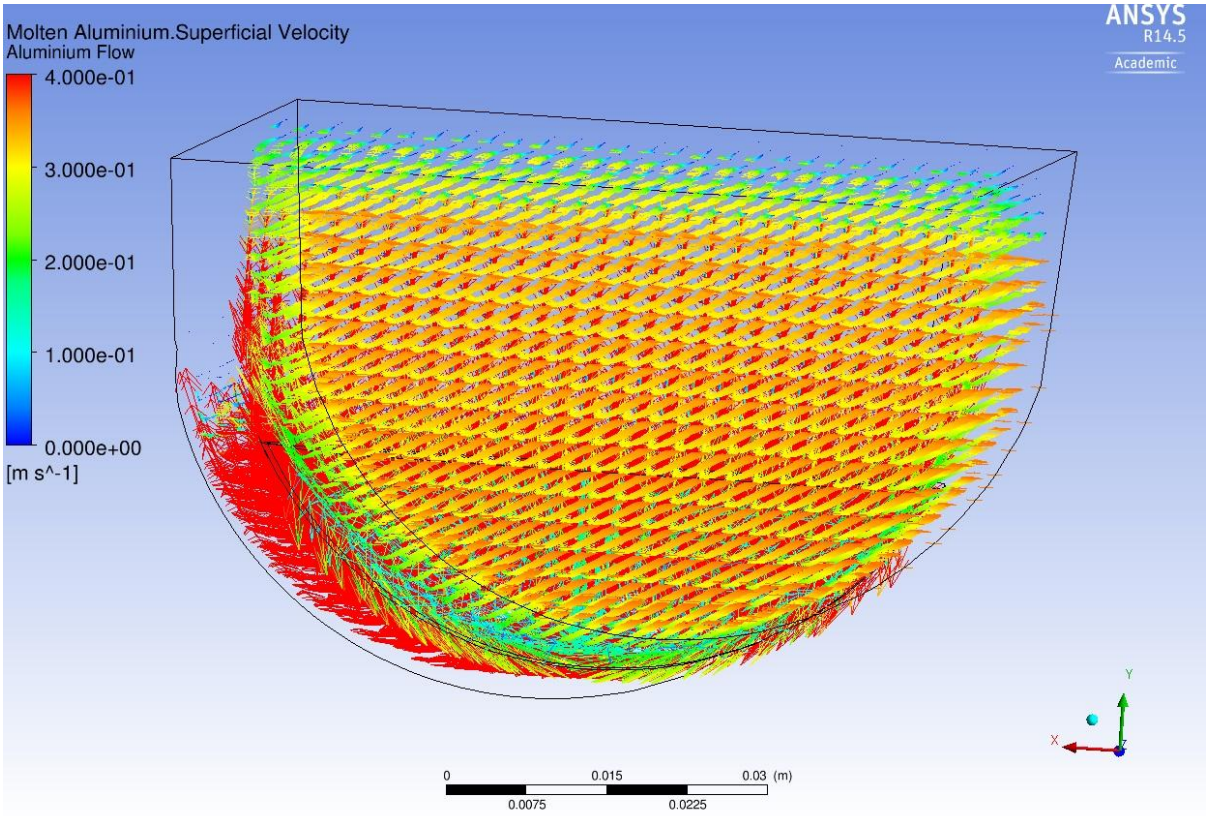

Figure 153. Flow Vector (angled to show slow boundary layer)

The boundary layer upstream of the baffle, (see Fig. 153), showed a lower velocity, where the surrounding flow was less than 0.35 ms^{-1}. After the baffle the majority of the flow velocity rose to around 0.8 ms^{-1} and the boundary layer flow dropped to around 0.6 ms^{-1} .This was lower than the 'core' velocity but was still higher than the main flow upstream of the baffle. The flow velocity at the free surface was determined by CFX to be lower than that of the bulk of the metal, however in common with most CFD packages the free surface is distributed over several computational cells, with the fraction of the liquid and gaseous phases transitioning from one phase to the other over these cells. Given that the air in the model had a very low velocity and the metal a much higher velocity, the velocity averaging applied to the cells which had both air and metal components indicated a lower overall velocity for the cells representing the free surface.

With the cell size used in the free surface fluid simulation (between 2 and 2.5mm) the particle simulation took 12 hours to complete the first one second of simulated 'real time' (without particle collision detection and processing).

The simulation was allowed to run until just over 1.8 simulated seconds had passed, this took over six days with particle collision detection included and just over two days with it turned off.

5.4.2 Model outputs

The simulation with particle collision detection ran for a simulated 1.815 seconds, with particle sizes randomly distributed between 200 and 600μm, in this time 7811 simulated particles were introduced into the system, 4283 particles collided with the launder wall and hence stopped moving, and there were 348 particle-to-particle collisions giving a predicted collision rate of 191.7 collisions per second. The fastest moving particle after 1.815 seconds was reported to be travelling at $0.838ms^{-1}$, just below the predicted maximum fluid velocity of $0.845ms^{-1}$.

The moving particle volume fraction had reached 0.0001 within the simulation, which was a preset limit for the inclusion content of the metal and the value given by Campbell as an inclusion volume fraction for a particularly dirty melt [58]. Accordingly new particles were only added to the simulation as particles were removed by launder wall collisions or by exiting the simulation by reaching the other end of the launder. After 1.815 seconds 187 particles had fully traversed the launder and had exited the simulation.

Figure 154. Particle simulation showing flow velocities– side view.

Figure 155. Particle simulation showing just particles – side view.

The side profile of the simulated aluminium flow shows how the metal height in the launder rose as it approached the baffle and dropped after the baffle (Fig. 154). This is a different representation of the same data shown in Figures 148 to 151, but is displayed by the particle simulation program, instead of CFX^{TM}. The higher the flow rate, the darker the shade of grey displayed. Comparing the particle simulation (Fig. 155) with the flow simulation (Fig. 154) it can be seen that for particles introduced below the surface of the metal it would be expected that they would gradually sink prior to encountering the effect caused by the baffle, which causes them to level off, then rise slightly before passing over it. They then continue their descent at a lower rate, and most exit the launder. The area immediately following the baffle is seen to be clear of particles, both in the metal stream itself and settled out. The high flow rate above this area seems to act to retain the inclusions in the metal stream and the low flow rates in the region after the baffle do not therefore allow particles to settle out.

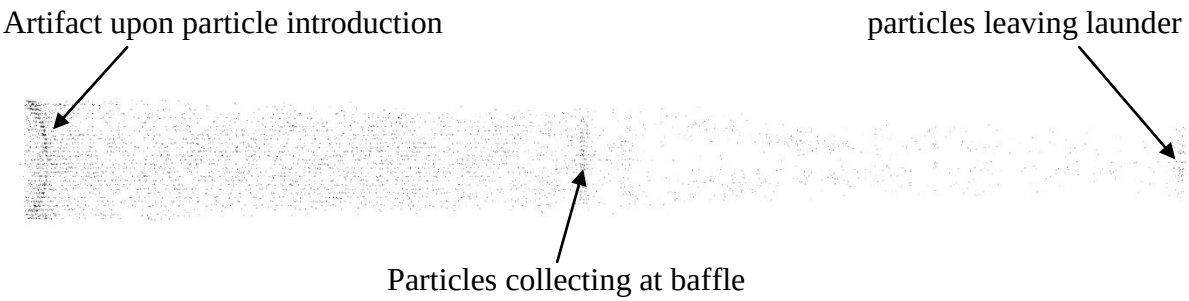

Figure 156. Particle simulation showing particles only - top view.

The top view of the particles in the launder, Fig. 156, shows particles collecting on the baffle face (146 particles) and also that particles introduced in the boundary layer settled out within a short distance, giving rise to the artifact observed at the edge of the inlet area, in reality the boundary layer would only contain a few particles at this location, and the settling seen is therefore not representative.

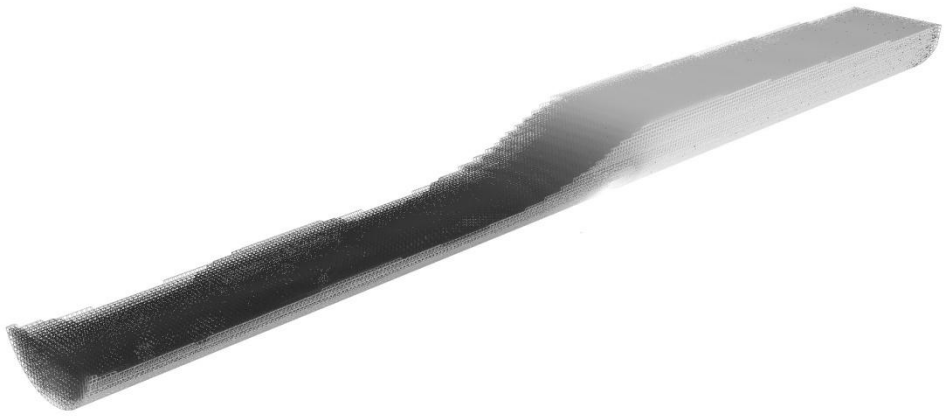

Figure 157. Particle simulation showing flow velocities - angled view.

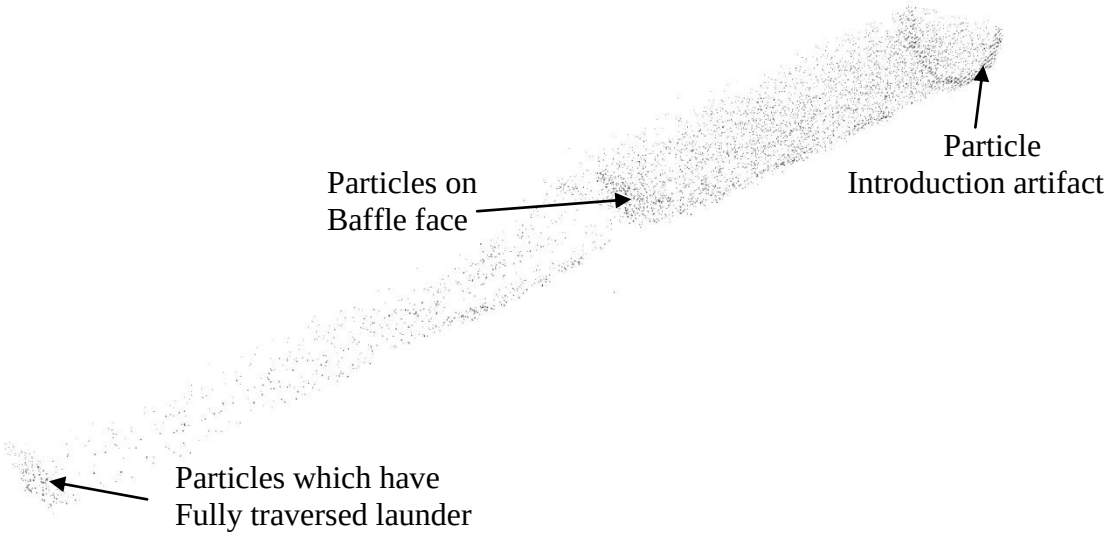

Figure 158. Particle simulation showing just particles - angled view.

The angled views of the simulated particle behaviour (Figs 157 and 158) shows a concentration of the particles prior to the baffle. They also show particles collecting at the outlet face, although these are particles at the outlet that have left the simulated region. Fig 157 shows that the boundary layer, as evidenced by the lighter shade of grey flowing more slowly than the rest of the metal.

5.5 Results Summary

In the first section it was found that there was some transfer of radioactivity into the fluid during metal casting operations, however this was not sufficient to significantly interfere with the tracking of the ^{18}F labelled particles. Careful design of the experiments so as to avoid too much attenuation from the liquid metal, and thermal protection of the positron camera, allowed particles to be tracked up to and including the temperature of molten steel at 1582^{o}C, this was the first time PEPT had been used at temperatures this high.

In the second section particles were tracked in the casting of aluminum plates, which had been performed before, but in addition a bulk particle release was used, again with an aluminium plate mould, though this time a filter was placed in the running system. The plate experiment gathered data about the expected levels of radioactivity needed to track particles (especially when taking attenuation into account) and the filter experiment using PET scans demonstrated that ceramic filters allow quite large particles to pass through even at 30 pores per inch. The PET scans also demonstrated the tendency of the particles in these experiments to float.

A new positron camera geometry was used for PEPT in the third section, this was the first time that this geometry was used. This geometry allowed particles to be tracked as they flowed through a launder, this process was prone to problems when introducing the particles and was subject to issues when particles became stuck within the launder geometry, however particle tracks were collected for both 600μm and 200μm γ alumina particles.

In the fourth section a simulation was created and used to model the particles in the metal flow. Validation of the flow rates was performed by regulating the flow into the model to that experienced in reality and by determining the flow rate at the exit of the launder, the exit flow rate from the model was in close agreement with that from the experiment, it was assumed the flow rates were thus representative elsewhere within the model. The particles were then overlaid , with one way coupling, within the flow model, the velocity of the fastest particle at $0.838ms^{-1}$ at 1.815 seconds confirming that the drag from the fluid 'pulls' the particles along at velocity which after an acceleration period, is slightly below that of the fluid itself, due to the low mass of the particles. The PET scans confirmed that not all particles fully traverse the launder, many collecting against its walls, but some 'sticking' against the surface of the melt mid stream. Particles took slightly less than the 1.815 seconds to traverse the launder in agreement with the 1.7 to 2 seconds in reality.

Chapter 6
DISCUSSION

6.1 Increase in Temperature

The first series of experiments showed the very strong effect of attenuation due to γ rays passing through materials. It is known that the passage of γ rays is impeded by the materials they pass through, and at energies above 1.022 MeV they can create pairs of electrons and positrons. The positrons in turn annihilate with electrons to create pairs of co-linear γ rays, each ray at 511keV.

Below 1.022 MeV, as in experiments using ^{18}F, no pair creation occurs, but positrons can still be emitted directly by the decay of the isotope, these interact with electrons in the same manner to create 511keV γ-rays. The 511 keV γ-rays, however they are created, interact with the electrons of the materials they pass through. At energies around 500 keV the predominant form of absorption is Compton scattering, in which a γ-photon may interact with an electron from an atom shell, changing the photon energy level. The change in energy is reflected in a new lower energy of the deflected γ photon. The amount of energy transferred is proportional to the incident angle of the photon to the particle it interacts with, thus an entire spectrum of γ-ray energies is created ranging from deflections of 180 degrees with the maximum amount of energy removed (the Compton edge) to virtually no deflection and hence only a small change in energy. The scattering of photons in this manner results in a γ-ray absorption co-efficient for any given material. This is not true absorption but is primarily a scattering mechanism, and the term commonly used for this form of attenuation is still absorption.

At energies below 50 keV the γ-photons can interact with electrons from the material, excite an electron and eject it from the shell of the parent atom, and in this case, the energy of the γ-ray is truly absorbed by the material. As the γ-photons from the positron annihilation events are emitted at the rest energy of the annihilated positron and electron at 511 KeV each, the true absorption effect is not predominant.

In the initial experiments (section 5.1.1) the material used was an alloy which was composed of elements which had high γ absorption coefficients, Pb, Bi, Sn, and In. Since the γ-ray absorption is proportional to the exponential of the linear γ absorption coefficient and the material thickness, as given by :

$$\gamma \text{ absorption } = e^{-(\gamma \text{ absorption coefficient } \times \text{ material thickness})} \qquad \text{Eq. 48.}$$

Only a small thickness of the liquid metal could be penetrated by the γ rays. It is of practical interest that American National Institute of Standards and Technology (NIST) quote linear attenuation coefficient in cm [117], rather than the SI unit of the metre, thus the material thickness is usually quoted in centimeters. In addition, in the initial experiments there was an amount of radioactivity being emitted from the metal after the radioactive particle had been removed. Some of the radioactivity had therefore become dispersed throughout the material. The mechanism for this radioactivity dispersion is unknown. The fact that particles could still be tracked in the experiments conducted implied that the radioactivity dispersal is low compared to the activity of the particles. It could be a short term process, which had ended, before too much radioactivity had transferred to the melt, or it is a slow process and the amount of activity transfer during the time taken to perform an experiment is low. One possibility was that any remaining radioactive water from the surface of the particle was transferring its activity to the melt, when it was vapourised by the heat used for casting.

The heat lamp that assisted evaporation of the radioactive water during the indirect particle activation procedure operated at 400^{o}C, it is possible that the surface of the particles made by indirect activation were not completely dry, even with the assistance of a stream of nitrogen assisting evaporation. It is thought that some aqueous ^{18}F physically unbound to the particle surface may still have existed.

Whatever the cause, the magnitude of the activity emanating from a labeled particle was significantly higher than the residual activity in the metal, thus particle tracking in metals remained practical. No significant shift in the apparent position of the particle was observed in the initial Lensalloy experiments, the implication being that the dispersed activity had little effect relative to the much larger effect of the radioactive particle. Motion when moving the entire apparatus was also successfully detected.

Following on from the initial experiment, the apparatus and procedure was modified to allow forced movement of the particle. Tin was also used as well as Lensalloy 136 and particle tracking these mediums was successfully demonstrated. Tin has a higher melting point than Lensalloy but attenuates γ-rays significantly less. A relatively weakly radioactive particle was successfully tracked in the molten tin at ~310^{o}C. It was noted that the Lensalloy and the tin, from which the particle had been removed, remained radioactive, as indicated by the reading from a Geiger counter.

It had originally been thought that the majority of the forces attaching the ^{18}F ions to the surface of a particle were caused by ionic bonding. Fluorine at low concentrations in a aqueous solution forms F- ions suspended within the water. As the water is evaporated, as part of the radioactive particle production process, these ions were thought to attach ionically to the particle surface. It is also possible that bonds could be formed between the particle and the ^{18}F ions by surface adhesion. Surface adhesion bonds relying upon van der Waals forces would be weaker, than ionic bonds, and it would be expected be that due to the high ambient thermal energy during experiments with molten metal, it may be possible to break a proportion of these adhesive bonds and for radioactive species to be transferred into the metal in which the particle is immersed.

Whether the radioactivity was dispersed by van der Waals bonds breaking or the surface water being vapourised, an increase in the number of events that needed rejecting by the tracking algorithm was experienced. The majority of the extra 'noise' this created should have been accounted for in the very early loops within the particle location code.

The next increase in temperature in the experiments was to that of molten aluminium alloy (2L99), this was poured at 750^{o}C. The increase in temperature at which the metal was poured compared to the previous experiments could possibly have increased the dispersal of the radioactivity by the mechanisms discussed earlier, but the attenuation of γ-photons by Al is lower than that of Lensalloy or tin and did not pose an additional problem. This experiment was designed to use steel for which γ-ray attenuation is an issue, as the distance at which the detected activity drops to half its original amount, the halving distance, is only 10.5mm, as compared to 30.5mm for aluminium.

	Lensalloy	Tin	Aluminium	Steel (Iron)
Halving Distance	5.924 mm	10.11 mm	30.41 mm	10.46 mm

Table 11. Halving distances for Lensalloy Tin, Al and steel at 500 keV.

In order to track the particles it was necessary carry out experiments in the castings laboratory and to switch from using an ADAC PET scanner to a modular positron camera which could be set up in the vicinity of the furnace needed to melt the metal.

The modular positron camera was constructed from BGO detector's, as described in section 3.2.3, and these needed protecting from the heat from the molten metal. As the temperature of a BGO detector rises the detectors efficiency decreases and the signal to noise ratio increases. The BGO detector's are also vulnerable to thermal shock, the BGO crystals themselves are vulnerable to cracking, rendering the entire detector block unserviceable.

These problems were solved by the careful design of the experiment, as described in section 3.2.4. The mould itself was an investment shell mould, made of Zircon and Mullite which are more highly attenuating materials than the silica of a conventional resin-bonded sand mould. However the new mould had a wall thickness of 5-7 mm as opposed to 60–70 mm for the sand moulds used for earlier experiments. It therefore had a lower overall attenuation, despite using materials with a higher attenuation coefficient as the γ-rays had significantly less material to penetrate. The 7mm thick investment shell mould attenuates 511 keV γ-rays by 19.4% in comparison to the 60 mm thick sand-resin mould which attenuated the γ-rays by

77.1%. A thin casting section was used, the maximum thickness of metal anywhere in the mould being 20mm. The temperature at the detector faces was managed by thermal protection in the form of MDF boards, two 9 mm thick boards, separated by a 9 mm air gap were used, and tests showed that even with steel at around 1600^{o}C the temperature at the outermost MDF board face rose to only 45 ^{o}C, this being a further 3mm in front of the detector faces. The detectors would thus be expected to experience a temperature lower than this due to the additional air gap. This temperature occurred over three minutes after the steel was poured into the mould. Since the rate of temperature change was low enough that it would not crack the detectors and tracking would have ceased long before the efficiency of the detectors became unacceptable the experiment was conducted to determine if it was possible to track particles in investment shell moulds using aluminium and steel.

These experiments using 2L99 Al alloy all showed particle tracks. One stopped part way down the downsprue, and two ended in the arms connecting the boss at the bottom of the downsprue to the lower ring. Another particle travelled to the base of one of the rods connecting the lower and upper collars, and possibly entered it. The remaining particle was seen to traverse the entire length of a connecting rod and presumably entered the upper ring. The particle which travelled up the connecting rod was then observed to have a great amount of scatter in its reported location, within the upper ring, so much that its location could no longer be determined accurately. Particle tracking was seen to be viable at temperatures around 750^{o}C, but it appears there were issues related to the positron camera at the extremities of its tracking range.

A further increase in the temperature at which particle tracking was carried out was shown when particles were tracked in liquid steel (CLA11), cast at 1580^{o}C. It was believed that this would only be possible if the ^{18}F was ionically bound to the particle surface as ionic bonds, particles which form ionic bonds take up more radioactivity during particle production and it is thought that these ionic bonds are stronger than the van der Waals bonds of surface adhesion and are more stable at high temperatures. Only γ-phase alumina particles were used as glass particles took up less radioactivity during tracer activation, due to a lower number of ionic bonds, but possibly made more bonds by surface adsorption.

The two initial experiments showed an issue with the sensitivity of the array of BGO detector blocks, the modules were arranged in stacks of 4, and there were 4 stacks arranged around the mould as described in 3.2.3, This meant that the lower extremity of the line of response (LOR) detection pattern, at the height of the lowest set of detectors and below, the detection pattern had fewer possible matches from opposing detector blocks and a corresponding drop in sensitivity.

The sensitivity of the positron camera within the viewable volume depended upon the number of possible γ-ray pairs that can strike the detectors at a given location. This relies upon a nearly simultaneous strike (within 7 ns) from the opposing bank of detectors , in the mid-height regions a γ-ray strike may be matched with another strike from detectors at the same height or from the tiers above and below; at the bottom it may only match with tiers above. The restriction on possible matching detectors at the bottom of the viewable volume means fewer γ-ray pairs were detected in this region, reducing the detection sensitivity, The same effect also occured at the top of the viewable volume as γ-ray pair matches can only occur with opposing detectors at the same height or lower. It was believed that the loss of the

particle in the Al experiment where the particle travelled to the upper ring was the same problem, but observed at the top of the positron camera geometry.

It was possible to track a calibration particle in these low sensitivity regions, but the sensitivity was reduced as evidenced by increased scatter in the detected particle location. In cases of high attenuation, it is in these regions that more γ-rays from the source are needed to compensate for the lower sensitivity, in order to track a particle. Particles fail to track in these two regions of the positron camera geometry first although the calibration particle unhindered by attenuation was not affected by this problem. This condition occurred in the first two experiments that were conducted with steel, resulting in the particle track being lost in both, as it entered the lower ring of the mould. The mould was then raised up 72 mm so that the lower ring was no longer in the less sensitive part of the viewable volume of the positron camera. A radioactive particle was then tracked in one of the arms leading to the lower ring of the mould, so it was concluded that the previous loss of tracking in this region was in large part due to the attenuation, contributed to by the metal and the mould and the geometry of the positron camera itself. The next two experiments in steel both tracked particles into the lower ring successfully.

The outcome of these experiments is that particles were tracked at temperatures in excess of 1500^{o}C, although some additional design considerations are required when tracking in highly γ-ray attenuating materials.

6.2 PEPT and PET of particles in Al plates; with and without a filter

Inclusions in aluminium castings are very often made of alumina, in order to try to better understand the movement of these particles, and the efficiency of filters, experiments were performed both with and without ceramic foam filters in the running system.

6.2.1 PEPT tracking of particles in Al plates without a filter

The path of the particles in Al was repeatable to some degree (see Figs. 78 to 90), it was noted however that a significant number of the particles did not make it into the mould cavity itself. The particles that did not pass into the mould cavity were tracked in some cases to the final bend of the running system immediately below and before the ingate. Some particles were trapped in the downsprue. An unanticipated behaviour of the particles was that some actually travelled upwards from the introduction point, coming to rest upon the downsprue wall, at a level higher than where they were inserted into the metal stream. The rising motion of the particles was unanticipated as alumina is almost twice as dense as molten aluminium. The porous γ-alumina particles used in the experiments were measured to have a density lower than that of pure alumina, but greater than that of the liquid aluminium in which they were immersed (see section 3.1) One explanation for this behavior is that the particles were introduced under the surface of the metal within holes made in aluminium rods, and when the rod melted in the metal stream the particle was released, to be carried along by the motion of the liquid metal. Inevitably the hole into which the particle was sealed also contained air (~1.3 mm^3). It would be expected that the air would quickly cause an oxide film to develop as the Al rod melted, and a bubble of air could thus be formed and possibly attach itself to the alumina particle, reducing its apparent density. The increased buoyancy of the particle due to an attached air bubble would then cause it to float upwards in the absence of a strong fluid flow carrying the particle along. Another possibility, but less probable, is that there was a

genuine upwards motion in the metal flow (as the surface of the melt backfilled the downsprue). As the Al rod melted the upward flow would then carry the particle upwards. This condition would not be expected before the downspue filled and the backfilling ceased. A third possibility is that a hydrogen pore develops, nucleating at the site of the inclusion, providing extra buoyancy.

The experiment performed using an Al alloy called A20X, provided a particle track and a final location of the particle. The cast plate containing the particle was machined on a milling machine, until the particle was exposed, confirming the accuracy of the tracking process (to within 5mm in all axes). The particle was attached to the side wall of a pore, which showed no significant oxide layer on the wall surface itself, this may be an indicator that this was a hydrogen pore nucleated around the particle. The particle would be expected to have a poorly wetted surface, and to behave in the same manner as the inside of a bifilm, which can act as a nucleation centre for porosity [129].

.

The particles which did traverse the entirety of the running system and pass into the mould plate cavity displayed a similar motion to each other, typically travelling in swirling patterns before coming to rest. This motion within the metal, was to be expected in a poor filling mould design.

It was noted from the experiment that the mould itself contributed very significantly to the total γ-ray attenuation experienced, the mould walls being 60 mm thick. The mould was positioned upon a diagonal line within the square pattern defined by the positioning of the positron camera detector modules. Since the mould was angled in this manner any γ-rays travelling perpendicular to the detector faces, the shortest distance possible, would have had

to travel through 85 mm of silica sand. This meant that even allowing for the porosity in the sand the mould attenuated the γ-rays by 77% out of a total attenuation of 86%. Tracking particles was achieved with only 14% of the 511 keV photons reaching the detectors, with tracking being lost at a level of around 50 μCi. Since 14% of 50 μCi is just 7 μCi, we would therefore expect to be able to track a single particle unshielded by attenuating materials, or a particle with attenuation, if the remaining radiation detected was equivalent to 7 μCi or more.

6.2.2 PET particle distribution in Al plates, after using a ceramic foam filter

This series of experiments demonstrated that using ceramic foam filters allowed a significant number of inclusions to pass through a filter (at least 7 – 13 distinct particles in each experiment). It should be remembered that the filters were not primed and that the particle count was based on those that were discernible from the images of the cast plates. Previously Beshay had tracked particles in Lensalloy and had shown that particles are removed from the melt by them, he recovered the particles from within the filters at the location given by PEPT [116].

It these experiments it appears that many of the particles did not even reach the filter (based on the 9 particles found in the downsprue in the first successful experiment, section 5.2.2 Figs 97 and 98, the downsprue was not scanned in subsequent experiments). The other two experiments displayed a similar percentage of particles in the plate and in the filter, leaving a number of particles unaccounted for. These were presumably also left in the running systems of these experiments. The filters used in these experiments were 10, 20 and 30 ppi, but no significant variation in the final particle distribution was observed, despite the significant

variation in pore size, all of these filters cannot remove 600 µm particles when used as a sieve and rely upon operating in a deep bed filtration mode which does not appear to be completely effective.

The first experiment had a count of 12 particles in the plate, 9 in the filter and 9 in the running system, three particles were not seen, but since three particles were introduced as pairs, in the same introduction hole as another particle, they may have travelled together, this then gave a total of 30 particles to be counted. It gave a ratio of 40:30:30 for the plate, running system and downsprue respectively. The second experiment had 8 particles in the plate, 7 in the filter and the remainder (7) in the running system. Out of 22 particles this gave a ratio of 36:32:32 for the plate running system and downsprue respectively . The third experiment had 12 particles in the plate, 7 in the filter and the remainder (11) in the running system. Out of 30 particles (again 3 may have travelled as pairs) this gave a ratio of 40:23:37 for the plate running system and downsprue respectively. The ratio of particles passing through the filter was consistent regardless of whether a 10, 20 or 30ppi filter was used.

The calculations for the amount of radioactivity retained by a filter were in large part affected by the unexpected variation in the measured activity levels of the ^{22}Na source used as a reference. This appears to be related to the source location relative to the detector plates, and implies that the sensitivity of the ADAC camera is uneven, was least for weak sources where the count rate is low.

A maximum and minimum (based on the highest and lowest reference count respectively) for the activity remaining in the filter was determined, based on the event count rate in the plate

and running system for the first experiment, this showed the radioactivity in the filter lay between 10.1% and 20.1% of the total radioactivity of all the particles.

The information from the count rate data should perhaps be taken as needing further investigation as the count rate at the start of an imaging session and the count rate at the end of an imaging session did not follow the expected decay curve for ^{18}F. This could possibly be explained by a non linearity of the PET scanners count rate sensitivity, and the change in detector dead time as the activity decreased, This observation throws doubt on the viability of this radiological method of accurately determining particle concentrations, using PET scanners originally intended for medical use.

The technique of counting the particles is dependant upon the clarity of the image produced. Too short a data collection period and particles could not be detected as the data needed to show them was not collected in sufficient quantity. Too long an ‘exposure’ and the particle image could saturate and the particles could not then be counted in the backscatter image reconstruction.

The indication from both the count rate data and the physical particle image counting is that in these experiments roughly 30% (~10) of the particles released were trapped in the downsprue, a 30% (~10) were trapped in the filter itself, and approximately 40% (12-13) of the particles made their way completely through the filter and into the mould cavity itself.

It should also be noted the envelope density of the particles used was greater than that of pure alumina and aluminium, and the particles were found largely trapped against the top-most

edge of the mould cavity, and some against the top edge of the running system overshoot (Figs.44 and 104). The positions the particles were found in, suggests that the additional buoyancy forces may also have been at work during these experiments.

The atmosphere surrounding each particle in the introduction plate could have been trapped with the particle during its transit through the mould. It is now understood that an atmospheric pocket within molten Aluminium would have its constituent gases consumed by reaction with the melt [62], into the film layer surrounding the gas pocket, though this would not be expected to occur within the few seconds the particles travelled before coming to rest. Alternatively the gas pocket could be formed by hydrogen following the nucleation of a pore at the site of the inclusion [129]. Either mechanism would have caused the particles to rise in the melt, but the film of the pore in which a tracked particle was found did not contain oxides and nitrides, suggesting some other gas formed the bubble, hydrogen being the most likely candidate given its high solubility in liquid aluminium.

An unexpected side effect of the PET process was observed, the shape of the plate itself could be discerned at lower particle radioactivity levels. At high activity levels noise from scattered random LOR events made it possible to detect a pattern in the collected data. The pattern matched the layout of the photomultiplier tubes of the ADAC camera and it was therefore assumed that it was due to the increased sensitivity of the positron camera at these points. Increasing the contrast of the low count rate areas of the scan also allowed this effect to be observed. At lower activity levels the shape of the cast plate itself was seen. This is difficult to explain, unless some activity had transferred to the metal and was evenly distributed within it. Alternatively it was possible that the plate was scattering γ-photons such that a significantly high proportion were able to cause additional coincident pair strikes

within the outline of the plate, but not outside it where there was no scattering effect. The count rate in the pixels showing the plate was typically around 10 counts per hour, as opposed to 2-3 counts per hour for the background, so whilst significant these γ-photon strikes were still at a very low level. It was several hours after particle production and use, before this effect could be seen, any earlier the 'random events' in the data swamp the signal and the plate cannot be seen. It is debatable as to whether this phenomenon could be the basis of a useful process.

6.3 The tracking experiment using a launder using aluminium

The object of the launder experiment was to track γ-alumina particles as they were carried down a launder and then to compare the path recorded for these particles with that from a simulation. The concept was to introduce particles so that they would be carried in the metal stream and observe how they negotiated an obstacle (a baffle) placed in their path.

6.3.1 Tracking experiment using a launder in aluminium with 600μm particles

It had been noted from previous experiments that the tracking apparatus displayed considerable scatter and inaccuracy in its predicted locations when the count rate, (at the time of use and allowing for the attenuation of the liquid metal, mould and thermal protection), dropped below a representative value of 7 μCi. This was not a true activity level (as it is an indirect, but proportional, indication of the radiation emitted, radioactivity is an absolute value) and hence the units of micro Curie is technically incorrect, however it gives an indicative level of when particle tracking is possible and when it is not. It was important that the attenuation in the experiment was kept low and it was thought that the experiment should represent a real industrial launder. A small cross section launder was used, made of calcium silicate, and this material had a relatively low density and thermal mass. It was therefore

suitable as it would not remove too much heat from the aluminium, whilst still allowing the γ-rays to pass through. The maximum measurement of launder cross section was its width, this was 74mm and calculations indicated that the attenuation of this thickness of aluminium in conjunction with the attenuation from the calcium silicate still fell within the limits required to track a 250 μCi γ-alumina particle. Particles with this level of radioactivity can be made routinely with the cyclotron available.

The results showed a tendency for the particles to have difficulty successfully entering the metal stream, where particles then get 'trapped' before the viewable region of the launder. The radioactivity of these particles added additional noise, that the detectors experience from outside their viewable volume, (the volume encompassed by the detectors and within which the detection sensitivity was acceptably high). The cause of this problem was suspected to be air entrained with the particle as it is released from the Al 'introduction' rod, possibly exacerbated by hydrogen infiltration. This it is thought, caused the particles to rise to the surface of the melt, whereupon particle becomes trapped at the oxide film. A similar particle rise effect was observed with the earlier filter experiment, in that experiment particles had floated up and become trapped at the top of the mould.

Some of the particles, which did track successfully, showed an upwards tendency at the start of their path through the metal. The data from the free surface simulation indicated that, although there was an upward component to the flow until it encountered the baffle, this was not large enough to explain the initial rise of the particles. In the particle simulation it was indicated that this upwards motion would only just overcome the particles tendency to sink to the bottom of the launder but not enough, to cause the rapid rise of the particles observed in

reality. It was therefore assumed that as in previous experiments an attached gas bubble added extra buoyancy.

None of the physical particles which were tracked, were seen to strike the front face of the baffle. This was not surprising as the simulation predicted that only around 2% of particles would become trapped against the baffle. A consequence of this is that we would expect to need to conduct around 50 such experiments before seeing any particles become attached to the baffle face. Add to this the lifting motion of some particles after introduction and a far larger number of physical experiments would be required. Since it was only practical to create around eight to ten particles per day, running the experiment several hundred times, in order to gather such statistical information, was not possible. In the experiments conducted 26 particles were released of which only ~11 entered the metal stream. We would need to use an electromagnetic stirring furnace, introduce a single particle and observe it going around a closed path, in order to observe such an event.

In addition the simulation showed that particles would not be expected to easily enter the boundary layer close to the launder wall, due to the drag from the flow tending to pull the particles along with it. The particles would only occasionally be expected to attach to the launder wall. The 600 μm PEPT particle tracking experiment did not show any such events. However the PET scans of the upper reaches of the particle introduction area did show some particles lying against the launder walls. This may perhaps be explained by a thickening of the surface oxide layer, a chevron pattern, in the oxide layer, being seen heading into the central flow, see section 5.3.3 Fig. 146, caused by a slower metal flow at the edges of the launder. Particles attached to the oxide skin may have been caught in this area, where the

boundary layer, at the side wall of the lauder, causes the aluminium to flow slower under the oxide film surface.

The particle introduction area was close to a joint between the launder, in which tracking took place, and the furnace launder. It was apparent that out gassing caused this area to be more turbulent than would be ideal, also possibly helping to lift the particle.

In conjunction with a high introduction point these mechanisms may have combined to bring particles to the surface, trapping them, before entering the metal stream proper. Particles introduced lower in the metal stream travelled more successfully along the launder, although the particle track in section 5.3.1 Fig 117 shows evidence of particles initially rising.

6.3.2 Tracking experiment using a launder in aluminium with 200µm particles

The experiments using 200µm particles were split into two exercises, the first to track particles within the liquid aluminium to show that this was possible, and also to look for differences in behaviour as the particle size was reduced. The second activity was to introduce a large number of particles simultaneously and perform PET scans covering the entire length of the launder in order to determine the final locations of the particles of this size in the solidified melt.

6.3.2.1 200µm particle tracking

The 200µm particle size experiments were very sensitive to the particle insertion depth within the metal at depths (measured from the top of the launder) of less than 40mm no particles traversed the launder. When the introduction depth was increased to 45mm a particle track,

was recorded, however there were many scattered predicted particle locations around 150 to 100mm before the baffle. These scattered locations were very high, above the height of the top of the launder. The particle which did track, emerged from this ‘noise’ and was also above the level of the top of the launder, and implies that something was distorting the reported particle position.

It is perhaps interesting that the tracking algorithm was not able to predict any particle locations in the first 150mm of the launder in many of the experiments even when no previous particles had been released. When the liquid metal had been run down the launder for some time (90 seconds or more) prior to the insertion of particle, tracking accuracy would be poor, or the track, completely lost in this region of the launder. The efficiency of the BGO detectors is known to decrease with an increase in temperature and it is logical that the detectors closest to the furnace are heated both by the radiant heat from the furnace itself and by the hottest metal in the launder, before it loses heat during its flow down from the furnace. It may have been that some particles which were not tracked were trapped in the upper reaches of the launder where the tracking was less effective.

The fifth particle in experiment four showed some abnormal behaviour in that immediately following the baffle the particle displayed an almost horizontal swirling motion. This had not been predicted from the fluid flow models. This was the only particle tracked that had travelled very low in the metal stream, and this brought it very close to the top of the baffle and into the zone immediately following the baffle, where the flow was adjusting after its’ passage over baffle. This region was predicted by the free surface model to have a very low flow rate inconsistent with the motion observed.

It is unfortunate that these experiments were so difficult to perform, as repeating the experiment significantly many more times may have revealed statistical trends in the passage of the particles down the launder. The inconsistencies found, indicates that the transport of inclusions in liquid metal is complex and that the tracking of particles is difficult. In most other uses of PEPT particles are passed though the same experimental region (as with mills and washing machines) many times [23,15,19], some experiments having a radioactive particle passes through apparatus many times [5], in order to generate statistical data regarding particle paths, this is not feasible in liquid metals due to the difficulties of recovering particles from hot dense metal melt.

6.3.2.2 Particle Cloud PET scans

The multiple particle release experiment was intended to show the final location of particles which failed to completely travel the length of the launder. The particles were tracked after release but the positron camera and its software was not capable of tracking any more than three particles at a time. The version of the software used in the experiment was intended to track just one particle, this meant that the results would not be entirely predictable, indicating a radioactive hotspot, with an error larger than that when tracking a single particle. The PEPT scan, section 5.3.3 Fig. 130, showed particle locations above the top of the launder, clearly these locations were erroneous. There was an area of predicted locations that lay inside the metal approximately 20 mm before the baffle, at this location, about 60-70 mm above the top of the launder, there was a ‘cloud’ of predicted particle positions. Coming out of this is ‘cloud’, there was a particle track. It is thought that the ‘track’ emerging from the upper cloud of particle positions was created as a result of miltiple particles passing through the liquid

metal at the same time. The track being at a height above the launder may have been due to selective attenuation as discussed for an earlier experiment,(section 6.3.2.1).

The image slices of the launder were generated as a series of attenuation and transmission scans of the entire launder as described in 3.2.7.2. Only nine or ten particles were seen in the solidified metal after the experiment, this includes several which remain at the free surface and some which appear to be attached to the launder walls, this is out of a total count of more than thirty five particles introduced. The particles which were retained within the metal stream consisted of four particles on the top surface of the metal but away from the edge of the launder. Four particles were found at the surface of the metal and alongside the launder wall., the model did not predict particles rising to the surface of the melt, perhaps because of gas bubbles lifting the particles. Particles which reach the surface of the melt are unlikely to re-enter the metal stream due to the effect of surface tension and the surface oxide film, and they may adhere to the underside of the oxide layer. They would be expected to travel at the same rate as the surface oxide layer which was expected in turn to be lower than the main body of the melt, due to its solid nature, forming, breaking and reforming under the influence of the surface turbulence and interfacial forces

.

A distorted image of at least one, but probably several particles, was found at the bottom of the metal alongside the launder wall in frame 36 (section 5.3.3 Fig. 133). The distribution suggested that many of the particles remaining in the melt had floated up to its surface, in the region before the baffle, where the maximum flow rate was 0.4 $ms^{-1,}$ below the critical velocity for surface turbulence. No particles were found downstream of the baffle. This is where the simulation showed the metal stream flows at its fastest rate, in excess of 0.5 ms^{-1}, and where particles would be expected to be kept in the metal stream by the drag force they

experience. Due to the particle's high superficial slip velocity (the velocity of the fluid slipping past the particle, relative to the particle's velocity) , a large drag force is induced in the direction of the flow, which shepherds them into the body of the metal.

The particles after the baffle would be travelling faster, and any collisions with the launder wall would involve more energy. The pull off force for the particles would be that of a 200μm alumina sphere in contact with calcium silicate (or more likely an alumina film, deposited as the metal was poured), this is not expected to be excessive (the surface energy of alumina is 2.36 J/m^{-2} [130]), and the contact area expected to be ~20μm, it is therefore unlikely that particles would be able to adhere to the launder walls in this region.

It is also notable that the fluid velocity after the baffle was above the critical velocity for aluminium, and that the flow would therefore be turbulent at its surface and particles may be returned to the body of the melt by this surface turbulence.

It could also be argued that a Saffman lift force would also be exerted upon the particle due to the shear flow in and near the launder boundary layer. The velocity gradient within the fluid, and across a particle causes an inertial lift. This too would contribute to the difficulty particles have reaching the launder wall as the lifting force would always be away from the launder surface.

6.4 Free Surface simulation

A CFD model was used to generate a free surface model of the aluminium flowing within the launder. The flow upstream of the baffle was relatively slow and the metal 'backs up' and rises as it flows over the baffle Fig.155. The flow in this region has an upward vector component and this helps lift the particles just before they encounter the baffle. Fig 148. The effects of surface tension and the oxide film were neglected in the simulation. It was assumed that since the free surface, (the surface of the metal open to the air) was calculated dependent upon the pressure within the liquid metal, that the surface tension and the oxide film would not significantly affect this parameter and would have a negligible effect upon the position of the free surface.

The particles which were thought to be under the surface of the metal displayed a more or less consistent behaviour of flowing initially upwards, presumably assisted by a pocket of air, entrained with the particle at its introduction into the metal stream, or by hydrogen nucleated from the melt at the particles' location. After this they would flow inside the metal stream, rising before the baffle and then falling with the metal level afterwards, before slow sinking as they travelled to exit the launder, in the simulation they showed a gentle rise before the baffle and a fall with the metal stream after it, followed by a slow descent before exiting the launder. Apart from the almost consistent initial rise of the particles at the start of their track in the experiments, the motion of the particles was confirmed by the experiments.

In the launder experiment with 35, 200μm particles released as a 'cloud' of particles, some particles were observed attached to the launder wall before the baffle. The flow in the boundary layer in the region before the baffle was shown by the simulation to be very low,

Particles in this region also progress relatively slowly, (less than 0.2 ms^{-1}), whilst in the main bulk of the metal and have a chance of adhering to the wall of the launder should they enter the boundary layer and decelerate through it, such that their momentum is less than the pull off force at the point of the collision with the launder wall. At the position of the baffle, the fluid flow accelerates to around 0.2 ms^{-1} and the velocity within the boundary layer also increased. When the particle simulation was run in these models they indicated that at and beyond the baffle position, that the boundary layer flow even though it is lower than the main flow at 0.7 to 0.845 ms^{-1}, it still exceeds 0.4 ms^{-1} for the majority of its flow downstream of the baffle, the boundary layer after the baffle, is faster than the main flow before the baffle. The higher rate of flow in the boundary layer, would carry the particles at a higher velocity and make it harder for them to adhere to the launder wall.

There was some evidence (Figs. 120 and 123) that perhaps particles did collect on (or under) the metal surface from the particle tracks and this was confirmed by the multiple particle 'cloud' experiment. No particles were seen to collect at the metal surface after the baffle in the experiments, the simulation indicated that particles did not reach the metal surface as it neglected the additional buoyancy of the attached gas bubble. Below the critical velocity, the velocity at which the surface turbulence exceeds that which the surface of a stream of liquid has the ability flow in a laminar fashion, it is assumed that the oxide film will be unbroken and stable upon the surface of the melt, for Aluminium this has a value of 0.5 ms^{-1} [58]. Above this value the surface film is assumed to break due to turbulence, the metal to flow, exposing new material and the film to reform. Surface tension (and presumably the oxide film, by surface adhesion) are capable of supporting masses upon the surface of a fluid. The expected consequence of this phenomena is that the surface oxide film before the baffle is effectively a sheet floating upon the surface of the metal stream, and would be expected to be

dragged along by the interfacial forces between itself and the metal, arrested by the forces exerted where the film contacts the launder walls. At less than $0.2ms^{-1}$ the underlying flow would not, on its own, be sufficient to break the oxide film at the surface directly, however the interfacial force would pull the metal from below and break the oxide film where it meets the launder wall by the shearing action at this location. Shear forces will be set up where the oxide layer adheres to the launder wall and the motion of the underlying fluid drags the oxide layer inboard of the boundary layer along, whilst that attached to the wall is stationary. The oxide layer appears to break and reform at this position and the oxide layer displays a "chevron" pattern, it is thought that any particles on the surface at the edge of the launder could be trapped with the static part of the oxide film, attached to the launder wall. Following the baffle the underlying flow is much higher, the surface becomes turbulent (as seen by the flow rates in the simulation exceeding the critical velocity) and particles at the surface may be reentrained in the metal stream, explaining why none are seen trapped on the surface, beyond the baffle.

The 5^{th} particle in the 4^{th} 200μm particle experiment travelled particularly low in the metal stream and indeed was the only particle to enter the area immediately beyond the baffle. This region was indicated by the simulation to have low flow rates. The particle swirled in the metal stream completing two elliptical rotations. However this was atypical of the motion observed in the simulations and not expected, given the low flow rates ($< 0.075ms^{-1}$,Section 5.4.1 Fig. 150) predicted by the simulation.

There are a great many more forces that could additionally be added to the model. An additional stress tensor force is known to exist whenever a fluid accelerates or decelerates and contact damping , magus lift, and Saffman, Hall or Mollinger lift could also be included. In

the case of the inertial lift forces caused by the shearing motion due to a velocity gradient around the particle, (Saffman, Hall or Mollinger lift), this has been reported to be negligible by Johnson at small shear rates and low (particle) Reynolds number. However, in denser materials such as metals the effect may be more significant. Brownian motion may also be additionally considered, by adding a random element to affect the particle path. Such variations may be important in explaining the path taken by individual particles during validation experiments, particularly as to why the particle paths taken are not entirely deterministic. Contact damping may have small effect upon colliding particles, given their small size <600 μm, elastic modulus ~300 GPa and velocity, up to ~0.83 m s^{-1} this may not be too significant. Magnus lift is applicable to rotating spheres and as many inclusions are not spherical, it is inappropriate to include this force.

6.5 Discussion Summary

The attenuation of γ-rays is critical to the success of the PEPT process, and although radioactivity dispersal to the metal was seen, provided the γ-rays attenuation is sufficiently low PEPT can still function, an activity level equivalent to 7μCi after attenuation was determined as the lower cut off point for successful tracking. Particles were tracked at temperatures in excess of 1500^{o}C and a particle was physically recovered at its anticipated position following an experiment. The recovered particle was attached to the side of a pore, and this may have been gas introduced alongside the particle (as originally suspected), or hydrogen which had nucleated at the site of the particle (as indicated by the lack of oxide on the inside wall of the pore, indicated by EDS analysis). Particles were found in a 4:3:3 ratio in the plate, filter and downsprue of a plate casting with filters of various pore densities (irrespective of pore size). Comparison with activity levels calculated from the count rate of the PET imaging, had large errors and only gave a crude agreement. The cast plate was seen

on some PET images where the radioactivity levels of the particles were low. Particles were tracked down a launder and some agreement with simulated particles was found, although tracked particles showed a rising motion following introduction into the metal stream where the simulated particles did not. Particles were seen in some experiments (erroneously) above the height of the metal and this may have been because of different levels of attenuation, above and below the particle when it was at or near the surface of the metal. In the launder experiment, particles were seen both on the surface of the aluminium and against the launder walls upstream of the baffle, but not in the main body of the solidified metal. None were seen in the metal remaining in the launder after the baffle. No particles were seen to collect upon the baffle face, even though the model predicted this was possible, one particle which travelled low in the metal stream showed an elliptical motion not predicted by the model. The forces not included in the model, such as inertial lift, magnus lift and contact damping were also considered.

Chapter 7
CONCLUSIONS

7. Conclusions

1. Tracking experiments were carried out successfully in a low melting point alloy, liquid tin and aluminium alloys, at temperatures of ~400, ~320 and ~750°C respectively. γ alumina was used for the tracking experiments in steel, due to its high melting point (over 2100^{o}C) and its high affinity for F- ions. PEPT was demonstrated at temperatures of up to 1582^{o}C, and it is thought that the ability to track particles at these temperatures indicated that ionic bonding of the ^{18}F to the surface of the particle had occurred.

2. The observed radioactivity spread into the bulk of the liquid metal may be possibly explained by some ^{18}F bonding by surface adhesion to the radioactive particle, (by van der Waals forces), or that some of the ^{18}F was still in an aqueous solution, in moisture on the surface of the particles, despite attempts to dry them. In either case it may be possible for loosely bound or unbound ^{18}F to disperse throughout the liquid metal

3. Particle tracks obtained during mould filling of a mould without a filter showed the general path of particles as they travelled unhindered into a simple plate mould. A degree of consistency of the paths taken by individual particles was observed.

4. An activity of about 7μCi or more, after allowing for attenuation, was determined to be the minimum activity necessary to allow particle tracking with the equipment used in these experiments.

5. When a filter was introduced into the running system it was apparent from the PET images enerated in each of the castings that a significant number of particles had passed through the filter and into the cast plate itself. This implies that the filters do not work well in their intended role of filtration and cannot be relied upon to make inclusion free castings. They do reduce the number of large inclusions in the casting but do not eliminate them. Further work with both pet and PEPT with varying filter pore sizes and varying particle sizes could more accurately quantify the effectiveness of these devices.

6. It was apparent that a significant number of particles were trapped within the filter, and although the downspue from only one experiment was imaged with a PET scan, this showed that particles were also deposited in this location within the casting.

7. It was possible to count the particles in the PET scans where their images were distinct, but it was not possible to determine if each observed region of activity was due to a single particle or a collection of particles, this was due to the differing radioactivity uptake of each particle, when they were produced.

8. Visual inspection of PET images showed that roughly 40% of the particles were found in the cast plate, 30% in the downsprue and 30% in the filter. Since only 70% of the particles, (by particle count), reached the filter, 57% of those that did, passed through it. At 43% the filter efficiency is low, but within specification for a 30ppi filter [131] and reasonable for the 20 and 10 ppi filters .

9. The calculations from the LOR count rates show, (despite a very large error band) that at least 10% of the original tracer activity, resided within the filter. This is indicated to be a minimum of 10% and up to 20% of the tracer activity, (allowing for the particles retained in the downspue this gave a filter efficiency of 11% to 23%). These figures show that some particles were present in the filter, but indicated that the manual particle count was a better method of determining the number of particles in a filter than the activity count rate.

11. The experiments were capable of tracking radioactive alumina particles as they travelled down a launder, although introducing particles into the metal stream, under the surface tension and surface oxide film of the molten aluminium was difficult.

12. The particle tracks had a generally reproducible form, This consisted of a rapid rise of the particle at the start of the launder, before gently rising over the baffle and falling with the metal stream over the edge of the baffle. After the baffle, in the faster flowing metal, the particles would continue on a gentle descent before exiting the launder.

13. The CFD simulation showed a correlation with both the free surface shape and the anticipated inlet and outlet flow velocities and the model was therefore assumed to be a reasonable representation of the metal as it flowed down the launder. Surface tension and the aluminium oxide film was neglected in the model. When simulated particles were released into the predicted liquid metal flow, the general form of the particle tracks had similarities to that from reality, in that they rose slightly as they approached the baffle, travelled over it before slowly sinking in the metal stream, the initial rise in the path of the particles, may have been due to entrained air introduced with the particle or hydrogen nucleating around it and did not match with the simulation.

14. A small number of particles in the simulation (~2%) collected after the baffle. In comparison the real particles which were tracked did not show any tendency to collect after the baffle. This may possibly be explained statistically as less than 40 particles were physically tracked in the launder and the majority of the particles in the simulation which did pass over the baffle, exited the simulation at the outlet.

15. Only one physical particle track was significantly different to the norm. In this, the particle travelled low in the metal stream. The particle made a pair of horizontal elliptical loops immediately following the baffle, a behaviour not observed in the simulation, where the region immediately after the baffle was calculated to have an exceptionally low flow rate ($3.6\ e^{-17}\ ms^{-1}$) and no simulated particles entered that particular region.

16. Some particle tracks were recorded to be above the height of the melt. It is thought that this may have been due to differential attenuation in dense materials, the degree to which all particle tracks are distorted by this effect is currently unknown.

Chapter 8
FURTHER WORK

8. Further Work

1. Further investigation into the phenomenon of radioactivity spread from particles made radioactive by the ion-exchange method into the metal is required.

2. Further investigation into the flow in a model and its effect on a simulated particle in the region immediately following the baffle may be needed.

3. Further work is required to improve the accuracy of the LOR counting technique to determine the activity in a sample, particularly with respect to the reference giving differing count rates defendant upon its location within the positron camera.

4. The effect which allows the plate shape to be detected by PET, whilst the plate contains a weakly radioactive particle could be investigated.

5. The effect which caused some particles to be tracked above the metal level needs to be investigated, to find a solution to this. PEPT had only previously been used in low density materials, or with particles equidistantly surrounded by dense material. There may be an effect upon the location accuracy of particles detected by PEPT, due to differential attenuation of γ-rays by differing thicknesses and density of materials.

Appendix A

Monte Carlo simulation example

A Monte Carlo algorithm to find the value of PI, coded in Napoleon Brandy Basic [132] (and BBC Basic for Windows [133]) is shown below;

```
 1 Squarecount=0
 2 Circlecount=0
 3 SquareSide=200
 4 MODE20
 5 COLOUR 0:COLOUR 128+7:CLS
 6 ORIGIN 640,512
 7 FOR N=1 TO 100000
 8   X=RND(SquareSide*2)-SquareSide
 9   Y=RND(SquareSide*2)-SquareSide
10   Squarecount=Squarecount+1
11   GCOL0,1:PLOT69,X*2,Y*2
12   IF SQR((X*X)+(Y*Y)) < SquareSide Circlecount=Circlecount+1:GCOL0,2:PLOT69,X*2,Y*2
13 NEXT
14 PRINT"Points in square ";Squarecount
15 PRINT"Points in Inscribed Circle ";Circlecount
16 PRINT"Calculated value of PI ";(Circlecount/Squarecount)*4
```

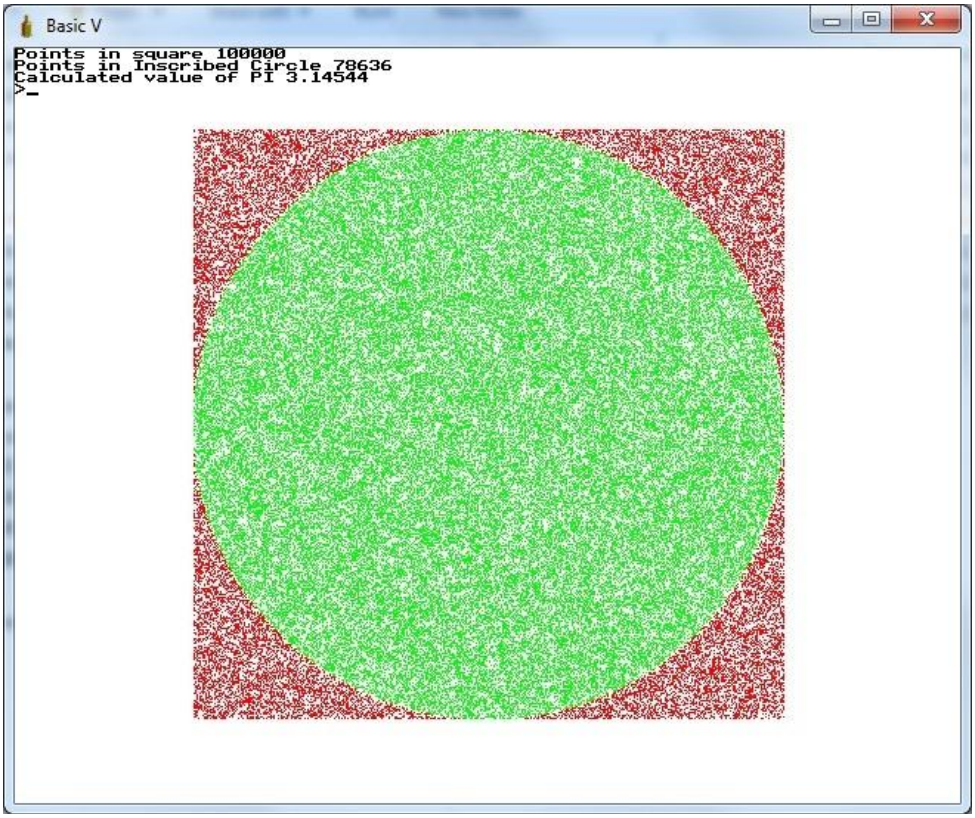

Figure A1. Output of a Monte Carlo method to find the value of Π

Appendix B

Experimental procedure data

B1.1 Particle tracking in Steel and Aluminium experiment

Experiment Number	Cast Material	Particle Type	Initial Radioactivity (Ai)	Time between production and use (t)	Calculated Radioactivity at time of use (At)	Reference value after attenuation
1	CLA11 Steel	γ Alumina	1845μCi	60m	1341μCi	91.72
2	CLA11 Steel	γ Alumina	1180μCi	90m	696μCi	47.68
3	CLA11 Steel	γ Alumina	1697μCi	120m	769μCi	52.67
4	L2-99 Al	γ Alumina	550μCi	45m	437μCi	110.39
5	L2-99 Al	γ Alumina	462μCi	75m	304μCi	76.79
6	L2-99 Al	γ Alumina	436μCi	105m	227μCi	47.34
7	L2-99 Al	γ Alumina	334μCi	125m	144μCi	36.37
8	CLA11 Steel	γ Alumina	1770μCi	90m	1040μCi	71.24
9	CLA11 Steel	γ Alumina	1740μCi	110m	868μCi	59.46
10	L2-99 Al	γ Alumina	1540μCi	130m	628μCi	158.63

Table B1. Particle Radioactivity levels, all particles 600 μm

B1.2 600µm particle tracking experiment

Radioactivity decay data for particles used for tracking experiments are detailed below.

12:55 Particle Creation -> 14:15 Pour time (80 Minutes elapsed time)

Particle Number	1	2	3	4	5	6
Initial Activity (µCi)	819	594	513	472	538	520
Activity at time of use (µCi)	494	358	310	284	325	314
Reference value allowing for attenuation	55	36	34	31	36	35

Table B2. Radioactivity levels for 600µm particle tracking experiment 1

16:25 Particle Creation -> Pour time 16:51 (26 Minutes Elapsed Time)

Particle Number	1	2	3	4	5	6
Initial Activity (µCi)	928	924	1074	813	935	1090
Activity at time of use (µCi)	788	784	911	690	793	924
Reference value allowing for attenuation	88	87	101	77	88	103

Table B3. Radioactivity levels for 600µm particle tracking experiment 2

13:01 Particle Creation -> Pour time 13:21 (20 Minutes Elapsed Time)

Particle Number	1	2	3	4	5	6
Initial Activity (µCi)	1346	1057	971	1381	940	957
Activity at time of use (µCi)	1186	931	855	1217	828	843
Reference value allowing for attenuation	132	103	95	136	92	94

Table B4. Radioactivity levels for 600µm particle tracking experiment 3

16:21 Particle Creation -> Pour time 16:57 (36 Minutes Elapsed Time)

Particle Number	1	2	3	4	5	6	7 (left)	8(right)
Initial Activity (µCi)	528	422	860	446	628	614	459	662
Activity at time of use (µCi)	421	336	685	355	500	489	365	527
Reference value allowing for attenuation	46	37	76	40	56	54	41	59

Table B5. Radioactivity levels for 600µm particle tracking experiment 4

The additional short rods ranged from 382uCi to 886uCi at production.

B1.3 200µm particle tracking experiment

Radioactivity decay data for particles used for tracking experiments are detailed below.

18/09/2013 11:30 Particle Creation -> Pour time 13:57 (177 Minutes Elapsed Time)

Temperature in pouring basin 801 ^{o}C

Particle Number	1	2	3	4	5	6	7	8
Initial Activity (µCi)	203	275	414	246	239	152	72	229
Activity at time of use (µCi)	80.2	108.7	163.6	97.2	94.5	60.1	28.5	90.5
Reference value allowing for attenuation	10.5	14.3	21.5	12.8	12.4	7.9	3.7	11.9

Table B6. Radioactivity levels for 200µm particle tracking experiment 1

All particles were introduced at a depth of approximately 45mm

18/09/2013 15:00 Particle Creation -> Pour time 16:59 (119 Minutes Elapsed Time)

Temperature in pouring basin 807 ^{o}C

Particle Number	1	2	3	4	5	6	7	8
Initial Activity (µCi)	31	344	294	239	215	146	313	178
Activity at time of use (µCi)	14.6	162.3	138.7	112.7	101.4	68.9	147.6	84.0
Reference value allowing for attenuation	1.2	21.3	18.2	14.8	13.3	9.05	19.4	11.0

Table B7. Radioactivity levels for 200µm particle tracking experiment 2

All particles were introduced at a depth of approximately 40mm

19/09/2013 12:24 Particle Creation -> Pour time 14:22 (118 Minutes Elapsed Time)

Temperature in pouring basin 810 ^{o}C

Particle Number	1	2	3	4	5	6	7	8
Initial Activity (µCi)	210	407	328	209	294	216	473	285
Activity at time of use (µCi)	99.6	193.2	155.7	99.2	139.6	102.5	224.5	135.3
Reference value allowing for attenuation	13.1	25.3	20.5	13.0	18.3	13.5	29.5	17.8

Table B8. Radioactivity levels for 200µm particle tracking experiment 3

All particles were introduced at a depth of approximately 35mm

19/09/2013 16:45 Particle Creation -> Pour time 18:02 (77 Minutes Elapsed Time)

Temperature in pouring basin 812 ^{o}C

Particle Number	1	2	3	4	5	6	7	8
Initial Activity (µCi)	288	640	193	163	1000	501	234	560
Activity at time of use (µCi)	177.1	393.6	118.7	100.2	614.9	308.0	143.9	344.4
Reference value allowing for attenuation	23.3	51.7	15.6	13.2	80.8	40.5	18.9	45.3

Table B9. Radioactivity levels for 200µm particle tracking experiment 4

All particles were introduced at a depth of approximately 35mm

20/09/2013 15:17 Particle Creation -> Pour time 16:16 (59 Minutes Elapsed Time)

Temperature in pouring basin 812 ^{o}C

Particle Number	1	2	3	4	5	6	7	8
Initial Activity (µCi)	608	332	328	241	474	368	469	560
Activity at time of use (µCi)	418.9	228.7	226.0	166.0	326.6	253.5	323.1	385.8
Reference value allowing for attenuation	55.0	30.0	29.7	21.8	42.9	33.3	42.5	50.7

Table B10. Radioactivity levels for 200µm particle tracking experiment 5

All particles were introduced at a depth of approximately 40mm

Appendix C
Simulation Expressions

The following expressions were used in the modeling of the free surface

DenH	2345[kg m^-3]
DownH	0.047 [m]
DownPres	DenH*g*DownVFLiquid*(DownH-OffsetY-HeightAdjustForSlope)
DownVFLiquid	1-DownVFAir
HeightAdjustForSlope	0.02181488*OffsetZ
LaunderBottom	0.026 [m]
OffsetY	y-LaunderBottom
OffsetZ	z+0.350 [m]
UpH	0.064 [m]
UpPres	DenH*g*UpVFLiquid*(UpH-OffsetY-HeightAdlustForSlope)
UpVFAir	step((y-UpH)/1[m])
UpVFLiquid	1-UpVFAir

References

[1] Basics of Pet Imaging Physics, Chemistry, and Regulations, Gopal B.Saha, Springer Science, ISBN 0-387-21307-4

[2] Positrons in Solids, Pekka Hautjarvi, ISBN: 978-3-642-81318-4

[3] Positron Emission Tomography - Basic Sciences, Dale L Bailey, David W. Townsend, Peter E Valk, Michael N. Maisey, Springer Science+Business Media, ISBN 1-85233-798-2

[4] Positron emission particle tracking – Application and labelling techniques David J Parker, Xianfeng Fan, Particology 6 (2008) 16-23

[5] Positron emission particle tracking using a modular positron camera, D.J.Parker, T.W.Leadbeater , X.Fan , M.N.Hausard, A Ingram, Z.Yang, Nuclear Instruments and Methods in Physics Research A,604 (2009) 339-342

[6] A method for characterising solids translational and rotational motions using Multiple-Positron Emission Particle Tracking (Multiple-PEPT), Z.Yang, X.Fan, S.Bakalis, D.J.Parker, P.J.Fryer, International journal of multiphase flow, 34 (2008) 1152-1160

[7] Principles and technology of PET, DW Townsend, Annals academy of medicine, Vol 33 No2, pp133-145 March 2004

[8] Process applications of emission tomography, D.J.Parker, M.R.Hawkesworth, T.D Beynon, The Chemical Engineering Journal 56 pp109-117 1995

[9] Positron emission particle tracking - a technique for studying flow within engineering equipment, D.J. Parker, C.J. Broadbent, P. Fowles, M.R. Hawkesworth, P. McNeil, Nuclear Instruments and Methods in Physics Research A, Volume 326, Issue 3, , Pages 592–607 1993

[10] , A phenomenological study of a batch mixer using a positron camera, C.J. Broadbent, J. Bridgwater, D.J. Parker, S.T. Keningley, P. Knight, Powder Technology 76 317–329. 1993

[11] A case study of particle mixing in a ploughshare mixer using Positron Emission Particle Tracking J.R. Jones, J. Bridgwater, International Journal of Mineral Processing 53 29–38. 1998

[12] Comparative study by PEPT and DEM for flow and mixing in a ploughshare mixer ,B.F.C. Laurent a, P.W. Cleary, Powder Technology 228 171–186 2012

[13] Simulated and measured flow of granules in a bladed mixer—a detailed comparison, R. L. Stewart, J. Bridgwater, Y. C. Zhou, A. B. Yu, Chemical Engineering Science 56 5457–5471 2001

[14] Microdynamic analysis of particle flow in a horizontal rotating drum, R.Y. Yang, R.P. Zou, A.B. Yu, Powder Technology 138– 146 130 2003

[15] CFD–DEM modelling of particle flow in IsaMills – Comparison between simulations and PEPT measurements, C.T. Jayasundara, R.Y. Yang, B.Y. Guo , A.B. Yu I,Govender, A. Mainza , A. van der Westhuizen, J. Rubenstein, Minerals Engineering 24 (2011) 181–187

[16] Experimental verification of the scaling relationships for bubbling gas-fluidised beds using the PEPT technique, M. Stein, Y.L. Ding, J.P.K. Seville Chemical Engineering Science Volume 57, Issue 17, September, Pages 3649–3658 2002

[17] PEPT combined with high speed digital imaging for particle tracking in dynamic foams, K.E.Cole, K,E.Waters, D.J.Parker, S,J.Neethling, J.J.Cilliers,Chemical Engineering science, 65 pp1887-1890 2010

[18] Positron emission particle tracking measurements with 50 micron tracers, K.E.Cole, A.Buffler, N.P vander Meulen, J.J.Cilliers, J.P.Fanzidis, I.Govender, C.Liu, M.R. van Heerden, Chemical Engineering Science 75 pp235-242 2012

[19] Understanding the mechanical action on fabrics in a front loading washing machine, C.Mac Namara, A, Gabriele, C.Amador, S.Bakalis, Unpublished work http:// www.birmingham.ac.uk/documents/college-eps/chemical/eng-d/projects/abstracts/engd-macnamara.pdf

[20] Tracking inclusions in aluminium alloy castings using positron emission particle tracking (PEPT), W. D. Griffiths, D. J. Parker, X. Fan and M. Hausard J. Mat. Sci., vol. 26,(2010) No5 528-533

[21] The determination of inclusion movement in steel castings by positron emission particle tracking (PEPT), W. D. Griffiths, Y. Beshay, D. J. Parker, X. Fan, J Mater Sci 43 pp6853–6856 2008

[22] Labelling a single particle for positron emission particle tracking using direct activation and ion-exchange techniques, X.Fan, D.J,Parker,M.D.Smith, Nuclear Instruments and Methods in Physics Research A 562 (2006) 345-350

[23] Positron imaging systems for studying particulate. Granular and multiphase flows, T.W.Leadbeater, D.J.Parker,J.

[24] http://www.tunl.duke.edu/nucldata/GroundStatedecays/18Ne.shtml

[25] 2D transient filtration model for aluminium,Duygu Kocaefe, Rung tien Bui, Peter Waite,Applied Mathematical modeling 33 (2009) 4013-4030

[26] A coupled DEM/CFD analysis of die filling process, Y. Guo, Thesis, University of Birmingham, 2010

[27] Mathematical modeling and computer simulation of molten aluminium cleansing by the rotating impeller degasser, VS.Warke, S.Shankar, M.M Makhlouf, Journal of materials processing technology 168 (2005) 119-126

[28] Removal of Inclusions from molten aluminium by floatation in a stirred reactor: A mathematical model and a computer simulation, Olivier Mirgaux, Dennis Ablitzer, Emanuel Waz, Jean-Pierre Bellot, International Journal of chemical reactor engineering Vol 6 (2008) Article A52

[29] Collision rates of small particles in a vigorously turbulent fluid, J Abrahamson, Chemical Engineering Science 30 (1975) 1371-1379

[30] P.G. Saffman and I.S. Turner, Journal of Fluid Mechanics, Vol 1, Issue 01, pp 16- 30, May 1956

[31] Velocity Gradients and internal work in fluid motion. Camp T. R. and Stein P. C., J. Boston Sac. Civil *Engrs.* 30, 219. 1943

[32] The Collision rate of particles in turbulent flow, F.E.Kruis, K.A.Kusters, Chem Eng. Comm,Vol 158 (1997) 201-230

[33]. Pressure Fluctuations in isotropic turbulence. G. K. Batchelor, Mathematical Proceedings of the Cambridge Philosophical Society, 47, pp 359-374 (1951) doi:10.1017/S0305004100026712

[34] "Brownian Dynamics, Molecular Dynamics and Monte carlo modeling of colloidal systems", Jim C Chen, Albert S.Kim, Advances in colloid and interface science 112 (2004) 159-173

[35] Markov Chain Monte Carlo Simulations and Their Statistical Analysis (With Web-Based Fortran Code). B.A Bernd: World Scientific. ISBN 981-238-935-0. 2004

[36] Computational Methods for Fluid Dynamics 3rd Edition, Joel.H.Ferziger, Milovan Peric, ISBN 3-540-42074-6

[37] A tribute to D.B. Spalding and his contributions in science and engineering, V. Artemov, S.B. Beale, G. de Vahl Davis, M.P. Escudier, N. Fueyo, B.E. Launder, E. Leonardi, M.R. Malin, W.J. Minkowycz, S.V. Patankar, A. Pollard, W. Rodi, A. Runchal, S.P. Vankam International Journal of Heat and Mass Transfer, vol 52, p3884–3905, 2009

[38] Applications of Computational Fluid Dynamics (CFD) in iron- and steelmaking: Part1, K. Chattopadhyay, M. Isac ,R. I. L. Guthrie, Ironmaking and steelmaking, 37 (2010) 8

[39] Mathematical models of turbulence, B. E. Launder and D. B. Spalding. London: Academic Press Inc. (London), 1972

[40] Applications of computational fluid dynamics (CFD) in the food industry: a review, Bin Xia, Da-Wen Sun, Computers and Electronics in Agricilture 34 (2002) 5-24

[41] Smoothed particle hydrodynamics, J.J.Monaghan, Reports on Progress in Physics 68 1703-1759 2005

[42] Review of dicrete particle modelling of fluidized beds, N.G.Deen, M.Van Sint Annaland,M.A.Van der Hoef, J.A.M. Kuipers, Chemical Engineering Science 62 (2007) 28-44

[43] Force schemes in simulations of granular materials. J.Schäfer,S.Dippel, D.E.Wolf, D.E. Journal de Physique I 6 (1), pp5–20. 1996.

[44] Viscosity and temperature calculations for assemblies of inelastic frictional disks. O.R.Walton, R.L. Braun, Journal of Rheology 30 (5),949–980. 1986.

[45] Continuous potential discrete particle simulations of stress and velocity fields in hoppers transition from fluid to granular flow, P.A..Langston, U, Tüzün and D.M Heyes, Chemical Engineering Science 49 (8), 1259–1275. 1994.

[46] Interparticle sliding in the presence of adhesion, C. Thornton Journal of Applied physics D, 24 (1991) 1942-1946

[47] Impact of elastic spheres with and without adhesion, C. Thornton, K. K. Yin, Powder Technology, 65 (1991) 153-166

[48] Particle-fluid coupling , C.W.Hirt, Flow Science Technical Note 1999, FSI-99-TN50.

[49] Surface energy and the contact of elastic solids, K.L.Johnson, K.Kendal, A.D.Robersts, Proc.R. Soc Lond. A 324, 301-313 (1971)

[50] Effect of Contact Deformations on the Adhesion of Particles, B. V. Derjaguin, V. M. Muller, YU. P. Toporov (1975)

[51] Contact Mechanics and friction, V.L.Popov ISBN 978-3-642-10802-0

[52] Comparison of various adhesion contact theories and the influence of dimensionless load parameter, Xinghua Shi, Ya-Pu Zhao, Journal of Adhesion Science Technology, Vol 18 No1 (2004) 55-68

[53] On the role of eletrostatic forces in the adhesion of polymer particles to solid surfaces, B. V. DERJAGUIN, I. N. ALE!NIKOVA A&D Yu. P. TOPOROV, Powder Technol., 2 (1968/69) 15-l-158

[54] The effect of tangential force on the contact of elastic solids in adhesion, A.R.Savkoor, G. A. D.Briggs, Proc. R. Soc. Lond. A 356, 103–114. (doi:10.1098/rspa.1977.0123) 1977

[55] Mindlin, R. D., Deresiewicz, H., 1953. Elastic spheres in contact under varying oblique forces. Journal of Applied Mechanics, 20, 327-344.

[56] Further Consideration of the DMT model for elastic contact, M.D.Pashley, Colloids and Surfaces 12 69-77 1984

[57] Using the Dugdale approximation to match a specific interaction in the adhesive contact of elastic objects, Zhijun Zheng, Jilin Yu, Journal of Colloid and interface science 310 (2007) 27-34

[58] Castings – John Campbell – Butterworth-Heinemann – ISBN 0 7506 1696 2

[59] Aluminum alloy castings: properties, processes, and applications - ASM International - John Gilbert Kaufman, Elwin L. Rooy - ISBN 0-87170-803-5

[60] Deep filtration of liquid metals: Application of a simplified model based on the limiting trajectory model - Separations Technology - Volume 2, Issue 1, January 1992, Pages 46-56

[61] The Influence of surface preparation and pretreatments on the oxidation of liquid aluminium and aluminium alloys, S.Impey, D.J. Stephenson and J.R.Nicholls , Microscopy of oxidation 2, p 323-336 1993

[62] R. Raiszadeh, "A Method to Study the Behavior of Double Oxide Film Defect in Aluminum Alloy", PhD thesis, University of Birmingham, 2005

[63] Modelling of inoculation of metallic melts: Application to grain refinement of Aluminium by Al-Ti-B, A.L. Greer, A.B. Bunn, A.Tronche, P.V.Evans, D.J. Bristow, Acta mater. , Vol 48, p 2823-2835, 2000

[64] A Brief history of grain refinement of cast light alloys, D.H. StJohn, M.A. Easton, P.Cao, M. Beringham and M. Qian, Materials science forum, Vol 690 123-129 Trans Tech Publications 2013

[65] Aluminium foil: Its typical quality problems and their causes, O. Keles, M.Dundar, Journal of Materials Processing Technology,Volume 186, Issues 1–3, , pp 125–137 7 May 2007

[66] Carbothermal reduction of alumina: Thermochemical equilibrium calculations and experimental investigation, M.Halmann, A Frei, A.Stienfield, Energy 32 (2007) 2420-2427

[67] Purifying effects and mechanism of a new composite filter – Materials Science and Engineering A – Vol 426 p53-58

[68] Effect of inclusions on the tensile properties of Al -7% Si -0.35% Mg (A356.2) aluminium casting alloy, L.Liu, F.H.Samuel, Journal of Material science 33 (1998) 2269-2281

[69] Fatigue behavior of A356-T6 aluminum cast alloys. Part I. Effect of casting defects Q.G. Wang, D. Apelian, D.A. Lados, Journal of Light Metals, Volume 1, Issue 1, February 2001, Pages 73–84

[70] Fatigue behaviour of AA356-T6 cast aluminium alloy weakened by cracks and notches, B. Atzori *, G. Meneghetti, L. Susmel, Engineering Fracture Mechanics 71 (2004) 759–768

[71] Cyclic plasticity at pores and inclusions in cast Al-Si alloys – Engineering fracture mechanics Vol 70 p1281- 1302

[72] Casting defects and the fatigue life of an aluminum casting alloy M.J. Couper, A.E. Neeson, J.R. Griffiths, Fatigue Fract. Eng.Mater. Struct. 13 (1990) 213-227.

[73] Filtration of Aluminium – Experiments, Wetting, and Modeling, S.Bao, phD thesis Norwegian University of science and technology, department of Materials science and engineering, October 2011

[74] Removal of Inclusions – A survey and comparison of principle, Light Metals, 1992: p. 324-326

[75] Modelling of solid particle aggregation dynamics in non-wetting liquid medium, Michel Cournil, Frederic Gruy, Pascal Gardin, Hubert Saint-Reynold, Chemical Engineering and processing 45 (2006) 586-597

[76] A Study of the behaviour of double oxide films in Al alloy melts, M. El-Sayed, H. Saleem, A Kwndeil and W.D. Griffiths, Materials science forum, Vol 690 260-265 Trans Tech Publications 2013

[77] Population Balances: theory and applications to particulate systems in engineering, D.Ramkrishna, 2000 ISBN-10: 0125769709

[78] Production of ceramic foam filters for molten metal filtration using expanded polystyrene - Journal of the European ceramic society Vol 27 p637-640

[79] Molten Aluminum Flow Control via Foam Filtration, B. Braun. Modern Casting, 2004. 94(3): p. 21-24.

[80] Application of Ceramic Foam Filter in Aluminum Manufacture, Q. Gui, Aluminum processing, 2003(1): p. 23.

[81] Purification technology of molten aluminium, S.Bao'de, D Weir jiang,Z Yao'he, J. Cent Univ. Technol. Vol 11 No2 2004 p134-141

[82] The modelling of oxide film entrainment in casting systems using computational modelling, C. Reilly, N.R. Green, M.R. Jolly, J.-C. Gebelin, Applied Mathematical Modelling 37 (2013) 8451–8466

[83] The properties and use of fluxes in molten aluminium processing, T.A. Utigard, K.Friesen. R.R.Roy, J.Lim, A.Silny, C.Dupuis, Journal of the minerals, metals and materials society, November 1998

[84] Study of fluxing temperature in molten aluminium refining process, Journal of materials processing technology 182 (2007) 450-455

[85] Melt Conditioned Direct Chill Casting (MC-DC) of Wrought Al-alloys - Solid State Phenomena. 141-143(2008) 403-408 2008 http://bura.brunel.ac.uk/handle/2438/2683

[86] A new technology for treating liquid metals with intensive melt shearing, Z.Y.Fan, Y.B.Zuo, B. Jiang, Proceedings of the fifth international light metals technology conference, Materials Science Forum 690 pp141-144 2011

[87] Inclusion & bubble in steel – a review Zhang Li Feng : Journal of Iron and steel research, International 2006 Volume 13 Issue 3 Pages 01-08

[88] Non-Metallic Inclusions in Steel, Part III, R. Kiessling, The Institute of Materials, London, 1989

[89] Innovation in Electric Arc Furnaces: Scientific Basis for Selection, Y. N. Toulouevski, I.Y.Zinurov, ISBN 978-3-642-03800-6

[90] Alumina inclusion behaviour during steel deoxidation, L.Zhang,B.G.Thomas, 7th European electric steelmaking conference, May 26-29 pp. 2,7702.86 2002

[91] Inclusions in continuous casting of steel, L. Zhang , BG Thomas: XXIV National Steelmaking Symposium, Morelia, Mich, Mexico, 26-28, Nov.2003, pp. 138-183.

[92] State of the Art in Evaluation and Control of Steel Cleanliness, L Zhang and B.G. Thomas, ISIJ International, 43 , No. 3, pp. 271–291 2003

[93] The state of the art in the control of inclusions in tire cord steels – a review, L.Zhang, Steel research Int, 77 No3 pp158-169 2006

[94] Modelling of reoxidation inclusion formation in steel sand casting, K.D.Carlson, A.J.Melendez, C.Beckerman, Proceedings of the 63rd SFSA technical and operating conference, paper No5.6, Steel Founders' society of America, Chicargo, IL. 2009.

[95] Characterization of inclusions in clean steels: a review including the statistics of extremes methods – Progress in materials science - Vol 48 p457-520 - 2003

[96] Effects of Undersized Inclusions on Ductile Fracture Behavior of FeNi42 Alloy in Sheet Tension - Journal of Iron and Steel Research Volume 14, Issue 5, Supplement 1, September 2007, Pages 53-58

[97] On the critical inclusion size of high strength steels under ultra-high cycle failure, Z.GYang, J.M.Zhang, S,X.Li, G.Y.Li, Q.Y.Wang, W.J.Hui,Y.Q.Weng, Materials Science and Engineering A, 427 pp167-174

[98] Extreme value models for the assessment of steels containing multiple types of inclusion, Stefano Beretta, Clive Anderson, Yukiaka Murikami, Acta Materialia 54 (2006) 2277-2289

[99] The influence of non-metallic inclusions on the corrosion fatigue of mild steel - Corrosion Science Vol 25 No 3 p171- 184 1985

[100] Review article on the influence of sulphide inclusions on the corrodibility of Fe and steel – Corrosion science Vol 9 p585-602 1985

[101] Role of iron sulfide in the formation of cracks in weld joints, G. F. Deev,V. V. Popovich, V. N. Palash, V. V. Karikh, Materials Science, Vol. 18, No. 3, pp. 109–112, May–June, 1982.

[102] The Influence of non metallic inclusions on the corrosion fatigue of mild steel, G. P. Ray, R. A. Jarman. J. G. N. Thomas, Corrosion Science, Vol. 25, No. 3, pp. 171 184, 1985

[103] TCH600 Nitrogen/Oxygen/Hydrogen Determinator Specification Sheet http://www.usbiocolombia.com/files/inorganica/tch600-hoja-tecnica.pdf

[104] http://www.leco.com/products/analytical-sciences/oxygen-nitrogen-hydrogen-analyzers/836-series

[105] Indirect Methods of Detecting and Evaluating Inclusions in Steel-A Review, L. Zhang, Journal of iron and steel research international, 13(4) pp 01-08

[106] Inclusion control in high=performance steels, L.E.K.Hoppa, A.S.Helle, Journal of materials processing technology 53 pp177-186 1995

[107] Behavior of argon bubbles during continuous casting of steel - ISS 80th Steelmaking Conference, Chicago, IL, ISS, April 13-16, 1997, Proceedings pp. 375-384.

[108] The clustering of alumina inclusions, T. B. Braun, J. F. Elliott, M. C Flemings, Metallurgical Transactions B, 10, 2, pp 171-184 1979

[109] Ladle Injection Metallurgy, L.E.K. Holappa, International Materials Reviews, 27, Number 2, 1982 (ASM-IOM-Maney)

[110] Development of novel carbon bonded filter compositions for steel melt filtration M.Emmel, C,Aneziris, Ceramics International 38 pp5165-5173 2012

[111] Removal of liquid non-metallic inclusion from molten steel using the method filtration. K. Janiszewski and Z. Kudlinski, Proceedings of 15th International Conference on Metallurgy and Materials Hradec nad Moravicí 23rd-25th may 2006, Metal pp1–9

[112] http://www.advancedmaterials.us/26R-0804UPG.htm

[113] An Introduction to Atmospheric Physics 2nd Edition, David G. Andrews, June 2010 ISBN: 9780521693189

[114]http://www.np.ph.bham.ac.uk/pic/forte

[115] http://www.lowdenlimited.co.uk/LowMelting/LensAlloy136.html

[116] The Application Of Positron Emission Particle Tracking To Study Non-Metallic Inclusions In Metal Castings, Youssef Beshay, University of Birmingham, July 2010

[117] http://physics.nist.gov/PhysRefData/XrayMassCoef/tab3.html

[118] http://www.nist.gov/pml/data/halflife-ascii.cfm

[119] Using gamma radiation to measure density gradients in reconstituted wood products Theodore L. Laufenberg, Forest Prod. J.36 (2) 59-62 February 1986

[120] http://www.mindat.org/min-4421.html

[121] http://www.mindat.org/min-2806.html

[122]http://www05.abb.com/global/scot/scot205.nsf/veritydisplay/f5b80ceeae8b806085257bf1006acc84/$file/LiMCA%20CM_Brochure%20Hr.pdf

[123]http://www.abb.co.uk/product/seitp330/c1256dde004b6b1d85256e2300764e3b.aspx?tabKey=6

[124] http://www.medx-inc.co/ecat_exact_47.html

[125] Temperature Dependence of Density and Thermal Expansion of Wrought Aluminum Alloys 7041, 7075 and 7095 by Gamma Ray Attenuation Method, K. Narender, A.S.M. Rao, K.G. K. Rao, N.G.Krishna, Journal of modern physics Vol 4 p331-336 2013

[126] The Development of Positron Imaging Systems for Applications in Industrial Process Tomography, T.W.Leadbeater, phD Thesis, Birmingham University.

[127] http://cgns.sourceforge.net/

[128] http://www.lmnoeng.com/TankDischarge.htm

[129] Refining grain structure and porosity of an aluminium alloy with intensive melt shearing, Y Zuo, H.Li, M. Xia, B. Jiang, G.M.Scamans, Z.Fan, Scripta Materialia 64, pp 209-212, 2011

[130] Dynamics of free energy of alpha alumina (0001) surfaces: I.Semi Empirical model - A Marmier and MW FINNIS. Journal of Physics Condensed matter

[131] Evaluation of the efficiency of ceramic foam and bonded particle cartridge fltrationsystems, N.J.Keegan, W.Schneider, H.P.Krug, V.Dopp, Foseco and V.A.W. Aluminium,
http://www.pyrotek.info/documents/techpapers/23_Ceramic_Foam_%26_Bonded_Particles.pdf

[132] http://sourceforge.net/projects/napoleonbrandy/ , D.Burnard

[133] http://www.bbcbasic.co.uk/bbcwin/download.html , R.T.Russell